1980

Neutron scattering studies of the magnetic properties and lattice dynamics of the mixed valent CeSn3

Chun-Keung Loong
Iowa State University

INFORMATION TO USERS

This was produced from a copy of a document sent to us for microfilming. While the most advanced technological means to photograph and reproduce this document have been used, the quality is heavily dependent upon the quality of the material submitted.

The following explanation of techniques is provided to help you understand markings or notations which may appear on this reproduction.

1. The sign or "target" for pages apparently lacking from the document photographed is "Missing Page(s)". If it was possible to obtain the missing page(s) or section, they are spliced into the film along with adjacent pages. This may have necessitated cutting through an image and duplicating adjacent pages to assure you of complete continuity.

2. When an image on the film is obliterated with a round black mark it is an indication that the film inspector noticed either blurred copy because of movement during exposure, or duplicate copy. Unless we meant to delete copyrighted materials that should not have been filmed, you will find a good image of the page in the adjacent frame.

3. When a map, drawing or chart, etc., is part of the material being photographed the photographer has followed a definite method in "sectioning" the material. It is customary to begin filming at the upper left hand corner of a large sheet and to continue from left to right in equal sections with small overlaps. If necessary, sectioning is continued again—beginning below the first row and continuing on until complete.

4. For any illustrations that cannot be reproduced satisfactorily by xerography, photographic prints can be purchased at additional cost and tipped into your xerographic copy. Requests can be made to our Dissertations Customer Services Department.

5. Some pages in any document may have indistinct print. In all cases we have filmed the best available copy.

University
Microfilms
International

300 N. ZEEB ROAD, ANN ARBOR, MI 48106
18 BEDFORD ROW, LONDON WC1R 4EJ, ENGLAND

INFORMATION TO USERS

This was produced from a copy of a document sent to us for microfilming. Wh
most advanced technological means to photograph and reproduce this doc
have been used, the quality is heavily dependent upon the quality of the m
submitted.

The following explanation of techniques is provided to help you unde
markings or notations which may appear on this reproduction.

1. The sign or "target" for pages apparently lacking from the docu
photographed is "Missing Page(s)". If it was possible to obtain the n
page(s) or section, they are spliced into the film along with adjacent
This may have necessitated cutting through an image and dupl
adjacent pages to assure you of complete continuity.

2. When an image on the film is obliterated with a round black mark
indication that the film inspector noticed either blurred copy beca
movement during exposure, or duplicate copy. Unless we meant to
copyrighted materials that should not have been filmed, you will
good image of the page in the adjacent frame.

3. When a map, drawing or chart, etc., is part of the material being
graphed the photographer has followed a definite method in "secti
the material. It is customary to begin filming at the upper left hand
of a large sheet and to continue from left to right in equal sectio
small overlaps. If necessary, sectioning is continued again—be
below the first row and continuing on until complete.

4. For any illustrations that cannot be reproduced satisfactor
xerography, photographic prints can be purchased at additional c
tipped into your xerographic copy. Requests can be made
Dissertations Customer Services Department.

5. Some pages in any document may have indistinct print. In all c
have filmed the best available copy.

University
Microfilms
international

300 N. ZEEB ROAD, ANN ARBOR, MI 48106
18 BEDFORD ROW, LONDON WC1R 4EJ, EN

LOONG, CHUN-KEUNG

NEUTRON SCATTERING STUDIES OF THE MAGNETIC PROPERTIES AND LATTICE DYNAMICS OF THE MIXED VALENT CERIUM-TIN(3)

Iowa State University PH.D. 1980

PLEASE NOTE:

In all cases this material has been filmed in the best possible way from the available copy. Problems encountered with this document have been identified here with a check mark ✓.

1. Glossy photographs _____
2. Colored illustrations _____
3. Photographs with dark background _____
4. Illustrations are poor copy _____
5. Print shows through as there is text on both sides of page _____
6. Indistinct, broken or small print on several pages ✓
7. Tightly bound copy with print lost in spine _____
8. Computer printout pages with indistinct print _____
9. Page(s) _____ lacking when material received, and not available from school or author
10. Page(s) _____ seem to be missing in numbering only as text follows
11. Poor carbon copy _____
12. Not original copy, several pages with blurred type _____
13. Appendix pages are poor copy _____
14. Original copy with light type _____
15. Curling and wrinkled pages _____
16. Other _____

Neutron scattering studies of the magnetic properties and lattice dynamics of the mixed valent $CeSn_3$

by

Chun-Keung Loong

A Dissertation Submitted to the

Graduate Faculty in Partial Fulfillment of the

Requirements for the Degree of

DOCTOR OF PHILOSOPHY

Department: Physics
Major: Solid State Physics

Approved:

Signature was redacted for privacy.

In Charge of Major Work

Signature was redacted for privacy.

For the Major Department

Signature was redacted for privacy.

For the Graduate College

Iowa State University
Ames, Iowa

1980

TABLE OF CONTENTS

I. INTRODUCTION

Among the rare earth metals and compounds there exists a class of materials which exhibit valence instabilities. Experimental results suggest that in these materials the electronic occupation of the 4f shell of the rare earth ion changes either continuously or discontinuously as their temperature, external pressure or composition is varied. In certain ranges of temperatures, pressure or composition these materials exist in a state in which the energy required to excite an f-electron from the ionic shell to the conduction band is small or zero and the average occupation of the f-shell is non-integral due to the fluctuations of the electrons between the localized f-shell and band states. To describe such a state and the associated materials, terms such as 'mixed valence', 'intermediate valence', 'valence fluctuation', 'configuration crossover', or 'interconfiguration fluctuation (ICF)' have appeared in the literature.

In recent years there has occurred a rapid growth in experimental and theoretical studies in this area; nevertheless, it is believed that the study of mixed valence materials is still in its adolescence. Experimentally, new materials are to be examined and more experiments aiming to obtain direct information on the mixed valent characters are to be performed. At present there is no adequate theory capable of explaining the unusual behavior observed in the mixed valence compounds and various theoretical models proposed to explain certain properties need to be reviewed critically in the light of existing experimental data.

Special conferences (1,2) and reviews (3-10) have been devoted to this research area in recent years. Therefore, in the introductory sections we shall make no effort to present a complete discussion of the mixed valence materials per se. Instead, we shall first outline the general properties of some well-known mixed valence materials (such as cerium metal and samarium chalcogenides) and then we shall discuss in greater detail the unusual characteristics of $CeSn_3$, the mixed valent compound with which we are primarily concerned.

A. Valence Instabilities in Rare Earth Materials

Today qualitative information on the electronic configurations of the rare earth elements in their metallic state has been obtained from extensive studies of their magnetic data and metallic radius data. The magnetic data provide information about the number of 4f electrons, from which the number of valence electrons can be inferred. On the other hand, an empirical relationship between the metallic radius, the coordinate number and the valence have been pointed out by Pauling (11) and Zachariasen (12). One may deduce the number of valence electrons by using this relationship once the metallic radius (13) of a rare earth ion in a solid is determined from the lattice constants. In Table 1.1, we list the rare earth elements, the ionic configuration of their oxidation states and the electronic structures of their metallic states. In metals, the 4f electrons could be considered as highly localized, with the rare earth ion retaining the ionic moment predicted by Hund's rules. In Fig. 1.1, we plot the radii of the rare earth metals versus their atomic numbers. Barium (divalent) and hafnium

Table 1.1. Electronic structures of the rare earth elements (after Ref. 13)

Atomic Number	Element	Ionic Configuration for Known Oxidation States[a]			Metallic State[b]		
					Bonding Electrons		
		M^{+2}	M^{+3}	M^{+4}			
		4f	4f	4f	6s	5d	4f
57	La	---	0	---	2	1	0
58	Ce	---	1	0	2	1	1
59	Pr	---	2	1	2	1	2
60	Nd	---	3	---	2	1	3
61	Pm	---	4	---	2	1	4
62	Sm	6	5	---	2	1	5
63	Eu	7	6	---	2	0	7
64	Gd	---	7	---	2	1	7
65	Tb	---	8	7	2	1	8
66	Dy	---	9	---	2	1	9
67	Ho	---	10	---	2	1	10
68	Er	---	11	---	2	1	11
69	Tm	---	12	---	2	1	12
70	Yb	14	13	---	2	0	14
71	Lu	---	14	---	2	1	14

[a]Based on spectral data. The ionic species M^{+2}, M^{+3} and M^{+4} have no 6s or 5d electrons.

[b]Based on magnetic and metallic radius data.

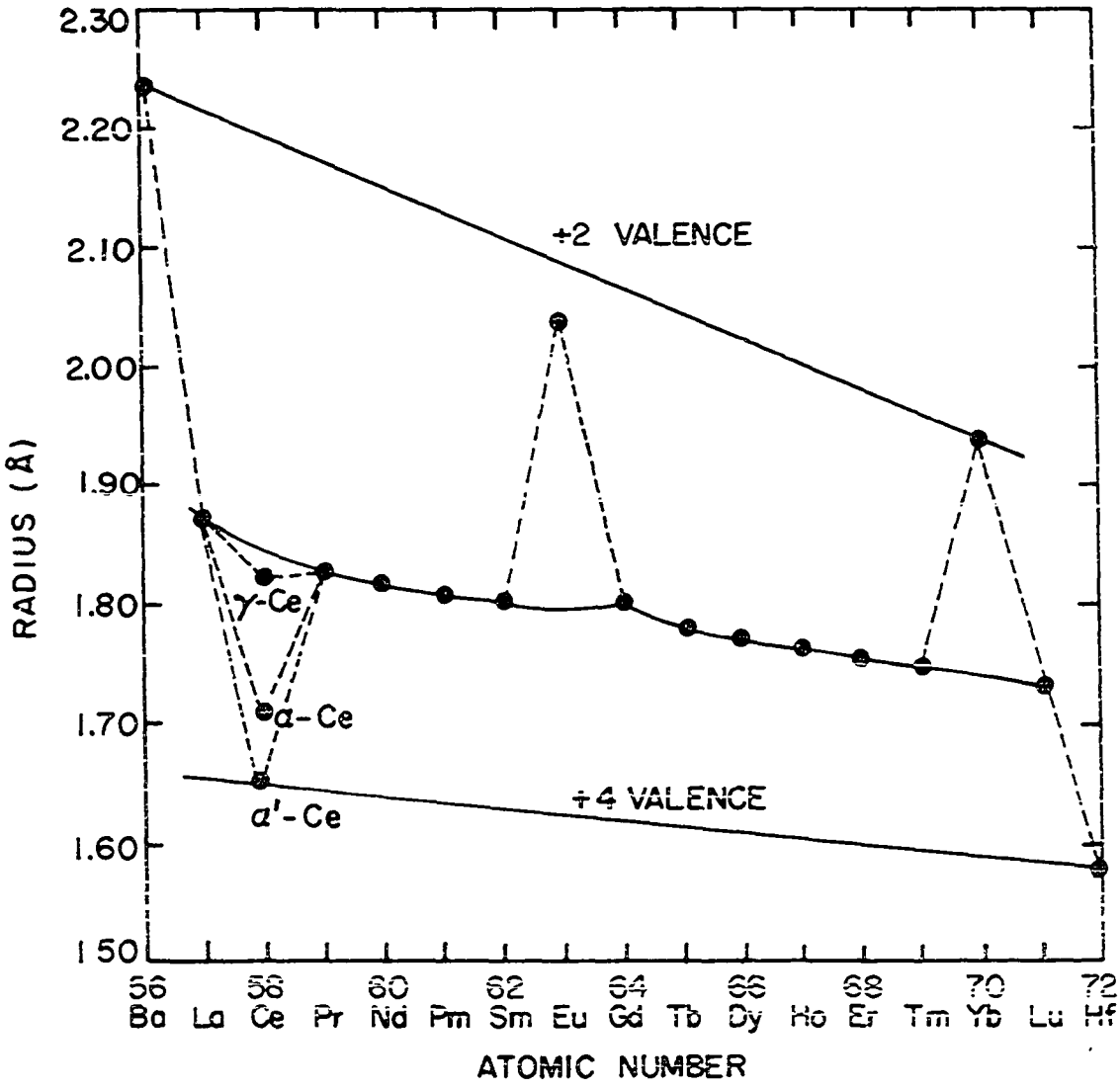

Figure 1.1. The metallic radii of rare earths versus their atomic numbers. Barium (divalent) and hafnium (tetravalent) are included for the purpose of comparison (after Ref. 13)

(tetravalent) are included for the purpose of comparison. As can be seen, there are three major deviations from the smooth curve occurring at Ce, Eu and Yb. The valences (13) of Eu and Yb deduced from metallic radius data are 2.1 ± 0.1 and $2.0 \pm .01$ respectively and agree favorably with those obtained from the magnetic data. This can be understood in terms of Hund's rule which states that states with half-filled or completely-filled 4f levels (the divalent states of Eu and Yb fall into this category) are quantum mechanically more favorable. The situation for Ce is very interesting because of the presence of electronic phase transitions in a certain range of temperatures and pressure. Now we proceed to discuss Ce and its phase transitions.

1. Cerium metal and Ce-Th alloy

The pressure-temperature relationships of the five established solid phases of Ce are summarized in the phase diagram (14) in Fig. 1.2. At room temperature and atmospheric pressure, Ce exists in the face-centered cubic (f.c.c.) γ phase with lattice constant $a = 5.16$ Å. A valence of 3.09 is obtained using the metallic radius based on this lattice constant (13). Above the room temperature the magnetic susceptibility of γ-Ce obeys the Curie-Weiss law, with an effective moment of approximately 2.54 Bohr magneton, the expected value for one 4f electron localized on each Ce atom in a $J = 5/2$ state (15,16). In addition, the measured field induced magnetic form factor (17) is found to be in good agreement with the free ion 4f magnetic form factor of Ce^{3+}. Therefore, the valence of Ce in the γ phase is estimated to be +3.0 to within a few percent.

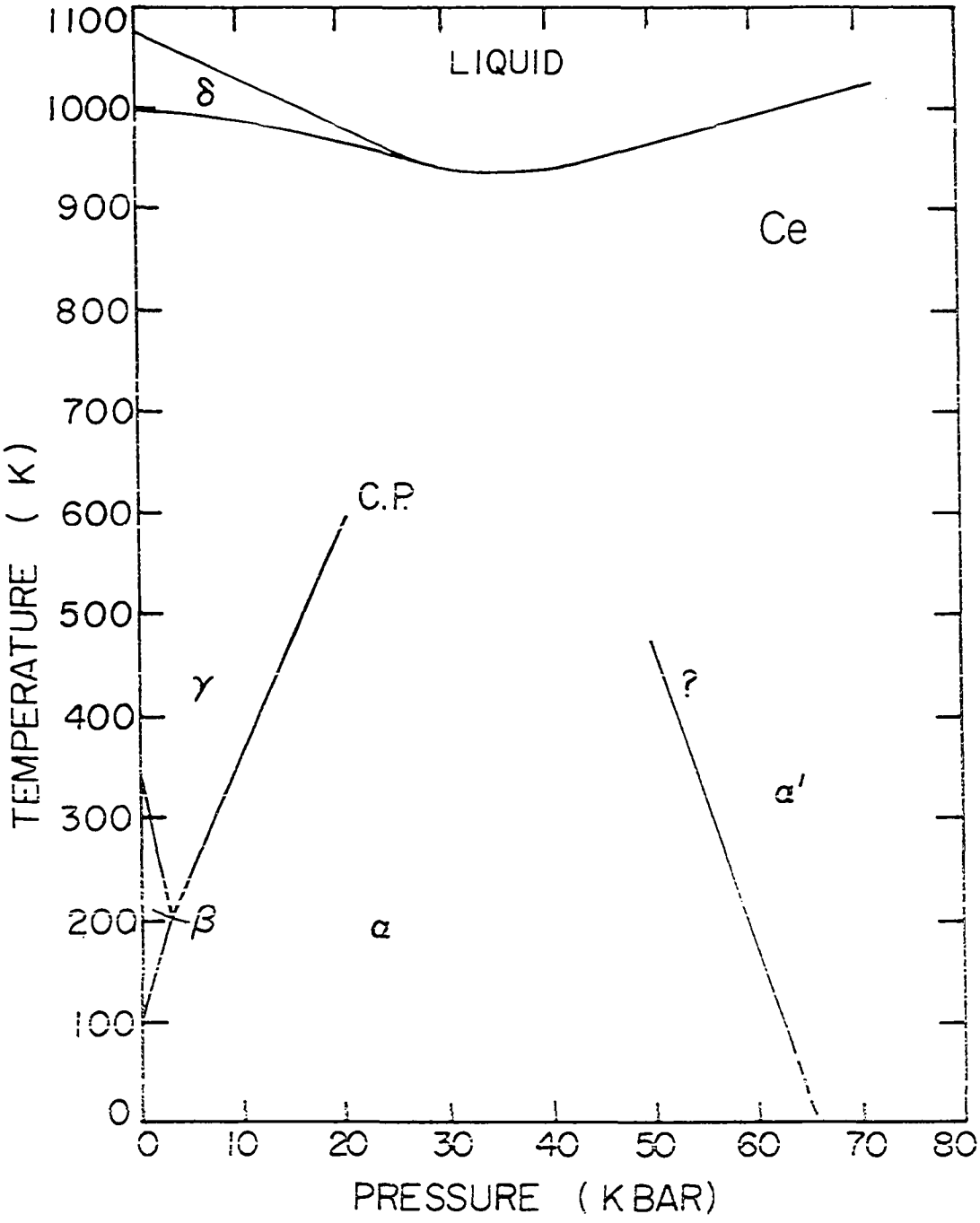

Figure 1.2. Phase diagram of cerium (after Ref. 14)

An interesting phase transition occurs when γ-Ce is compressed to modest pressures about 8 kbar at room temperature. At this critical pressure the lattice constant suddenly collapses from 5.16 Å to 4.85 Å (Fig. 1.3a) resulting in a volume change of about 17%, but no corresponding change in lattice symmetry (18-20). This collapsed phase is known as the α phase. At the γ-α phase transition the electrical resistivity (21,22) drops by a factor of almost 2 (Fig. 1.3b), indicating that additional electrons are promoted to the conduction band. Furthermore, the magnetic susceptibility (23,24) decreases sharply (Fig. 1.3c) suggesting the number of 4f electrons on each Ce atom is reduced in the α phase. The valence of Ce (Fig. 1.3d) in the α phase was estimated to be 3.67 (20,25) based on the metallic radius data and the Hall effect measurement. The electronic specific heat coefficient γ(= 12.8 mJ/mole·K^2) (26,27) is about 3 to 5 times larger than the values for other tetravalent metals such as Th (28) and Hf (27). This indicates that the 4f states of α-Ce are close to the Fermi level so that electronic transitions between the 4f and the band states are energetically possible.

The experimental results above indicate that in the α phase the Ce ions are in a mixed valence state such that on the time average almost 65% of the 4f electrons are promoted to the conduction band. This idea is supported by the discovery of the higher-pressure α' phase (20,22,29) (∿50 kbar, room temperature) exhibiting a C-centered orthorhombic structure. From metallic radius considerations, it is

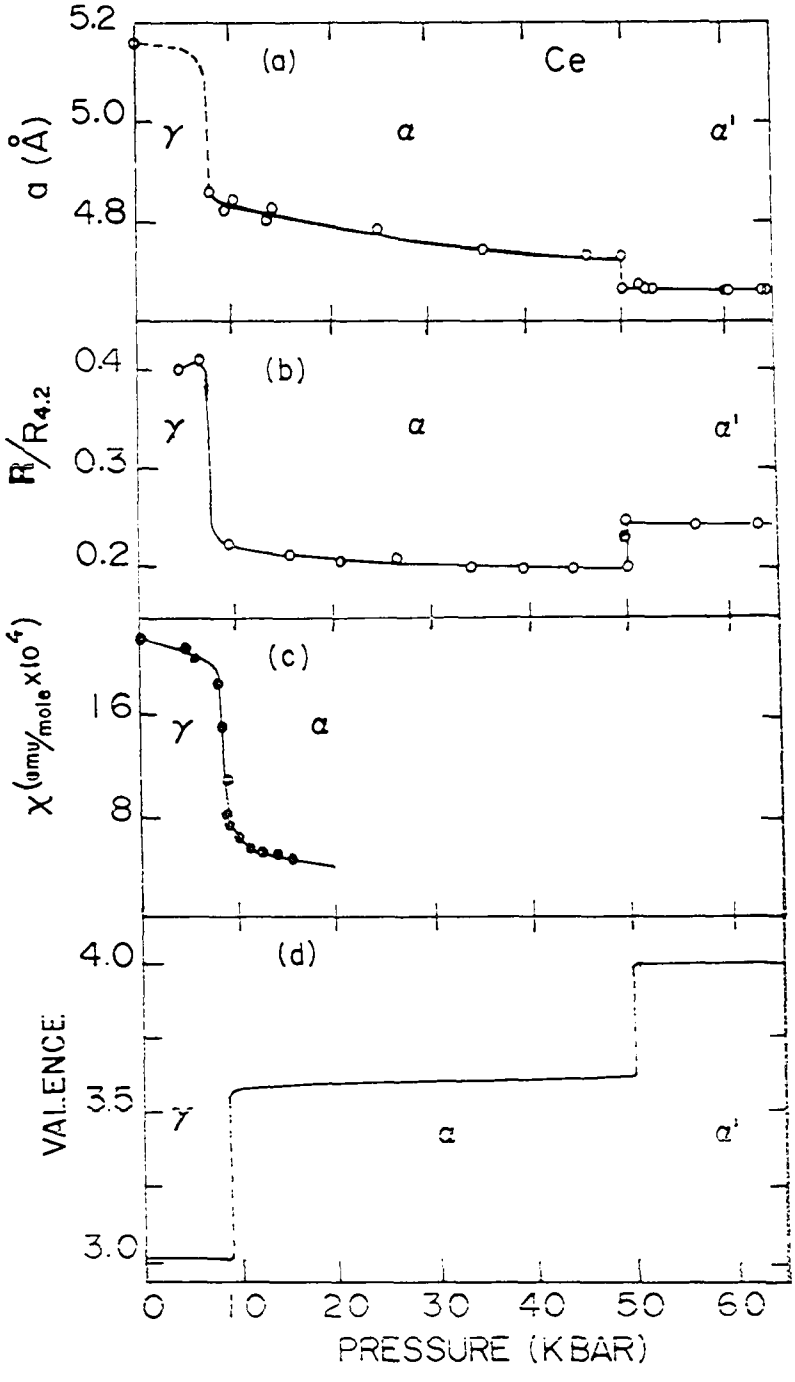

Figure 1.3. The lattice constant a (18), the electrical resistivity R relative to its value at 4.2K (21), the magnetic susceptibility χ (23) and the valence of Ce (14) versus temperature

believed that α'-Ce is tetravalent (Fig. 1.3d), and thus has no localized 4f electrons, which is consistent with its superconducting behavior (29).

On the other hand, a closer look at other experimental data reveals that the valence-change scheme is an oversimplified description of the electronic and magnetic natures of cerium and its allotropes. For example, as shown in Fig. 1.4, the magnetic susceptibility (24,26,30,31) of α-Ce actually increases gradually as the temperature is increased from 80 to 150K. Moreover, there is a sharp rise in the susceptibility below 20K whose origin is presently not understood and no evidence of magnetic ordering is found (24). There are other experiments such as positron annihilation (32) and photoemission (33) experiments which cannot be explained by the valence-change model. In short, in spite of the fact that the electronic phase transition of Ce metal was known since 1912 (34) and Zachariasen and Pauling pointed out more than thirty years ago (35,36) that its origin was related to a valence change, our present day understanding of the electronic nature and the mechanism of the phase transitions in Ce is still incomplete.

It is known that the γ to α phase transition of Ce can also be induced by lowering the temperature after alloying with thorium (37). By studying polycrystalline samples of $Ce_{1-x}Th_x$, $x \cong 0.26$ (38), it has been observed that the lattice constant (Fig. 1.5a), the magnetic susceptibility (Fig. 1.5b) and hence the effective moments (Fig. 1.5c) decrease suddenly at the transition temperature of about 150K. From the analysis of the temperature dependence of the lattice constant it was inferred that the Ce valence began to increase from a value of

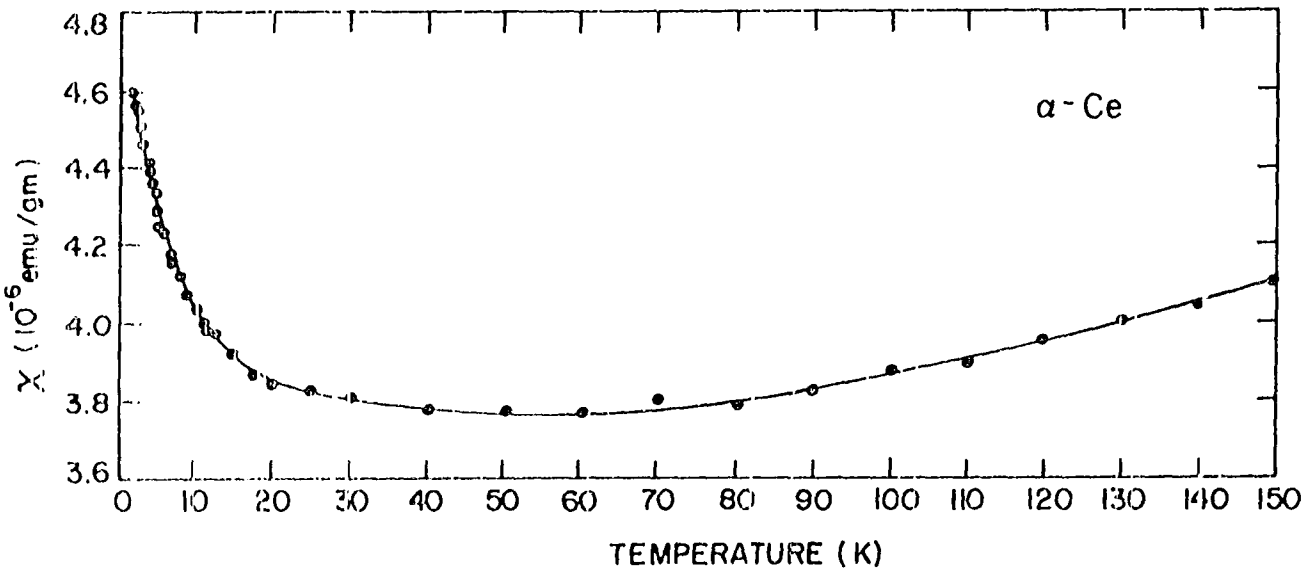

Figure 1.4. The magnetic susceptibility of α-Ce (after Ref. 14)

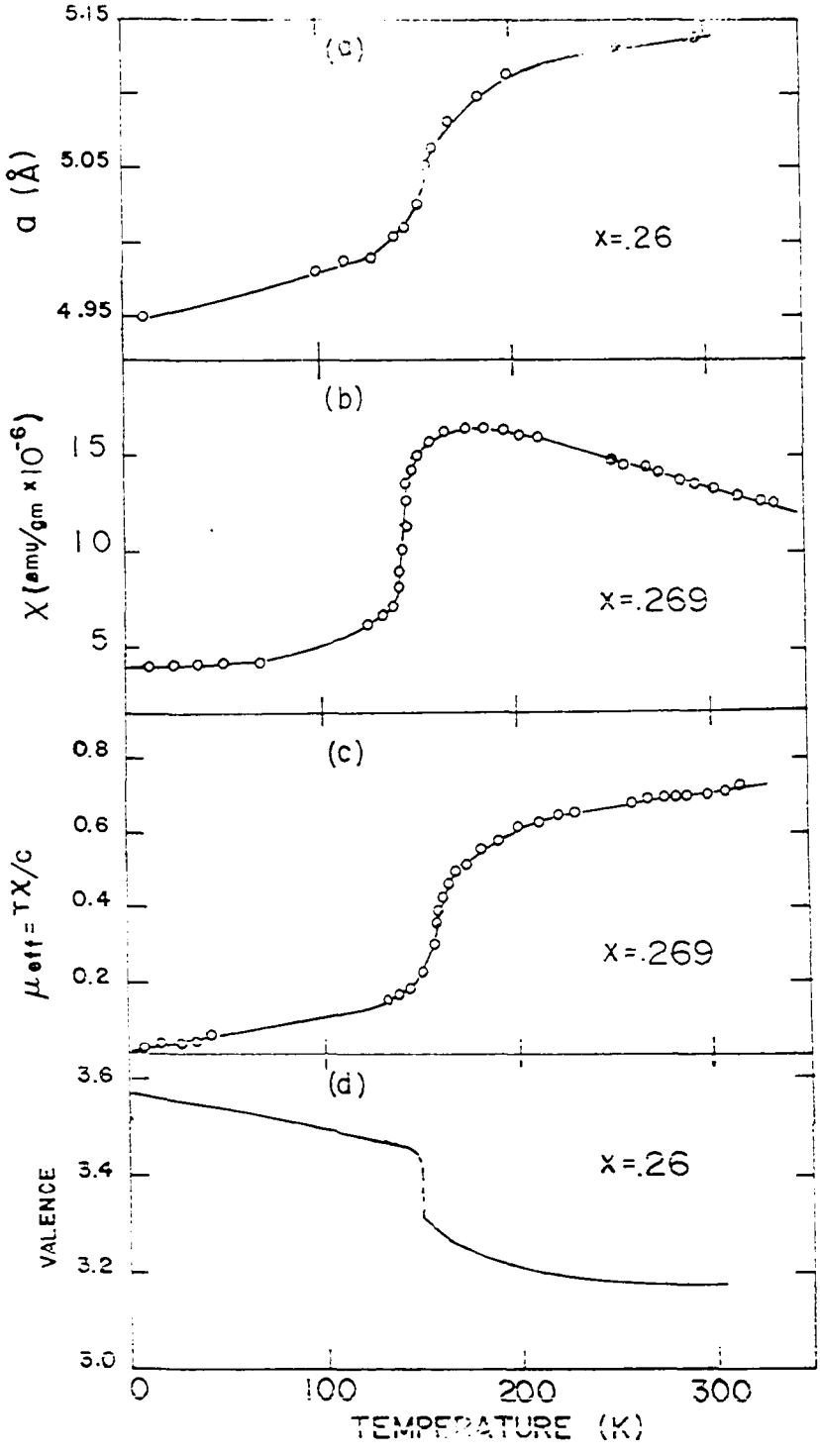

Figure 1.5. The lattice constant a, the magnetic susceptibility χ, the effective moments and the valence in $Ce_{1-x}Th_x$ versus temperature (after Ref. 15).

3.17 in the γ phase at room temperature, changed abruptly from 3.29 to 3.39 at the phase transition, and leveled off at 3.59 at T = 10K (Fig. 1.5d).

2. Samarium chalcogenides and cation-substituted SmS

The mixed valent characters of SmS, SmSe and SmTe have received much attention in recent years (39). At room temperature and atmospheric pressure they are semiconductors and crystallize in the NaCl structure. Both the metallic radius measurements (40) and magnetic data (41,42) indicate that the Sm ions in these materials are divalent. At a pressure about 6.5 kbar, as shown in Fig. 1.6a, the volume of SmS collapses by 13% without changing its lattice symmetry (40,43). The volume reduction for SmSe and SmTe, on the other hand, occur continuously with increasing pressure to 50 kbar (40). As the pressure increases, the electrical resistivities (44,45) of SmS, SmSe and SmTe decrease (Fig. 1.6b) and their colors change from black to gold, black to tan and black to purple, respectively, indicating a phase transition from a low pressure semiconducting state to a collapsed metallic state. The intermediate valences of Sm deduced from the lattice data for SmS; SmSe and SmTe in the collapsed high pressure phase are 2.8, 2.76 and 2.66 (43) respectively. Similar to the case of α-Ce, the magnetic susceptibility of SmS decreases abruptly at the valence-change transition and evidence of magnetic ordering at low temperatures is not found (42). SmS in the collapsed phase also has a large electronic specific heat coefficient, 145 $mJ/mole \cdot K^2$ (46), indicating that the 4f levels are very close to the Fermi energy.

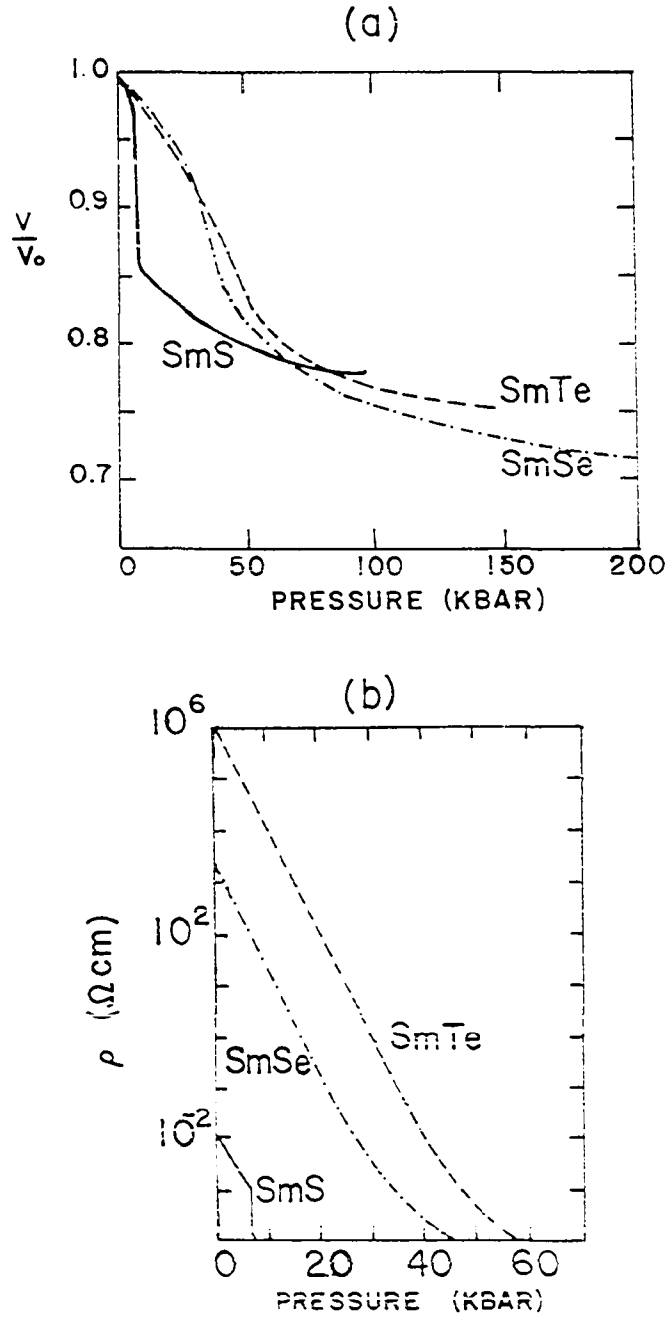

Figure 1.6. (a) Pressure-volume relationship for Sm monochalcogenides (after Ref. 39); (b) resistivity as a function of pressure for Sm monochalcogenides (after Ref. 39)

Similar to $Ce_{.74}Th_{.26}$, the system $Sm_{.75}Y_{.25}S$ exhibits a temperature-induced phase transition at atmospheric pressure (47). As can be seen in Fig. 1.7, at room temperature, $Sm_{.75}Y_{.25}S$ is in the gold-color phase and the lattice expands as the temperature decreases. It goes through a broad transition at about 200K and transforms into the black-color phase at lower temperatures. The Sm valences deduced from the temperature dependence of the lattice constants are 2.7 at 293K, 2.5 at 200K and 2.3 at 10K. There are other interesting experimental studies of this system including the phonon measurements using inelastic neutron scattering techniques. They will be discussed and compared with the $CeSn_3$ data later in Chapter VII.

B. Physical Properties of $CeSn_3$ and Evidence of its Mixed Valent Character

We pointed out in the last section that experimental observations of the changes in lattice constants, magnetic susceptibilities and electric resistivities in systems like Ce metal, SmS, SmSe and SmTe could be explained qualitatively by a scheme of valence-change. However, quantitative understanding of the phenomenon of mixed valence has to rely on extensive investigations of the nature of the electronic wave functions of the mixed valence materials. Experiments performed on α-Ce would provide direct information, yet the preparation of allotropically pure α-Ce samples suitable for experimental studies is often too difficult to be realized in practice. We also mentioned that one may avoid the necessity of high-pressure study by alloying the system with appropriate metals, as in the cases of $Ce_{1-x}Th_x$ and

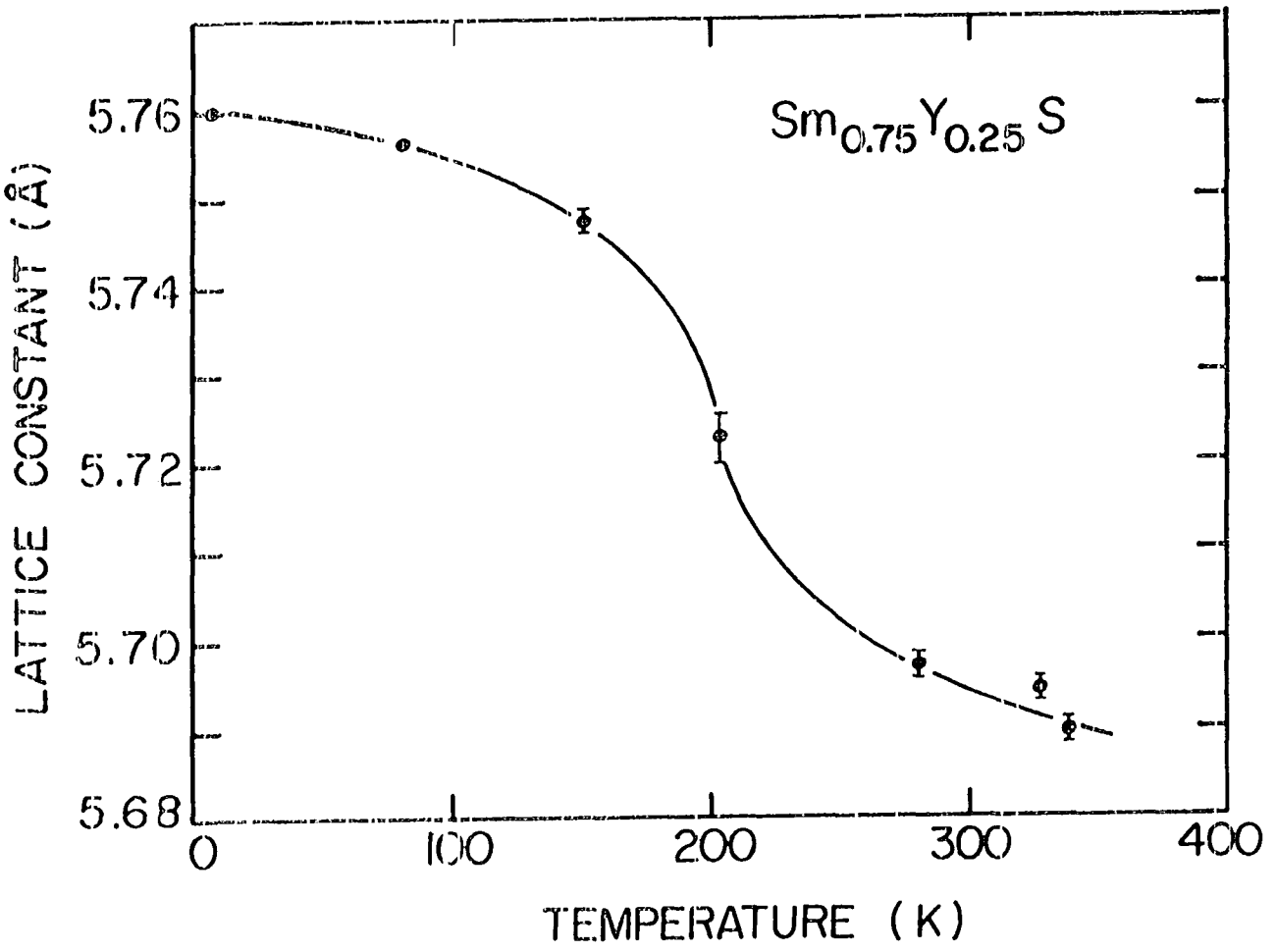

Figure 1.7. The lattice constant of $Sm_{.75}Y_{.25}S$ as a function of temperature (after Ref. 47)

$Sm_{1-x}Y_xS$. One may explain the effect of alloying on the pressure-induced phase transition in terms of the following picture (19,37,48): if the atomic diameter and the valency of the solute ion are greater than those of the rare earth, the interaction between the rare earth atoms and their nearest neighboring solute atoms will give rise to an effect similar to that arising from the application of external pressure. As a result, the study of the mixed valent state can be achieved by simply varying the temperature of the material at atmospheric pressure. However, in this case one often has to employ an interpolation scheme such as the Végard's law (49) in order to estimate the full effect of a pure mixed valence system apart from the alloying element. Therefore, it is desirable to perform experiments on a series of alloys of varying composition so that more information on the mixed valence component can be obtained. This will require a great deal of experimental effort and the experiments will be more vulnerable to contaminations by sample dependent effects such as impurities, differences in quality between samples, etc.

In parallel with a series of studies on the electronic state of Ce in Zr-Ce (50), Th-Ce (51), Pd-Ce (52) and Y-Ce (53) alloys, in 1965 Harris and Raynor measured the temperature dependence of the lattice constants of more than forty rare earth intermetallic compounds of the type REX_3, X = Sn, In and Pd (54). These materials crystallize in the simple cubic Cu_3Au structure. This crystal structure, using $CeSn_3$ as an example, is shown in Fig. 1.8. The Ce atoms are located at the corners of the cube and the Sn atoms are at the centers of the faces.

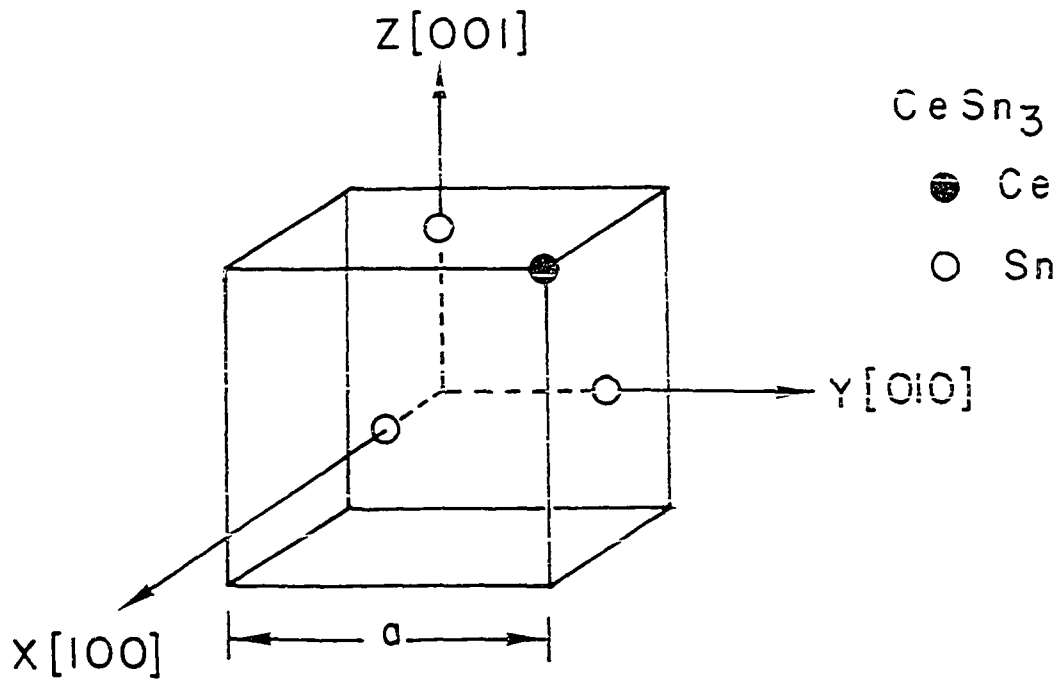

UNIT CELL		ℓ = 000
ATOM	k	$x(\vec{k})$ in units of a
Sn	1	(1/2,0,0)
Sn	2	(0,1/2,0)
Sn	3	(0,0,1/2)
Ce	4	(1/2,1/2,1/2)

Figure 1.8. The unit cell $CeSn_3$

In Fig. 1.9 the room-temperature lattice constants of the stable $RESn_3$ and $REIn_3$ compounds are plotted against the atomic number of the rare earth metal component. There are three deviations from the smooth curve for $RESn_3$ occurring at Ce, Eu and Yb. It follows from the comparison of Figs. 1.9 and 1.1 that the anomaly of the $CeSn_3$ lattice constant may be related to mixed valent character of Cerium metal. The absence of an anomaly in the lattice constant of $CeIn_3$ is presumably due to the fact that the valency of the In ions (+3) is lower (hence less bonding effect) than that of the Sn ions (+4) (37). The anomalous behavior of $CeSn_3$ is more obvious from comparison of the temperature dependence of the lattice constants with other $RESn_3$ compounds. As can be seen in Fig. 1.10, the thermal expansion of $CeSn_3$ in the 90-300K temperature range is about twice that of $LaSn_3$ and $PrSn_3$ in which the La and Pr ions are in the tripositive state. Consequently, Harris and Raynor suggested that the Ce effective valency in $CeSn_3$ is larger than 3 and increases continuously as the temperature is lowered from about 410K to about 90K.

At about the same time of Harris and Raynor's investigation of the thermal expansion of $CeSn_3$ and other compounds. Tsuchida and Wallace (55) studied the magnetic behaviors of $CeIn_3$, $CePb_3$ and a series of $RESn_3$ compounds. From the susceptibility measurements, they observed large deviations from Curie-Weiss behavior for $CeSn_3$ (Fig. 1.11) and found no evidence of magnetic ordering down to 2K. They attributed the development of the broad maximum in the susceptibility at about 135K

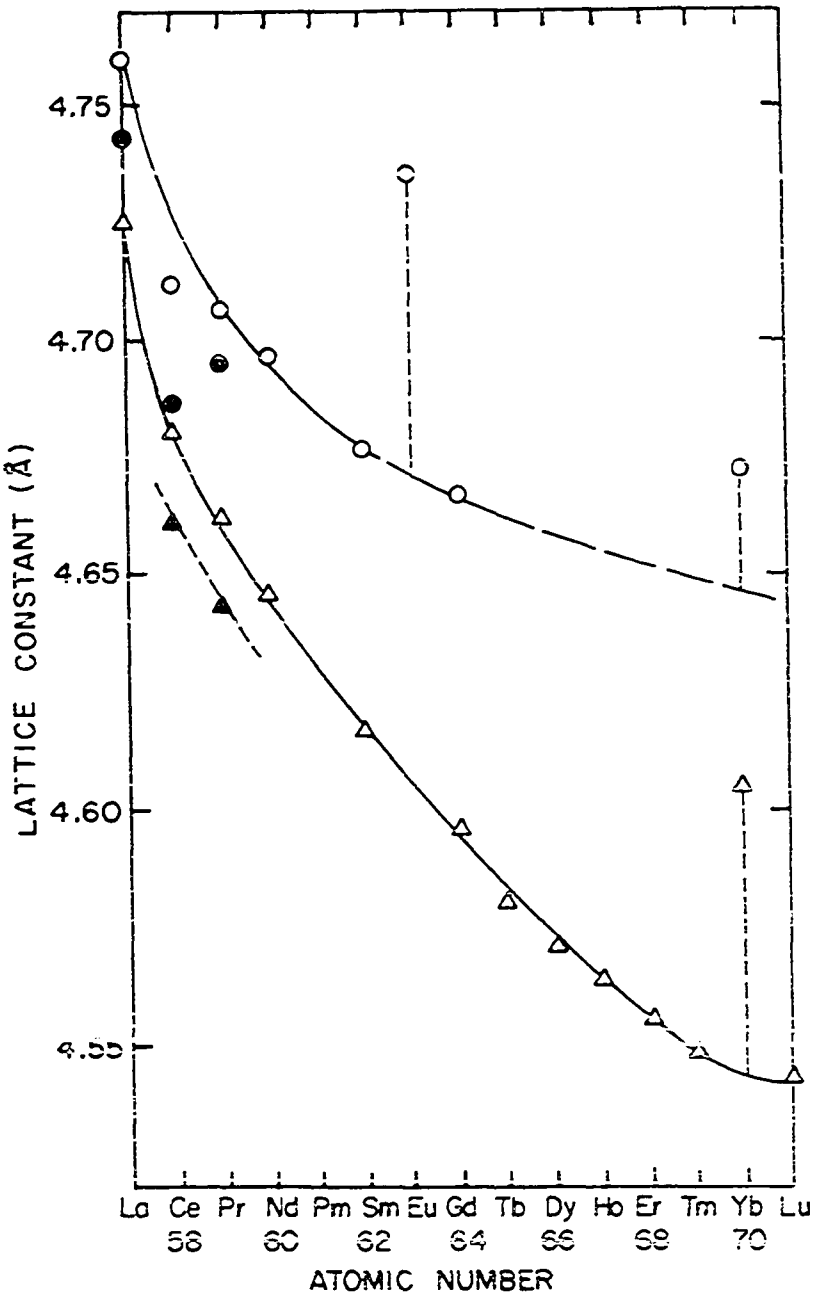

Figure 1.9. The room-temperature lattice constants of the stable $RESn_3$ and $REIn_3$ phases plotted against atomic number of the rare earths metal component. ○ $RESn_3$; △ $REIn_3$; full symbols denote lattice constants at -186°C (after Ref. 54)

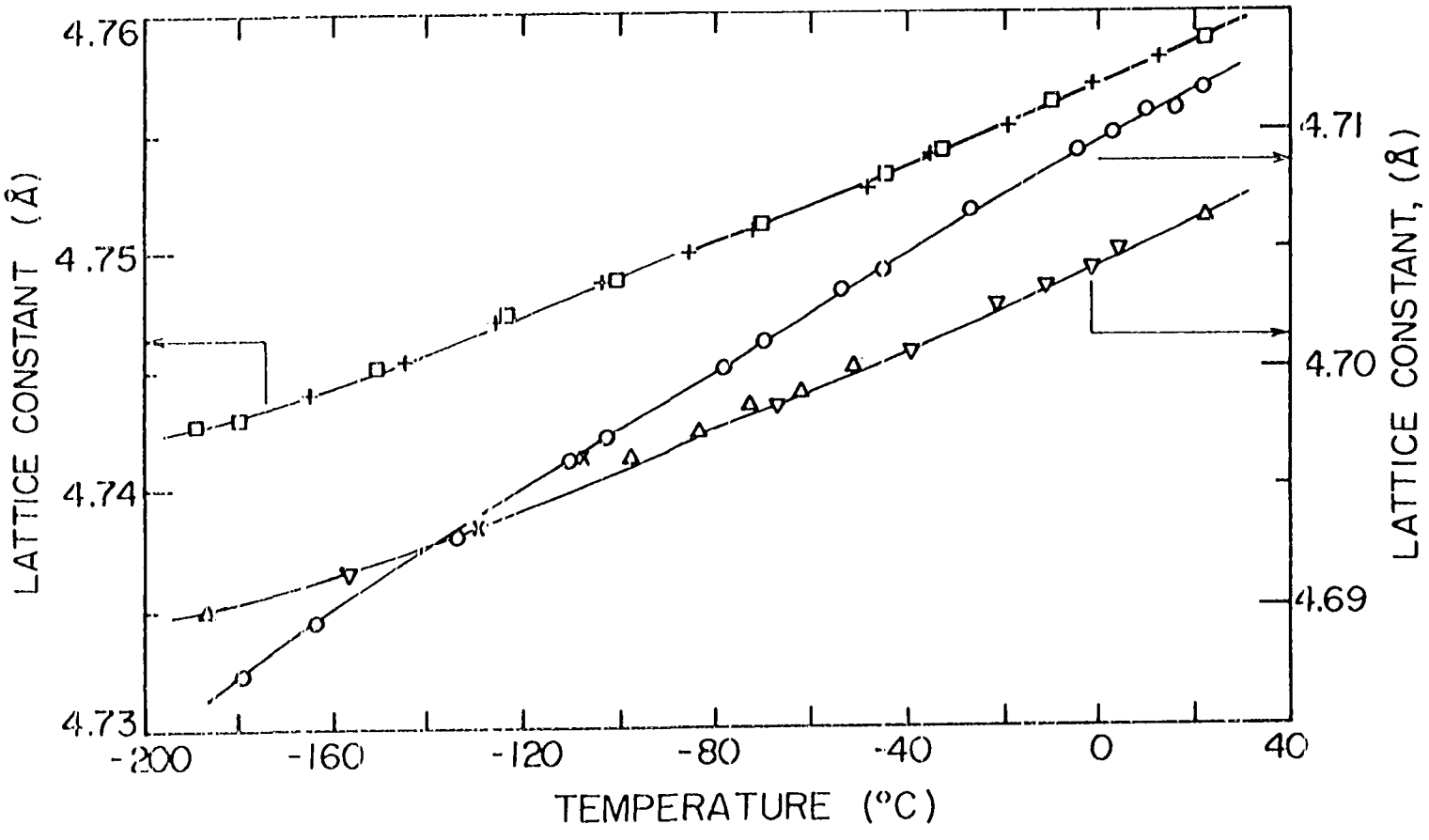

Figure 1.10. The temperature dependence of the lattice constant of $CeSn_3$ as compared to those of $LaSn_3$ and $PrSn_3$ (after Ref. 54). $CeSn_3$ (○ cooling, x heating), $LaSn_3$ (□ cooling, + heating), $PrSn_3$ (Δ cooling, ▽ heating)

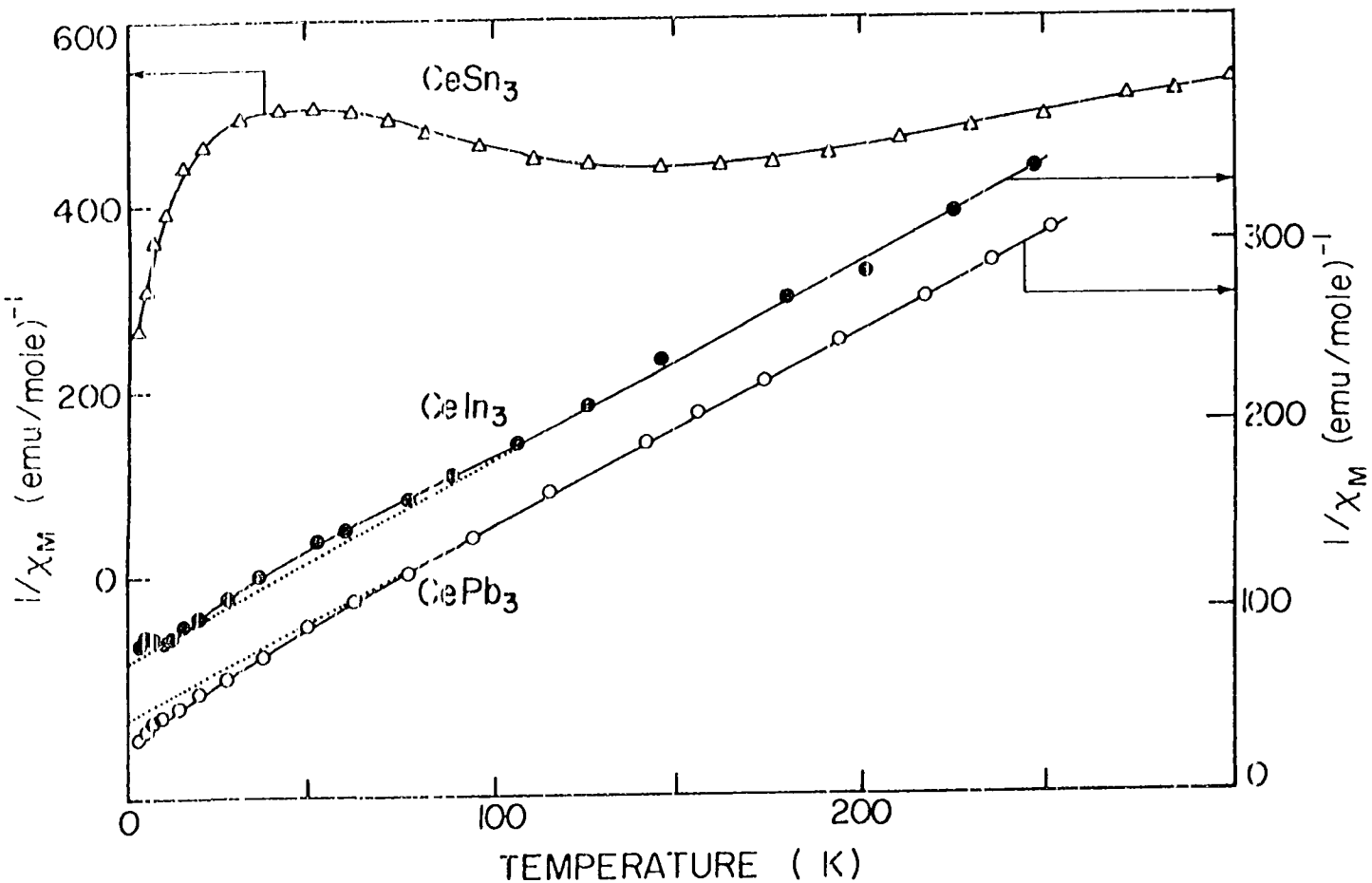

Figure 1.11. Reciprocal susceptibilities versus temperature for $CeSn_3$, $CeIn_3$ and $CePb_3$ (after Ref. 56)

(Fig. 1.12) to partial conversion of the Ce^{3+} ions into the quadripositive state.

The bulk magnetic susceptibility of $CeSn_3$ has been measured by a number of authors (Fig. 1.12) (55-59). The high-temperature susceptibility in the 300-500K temperature range follows a Curie-Weiss law with θp = -203K and μ_{eff} = 2.78 μ_B, a value to be compared with 2.54 μ_B for the Ce^{3+} free ion. From 300-40K the susceptibility remains approximately constant (with a broad maximum in the vicinity of 150K) and below 40K, it increases rapidly with decreasing temperature. Although this sharp rise at temperatures below 40K is present in all measurements the rate of rise differs from one to the next. This presumably is due to the differences in impurities between samples. Tsuchida and Wallace (55) attributed this rise to the onset of incipient ferromagnetism but Sn nuclear magnetic resonance data of Malik et al. (57) showed no evidence of magnetic ordering down to 1.2K. Misawa (60) has pointed out that by regarding the 4f electrons of Ce as itinerant a Fermi liquid model can account for the temperature dependence of the susceptibility in the 40-300K temperature range. There has been no satisfactory explanation as to the origin of the sharp rise in the susceptibility at low temperatures.

The more recent measurements of Beille et al. (61) on the compressibility and pressure dependence of the magnetic susceptibility of $CeSn_3$ supported the idea of mixed valence. The compressibility of $CeSn_3$, (2.3 ± 0.3) X 10^{-3} $kbar^{-1}$, was identical at 4 and 300K but was about two and a half times larger than that of $PrSn_3$ at room temperature.

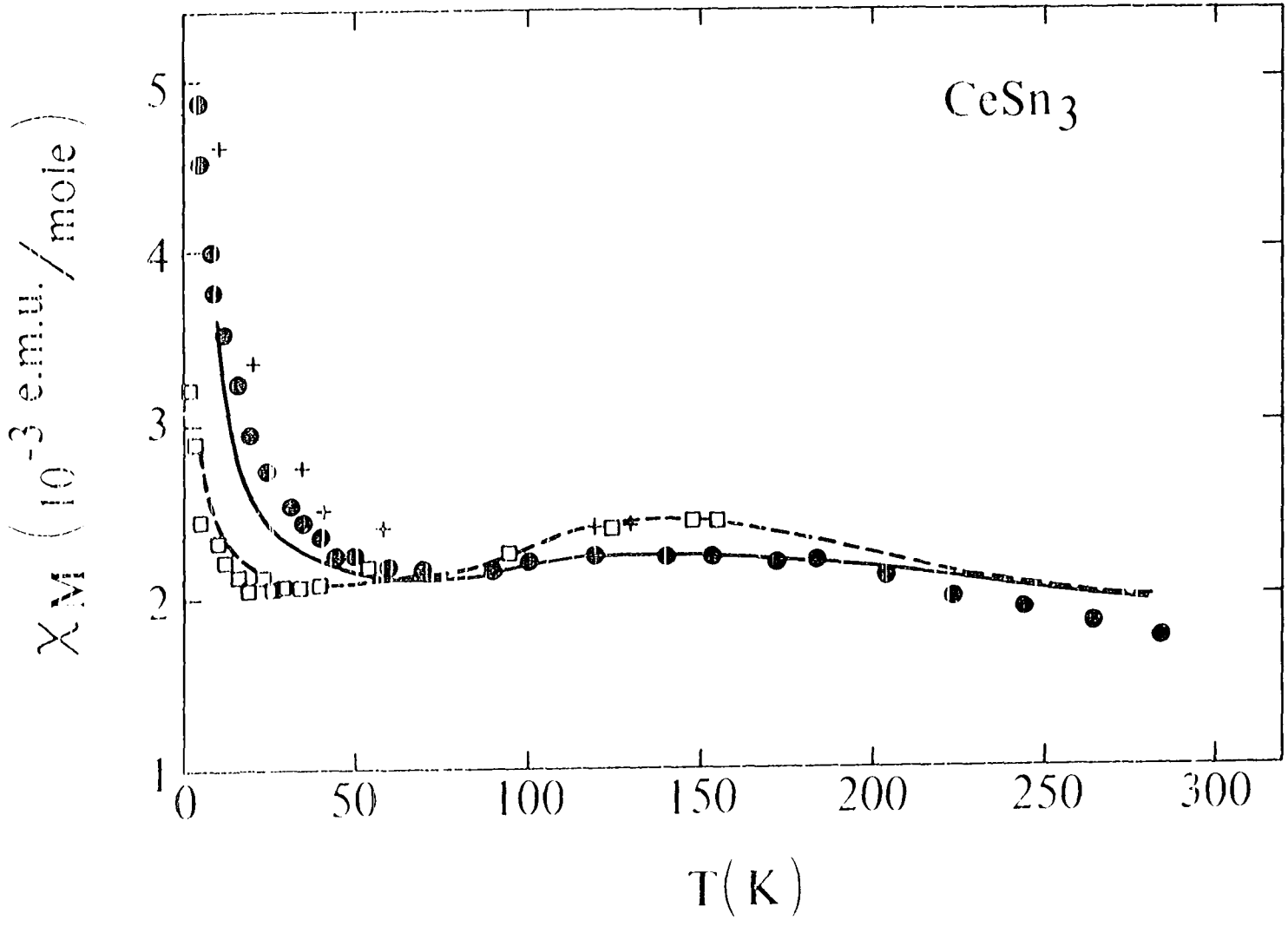

Figure 1.12. Bulk susceptibility measurements by various workers (+, □ Ref. 59; full circles Ref. 56; solid line Ref. 55; dashed line Ref. 57)

Thus Beille et al. concluded that $CeSn_3$ was in an intermediate valence state at 4K as well as 300K. The magnetic susceptibility between 4 and 300K under a pressure of 7 kbar exhibited an approximately Pauli like temperature independence, with a broad maximum at 130K. The pressure derivative of the susceptibility was found to be $d(\ln\chi)/dP = (-8 \pm 4) \times 10^{-3}$ $kbar^{-1}$. The change in the lattice constant associated with the contraction of the lattice between 300 and 4K was equivalent to that obtained with an 8 kbar pressure (Fig. 1.13). Since the susceptibility would only decrease by about 5 percent with such a pressure, it was concluded that thermal expansion alone could not induce a "magnetic-nonmagnetic" transition in $CeSn_3$.

From the low temperature heat capacity measurements, Cooper et al. (58) obtained a coefficient of the electronic specific heat for $CeSn_3$, $\gamma = (53 \pm 10)$ mJ/mole $-K^2$, a very large number compared to $\gamma \cong 10$mJ/mole $-K^2$ for $LaSn_3$. This observation indicates that the density of states is large at the Fermi level, a characteristic common to many mixed valence systems. Cooper et al. also observed a very broad maximum in the absolute thermoelectric power of $CeSn_3$ as a function of temperature between 100 and 300K. In addition, they found that the electrical resistivity of $CeSn_3$ did not increase as fast as one would have expected; (one expects ρ to be proportional to T at room temperature which is well above the Debye temperature for $CeSn_3$). They noted that this could be attributed to the presence of a narrow conduction band of width $\cong$ 100K. This narrow band behavior was corroborated by the electrical resistivity measurements on $CeSn_3$ single crystals between 2

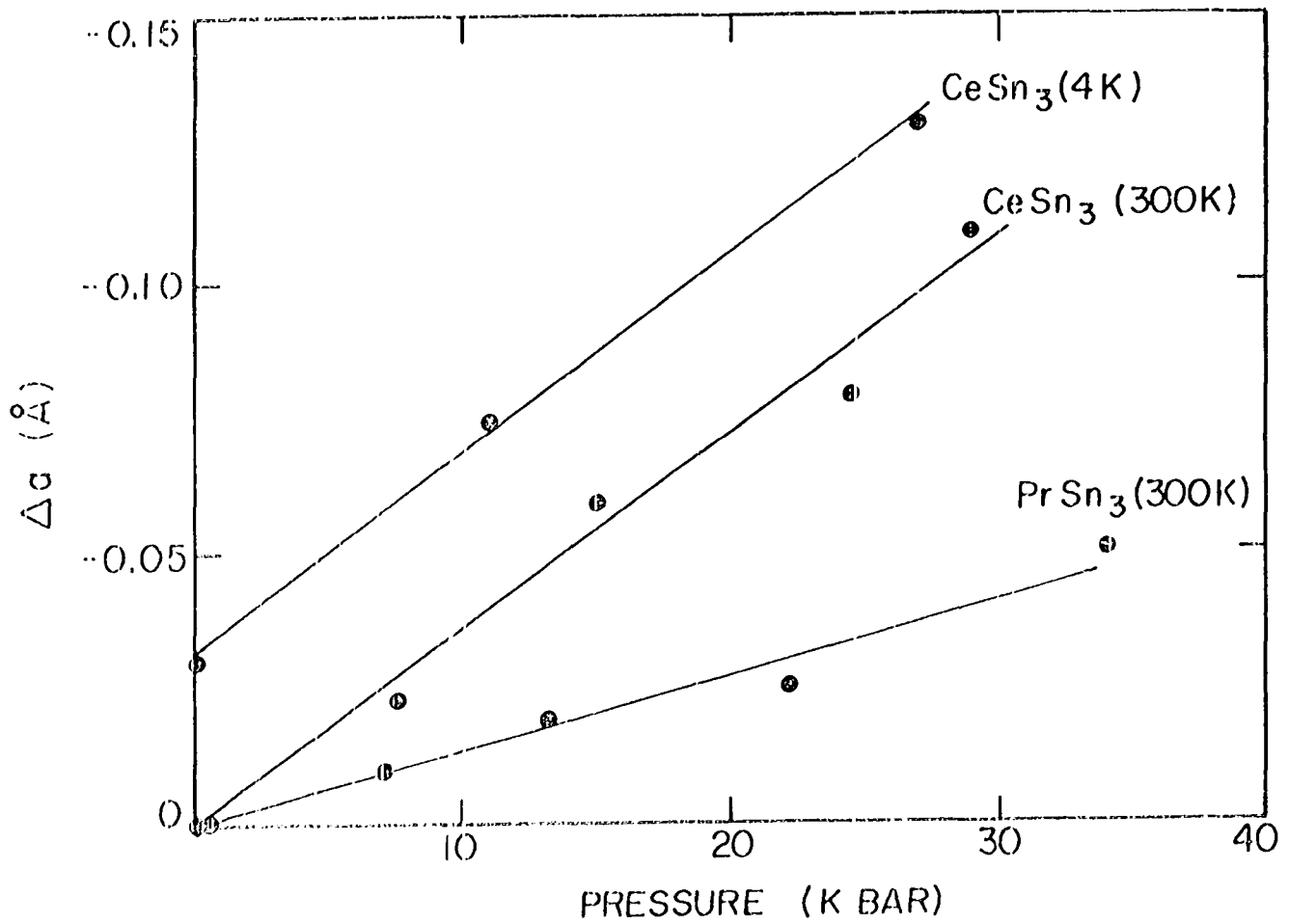

Figure 1.13. The pressure dependence of the lattice constants of $CeSn_3$ and $PrSn_3$ (after Ref. 61)

to 300K reported by Staliński et al. (62). They observed that for $T > 180K$, $\rho \propto T^{2.7}$ and for $T < 17K$, $\rho \propto T^2$. This low temperature T^2 dependence of ρ was attributed to the spin fluctuation scattering mechanism as observed in metallic Ce and certain uranium compounds of UX_3 type (X = Sn, In, Ga, Al). However, in the recent measurements of the temperature dependence of the electrical resistivity on polycrystalline samples of $La_{1-x}Ce_xSn_3$ and $CeIn_{3-y}Sn_y$, Maury (63) and his collaborators reported that the maximum $\rho(T)$ for $CeSn_3$ was nearly an order of magnitude smaller than that observed in other mixed valence systems such as $CePd_3$, $CeAl_3$ and $CeCu_2Si_2$. Moreover, they failed to observe the low temperature T^2 dependence in the resistivity of $CeSn_3$ reported by Staliński et al., instead they discovered a Kondo-like minimum at 38K. Based on the analysis of high-temperature susceptibility and the temperature dependence of the thermopower Lethuillier and Lacroix-Lyon-Caen (64) suggested that $CeSn_3$ was a Kondo metal. A recent nuclear orientation experiment performed by Benoit et al. (65) resulted in the same conclusion.

Several NMR measurements have been performed on $CeSn_3$. Shenoy (66) and his coworkers found that the ^{119}Sn isomer shift and quadrupole interaction were approximately the same as in $PrSn_3$ or $NdSn_3$ in which the rare-earth ion was in the tripositive state. This implies that the electronic distribution around the Sn nucleus has not been significantly disturbed by the presence of the Ce ions in an intermediate valence state. Welsh and Darby (67) found that the ^{119}Sn NMR properties in $CeSn_3$ were qualitatively similar to those in $LaSn_3$ and thus suggested

that the Ce 4f electron occupied a virtual bound state in the Friedel-Anderson sense, behaving like an itinerant electron in a transition metal. Both Borsa et al. (68) and Malik et al. (57,69) reported that the Knight shift data at temperatures below about 240K could not be ascribed to the cubic crystal field splitting of the J = 5/2 ground state of the Ce^{3+} ion. Malik et al. noted that at low temperatures, the ^{119}Sn spin-lattice relaxation time approached that of pure Sn metal, implying that the 4f electrons did not contribute appreciably to the observed relaxation time at low temperatures. On the other hand, recently Buschow and his coworkers (70) remeasured the temperature dependence of the ^{119}Sn Knight shift in $CeSn_3$. They were able to recover the linear relationship between the Knight shift and the bulk susceptibility that Malik et al. did not observe by assuming the presence of 2.4% of Ce^{3+} impurity in the sample. Consequently, the temperature dependence of the Knight shift as well as the magnetic susceptibility could be interpreted by a so-called two-level model in which the rare earth trivalent state Ce^{3+} ($4f^1$) was treated as an excited state located slightly higher in energy than the tetravalent state Ce^{4+} ($4f^0$). Quantum fluctuations between these two levels are responsible for the 'non-magnetic' behavior in the 300-40K temperature range while thermal excitations are responsible for the Curie-Weiss behavior at high temperatures.

We have discussed various experimental investigations of the anomalous properties of $CeSn_3$. As it can be noted, a majority of the experimental results can be interpreted qualitatively as a valence

change in the rare earth ions. Nevertheless, certain physical properties of $CeSn_3$, such as the magnetic susceptibility and the electrical resistivity at low temperatures, appear to be unique among the mixed valence systems. So far a quantitative description of the intermediate valence state and the mechanism of valence transition has not been worked out. In the next section, we shall discuss the need for an experimental study of $CeSn_3$ using neutron scattering techniques and the kind of information we expect to obtain from such experiments.

C. Neutron Scattering

As we explained earlier the mixed-valent character of a large number of materials has been inferred from measurements of the bulk properties of these systems. However, in most cases no direct experimental evidence for the mixed-valent character of these systems is presently available. The polarized neutron technique is probably the only experimental technique which can provide such evidence and, in addition information about the exact nature of the ground state of the mixed valent systems.

It is believed (5) that the rather spectacular properties of the mixed valence compounds are dictated by the coexistence at the Fermi level of ionic-like localized 4f levels and a wide 5d conduction band. Using polarized neutrons one senses the electronic wavefunctions at the Fermi level and therefore the mixed valent character of the system can be assessed directly. Through Fourier inversion of the measured form factor, detailed information about the spatial distribution of the

magnetization density can be obtained. For rare earth metals or compounds in which the rare earth ions are in a well-defined valence state, the magnetic form factors have been found to be characteristic of the 4f electrons. Thus, deviations from the 4f magnetic form factor are expected in the case of mixed valence system in which the rare earth ions are in an intermediate valence state. Therefore, by comparison of the 4f magnetic form factor with the measured magnetic form factor of a mixed valence compound, direct evidence of the mixed valent character can be obtained. Furthermore, the study of the temperature dependence of the magnetic form factors of a system which exhibits temperature-induced valence fluctuation would provide insight into the mechanism of valence fluctuation.

On the other hand, since valence fluctuation is often accompanied by large changes in the crystal volume, it is expected that phonon modes which involve a volume change would be strongly affected. Recently, phonon anomalies have indeed been observed on SmYS (47) (one of the well-known mixed valence materials). Thus inelastic neutron scattering measurements can provide information about the electron-phonon coupling in these systems and the role of this interaction in inducing the mixed-valent transition.

Recently, large single crystals of $CeSn_3$ were prepared in the Ames Laboratory; therefore, with the above rationale, we initiated a systematic study of the mixed valent character of this compound using the techniques of neutron scattering. Such an investigation consists of two major experiments, namely, the study of the temperature dependence

of the field induced magnetic form factors of $CeSn_3$ using polarized neutron techniques and the study of the lattice dynamics of $CeSn_3$ using inelastic neutron scattering technique. In order to identify unambiguously any phonon anomalies due to valence fluctuation we are presently measuring the phonon dispersion curves of $LaSn_3$. In the absence of any mixed-valent effect, one would expect the phonon dispersion curves of these two compounds to be identical since La has almost the same mass as Ce and La has the same electronic configuration as Ce except that there is no 4f electron in La. Thus, by comparison of the $CeSn_3$ data with those of $LaSn_3$, the effect of valence fluctuation on phonon spectrum can be studied.

The experimental investigation consisted of two parts. The first part of this work, covered in the next three chapters involved the measurements of the field-induced magnetic form factors of $CeSn_3$ at various temperatures ranging from 1.7-300K. Chapter II deals with the basic techniques involving the use of polarized neutrons in the magnetic form factor measurements and the details of the experiment. Chapter III briefly outlines the basic principles of magnetic scattering. Chapter IV presents analysis and discussion of the experimental results of the polarized neutron studies. The second part of this work begins with Chapter V, a discussion of the fundamentals of lattice dynamics and the application of the Born-von Kármán force constant model to the analysis of the phonon dispersion curves of $CeSn_3$. Chapter VI discusses the technique of inelastic neutron scattering and presents the experimental results of lattice dynamics of $CeSn_3$. A standard Born-von Kármán

analysis of the phonon dispersion relations, the calculation of thermophysical properties of $CeSn_3$ and a discussion of the observed phonon spectrum of $CeSn_3$ as compared with those of $LaSn_3$ and $Sm_{.75}Y_{.25}S$ will be presented in Chapter VII. An overall view of the neutron scattering studies of $CeSn_3$ will be summarized in Chapter VIII.

II. POLARIZED NEUTRON TECHNIQUE

It has been over 20 years since the first brilliant experiment involving the use of polarized neutrons in the determination of magnetic form factors was reported by Nathans, Shull, Shirane and Andresen (71). Today the polarized neutron technique has been developed into a powerful and indispensable tool for studying magnetic phenomena. Presently the technique is being exploited to study problems associated with new classes of materials (e.g., investigation of protons in organic molecules (72)) and attempts are being made to improve the capability of the instruments and the efficiency of neutron utilization (e.g., the application of neutron spin-echo spectrometry (73)).

Realizing the diversity of this topic, we shall confine our discussion in the present chapter to the experimental techniques involved in magnetic form factor measurements of paramagnetic materials. This is one of the areas of major interest in polarized neutron studies since it provides information essential in understanding important physical properties in solids. We shall begin by defining the field induced magnetic form factor and then shall go on to discuss the apparatus and the experimental details concerning the measurements. We shall conclude this chapter with a description of the sample preparation and some important crystal effects. Details concerning various corrections to the experimental data are presented in the Appendix.

A. Field Induced Magnetic Form Factor

The scattering of neutrons by a nucleus and its electronic environment involves contributions from several different types of interactions (see Chapter III). In the present experiment, we are interested in the elastic coherent scattering from a paramagnetic crystal of rare earth metal or compound to which a uniform magnetic field has been applied. In this case, the major contributions to the scattering are the nuclear scattering by the atomic nuclei and the magnetic scattering by the field induced magnetic moments of the atoms. The differential cross section in the first Born approximation can be written as

$$\frac{d\sigma}{d\Omega} = \left| \langle s' | \sum_i [b_i + p_i^{ind}(\vec{q})] e^{i\vec{q}\cdot\vec{r}_i} | s \rangle \right|^2 \qquad (2.1)$$

where i is an index representing the atoms in the crystal, $\vec{q}$ is the scattering vector equal to the momentum transfer vector of the neutron, s and s' denote the initial and final spin states of the neutron respectively, and b is the nuclear scattering amplitude averaged over the nuclear spin and isotope distributions of an element. The field induced magnetic scattering amplitude, $p^{ind}(\vec{q})$ in the above equation is given by

$$\begin{aligned} p^{ind}(\vec{q}) &= \langle s_z \rangle p(\vec{q}) \\ &= |\gamma| v_o \langle s_z \rangle f(\vec{q}) \quad , \end{aligned} \qquad (2.2)$$

where $\langle s_z \rangle$ is the polarization of the atomic spin by the external magnetic field $\vec{H}$ (the z-axis has been chosen to coincide with the

direction of $\vec{H}$), $f(\vec{q})$ is the form factor of the magnetic atomic electrons, $\gamma = -1.91$ is the neutron magnetic moment in nuclear magnetons, v_o is the classical electron radius, and $p(\vec{q})$ is the magnetic scattering amplitude of the atom; $p(\vec{q})$ will be discussed in detail in the next chapter. For a molar susceptibility χ_m and an applied field H the effective magnetic moment per individual atom is $\chi_m H/N_A$, where N_A is Avogadro's number. Thus Eq. (2.2) can be written as

$$p^{ind}(\vec{q}) = |\gamma| v_o \frac{\chi_m H}{2\mu_B N_A} f(\vec{q}) = 0.484 \times 10^{-16} \chi_m H f(\vec{q}) \text{cm} \quad ,(2.3)$$

with χ_m in c.g.s. unit per mole, H in Oersteds and f normalized to unity at $q = 0$.

At this point it is desirable to mention an important property of the nuclear scattering amplitude. In contrast to magnetic scattering the scattering of a thermal neutron by a nucleus can be characterized by a single parameter b. This is due to the fact that the wavelength of a thermal neutron (of the order of 10^{-8} cm) is much greater than the range of the neutron-nucleus interaction (10^{-12} to 10^{-13} cm) so that the scattering is isotropic. In general b may be complex and varies with the energy of the neutron. However, in the energy range of thermal neutrons and for most of the materials of interest in neutron experiments, b may be regarded as an energy independent real quantity.

Neglecting momentarily the effects due to thermal vibrations of the atoms (see Section B of Chapter IV for the discussion of temperature effects), it can be shown that the intensity I of a Bragg reflection is given by

$$I_{hk\ell} \sim |F_{hk\ell}|^2 = |\langle s'| \sum_j [b_j + p_j^{ind}(hk\ell)]\exp\{2\pi i(hx_j + ky_j + \ell z_j)\}|s\rangle|^2 \tag{2.4}$$

where $(hk\ell)$ are the Miller indices of a reflection. The summation in Eq. (2.4) is over all the atoms in a unit cell defined by the unit cell axes $\vec{a}$, $\vec{b}$, $\vec{c}$. The position of the j^{th} atomic nucleus is given by $\vec{r}_j = x_j\vec{a} + y_j\vec{b} + z_j\vec{c}$. For $CeSn_3$ the positions of the Ce and the three Sn atoms are defined by vectors (0,0,0), (0,1/2,1/2), (1/2,0,1/2) and (1/2,1/2,0) in units of the unit cell dimension (see Fig. 1.8).

Under ideal conditions, the spin orientations of the incident neutrons in a polarized beam experiment are either parallel or anti-parallel to the applied magnetic field. The experiment consists of measuring the ratio R of the Bragg peak intensities for these two states of neutron polarization, I^+ and I^-. R is called the polarization ratio or intensity ratio and is given by

$$R = \frac{I^+}{I^-} = \left[\frac{F_N + F_M(\vec{q})}{F_N - F_M(\vec{q})}\right]^2 \tag{2.5}$$

where

$$F_M(\vec{q}) = \sum_j p_j^{ind}(\vec{q})\exp[2\pi i(hx_j + ky_j + \ell z_j)] \quad , \tag{2.6}$$

$$F_N = \sum_j b_j \exp[2\pi i(hx_j + ky_j + \ell z_j)] \tag{2.7}$$

denote the magnetic and the nuclear structure factor respectively. For

$F_M(\vec{q})/F_N \ll 1$, R reduces to

$$R \cong 1 + 4\frac{F_M(\vec{q})}{F_N} \quad . \tag{2.8}$$

For $CeSn_3$, F_N is equal to $b_{Ce} + 3b_{Sn}$ and $b_{Ce} - b_{Sn}$ for the unmixed and mixed Miller indices reflection respectively (b_{Ce} and b_{Sn} are the coherent nuclear scattering amplitudes of Ce and Sn respectively).

The experimental results of a polarized neutron experiment are often presented by showing the values of F_M/F_N of various reflections versus $q = \frac{\sin\theta}{\lambda}$ (θ is the Bragg angle and λ is the wavelength of the neutrons). Since F_N is q independent, $F_M(\vec{q})/F_N$ contains the essential information about the magnetic scattering amplitude of the system in question. Therefore, $F_M(\vec{q})/F_N$ is referred to as the field induced magnetic form factor, or simply the magnetic form factor.

B. Apparatus and Experimental Details

The measurements of the field induced magnetic form factor of $CeSn_3$ were performed using the HB-1 polarized neutron spectrometer at the High Flux Isotope Reactor (HFIR) of Oak Ridge National Laboratory. A schematic diagram of the experimental arrangement is shown in Fig. 2.1. It consists of a triple axis spectrometer with a monochromator and analyzer made of ferromagnetic crystals, for example, an f.c.c. $Co_{.92}Fe_{.08}$ crystal. The monochromating crystal functions as both monochromator and polarizer. It is mounted in the magnetic field of a small permanent magnet (~3 kG) in such a way that the magnetization of the crystal is perpendicular to the scattering vector. The incident

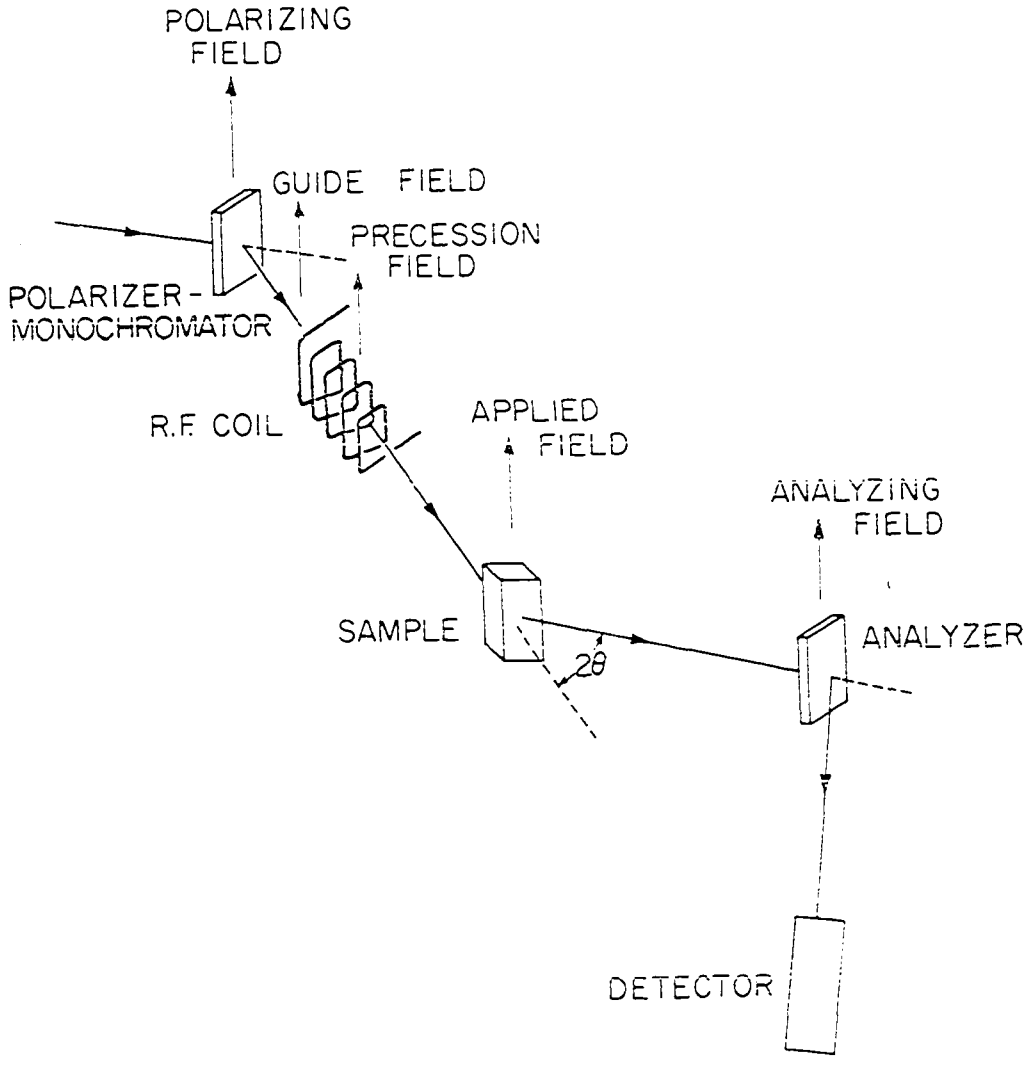

Figure 2.1. Schematic diagram of polarized neutron spectrometer

unpolarized beam may then be analyzed into two equally populated spin states along the direction of the crystal magnetization. The crystal reflectivities for the two spin states are proportional to $(b \pm p)^2$ where b and p are the coherent nuclear scattering amplitude and the coherent magnetic scattering amplitude respectively. By selecting a crystal reflection such that $p \cong b$ (e.g., the (200) reflection of a $Co_{.92}Fe_{.08}$ crystal), the reflectivity for one spin state vanishes and the reflected beam is highly polarized. The wavelength of the polarized neutron beam is selected by rotating the monochromator to an appropriate scattering angle. Contaminations from higher orders can be minimized by using effective filters. In the present experiment, most of the measurements were performed for neutron wavelengths around 1.05 Å with a plutonium filter placed in front of the counter. It was estimated that half-wavelength contamination would result in less than one-tenth of a percent error in the intensity ratio.

The degree of polarization of a neutron beam is given by

$$\mathcal{P} = \frac{n^+ - n^-}{n^+ + n^-} = \frac{I^+ - I^-}{I^+ + I^-} \tag{2.9}$$

where n^+, I^+ (n^-, I^-) respectively are the number and intensity of the neutrons in a beam with spins parallel (antiparallel) to the direction of the applied field. When the beam is fully polarized, $\mathcal{P} = +1$ or -1 and for a partially polarized beam $-1 < \mathcal{P} < +1$.

Unlike many polarized neutron spectrometers which use Co-Fe crystals as monochromators and polarizers, the HB-1 spectrometers at the

HFIR employs a Si-Fe crystal as monochromator and polarizer. The advantage in using such a crystal is that it has a high reflectivity and consequently yields a monochromatic beam of high intensity. On the other hand, the Co-Fe monochromator yields a more highly polarized reflected beam. Hence when using a Si-Fe monochromator a correction to the measured intensity ratio of the two neutron spin states must be introduced (see the Appendix). At regular intervals throughout the experiment, the degree of polarization of the incident beam was measured by using a Co-Fe analyzer crystal.

A guide field in the order of 100 Gauss, produced by permanent magnets, is maintained along the neutron path between the monochromator and the sample. In one section of this path, a solenoid is placed so that the neutrons pass down its axis. The solenoid is used to produce a radio-frequency (RF) field directed perpendicular to the constant guide field. When the frequency is matched to the energy level separation of the two neutron spin states in the guide field transitions are induced between these two states. By adjusting the strength of the RF field relative to the neutron time-of-flight through the solenoid, nearly perfect spin reversal can be attained. Hence such a device is called a 'flipper' (74). The sample is mounted in a 5/8-inch 'window' of a split-coil superconducting magnet capable of producing magnetic fields up to 60 kG. The basic experiment to measure the magnetic form factor is performed by setting the sample for a Bragg reflection and counting the reflected beam with the flipper off and again with the flipper on. The background correction is determined by rotating the

sample off the Bragg peak while leaving the counter fixed. The Co-Fe analyzer crystal is used only to measure the degree of polarization of the incident beam or to optimize the flipper efficiency. The experiment differs from the conventional diffraction experiments in that only peak intensities rather than integrated intensities are measured. This procedure is justified since only the ratio of the intensities for the two neutron spin components belonging to the same reflection is measured; hence all but the peak intensities presumably cancel. The ratio method also has the advantage that systematic errors tend to cancel so that high precision absolute measurements can be achieved.

There are two separate counting channels: one receives pulses from a low efficiency detector which monitors the beam incident on the sample; the other records the pulses from a high efficiency detector set to receive the reflected beam. After a preset number of counts in the monitor channel has been accumulated, the number of counts in the signal channel is registered by an on-line computer and printed out by a teletype. In this way, automatic compensation for small changes in the incident beam flux is achieved. However, for some strong reflections with intensities higher than 5000 counts per second, the statistical uncertainty in the intensity ratio R is determined by the low efficiency of the monitor. Therefore, when counting the reflected intensities, it is preferable to leave the flipper on (off) for only a short period of time (less than 10 seconds), assuming that the incident beam flux is constant. If a drift in the reactor power is observed, the measured intensity ratio must be corrected for the drift.

The detectors are BF_3 proportional counters. If standard commercial preamplifiers and amplifiers are employed, the effect of the finite resolving time of the counting instrument will cause a considerable counting loss for some strong Bragg reflections (typically for intensities above 15,000 counts per second). It has been found that only pulses separated by time intervals greater than the resolving time ρ can be recorded by the counting system. Consequently the system fails to record certain ionizing events. The resolving time can be determined experimentally and if we let I be the average number of true events per unit time interval, the observed counting rate is simply $I' = Ie^{-I\rho}$. High counting rate preamplifiers and amplifiers with resolving time as short as 0.5 μsec are available.

In the polarized beam measurement, one uses the polarized neutrons as a probe to measure the response of a paramagnetic material to an applied magnetic field. But at the same time the neutrons themselves also respond to the field and give rise to some undesirable experimental effects which affect the observed intensity ratio R. As the neutrons enter the magnetic field at the sample position they are subject to a force. This force, which gives rise to the aforementioned effects, is proportional in magnitude to the gradient of the field modulus and oppositely directed for the two different neutron spin states. As a result, the velocity and the Bragg scattering angle corresponding to the up spin neutrons at the sample location are different from those corresponding to the down spin neutrons. Moon et al. (75) have shown that the resulting error in the intensity ratio R is given by

$$\Delta R = -\frac{2|\mu|}{Mv_0^2} \tan\theta \, H \frac{1}{s(\theta')} \frac{ds(\theta')}{d\theta'} \tag{2.10}$$

where μ is the neutron magnetic moment, v_0 is the neutron velocity, M is the neutron mass, H is the applied field, θ is the Bragg angle of a reflection and $s(\theta')$ defines the slope of the crystal rocking curve. Since the measured quantity $R - 1 = 4 F_M/F_N$ is often of the order of 10^{-4} or smaller, the above error can be very serious even if the peak position is off by only 0.02°. The task of setting and maintaining the crystal position to better than 0.02° over the course of the measuring period is nontrivial, especially since the crystal is mounted at the center of a superconducting magnet. Therefore, the ideal crystal for measurement should have a broad, flat-topped rocking curve.

In the present experiment the observed rocking curves for various reflections all exhibited a full width at half maximum of 45 minutes of arc or greater and the peaks were reasonably rounded. Thus setting the crystal at the peak positions was not difficult. Before the measurement for a reflection was begun, the crystal was rotated through the peak position with a step size of 0.02° and the rocking curve was plotted. Then the crystal was brought back to the starting position, stepped towards and stopped at the peak position. When the measurement was finished, the crystal was stepped away from the peak. The maintenance of the peak position throughout the period of measurement was ensured by reproduction of the original rocking curve within the limits of experimental accuracy.

Another undesirable side-effect arises from the design of the split-coil superconducting magnet used for polarized neutron experiments. When the first split-coil superconducting magnet was constructed at Brookhaven, it was found (76) that provided the two coils were built symmetrically and operated with equal current, severe depolarization occurred for neutrons traveling in the median plane between the two coils through the zero-field region where the magnetic field reversed direction. Subsequently, most of the magnet for polarized neutron experiments were designed with unequal turns in the two coil so that the coils could be operated with equal currents and yet zero-field regions along the neutron path would be avoided. However, this produced a vertical separation of the two neutron spin states due to the vertical field gradient along the entire neutron flight-path. The vertical angular deviation between two neutrons with opposite spins, each initially traveling on the same horizontal track with equal velocities, is given by Moon et al. (75):

$$\Delta\delta = -\frac{2|\mu|}{Mv_0^2}\int \frac{\partial H}{\partial z}\, dS \qquad (2.11)$$

where the integration is along the neutron path, both into and out of the magnet. For the magnet of the HB-1 spectrometer at the HFIR operating at 60 kG, this angular deviation is about 6×10^{-4} degree, which results in a vertical separation at the counter position of about 10^{-3} cm. Under normal conditions, this effect will not cause a problem since the diameter of the counter and the width of the slit in front of it are wide enough to accept the entire reflected beam. However, if the crystal

is slightly misaligned so that the scattering vector is not exactly in the horizontal plane, the observed intensity may be sensitive to the vertical divergence with a resulting error in the intensity ratio. Necessary precautions were taken in the present experiment to minimize this problem. Initially the sample was carefully positioned at the center of the beam. Then using a pair of large-scattering-angle-reflections separated by 90° such as the (220) and (004) reflections, the goniometer arcs were adjusted until the intensities of both reflections were optimized and centered with respect to the counter position. In addition, the vertical position of the reflected beam of each reflection was checked before the measurement was begun.

We have discussed the apparatus employed in a polarized neutron experiment and the major effects due to instrumental imperfections. The detailed derivation of the formulas to correct for incomplete beam polarization and imperfect spin flipping is presented in Appendix A. In addition, there are other important effects which complicate the interpretation of the experimental results. We shall mention these effects in the next section which is devoted to the discussion of the samples.

C. Sample Preparation

The samples of $CeSn_3$ used in the present experiments were prepared by Mr. O. D. McMasters of the Ames Laboratory. Correct amounts of 99.9% pure Ce and 99.9999% Sn were first acr-melted into a cylinder about 70 gm in mass. The melt was then placed in a tungsten crucible 3/4-inch in diameter and 3 inches in length with a 60° cone angle. Single crystals

were grown from the melt using the Bridgman technique (77). The main part of the furnace employed in this method of crystal growth is shown schematically in Fig. 2.2.

Inside the chamber of the quartz tube, the crucible was held in position in a tantalum susceptor which was set on a molybdenum heat sink connected to a water cooled copper pull rod. Induction heating was used to heat the susceptor and melt the sample. At about 1100°C the susceptor, crucible and sample were outgassed under vacuum. The chamber was then filled with purified argon gas to a pressure of about 15 psi before the melting took place at about 1170°C. The sample was heated to about 1250°C and pulled from the induction coil area at a rate of 1/4-inch per hour. As the sample passed through the heating zone which had a certain temperature gradient, the nucleation of a single crystal was promoted to start from the tip of the crucible. After cooling the entire sample easily slid out of the crucible. No evidence was found of any appreciable oxidation or reaction with the tungsten crucible.

Single crystals could be extracted from the sample by using standard commercial low speed diamond cutters, wire cutters or spark cutters. Experience showed that the best results were attained by using a spark cutter.

In a polarized neutron experiment the use of a single crystal of appropriate size is essential. For the present experiment a wedge about 6 mm thick, 35 mm long was first separated from a large sample of $CeSn_3$ which contained several single crystals. Examination of the wedge

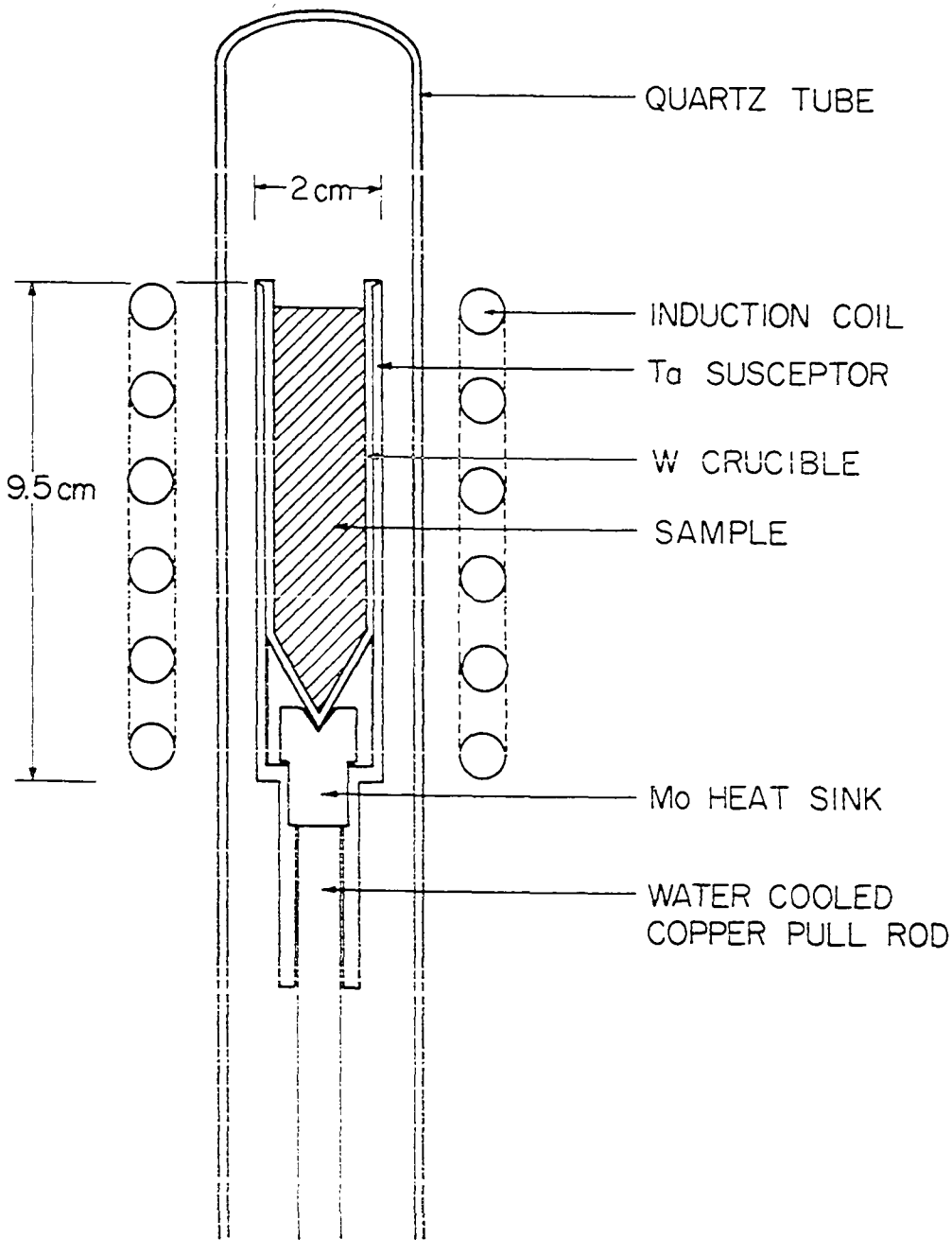

Figure 2.1. The apparatus used in growing single crystals of $CeSn_3$--the main part of the furnace employed in the Bridgman method is shown schematically

using standard neutron diffraction techniques established that at least two-thirds of the wedge contained a single crystal of $CeSn_3$ exhibiting the Cu_3Au crystal structure. Subsequently a single crystal, a parallelepiped approximately 5 mm thick and 15 mm long was extracted. One of the faces perpendicular to the long axis of the parallelepiped corresponded to a $(1\bar{1}0)$ plane of the crystal. Aided by an orientation device and the crystal lapping equipment, the $(1\bar{1}0)$ plane was accurate to within a few tenths of a degree. To help avoid oxidation of the samples during crystal preparation and handling, the samples were either kept in an argon atmosphere or entirely submerged in oil during the cutting process.

The single crystal was first used in a preliminary study by polarized neutrons at the Ames Laboratory Research Reactor (ALRR). Later, when the experiment was continued at the HFIR, the sample was cut into two pieces in order to examine effects related to the size of the crystal. A description of the two pieces follows:

1. Polarized neutron sample 1 (PN1): a 4.57 mm x 4.57 mm x 12.32 mm pillar with the basal plane corresponding to the $(1\bar{1}0)$ plane.
2. Polarized neutron sample 2 (PN2): a 5.28 mm x 5.03 mm x 2.36 mm plate with both faces parallel to the $(1\bar{1}0)$ plane.

D. Crystal Effects

In the following we shall discuss two major crystal effects; namely, effects due to extinction and those due to simultaneous reflections. Failure to identify or correct these effects will lead to

inaccurate interpretation of the experimental data. The strategy, however, is to design the experiment to avoid or minimize these effects as much as possible. If such an effect cannot be avoided, the errors caused by it have to be assessed and the corresponding corrections should be made in the course of data analysis.

1. Extinction

It is well-known (78) in diffraction theory that the integrated intensity of a Bragg reflection, $\mathcal{R}$, can be written as

$$\mathcal{R} = Q\delta V \tag{2.12}$$

where δV is a volume element of the crystal being irradiated and Q is a crystallographic quantity given by

$$Q = \frac{\lambda^3 N_c {}^3F^2}{\sin 2\theta} \quad . \tag{2.13}$$

In the above expression, λ is the wavelength of the neutrons, N_c is the number of unit cells per unit volume, F is the structure factor corresponding to the Bragg reflection with scattering angle 2θ.

In practice, Eq. (2.12) holds only when δV is so small that only a few percent of the incident energy can be reflected by it. The incident beam diminishes in strength as it penetrates through an extended volume of the crystal. This phenomenon is known as 'extinction'. It should be stressed that extinction is fundamentally different from absorption (e.g., the neutrons are captured by nuclei which subsequently emit γ-rays).

Attenuation of the incident neutron beam in a 'perfect' crystal (one in which the atoms are ordered in a perfectly uniform and regular array) may be regarded as destructive interference between the neutron forward-travelling waves and the repeatedly reflected components travelling in the same direction with opposite phase. In such a case effective reflections take place only in a very thin layer, a penetration distance on the order of 10^{-4} cm. Extinction in this case is called 'primary extinction'.

Most crystals are far from being perfect, and the ideal lattice regularity only extends over small regions called 'mosaic blocks'. These blocks are tilted slightly in orientation with respect to each other. If the dimension of the mosaic blocks in a crystal are small compared to the penetration distance so that primary extinction may be neglected, the crystal is said to be 'ideally imperfect'. In this case 'secondary extinction' can occur presumably only when two or more mosaic blocks in the crystal have identical orientations. As expected, extinction in an ideally imperfect crystal is much less severe than in a perfect crystal. Therefore, crystals with a reasonable mosaic structure are preferred for use in polarized neutron experiments.

The mosaic spread of the polarized neutron samples of $CeSn_3$, PN1 and PN2, was estimated to be 25 minutes of arc by measuring the full width at half maximum of the (002) reflection, using a monochromatic neutron beam obtained by reflection from the (111) planes of a perfect Ge crystal. This indicated that the samples exhibited acceptable mosaic structures. Thus it is probably safe to assume that the crystals are

free of primary extinction and we only need to consider the effects due to secondary extinction.

The theoretical formulation of the effects of extinction in diffraction experiments was first developed by Darwin (79) in 1922, and further studies of the theories and their applications to the interpretation of x-ray and neutron diffraction data were carried out by Zachariasen (80,81) and Bacon and Lowde (82). The importance of secondary extinction in a polarized neutron experiment was realized and pointed out by Nathans et al. (71) in their pioneering experiment in 1959 and has been recently reviewed by a number of authors (83). In the following we shall briefly summarize the major conclusions of the studies by Bacon and his collaborators and leave the treatment of the extinction correction to the Appendix.

The mosaic structure of an imperfect crystal can only be approximated. Of the various models available, one which is frequently used assumes a Gaussian distribution $W(\Delta)$ for the mosaic blocks, i.e.,

$$W(\Delta) = \frac{1}{\eta\sqrt{2\pi}} \exp(-\Delta^2/2\eta^2) \quad . \tag{2.14}$$

In the above equation $W(\Delta)$ is defined so that $W(\Delta)d\Delta$ is the fraction of mosaic blocks which have their normals between the angles Δ and $\Delta + d\Delta$ from the crystal surface and η is the standard deviation of the mosaic blocks. Using such a model, Bacon and Lowde (82) calculated the integrated reflectivity $\Re$ from an ideally imperfect nonabsorbing crystal plate as a function of crystal thickness, structure factor and mosaic spread; the result is shown in Fig. 2.3. By comparison to the straight

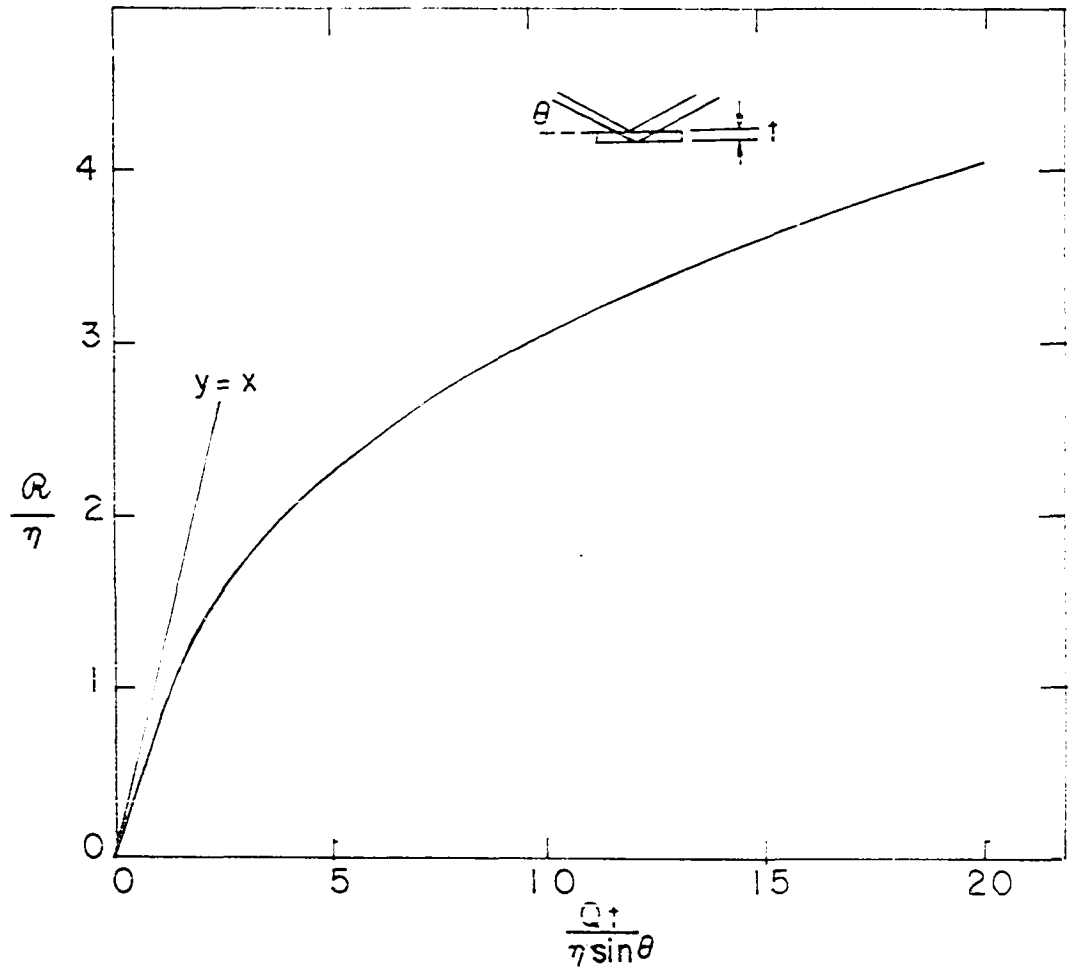

Figure 2.3. Calculated integrated reflectivity from an ideally imperfect nonabsorbing plate (after Ref. 82)

line y = x in the figure which represents the extinction-free reflectivity, it can be seen that extinction is more pronounced for the reflections with large structure factors, for thick crystals and for crystals with small mosaic spreads (i.e., small η). Bacon and Lowde proposed a criterion for a 'thin crystal', i.e., a crystal slab for which extinction will cause less than 5 percent error in the integrated reflectivity. This criterion may be written in the following form:

$$\frac{\alpha}{\eta} = \frac{Qt}{\eta \sin\theta} < \frac{1}{4} \tag{2.15}$$

where $\alpha = Qt/\sin\theta$ and t is the thickness of a nonabsorbing crystal. For a crystal with a linear absorption coefficient μ_0, the permissible thickness is actually less than t. However, this fact should not cause undue concern since, for most of the substances investigated by neutron scattering techniques, the dependence of R on μ_0 is less sensitive than on the other factors.

For the small crystal of $CeSn_3$ (PN2) used in the polarized beam experiment, we obtain a value of α/η for the (111) reflection equal to 0.193. Thus it satisfies the criterion for a 'thin crystal'. Therefore we expect only small effects due to secondary extinction. A method which we have adapted to correct for extinction for the large crystal PN1 is outlined in the Appendix.

2. Simultaneous reflections

Simultaneous reflections occur when a single crystal is so oriented in a neutron beam that two, or more, sets of planes in the crystal simultaneously satisfy Bragg's law for a single wavelength. In terms

of the reciprocal lattice, this situation occurs when, in addition to the reflection of interest (primary reflection), other reflection(s) (secondary reflection(s)) simultaneously lie on the Ewald sphere of reflection. The case of one secondary reflection is illustrated in Fig. 2.4. As a result, the intensity of the primary reflection may undergo diminution, known as 'aufhellung', or augmentation, known as 'umweganregung'. For example, in Fig. 2.4, reflection processes $0 \rightarrow 2$ and $1 \rightarrow 2$ would decrease the primary intensity of $0 \rightarrow 1$ reflection whereas process $0 \rightarrow 2 \rightarrow 1$ would increase the primary intensity. Experimentally, the effects may be observed by rotating the crystal slowly around the scattering vector of a given reflection.

The effects of simultaneous reflection were first reported by Wagner (84) in 1920 and studied experimentally by Renninger (85) in 1937. Studies to date separate in two categories: the determination of the crystal orientation at which simultaneous reflections occur, and the estimation of the effect on the intensity of a given primary reflection due to one or more secondary reflections.

In simple cases, the determination of the crystal orientation at which simultaneous reflections occur is straightforward. Hastings et al. (86) have developed a FORTRAN IV computer code, based on the geometric construction of Cole et al. (87), to calculate the positions of simultaneous reflections in terms of wavelength and angle coordinates for all orientations in any cubic system. Recently, their code has been generalized to permit the analysis of any orthorhombic lattice (88).

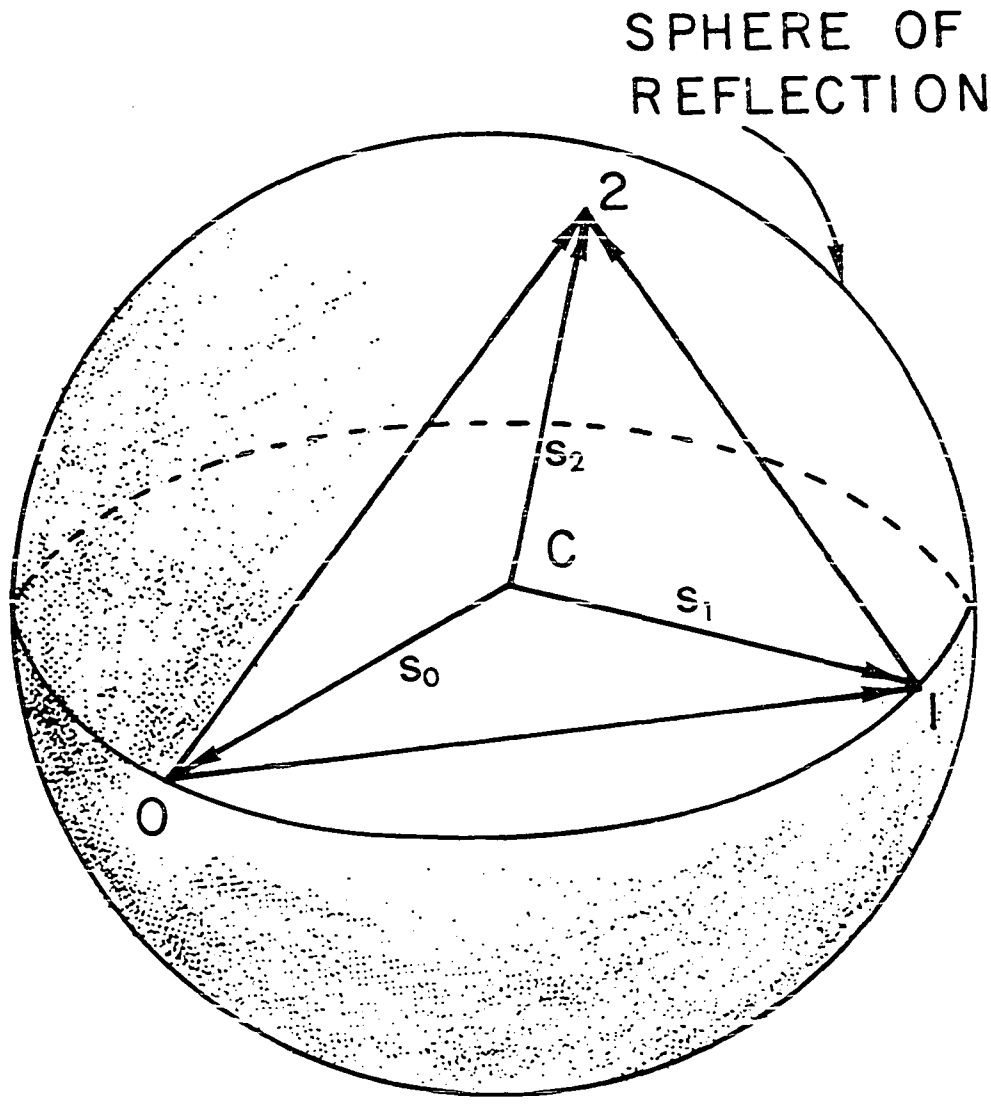

Figure 2.4. Geometric representation of simultaneous reflections in the reciprocal lattice. Points, O, 1 and 2 lie on the sphere of reflection. The vectors S_0, S_1 and S_2 define the direction of the incident, primary and secondary beams (after Ref. 89)

Using the distribution function given in Eq. (2.14) to approximate the mosaic structure of the crystal, Moon and Shull (89) in 1964 investigated the effects of simultaneous reflections on single crystal neutron diffraction intensities. They concluded that the effects of simultaneous reflections may become important when secondary extinction is not negligible and the magnitude of the intensity perturbation is determined by the quantities responsible for secondary extinction, namely the factor Qt/η in Eq. (2.15). Thus extraneous intensity effects may be reduced by using small crystals with broad mosaic spreads. In addition, it is preferable to use a specimen crystal which is long in only one direction rather than a flat plate in order to limit the path length of the secondary reflections.

In the present experiment, we used a computer program provided by Dr. R. M. Moon to calculate all the simultaneous reflections occurring with a given primary reflection and a given crystal orientation between two limiting neutron wavelengths. Based on the results of the calculation for a certain (primary) reflection, we chose the wavelengths of the incident neutrons to minimize contamination from simultaneous reflections. Since the number of simultaneous reflections increases dramatically as the wavelength decreases, a wavelength as long as 1.31 Å was used on same occasions. A few reflections were repeated more than seven times under various configurations including measurements at many selected wavelengths or with the sample rotated to a slightly different position about the scattering vector. In addition, the induced magnetic form factors at various temperatures were measured using two

single crystals (PN1 and PN2) so that effects of simultaneous reflections due to differences in crystal size or shape could be identified. Nevertheless, based on the experimental evidence, we concluded that simultaneous reflections did not significantly affect the results.

III. FUNDAMENTAL THEORIES OF MAGNETIC SCATTERING

The electromagnetic interaction between a neutron and a nucleus and its electronic environment has been a subject of theoretical study since the discovery of neutrons in 1932. To aid in this study the idea of magnetic scattering of slow neutrons was introduced and later was applied to the investigation of magnetic phenomena. Today, as well as in the past, new understanding of electronic and magnetic properties of matter can be obtained by a systematic analysis of the experimental results within the framework of the existing theory. In the following an overall view of the problem of elastic scattering of neutrons by an atom in an external magnetic field will first be presented and followed by a discussion of the principal interaction; namely, the magnetic interaction between a neutron and the atomic electrons. The formulas outlined in this chapter will be helpful in the analysis of the experimental results of the polarized neutron studies of $CeSn_3$.

A. Elastic Scattering of Neutrons by an Atom in an External Magnetic Field

The interaction between a slow neutron and an atom whose nucleus is positioned at the origin can be described by the following Hamiltonian

$$\mathcal{H} = -\mu\vec{\sigma}\cdot(\vec{H}_{so} + \vec{H}_{d}) - \frac{\mu}{2Mc}(\nabla\cdot\vec{E}) - \mu\vec{\sigma}\cdot\frac{\vec{E}\times\vec{p}}{Mc} + V, \qquad (3.1)$$

when V is the Fermi pseudopotential (90)

$$V = \frac{2\mu\hbar^2}{M}[b + ib' + B\vec{I} \cdot \vec{\sigma}]\delta(\vec{r}), \tag{3.2}$$

with

$$B = \frac{b_+ - b_-}{2I + 1}, \quad b' = \sigma_t/2\lambda. \tag{3.3}$$

In the above equations

$\mu = \mu_n(e\hbar/2Mc)$ = neutron magnetic moment

M = neutron mass

$\vec{p}$ = neutron momentum

$\vec{I}$ = spin of the nucleus

$\vec{\sigma}$ = Pauli matrix

b = coherent nuclear scattering amplitude

b_+, b_- = nuclear scattering amplitudes for the I + 1/2 and I - 1/2 neutron-nucleus states respectively

b' = imaginary part of the nuclear scattering amplitude

σ_t = total neutron-nucleus cross section

λ = neutron wavelength

$\vec{E}$ = Coulomb field of the atom

$\vec{H}_{so}$ = magnetic field due to the induced electronic spin and orbital moments

$\vec{H}_d$ = magnetic field produced by the field induced diamagnetic currents in the atom

The coherent elastic scattering amplitude in the first Born approximation is obtained by taking the matrix element of the

Hamiltonian in Eq. (3.1) between the plane wave states $|\vec{k}_0\rangle$ and $|\vec{k}\rangle$ of the incident and scattered neutrons. ($\vec{k}_0$ and $\vec{k}$ are the incident and scattered neutron wave vectors respectively)

$$a(\theta) = (p + p_d)\vec{q}_m \cdot \vec{\sigma} + (b + \langle BI_z \rangle \vec{n} \cdot \vec{\sigma} + \gamma_0) + i(\gamma \cot\theta \vec{\sigma} \cdot \vec{n} + b'), \qquad (3.4)$$

where

$$\vec{q}_m = (\hat{q} \cdot \vec{\varepsilon}_3)\hat{q} - \vec{\varepsilon}_3 \ , \qquad (3.5)$$

$$\langle BI_z \rangle = \frac{(b_+ - b_-)}{3} \mu_N \frac{(I + 1)}{(2I + 1} \frac{H}{k_B T} \ , \qquad (3.6)$$

$$\gamma_0 = \frac{\mu_n e^2}{2Mc^2} Z[1 - f_c(\theta)] = 1.463Z[1 - f_c(\theta)] \times 10^{-16} \text{cm} \qquad (3.7)$$

$$\vec{n} = \frac{\vec{k}_0 \times \vec{k}}{|\vec{k}_0 \times \vec{k}|} \qquad (3.8)$$

In Eqs. (3.4) to (3.7) above, p is the magnetic scattering amplitude which will be discussed in more detail in the following sections, p_d is the diamagnetic scattering amplitude, $\hat{q}$ is a unit vector in the direction of the neutron momentum transfer vector $\vec{q}$, $\vec{\varepsilon}_3$ is a unit vector in the direction of the external magnetic field $\vec{H}$ (along z axis), k_B is the Boltzmann constant, μ_N is the magnetic moment of the nucleus, Z is the atomic number of the atom, $f_c(\theta)$ is the atomic charge form factor and θ is the Bragg angle.

As can be seen from Eq. (3.4), $a(\theta)$ is expressed as the sum of the three groups of terms, the first two groups being real while the final group is imaginary. The first term of the first group

characterizes the magnetic interaction of the neutron with the induced spin and orbital magnetic moments of the atomic electrons. The second term arises from the magnetic interaction of the neutron with the field-induced diamagnetic currents (91) in the atom. Since diamagnetism is a universal property, this term is always present. For paramagnetic materials, it is usually small compared to the first term; nevertheless, corrections have to be introduced to the measured magnetic scattering amplitudes (see Appendix A). In the second group, the first term is the familiar spin-independent neutron-nucleus interaction. The second term is the spin-dependent part of the nuclear scattering amplitude and is known as the nuclear polarization term (92). In general, the contribution from this interaction is quite small. However, as can be seen in Eq. (3.6), it may become significant at low temperatures for certain materials as was indeed observed (93) to be the case for vanadium. For $CeSn_3$ the non-zero nuclear spins are from three Sn isotopes constituting about 17 percent of natural abundance. The nuclear polarization correction to the measured intensity ratio R (see Eq. (2.5)), at T = 4.2K with an applied field of 42.5kG, was estimated to be about one percent and hence was neglected. The third term in this group is known as the Foldy term (94) which arises from the relativistic interaction between the electric charges in the atom and the anomalous moment of the neutron. As can be seen in Eq. (3.7), this term can be neglected since γ_0 is smaller than b for most of the atoms by a factor of 10^2-10^3 (hence 10^4-10^6 smaller

in intensity). The first term in the third group is the neutron spin-neutron orbit interaction first considered by Schwinger (95) for the case of fast neutrons. This spin-orbit interaction which arises from the motion of the neutron magnetic moment in the nuclear Coulomb field is small compared to the main interactions, nevertheless it has been detected (96) experimentally. Consequently, we need to introduce a correction to the measured intensity ratio (see the Appendix). The last term contains the imaginary part of the nuclear scattering amplitude which in general is small (on the order of 10^{-16}cm) for most of the materials investigated by neutron scattering techniques.

B. Magnetic Scattering of Neutrons by Atoms

The theory of the magnetic interaction between a neutron and the spin and orbital moments of the electrons in an atom have been studied by many authors in the last 40 years. Its development occurred in the following stages:

1. Following the original investigation of the interaction between the magnetic moments of a neutron and that of a ferromagnetic ion given by Bloch (97) and Schwinger (98), in 1939 Halpern and Johnson (99) presented a detailed formalism of magnetic scattering of neutrons by an atom with zero orbital magnetic moment.
2. The general case of scattering by ions possessing both a spin and an orbital magnetic moment, such as the rare-earth ions, was first examined by Trammell (100) and subsequently extended by Odiot and Saint-James (101) to include the scattering from

crystal field levels. The matrix elements of the interaction Hamiltonian were evaluated using the traditional Condon and Shortley (102) formalism which required involved calculations offering little physical insight into the problem.

3. A more powerful tensor operator technique was introduced by Johnston (103) in 1966 to simplify the calculation of the matrix elements in the scattering cross section. His work was expanded upon in articles by a number of authors (104-110) and later was summarized in Chapter 6 of the book by Marshall and Lovesey (111).
4. Recently Stassis and Deckman (112-115) presented a new treatment of the theory which made possible the application of the techniques of modern spectroscopy to the magnetic scattering of neutrons by an arbitrary system of particles. The magnetic scattering amplitude was expressed in terms of the magnetic and electric multipole moments the number of which was limited by selection rules based on the symmetry properties of the states of the system, in particular parity and angular momentum conservation. This formalism was subsequently used by Stassis et al. (116) to calculate the relativistic form factors of all the tripositive rare-earth ions.

Since reviews of this latter approach can be found in the recent articles by Sinha (117) and Stassis (118), we shall proceed to outline the results of their formulation with emphasis on its application to the interpretation of the experimental results of the polarized neutron studies of $CeSn_3$.

In general, both the ionic and conduction electrons in a metal contribute to the neutron magnetic scattering amplitude. The ionic contribution can be evaluated using electronic wavefunctions obtained by some type of self-consistent field atomic calculation using a potential appropriate for the metallic environment; the conduction electron contribution, on the other hand, has to be evaluated using the solid state electronic wavefunctions otbtained in a detailed study of the band structure of the metal.

In rare earth metals and compounds the 4f electrons are considered highly localized, with the rare earth ion retaining the magnetic moment predicted by Hund's rules. When the unfilled 4f shell is well separated from the conduction band, within which the Fermi level lies, the ionic contribution to the magnetic scattering is dominant and this contribution can be calculated to excellent approximation by using the appropriate free ionic configuration. However, in the case of mixed-valence systems in which the energies of the f-electrons are no longer well separated from the conduction band energies, effects such as 4f-conduction band hybridization may become important on some occasions and large deviations of the magnetic scattering amplitude from that of the ionic part would be expected. Therefore, the ionic contribution to the magnetic scattering amplitude may serve as a reference for the detection of mixed-valent character.

1. The ionic contribution to the magnetic scattering amplitude

The magnetic scattering of neutron arises from the interaction of both the spin and orbital currents of the electrons with the magnetic

moment of the neutron. It can be shown that the magnetic scattering amplitude for neutron momentum transfer vector $\vec{q}$ is given by

$$p(\vec{q}) = (|\gamma| r_o)\vec{\sigma} \cdot \vec{\mathcal{J}}_\perp \tag{3.9}$$

where $\gamma = -1.91$ is the neutron magnetic moment in nuclear magnetons, r_o is the classical electron radius, $\vec{\sigma}$ is a Pauli matrix, and $\vec{\ }$ is a dimensionless operator related to the Fourier transform of the current density $\vec{j}(r)$ of the system by

$$\vec{\mathcal{J}}_\perp = -i \left(\frac{m}{e\hbar q} \right) \hat{q} \times \langle f | \int \vec{j}(\vec{r}) \exp(i\vec{q} \cdot \vec{r}) d\vec{r} | i \rangle \tag{3.10}$$

where m is the electron mass, $e = -|e|$ is the electronic charge, $\hat{q}$ is a unit vector along $\vec{q}$, and $|i\rangle$ and $|f\rangle$ denote the initial and final states of the system respectively. By analogy with the matrix elements in Eq. (3.10) which appear in the well-known problem concerning the interaction of polarized electromagnetic radiation with atoms, one obtains

$$p(\vec{q}) = (|\gamma| r_o)\vec{\sigma} \cdot \left[\sum_{k,m} \left(\frac{8\pi}{2k+1} \right)^{1/2} \{ \vec{X}^*_{km}(\hat{q}) \langle f | T^{(e)}_{km} | i \rangle - i(\hat{q} \times \vec{X}^*_{km}(\hat{q})) \langle f | T^{(m)}_{km} | i \rangle \} \right] \tag{3.11}$$

where $\vec{X}_{km}(\hat{q})$ denotes the vector sperical harmonic $Y^m_{k,k,1}(\hat{q})$ and $T^{(e)}_{km}$ and $T^{(m)}_{km}$ are irreducible tensor operators corresponding to the electric and magnetic multipoles of the system respectively. Note that since both $\vec{X}_{km}$ and $(\hat{q} \times \vec{X}_{km})$ are transverse to $\vec{q}$, Eq. (3.11) explicitly exhibits the fundamental property of magnetic scattering, namely, that the magnetic moment of the neutron couples only to the transverse

components of the current density. In addition, in the limit $\vec{q} \to 0$ these operators are, of course, proportional to the static multipole moments of the system.

Let us consider only scattering within the ℓ^n configuration. By parity conservation only even order electric and odd order magnetic multipoles contribute to the magnetic scattering amplitude. In addition, since the multipole operators are one-electron operators, their rank must be less than or equal to $(2\ell + 1)$. Thus the magnetic scattering amplitude is determined by the matrix elements of a limited number of electric ($k = 2, 4, \ldots, 2\ell$) and magnetic ($k = 1, 3, \ldots, 2\ell+1$) multipoles. Furthermore, by conservation of angular momentum, we obtain the conditions: $|J - J'| \leq k \leq |J + J'|$, and $M = M' + m$, where J', M' and J, M are the angular momentum quantum numbers of the initial and final ionic states respectively. It can be shown that the multipole operators can be written as

$$T^{(e)}_{km} = i^{k+1}\left[R^{(e)}_{(0,k,k)} W^{(0,k)k}_m + \sum_{k'=k,k\pm1} R^{(e)}_{(1,k',k)} W^{(1,k')k}_m \right] ,$$

$$k = 2, 4, \ldots, 2\ell; \; k' \leq 2\ell \qquad (3.12)$$

$$T^{(m)}_{km} = i^{k+1}\left[R^{(m)}_{(0,k,k)} W^{(0,k)k}_m + \sum_{k'=k,k\pm1} R^{(m)}_{(1,k',k)} W^{(1,k')k}_m \right] ,$$

$$k = 1, 3, \ldots, 2\ell+1; \; k' \leq 2\ell \qquad (3.13)$$

where the non-vanishing matrix elements of the tensors $W^{(0,k)k}_m$ and $W^{(1,k')k}_m$ can be calculated using the generalized Wigner-Eckart theorem

$$(\theta JM|W_m^{(\kappa',k')k}|\theta'J'M') = (-)^{J-M}\begin{pmatrix} J & k & J' \\ -M & m & M' \end{pmatrix}(\theta J||W^{(\kappa',k')k}||\theta'J')$$

$$= (-)^{J-M}[(2J+1)(2k+k)(2J'+1)]^{1/2}\begin{pmatrix} J & k & J' \\ -M & m & M' \end{pmatrix}$$

$$\cdot\begin{Bmatrix} S & S' & \kappa' \\ L & L' & k' \\ J & J' & k \end{Bmatrix}(\theta||W^{(\kappa',k')}||\theta') \quad . \qquad (3.14)$$

In this equation, θ is the set of additional quantum numbers needed to completely specify the state, the quantities $\begin{pmatrix} \cdot & \cdot & \cdot \\ \cdot & \cdot & \cdot \end{pmatrix}$ and $\begin{Bmatrix} \cdot & \cdot & \cdot \\ \cdot & \cdot & \cdot \end{Bmatrix}$ are conventional 6-j and 9-j symbols. The R's in Eqs. (3.12) and (3.13) are the relativistic radial integrals given in explicit expressions by Stassis and Deckman in Ref. 115. In the nonrelativistic limit, only the R's in the Eqs. (3.12) and (3.13) need to be replaced by their corresponding nonrelativistic form. More specifically, the multipole operators in Eqs. (3.12) and (3.13) are replaced by the following expressions:

$$T_{km}^{(e)} = i^{k+1}[R_2(k)W_m^{(0,k)k} + R_1(k,k)W_m^{(1,k)k}] \quad , \quad k = 2, 4, \ldots, 2\ell \qquad (3.15)$$

$$T_{km}^{(m)} = i^{k+1}\left[R_0(k)W_m^{(0,k)k} + \sum_{k'=k\pm1} R_1(k',k)W_m^{(1,k')k} \right],$$

$$k = 1, 3, \ldots, 2\ell+1 \qquad (3.16)$$

where the nonrelativistic radial integrals $R_0(k)$ and $R_1(k',k)$ for d- and f-electrons can be found in Ref. 114.

In the following we summarize the important expressions for the magnetic scattering amplitude in the case of elastic scattering by an atom or ion whose state is either a single or mixed Russell-Saunders

state of the ℓ^n configuration. These formulas are useful in the analysis of the polarized neutron results for $CeSn_3$ which will be discussed in Chapter IV. Only nonrelativistic expressions, which are excellent approximations, are given here.

a. Scattering from a single Russell-Saunders state $|\theta JM\rangle$ In this case the electric multipole contribution vanishes and only the m = 0 component of the magnetic multipoles contributes to the scattering amplitude. This scattering amplitude can be written as

$$p^{\theta JM}_{\theta JM}(\vec{q}) = (|\gamma|r_o)\vec{\sigma}\cdot\vec{q}_m\langle\theta JM|\sum_k i^{k+1}\left(\frac{2}{k(k+1)}\right)^{1/2} p_k'(\cos\varphi)\{R_0(k)W_0^{(0,k)k} + \sum_{k'=k\pm1} R_1(k',k)W_0^{(1,k')k}\}|\theta JM\rangle \quad , \quad k = 1, 3, \ldots, 2\ell+1 \quad . \tag{3.17}$$

Here $\vec{q}_m$ is the so-called magnetic scattering vector defined by

$$\vec{q}_m = (\hat{q}\cdot\vec{\varepsilon}_3)\hat{q} - \vec{\varepsilon}_3 \tag{3.18}$$

where $\vec{\varepsilon}_3$ is a unit vector along the z-axis (quantization axis of the ion). p_k' is the derivative of a Legendre polynomial and φ is the angle between $\vec{q}$ and $\vec{\varepsilon}$.

b. Scattering amplitude for the transition $\theta'J'M' \rightarrow \theta JM$ If the initial (final) state $|\phi'\rangle$ ($|\phi\rangle$) can be expressed in terms of Russell-Saunders states $|\theta'J'M'\rangle$ ($|\theta JM\rangle$) of the ℓ^n configuration, i.e.,

$$|\phi'\rangle = \sum_{\theta',J',M'} a(\theta',J',M')|\theta'J'M'\rangle \qquad (|\phi\rangle = \sum_{\theta,J,M} a(\theta,J,M)|\theta JM\rangle) \quad , \tag{3.19}$$

the magnetic scattering amplitude can be written as

$$p(\vec{q}) = \sum_{\substack{\theta,J,M \\ \theta',J',M'}} a^*(\theta JM)a(\theta'J'M')\, p^{\theta JM}_{\theta'J'M'}(\vec{q}) \quad , \qquad (3.20)$$

where

$$p^{\theta JM}_{\theta'J'M'}(\vec{q}) = (|\gamma|r_o)\vec{\sigma}\cdot\langle\theta JM|\sum_{k,m} i^{k+1}\left(\frac{8\pi}{2k+1}\right)^{1/2}\{\vec{X}^*_{km}(\hat{q})[R_2(k)W_m^{(0,k)k} + R_1(k,k)W_m^{(1,k)k}] - i[\hat{q}\times\vec{X}^*_{km}(\hat{q})][R_0(k)W_m^{(0,k)k} + \sum_{k'=k\pm1} R_1(k',k)W_m^{(1,k')k}]\}|\theta'J'M'\rangle \quad . \qquad (3.21)$$

The first term in curly brackets gives the electric multipole contribution consisting of terms for k = 2, 4, ..., 2ℓ and thh second gives the magnetic multipole contribution consisting of terms for k = 1, 3, ..., 2ℓ+1.

This formulation will be applicable, for example, when crystal field effects are present.

c. Magnetic scattering by a paramagnetic crystal in an external magnetic field $\vec{B}$ The calculation of the coherent magnetic scattering of neutrons by a paramagnetic crystal in an external magnetic field B, a problem of primary interest in polarized neutron experiments, can be quite complicated. However, once the crystal electronic ground state has been determined or assumed the calculation is, in principle, straightforward. The simplest case is that of an ion whose ground state is a single Russell-Sanuders state $|\theta JM\rangle$. In the presence of the

magnetic field the ground state is split into (2J+1) levels whose probability of occupation is $e^{-\beta M}/(\sum_M e^{-\beta M})$ where $\beta = -g\mu_B B/k_B T$ (g is the Landé splitting factor, k_B the Boltzmann's constant, μ_B the Bohr magneton and T the temperature). The coherent paramagnetic scattering amplitude is then

$$\langle p(\vec{q})\rangle = \frac{\sum_M e^{-\beta M} p(\vec{q})}{\sum_M e^{-\beta M}} \qquad (3.22)$$

where $p(\vec{q}) = p_{\theta JM}^{\theta JM}(\vec{q})$ is given in Eq. (3.17).

If the crystal ground state is not a single state and the energies of the splitting due to the magnetic field are small relative to the unperturbed energy levels (with no external field), perturbation theory can be applied to determine the energies and wavefunctions of the splitting levels. Then the magnetic scattering amplitude of each level can be calculated using the formulas given in case 2 above and the coherent magnetic scattering amplitude is obtained from Eq. (3.22) by replacing βM with ε_M denoting the energy of the M^{th} level.

2. The conduction electron contribution to the magnetic scattering amplitude

As we pointed out earlier, the calculation of the conduction electron contribution to the coherent magnetic scattering by a metal in a magnetic field requires the use of the solid state electronic wavefunctions of the metal. Unfortunately, accurate calculations of the electronic ground state for rare earth metals and compounds, especially

those exhibiting valence fluctuations, are not presently available (119). In the first place, as a result of being highly localized, the 4f electrons in an open shell experience large intra-atomic Coulomb and exchange correlation interactions which are not treated properly by the traditional band structure approach. Second, the hybridization between the 4f states and the conduction electrons which gives rise to many anomalous properties is very sensitive to the potential used in the calculation. But the potentials used in band calculations, such as the muffin-tin potential used in the APW method, are not accurate enough to provide reliable results (120). Finally, not all the band calculations are performed in a self-consistent fashion. Therefore, new models or techniques are undoubtedly needed for band structure studies of rare earth metallic systems. These problems notwithstanding we shall outline the formalism in the calculation of the conduction electron contribution to the magnetic scattering amplitude as if an accurate potential and the solid state electronic wavefunctions had been obtained.

The conduction electron contribution to the magnetic scattering amplitude can be written in the conventional form

$$\vec{p}(\vec{q}) = f(\vec{q})\vec{\sigma} \cdot \vec{q}_m \tag{3.23}$$

where $\vec{\sigma}$ and $\vec{q}_m$ have been defined above and $f(\vec{q})$ is the induced magnetic form factor given by

$$f(\vec{q}) = \frac{|\gamma| r_o}{2\mu_B} B\chi_{zz}(\vec{q},0) \quad . \tag{3.24}$$

The z-axis is chosen to coincide with the direction of the external

magnetic field and $\chi_{zz}(\vec{q},0)$ is the generalized susceptibility function. In the absence of significant spin-orbit coupling the generalized susceptibility consists of a spin $\chi_{zz}^{(s)}$ and an orbital $\chi_{zz}^{(o)}$ component:

$$\chi_{zz}(\vec{q},0) = \chi_{zz}^{(s)}(\vec{q},0) + \chi_{zz}^{(o)}(\vec{q},0) \quad . \tag{3.25}$$

The spin part of the susceptibility function in the absence of exchange interactions is simply the Fourier transform of the induced spin magnetization at the Fermi level:

$$\begin{aligned} \chi_{zz}^{(s)}(\vec{q},0) &= \mu_B^2 \sum_{k\sigma} \langle \psi_{k\sigma} | e^{-i\vec{q}\cdot r} | \psi_{k\sigma} \rangle \delta(E_{k\sigma} - E_F) \\ &= 2\mu_B^2 \int_{E=E_F} \frac{dS}{|\nabla_k E_k|} \langle \psi_k | e^{-i\vec{q}\cdot\vec{r}} | \psi_k \rangle \end{aligned} \tag{3.26}$$

where k denotes the electronic wavevector, σ is a spin index, $\psi_{k\sigma}$ denotes the Bloch wavefunction with energy eigenvalue $E_{k\sigma}$, and E_F is the Fermi level. Thus, once a detailed band structure analysis of the system has been made, the evaluation of the generalized spin susceptibility is relatively straightforward.

On the other hand, the practical evaluation of the generalized orbital susceptibility is a difficult computational problem. Even in the tight binding approximation the calculation requires the evaluation of matrix elements of complicated operators between all occupied and unoccupied states. The only calculationof this kind to date is that for chromium by Oh et al. (121).

IV. RESULTS AND DISCUSSION OF THE POLARIZED NEUTRON EXPERIMENTS

A. Presentation of Experimental Data

The magnetic form factor measurements (122,123) were performed using the HB-1 polarized neutron spectrometer at the High Flux Isotope Reactor (HFIR) of the Oak Ridge National Laboratory. The angular dependence of the quantity $4\ F_M(\theta)/F_N$ (see section A of Chapter II) of $CeSn_3$ in an applied magnetic field of 42.5kG has been determined at 300, 150, 70, 40, 15, 4.2, 3.0 and 1.7K. The magnetic field was provided by a split-coil superconducting magnet installed on the sample table of the spectrometer. All the measurements, except those at 3.0 and 1.7K, were performed on both samples PN1 and PN2 (see section C of Chapter II for sample description). At all the temperatures, the field was applied parallel to the [110] direction so that intensity ratios for the $(hh\bar{l})$ reflections were measured. In addition, measurements of intensity ratio for the (hk0) reflections were performed on the PN2 crystal at 4.2 and 40K, with the field applied parallel to the [001] direction. All data were corrected for the inefficiency of the counting system, the incomplete beam polarization and imperfect spin flipping, and for the contributions arising from the field induced diamagnetism and the neutron spin-neutron orbit interaction (see the Appendix). The data of the PN1 sample, the crystal with a larger thickness, were corrected for secondary extinction (see the Appendix).

The value of $q = \frac{\sin\theta}{\lambda}$ for a reflection (khℓ) was calculated from

$$\frac{\sin\theta}{\lambda} = \frac{\sqrt{h^2 + k^2 + \ell^2}}{2a} \tag{4.1}$$

by using the lattice constant (54) $a = 4.271\text{Å}$. As mentioned earlier in Chapter II, there are two types of Bragg reflections giving different values for the elastic nuclear structure factor. That is, neglecting effects due to thermal vibrations of the atoms,

$$F_N = \begin{cases} b_{Ce} + 3\, b_{Sn}, & \text{for unmixed Miller indicies (fundamental) reflections,} \\ b_{Ce} - b_{Sn}, & \text{for mixed Miller indicies (superlattice) reflections.} \end{cases} \tag{4.2}$$

The values of $4F_M(\theta)/F_N$ were normalized to the fundamental reflections; i.e., the values of $4F_M(\theta)/F_N$ for the superlattice reflections were multiplied by the follow factor:

$$\frac{b_{Ce} - b_{Sn}}{b_{Ce} + 3b_{Sn}} = -18.0625 \tag{4.3}$$

Here values (124) of $b_{Ce} = 0.482 \times 10^{-12}$cm and $b_{Sn} = 0.61 \times 10^{-12}$cm have been used for the nuclear scattering amplitudes of Ce and Sn respectively.

The experimental results are summarized in Tables 4.1 and 4.2. If a single reflection has been measured more than one time, the weighted average of the observed values is given. Furthermore, a preliminary set of measurements in a field of 60kG, was performed on the original crystal (before it was separated into the PN1 and PN2 samples) using the polarized neutron spectrometer at the Ames Laboratory Research Reactor (ALRR). The results of these measurements, which are

Table 4.1. Magnetic form factor data of $CeSn_3$ obtained at the HFIR and the results of form factor fitting

T = 300K, H = 42.5kG, $\vec{H}$//[110].

h k ℓ	$\sin\theta/\lambda$ ($\mathring{A}^{-1}$)	$y^{obs.}$ [a]	$y^{calc.}$ [b]	$y^{obs.}$ [c]	$y^{calc.}$ [d]
0 0 0	0.0		5.700		5.411
0 0 1	.106	5.208±.18	5.479	5.137±.15	5.201
1 1 0	.150	5.595±.18	5.275	5.347±.19	5.007
1 1 1	.183	5.017±.14	5.120	4.933±.18	4.859
0 0 2	.212	4.630±.22	4.883		
1 1 2	.259	4.127±.21	4.537		
2 2 0	.300	4.344±.14	4.213	4.042±.19	3.999
2 2 1	.318	4.001±.26	4.066		
2 2 2	.367	3.559±.18	3.665		
2 2 3	.437	2.854±.31	3.106	3.078±.22	2.949
3 3 0	.449	3.101±.40	3.013		
1 1 4	.449	2.650±.38	3.013		
3 3 1	.462	3.232±.15	2.916		
3 3 2	.497	2.521±.27	2.659		
2 2 4	.519	2.701±.20	2.509		
3 3 3	.550	2.365±.15	2.299		
4 4 2	.635	2.288±.22	1.801	2.184±.20	2.182

[a] Measured values of $4\ F_M/F_N \times 10^3$ obtained using the PN1 sample.

[b] Calculated values of $4\ F_M/F_N \times 10^3$ obtained using the PN1 sample.

[c] Measured values of $4\ F_M/F_N \times 10^3$ obtained using the PN2 sample.

[d] Calculated values of $4\ F_M/F_N \times 10^3$ obtained using the PN2 sample.

Table 4.1. Continued

T = 150K, H = 42.5kG, H//[001]

h k ℓ	$\sin\theta/\lambda$ ($\mathring{A}^{-1}$)	$y^{obs.a}$	$y^{calc.b}$	$y^{obs.c}$	$y^{calc.d}$
0 0 0	0.0		7.005		6.876
0 0 1	.106	6.721±.16	6.734	6.467±.18	6.609
1 1 0	.150	6.461±.17	6.483	6.359±.17	6.363
1 1 1	.183	6.279±.15	6.235	6.488±.19	6.119
0 0 2	.212			6.207±.21	5.890
2 2 0	.300	4.942±.15	5.187	4.781±.19	5.082
2 2 1	.318	4.882±.25	4.996	4.702±.25	4.904
2 2 2	.367	4.543±.19	4.504		
0 0 4	.427			3.979±.27	3.870
3 3 0	.449	4.199±.28	3.702		
3 3 1	.462	3.776±.16	3.584		
3 3 2	.497			3.407±.26	3.207
3 3 3	.550			2.614±.19	2.773
4 4 2	.635	2.291±.20			

Table 4.1. Continued

T = 70K, H = 42.5kG, $\vec{H}$//[110]

h k ℓ	$\sin\theta/\lambda$ ($\mathring{A}^{-1}$)	$y^{obs.a}$	$y^{calc.b}$	$y^{obs.c}$	$y^{calc.d}$
0 0 0	0.0		5.919		5.912
0 0 1	.106	5.927±.19	5.689	5.735±.19	5.683
1 1 0	.150	5.618±.18	5.477	5.296±.19	5.471
1 1 1	.183	5.560±.15	5.268	5.353±.20	5.262
0 0 2	.212			5.198±.24	5.064
2 2 0	.300	4.147±.15	4.374	4.480±.18	4.369
2 2 1	.318	4.058±.21	4.221		
2 2 2	.367	3.806±.18	3.805		
3 3 0	.449	2.708±.27	3.128		
3 3 1	.462	2.727±.16	3.028		
2 2 4	.519			2.404±.25	2.602
3 3 3	.550	2.199±.17	2.387		
4 4 2	.635	1.850±.20	1.869		

Table 4.1. Continued

T = 40K, H = 42.5xG

h k ℓ	$\sin\theta/\lambda(\text{Å}^{-1})$	$y^{obs.a,e}$	$y^{calc.b,e}$	$y^{obs.c,e}$	$y^{calc.d,e}$	$y^{obs.c,f}$	$y^{calc.d,f}$
0 0 0	0.0		5.559		5.455		5.452
0 0 1	.106	5.458±.17	5.344	5.567±.19	5.244	5.453±.19	5.241
1 1 0	.150	5.057±.16	5.145	4.929±.18	5.048	5.009±.18	5.046
0 0 2	.212			4.927±.22	4.673	4.907±.21	4.670
2 2 0	.300	3.971±.18	4.109	3.564±.21	4.032	3.430±.22	4.030
0 0 3	.318			3.393±.31	3.891	3.747±.30	3.889
0 0 4	.424			3.270±.20	3.070		
2 2 4	.519			2.430±.26	2.401		

[e] $\vec{H}$//[110].

[f] $\vec{H}$//[001].

Table 4.2. Magnetic form factor data of $CeSn_3$ in the 1.7-40K temperature range and the results of the form factor fitting

h k ℓ	$\frac{\sin\theta}{\lambda}$ ($\AA^{-1}$)	PN1[a]		PN2[a]		PN2[b]
		$y^{obs.}$[c]	$y^{calc.}$[d]	$y^{obs.}$[c]	$y^{calc.}$[d]	$y^{obs.}$[c]
0 0 0	0.0		9.179		11.118	
0 0 1	0.150	7.308 ± .20	7.296	8.288 ± .20	8.470	7.308 ± .20
1 1 0	0.183	6.140 ± .19	6.137	6.983 ± .20	6.869	5.034 ± .19
1 1 1	0.212	4.847 ± .18	5.295	5.055 ± .18	5.728	
0 0 2	0.300	5.522 ± .19	5.531	6.310 ± .30	6.142	5.500 ± .19
2 2 0	0.318	4.353 ± .20	3.947	4.369 ± .18	4.104	4.248 ± .23
2 2 1	0.318	3.544 ± .18	3.671	3.498 ± .18	3.760	
0 0 3	0.318	4.700 ± .21	4.503	5.501 ± .22	4.966	5.165 ± .22
1 1 3	0.351	3.438 ± .15	3.321			
2 2 2	0.367	3.381 ± .17	3.225	3.337 ± .18	3.087	
0 0 4	0.424	3.596 ± .19	3.586	3.925 ± .20	3.966	3.714 ± .20
3 3 0	0.449	2.316 ± .40	2.912	2.884 ± .39	3.064	
3 3 1	0.462	2.423 ± .15	2.789			
4 2 0	0.474					2.649 ± .20
2 2 4	0.519	2.542 ± .15	2.485	2.339 ± .18	2.638	
3 3 3	0.550	2.002 ± .15	2.225	1.818 ± .20	2.343	
4 4 2	0.635	1.560 ± .22	1.759	1.694 ± .23	1.858	

[a] $\vec{H}$//[110], T = 4.2K, H = 42.5kG.

[b] $\vec{H}$//[001], T = 4.2K, H = 4.25kG.

[c] Measured values of $4\ F_M/F_N \times 10^3$.

[d] Calculated values of $4\ F_M/F_N \times 10^3$.

Table 4.2. Continued

h k ℓ	$\frac{\sin\theta}{\lambda}(\mathring{A}^{-1})$	$\frac{PN1^{e}}{y^{obs.}{}^{c}}$	$\frac{PN2^{e}}{y^{calc.}{}^{d}}$	$\frac{PN1^{f}}{y^{obs.}{}^{c}}$	$\frac{PN1^{g}}{y^{obs.}{}^{c}}$
0 0 0					
0 0 1	.106	5.732 ± .15	6.909 ± .18	7.066 ± .15	6.742 ± .15
1 1 0	.150	5.234 ± .16	5.833 ± .18	6.014 ± .15	6.106 ± .15
1 1 1	.183	4.768 ± .16	4.845 ± .20	5.072 ± .18	5.138 ± .18
0 0 2	.212		5.614 ± .22		
2 2 0	.300	3.601 ± .18	3.696 ± .22	4.018 ± .18	4.039 ± .18
0 0 3	.318		4.280 ± .27		
0 0 4	.424		3.679 ± .20		
3 3 0					2.223 ± .20
2 2 4	.519		2.247 ± .21		

[e] T = 15K, H = 42.5kG.
[f] T = 3.0K, H = 42.5kG.
[g] T = 1.7K, H = 42.5kG.

} $\vec{H}$//[110].

Table 4.3 Experimental results of the magnetic form factor measurements of $CeSn_3$ obtained at the ALRR[a]

Experimental conditions:	original crystal $\vec{H}$// [001] λ = 1.05Å Co-Fe monochromator Pu filter before sample			

h k ℓ	sinΘ/λ (Å^{-1})	T = 300.2K $y^{obs.}$ (10^{-3})	T = 150.2K $y^{obs.}$ (10^{-3})	T = 70.2K $y^{obs.}$ (10^{-3})	T = 4.2K $y^{obs.}$ (10^{-3})
1 1 1	0.183	5.139±.10	6.011±.11	5.313±.13	4.844±.13
2 2 0	0.300	4.250±.17	4.854±.16	4.262±.20	3.815±.20
0 0 4	0.427	3.211±.20			
2 2 4	0.519	2.761±.25			

[a]The measurements were performed with an applied magnetic field of 60kG; the data given in this table are normalized to H = 42.5kG.

given in Table 4.3, were found to be in good agreement with those obtained at the HFIR.

B. Discussion of Experiment Results

The goal of the polarized neutron experiment is to study the field-induced magnetic form factors of $CeSn_3$ at various temperatures. Since the magnetic form factor is related to the electronic wavefunctions at the Fermi level, information about the exact nature of the ground state of a mixed valence compound can be obtained. Furthermore, if the system exhibits temperature-induced valence fluctuation, a study of the temperature dependence of the magnetic form factors of this material can provide insight into the mechanism of valence fluctuation.

One important conclusion can be reached immediately by inspection of Figs. 4.1 to 4.3 which illustrate the general features of the magnetic form factor data of $CeSn_3$ at temperatures ranging from 300-4.2K. At temperatures between 300 to 40K, the smooth fall-off of the experimental points with increasing θ indicates that the magnetic moment distributions in this temperature range are almost spherical, resembling to those of isolated free ions. On the other hand, at temperatures below 40K (e.g. at 4.2K) the magnetic form factor data show large deviations from a smooth curve suggesting a significant anisotropy in the spatial distribution of the induced magnetization. Therefore it is natural to present the data analysis into two parts corresponding to these two ranges of temperatures. We shall first discuss the results at temperatures between 300 to 40K.

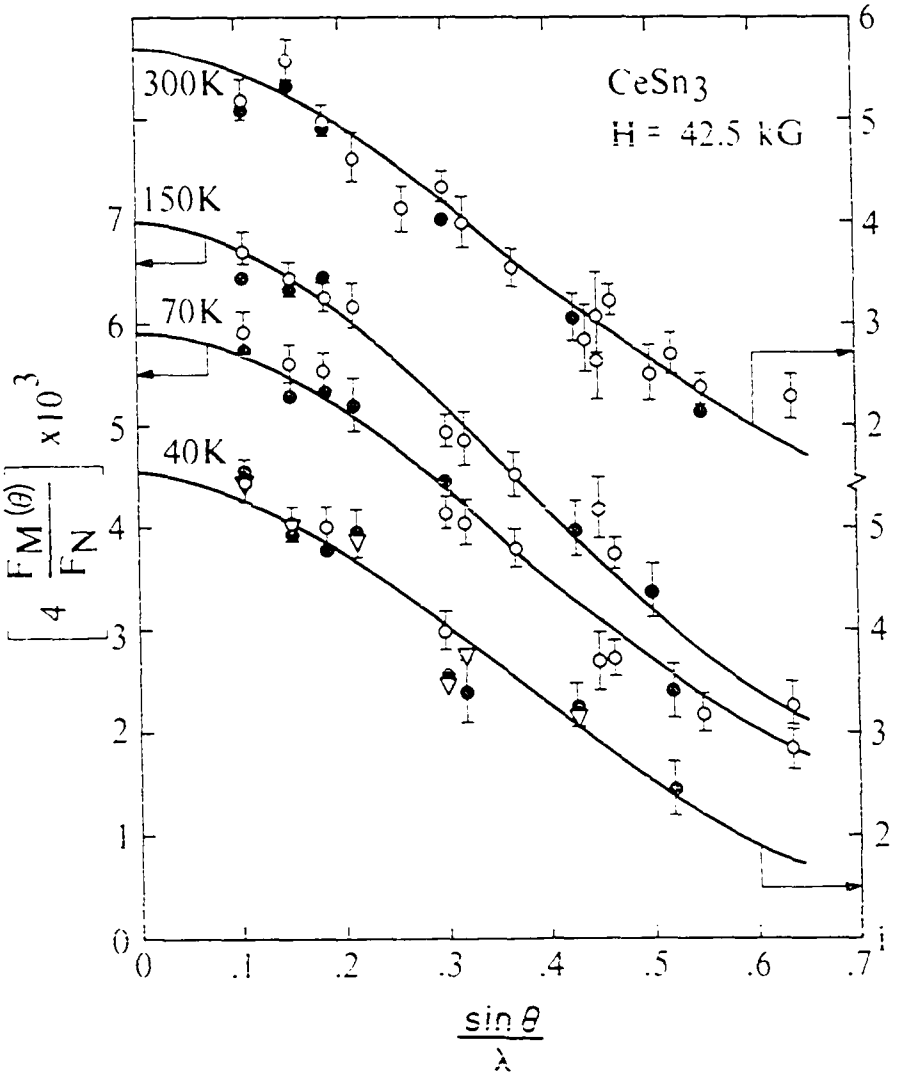

Figure 4.1. Magnetic form factor data obtained with the PN1 (open circles) and PN2 crystal (solid circles) at 300, 70, 40K with the field parallel to the [110] direction. The triangles are data obtained with the 2 mm thick crystal at 40K with the field parallel to the [100] direction. For the sake of clarity we omitted the error bars of some data points

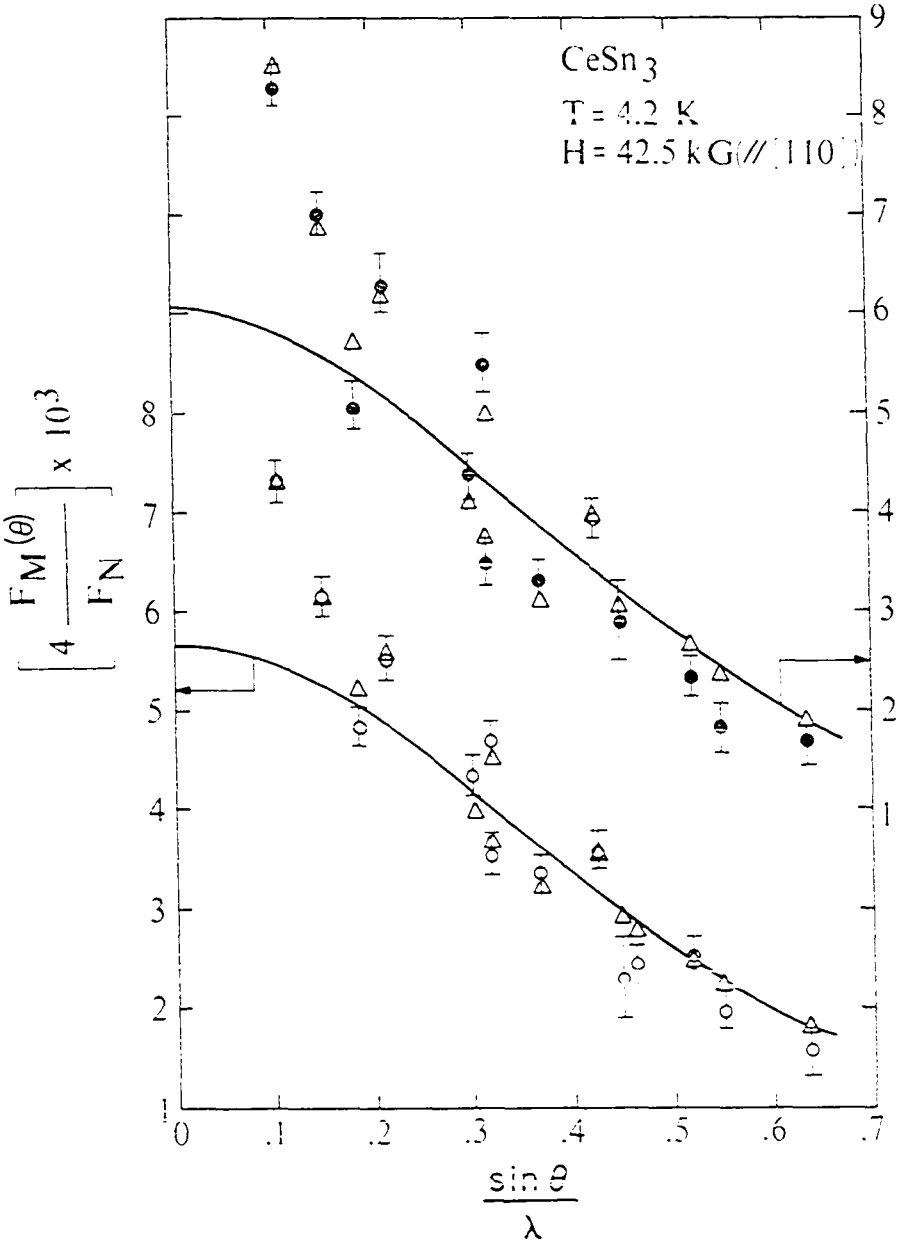

Figure 4.2. Magnetic form factor data obtained with the PN1 (solid circles) and PN2 crystal (open circles) at 4.2K with the field parallel to the [110] direction. The triangles are calculated values assuming that the induced moment consists of a 4f and a Ce 5d component of e_g symmetry (see text). The solid lines represent the 4f contribution

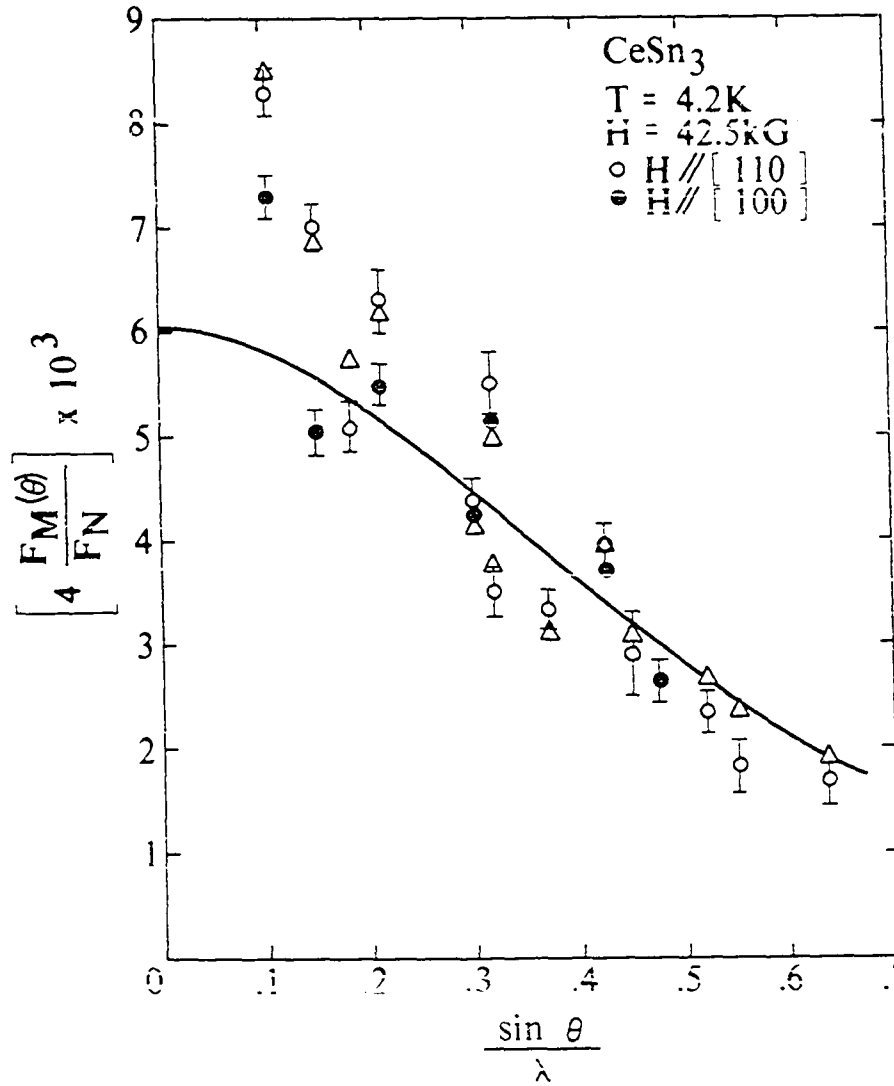

Figure 4.3. Comparison of the magnetic form factors obtained with the PN2 crystal at 4.2K with the field parallel to the [110] (open circles) and with the field parallel to the [100] direction (full circles). Notice the large difference in the values of the (110) reflection (the second inner reflection)

1. Magnetic form factors in the 40-300K temperature range

In general for rare earth ionic compounds it is expected that the chief contribution to the magnetic form factor arises from the 4f electrons of the rare earth ions. In addition, in the 40-300K temperature range the smooth fall-off of the magnetic form factor data with increasing θ indicates spherical moment distributions like those of isolated ions. Therefore, it is suggestive to compare the observed data with the free 4f magnetic form factor of Ce^{3+}. Comparison of experiment with theory consisted of a least squares fitting procedure which minimized the chi-squared (χ^2) function defined as

$$\chi^2 = \sum_i \frac{1}{\sigma_i^2} \left[\left(4 \frac{F_M}{F_N} \right)_i^{obs} - x f_i^{4f} \right]^2 . \qquad (4.4)$$

In the above equation i is an index of the measured reflections, $(4\ F_M/F_N)^{obs}$ is the observed value of $4\ F_M/F_N$ (see Table 4.1) normalized to the fundamental reflections, σ is the associated error, f^{4f} is the theoretical magnetic form factor of the Ce^{3+} free ion, evaluated using relativistic electronic wavefunctions (116), and x is a fitting parameter.

The results of fitting the observed data at 300, 150, 70 and 40K to the free ion 4f magnetic form factor of Ce^{3+} are shown in Fig. 4.1 (for numerical values, see Table 4.1). As can be seen, first, the data obtained with both the PN1 and PN2 crystals in the 300-40K temperature range and the field applied parallel to the [110] direction

are in good agreement; second, data taken with the PN2 crystal at 40K and the field parallel to the [100] direction are in good agreement with those obtained with the field parallel to the [110] direction; third, in this temperature range the experimental data can be fitted quite well with the theoretical magnetic form factor of the Ce^{3+} free ion. This observation implies that in the 300-40K temperature range the induced magnetization has a spatial distribution characteristic of the localized 4f electronic density of the Ce^{3+} free ion.

2. Temperature effects

In this section we shall examine the temperature effects on the magnetic form factor data due to thermal vibrations of the atoms. Thermal displacements of the atomic nuclei and thermal fluctuation of the electronic magnetic moments lead to a modification of the coherent nuclear and magnetic structure factors by inclusion of the appropriate Debye-Waller factor to each atom. If one assumes that only the localized 4f electrons of the Ce ions contribute to the magnetic scattering amplitude, Eqs. (2.6) and (2.7) need to be modified as follows:

$$F_M(\theta) = P_2^{ind}(\theta)\exp\left\{-\frac{B_2}{(4\pi a)^2}(h^2+k^2+\ell^2)\right\}$$

$$\sim f_2^{4f}(\theta)\exp\left\{-\frac{B_2}{(4\pi a)^2}(h^2+k^2+\ell^2)\right\} \qquad (4.5)$$

$$F_N(\theta) = b_2 \exp\left\{-\frac{B_2}{(4\pi a)^2}(h^2 + k^2 + \ell^2)\right\}$$

$$+ b_1 \left\{ \exp[i\pi(k + \ell)] \exp\left\{-\frac{1}{(4\pi a)^2}[B_1^{\perp} h^2 + B_1^{//}(k^2 + \ell^2)]\right\}\right.$$

$$+ \exp[i\pi(h + \ell)] \exp\left\{-\frac{1}{(4\pi a)^2}[B_1^{\perp} k^2 + B_1^{//}(h^2 + \ell^2)]\right\}$$

$$\left. + \exp[i\pi(h + k)] \exp\left\{-\frac{1}{(4\pi a)^2}[B_1 \ell^2 + B_1^{//}(h^2 + k^2)]\right\}\right\} \qquad (4.6)$$

where subscripts 1 and 2 refer to Sn and Ce respectively, hkℓ are the Miller indicies of a reflection, a is the lattice constant and the "B-factors" (125) B_2, $B_1^{\perp}$, $B_1^{//}$, are the independent elements of the so-called mean-square displacement matrices $\underline{B}$ for the Ce and Sn atoms.

In general it requires six independent matrix elements to define the 3 x 3 matrix $\underline{B}$ for each atom in the unit cell; an element B_{ij} represents the time-average value of the atomic displacements along the Cartesian i-axis multiplied by the displacement along the j-axis. However, site symmetry of an atom in the unit cell often reduces the number of independent matrix elements. For $CeSn_3$ the cubic symmetry (O_h) of the Ce atom sites demands an isotropic B-factor (125) (one independent element) whereas the tetragonal symmetry (D_{4h}) of the Sn atom sites requires two independent elements, $B_1^{\perp}$ and $B_1^{//}$, respectively representing the time average of the atomic displacement squared perpendicular the cube face and in the plane of the face. The anisotropic thermal vibrations of the Sn atoms are illustrated schematically in Fig. 4.4.

The B-factors can be determined experimentally by neutron diffraction techniques. Recently neutron Bragg diffraction measurements (126) have been performed on the PN1 crystal of $CeSn_3$ at the CP-5 research reactor of the Argonne National Laboratory. At room temperature the integrated intensities of over 230 hkℓ Bragg reflections (which reduced to 28 independent superlattice reflections and 13 independent fundamental reflections) were measured using a four-circle diffractometer. The experimental results confirmed the ordered Cu_3Au crystal structure of this material. Furthermore, the observed intensities could be explained satisfactorily by the elastic structure factor given in Eq. (4.6) (see Fig. 4.5). From a least-squares analysis the following values of the B-factors were found:

$$\begin{aligned} B_2 &= 1.54 \pm .055 \ \text{Å}^2 && \text{for the Ce atoms;} \\ B_1^{\perp} &= 1.95 \pm .043 \ \text{Å}^2 \ , \quad B_1^{/\!/} = 1.34 \pm .049 \ \text{Å}^2 && \text{for the Sn atoms.} \end{aligned} \tag{4.7}$$

In addition, the B-factors at room temperature obtained from an independent X-ray diffraction experiment (125) using a different single crystal of $CeSn_3$ were found to be in good agreement with the above values.

Taking the temperature effects into consideration, one needs to compare the magnetic form factor data (those are not normalized to the fundamental reflections) with the theoretical values of $4F_M(\theta)/F_N(\theta)$ using the modified structure factors given by Eq. (4.5) and (4.6). From the results of a least-squares fitting (see Fig. 4.6), it was

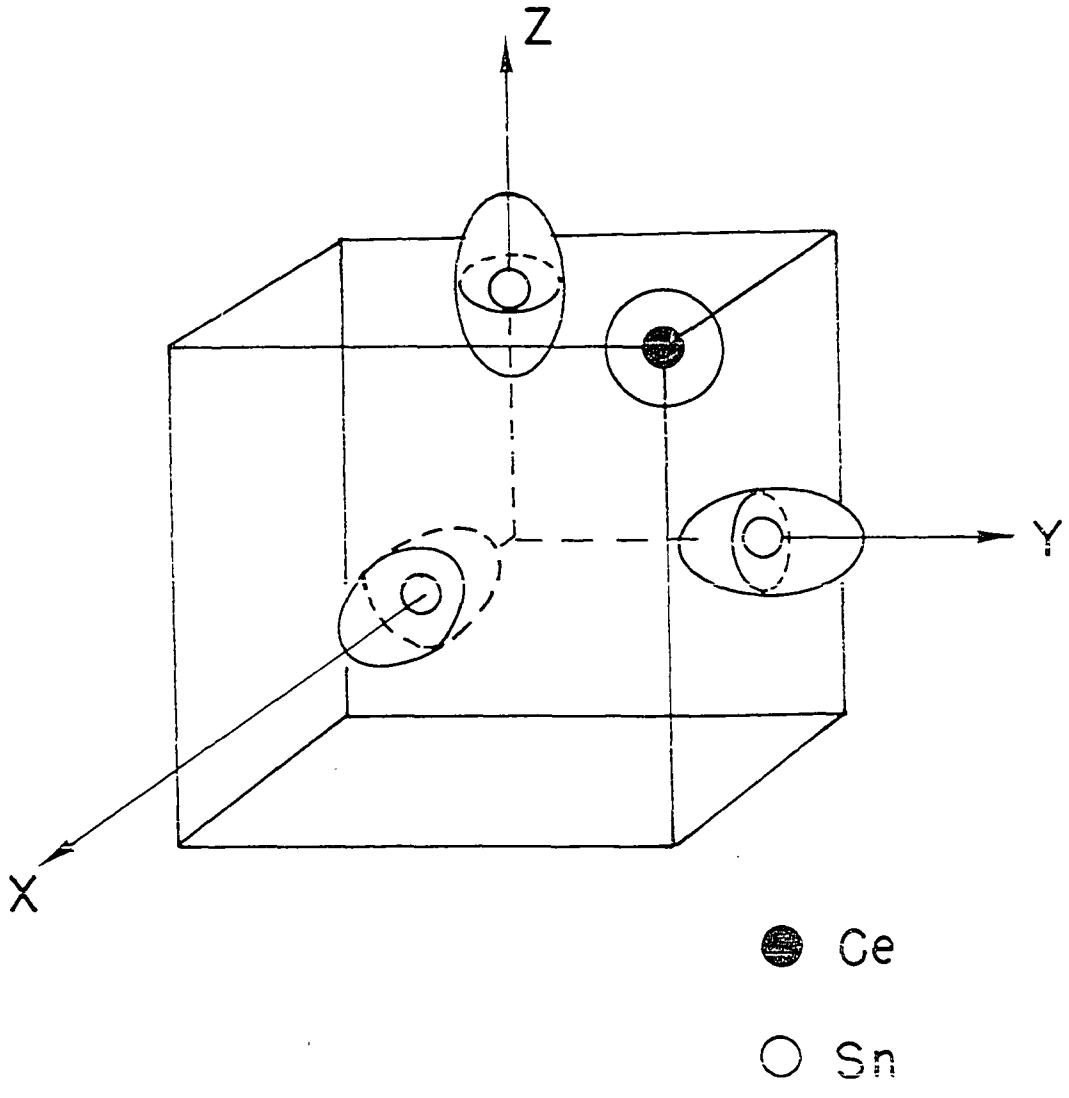

Figure 4.4. Anisotropic thermal vibrations of the Sn atoms in $CeSn_3$ illustrated by the thermal ellipsoids of the Sn atoms. Results of the neutron and x-ray diffraction experiments (126) indicated that the average atomic displacements of the Sn atoms along the directions perpendicular to the cube faces are considerably larger than those in the planes of the faces. Thus, it seems that in this compound, the Sn atoms exhibit a tendency to move towards the empty space in the center of the cube

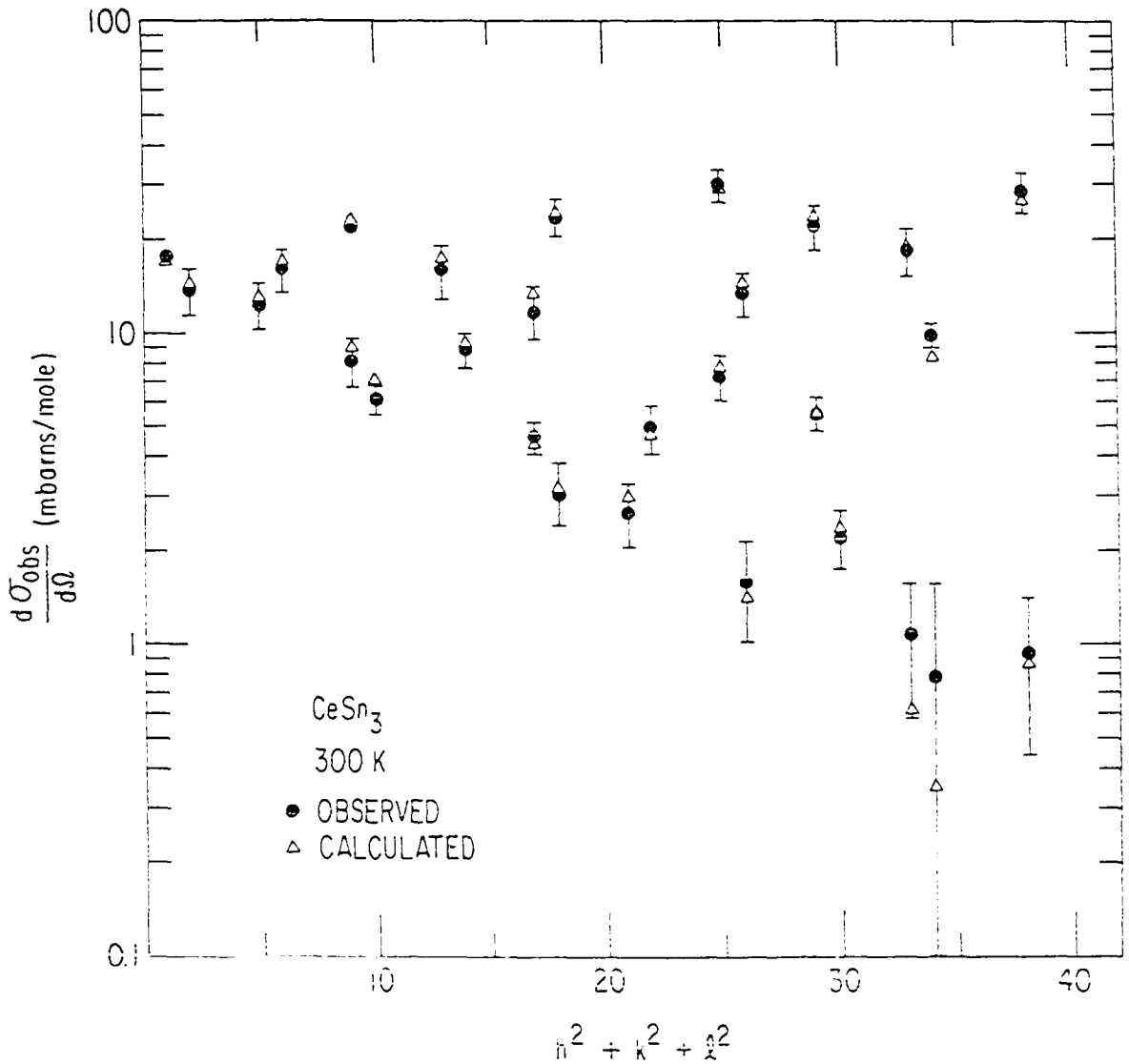

Figure 4.5. The results of the least-squares fitting of the observed integrated intensities of the Bragg reflections to the theoretical nuclear structure factors given by Eqs. (4.5) and (4.6) (126). This satisfactory fit was obtained by assuming that the Sn atomic B-factor perpendicular to the cube faces is about 50% larger than that in the planes of the faces (see text)

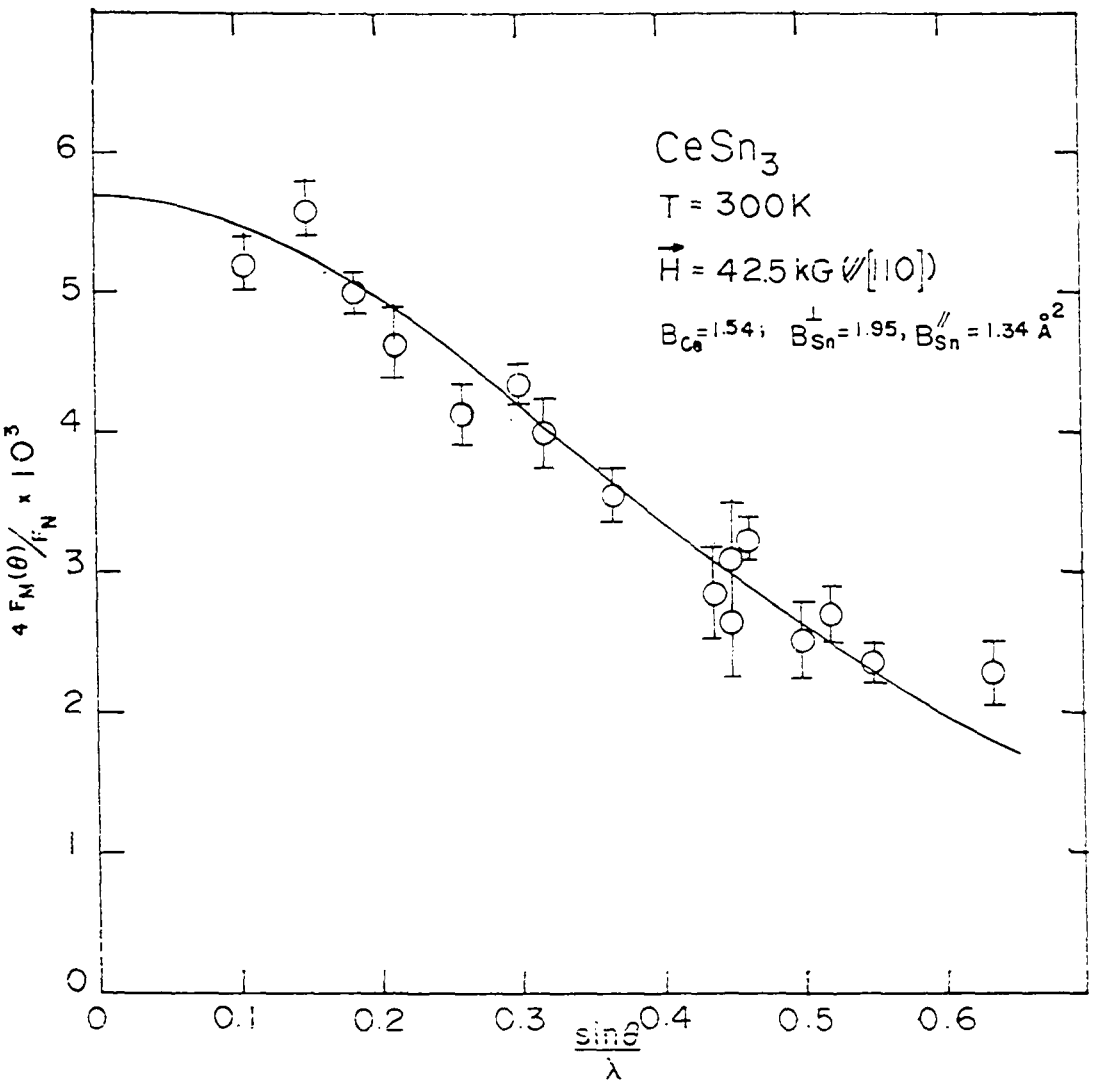

Figure 4.6. Results of fitting the magnetic form factor data obtained at 300K to the 4f magnetic form factor of Ce^{3+} ions taken the temperature effects into consideration

found that the temperature effects on the magnetic form factor data were insignificant (see Table 4.4). Comparing Figs. 4.1 and 4.6 one observes very little difference between the calculated values given by the two fits, one includes temperature effects and the other does not. Therefore, we concluded that thermal vibrations of the atoms do not influence our interpretation of the room temperature data in the previous section. Since the form factor data are similar in the 300-40K temperature range, it is reasonable to assume that effects of thermal vibrations of the atoms do not play an important role in our data analysis in this temperature range. Moreover, we did not observe any remarkable differences in the phonon frequencies of $CeSn_3$ between the room temperature and the low temperature (T below 15K) measurements (see Chapter VII). Therefore we assumed that effects of thermal vibrations on the low temperature magnetic form factor measurements are negligible. With this assumption in mind, we shall proceed to analyze the magnetic form factor data at temperatures below 40K.

3. Magnetic form factors at temperatures below 40K

As shown in Fig. 4.2 and Table 4.2, at temperatures below approximately 40K large deviations from the 4f magnetic form factor were observed. The data do not follow a smooth curve which is indicative of a large anistropy in the spatial distribution of the induced magnetization. This led us to investigate the possibility of additional contribution to the magnetic form factor arising from

Table 4.4. Fitting of the magnetic form factor data at 300K including temperature effects

h k ℓ	$\sin\theta/\lambda$ ($\AA^{-1}$)	$y^{obs.}$	$y^{calc.}$	$y^{obs.}_{norm}$	$y^{calc.}_{norm}$
0 0 0	0.0				5.687
0 0 1	.106	-94.070 ± 3.25	-98.629	5.214	5.466
1 1 0	.150	-101.060 ± 3.25	-95.164	5.590	5.263
1 1 1	.183	5.017 ± .14	5.107	5.017	5.107
0 0 2	.212	4.630 ± .22	4.871	4.630	4.871
1 1 2	.259	-74.544 ± 3.79	-81.495	4.141	4.527
2 2 0	.300	4.344 ± .14	4.203	4.344	4.203
2 2 1	.318	-72.268 ± 4.70	-73.509	3.988	4.056
2 2 2	.367	3.559 ± .18	3.656	3.559	3.656
2 2 3	.437	-51.550 ± 5.60	-55.678	2.870	3.099
3 3 0	.449	-56.012 ± 7.23	-54.834	3.070	3.006
1 1 4	.449	-47.866 ± 6.86	-53.408	2.694	3.006
3 3 1	.462	3.232 ± .15	2.910	3.232	2.910
3 3 2	.497	-45.536 ± 4.88	-48.190	2.507	2.653
2 2 4	.519	2.701 ± .20	2.503	2.701	2.503
3 3 3	.550	2.365 ± .15	2.294	2.365	2.294
4 4 2	.635	2.288 ± .22	1.796	2.288	1.796

a 5d electronic component exhibiting certain cubic symmetry. It is well-known that by combining the five-fold one-electron orbitals of a d-shell one may form the so-called e_g and t_{2g} orbitals each yielding charge density with cubic symmetry.

The e_g and t_{2g} scattering form factors (127) can be written respectively as follows:

$$f_{e_g}(q) = \langle j_o(qr)\rangle + \frac{1}{2} A\langle j_4(qr)\rangle \quad , \tag{4.8}$$

$$f_{t_{2g}}(q) = \langle j_o(qr)\rangle - \frac{1}{3} A\langle j_4(qr)\rangle \quad , \tag{4.9}$$

where

$$A = \frac{3(h^4 + k^4 + \ell^4) - 9(h^2k^2 + h^2\ell^2 + k^2\ell^2)}{(h^2 + k^2 + \ell^2)^2} \quad , \tag{4.10}$$

and

$$\langle j_n(qr)\rangle = \int_o^\infty r^2\rho^2 j_n(qr)\,dr \quad . \tag{4.11}$$

In Eq. (4.11) $j_n(qr)$ is the n-th order spherical Bessel functions and ρ^2 is the radial part of the charge density function. (Other quantities have their conventional meanings).

Using the 5d relativistic Dirac-Slater wavefunctions of a Ce atom ($[Xe]4f^2 5d^1 6s^2$) and the above formulas, we obtained the e_g and t_{2g} form factors for various reflections of $CeSn_3$. (See Fig. 4.7 and Table 4.5 for numerical values). From a least-squares analysis of the experimental data, obtained with the field applied parallel to the

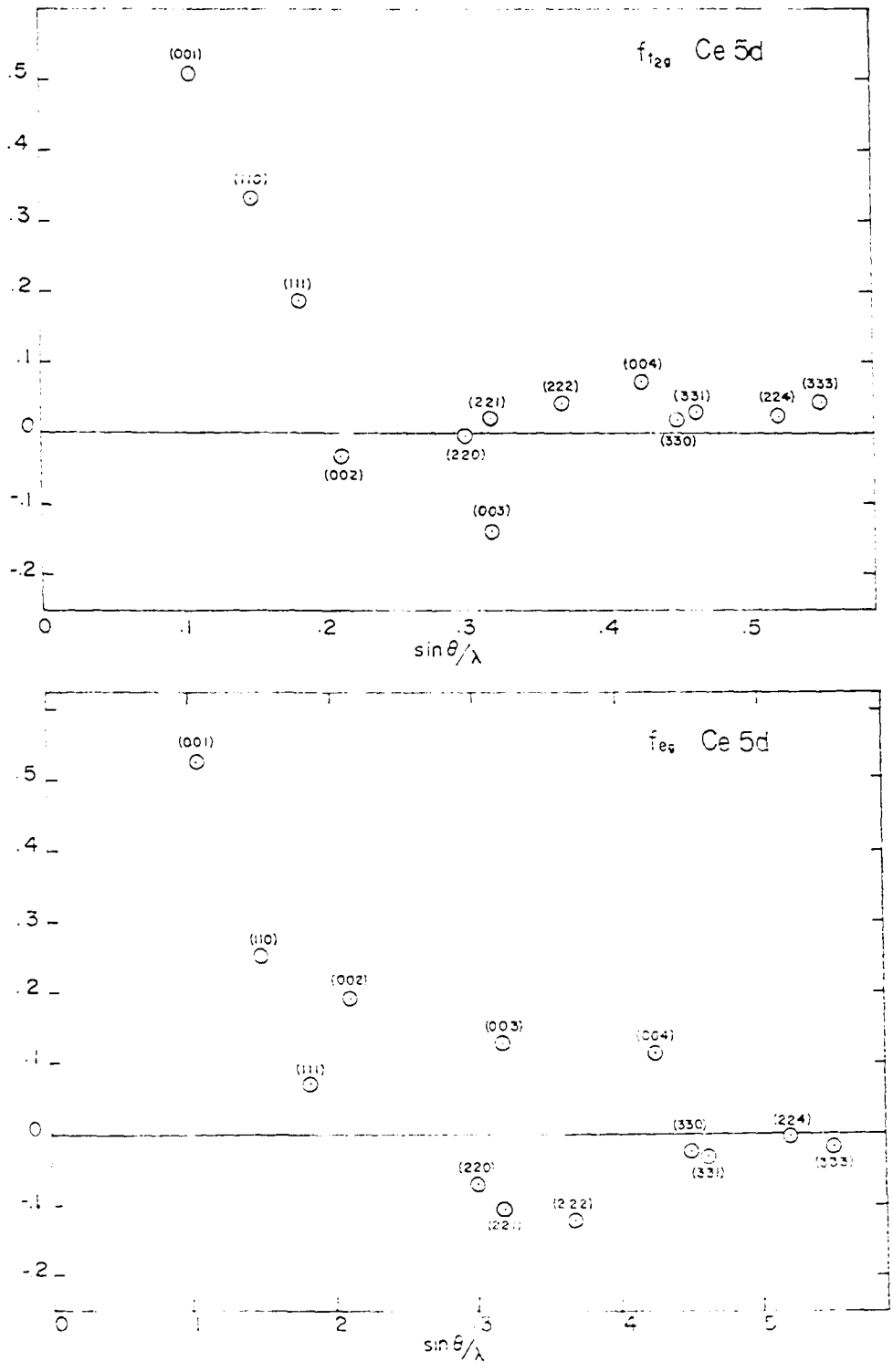

Figure 4.7. The e_g and t_{2g} form factors for Ce 5d electrons

Table 4. Ce 5d e_g and t_{2g} form factors

h k ℓ	sinθ/λ	f_{e_g}	$f_{t_{2g}}$
0 0 0	0.0	1.00	1.00
0 0 1	.106	.525	.507
1 1 0	.150	.252	.335
1 1 1	.183	.069	.187
0 0 2	.212	.191	-.0320
2 2 0	.300	-.0714	-.0033
2 2 1	.318	-.108	.0205
0 0 3	.318	.1295	-.138
2 2 2	.367	-.122	.0410
0 0 4	.424	.112	.0720
3 3 0	.449	-.0255	.0176
3 3 1	.462	-.0332	.0271
2 2 4	.519	-.0041	.0228
3 3 3	.550	-.0186	.0422
4 4 2	.635	.0099	.0301

[110] direction at 4.2K for both the PN1 and PN2 crystals, with the 4f Ce^{3+} and Ce 5d theoretical magnetic form factors, we obtained the following results (see Fig. 4.2 and Table 4.2):

1) A satisfactory fit to the experimental data obtained using the PN1 crystal is achieved by assuming that approximately 38% of the induced magnetization of 4.2K is of Ce5d electronic character of e_g symmetry.
2) An equally satisfactory fit to the experimental data taken with the PN2 crystal was obtained by assuming a 49% 5d contribution of e_g symmetry to the induced magnetization.

Therefore the data obtained with both crystals suggest that below 40K the field induced moment contains a relatively large 5d electronic component of e_g character. It should be noted that the e_g orbitals are doubly degenerate, capable of accomodating two of the five d-electrons of each spin, and their charge density has six lobes pointing along the cube axes of the crystal. Consequently, the above observations suggest that as the temperature decreases below about 40K the energy of the 5d electrons is lowered by redistribute their charge density pointing toward the nearest neighbors of Ce atoms (each Ce atom has six nearest neighboring Ce atoms along the directions of the cube axes separated by the unit cell dimension). This interpretation may explain the results of the Mössbauer experiments performed by Shenoy *et al.* (66) since they observed that in the 293 - 1.6K temperature range the ^{119}Sn isomer shift in $CeSn_3$ was approximately the same as in $PrSn_3$ and $NdSn_3$, implying a stable electronic distribution around the

Sn nucleus at low temperatures. In fact since the lobes of a magnetization distribution of e_g character are along the cube axes of the crystal one does not expect the ^{119}Sn isomer shift to be very sensitive to this component of the magnetization density.

4. Comparison between localized susceptibility and bulk susceptibility

We have seen that the magnetic form factor data, obtained using both the PN1 and PN2 crystals with H//[110] at T = 4.2K, can be fitted equally well by assuming certain amounts of 5d contributions of e_g symmetry to the induced magnetization. However, a closer look at the experimental results reveals that the PN1 data differ from those of PN2 in absolute values by about 10%; consequently, the amounts of 5d components resulting from the fits are different. We attribute the difference between these results to a difference in the bulk susceptibility of the two samples at low temperatures. Although these two samples were originally separated from the same single crystal, it is not inconceivable that their low temperature susceptibilities differ from each other due to differences in impurity content and/or their state of oxidation. As a matter of fact, all of the bulk susceptibilities of $CeSn_3$ reported by various authors (55-59) (see Fig. 1.12) exhibited the sharp rising features at low temperatures but differed in absolute values.

Conduction electrons spread out farther away from the nuclei in real space which corresponds to very small values of q in the reciprocal lattice space. The neutron measurements are performed at non-zero values of the scattering vector and therefore they sense only the relatively localized part of the induced magnetization. The corresponding localized static susceptibility can be calculated by Eq. (2.3) using the value of the measured magnetic form factor exterapolated to the forward direction, i.e.,

$$\chi_M^{loc.} = 2.066 \times 10^{16} \frac{F_{M(0)}}{H} \qquad (4.12)$$

with F_M in cm and H is Oersteds. Of course the values obtained from Eq. (4.12) depend on the form of the theoretical form factor used to fit the experimental data.

The comparison of the localized static susceptibility obtained from the neutron experiments with the bulk susceptibility measurements is shown in Fig. 4.8. Although a detailed comparison is complicated by the sample dependence of the latter measurements at low temperatures, it can be seen that the 5d component of the magnetization can account at least partly for the increase in the bulk susceptibility below approximately 40K. It can also be seen that the values of the localized susceptibility as determined in the present experiment are in general lower than those of the bulk susceptibility measurements, indicating an additional contribution to the static susceptibility presumably of p and or s electronic character which is not sensed in the neutron measurements.

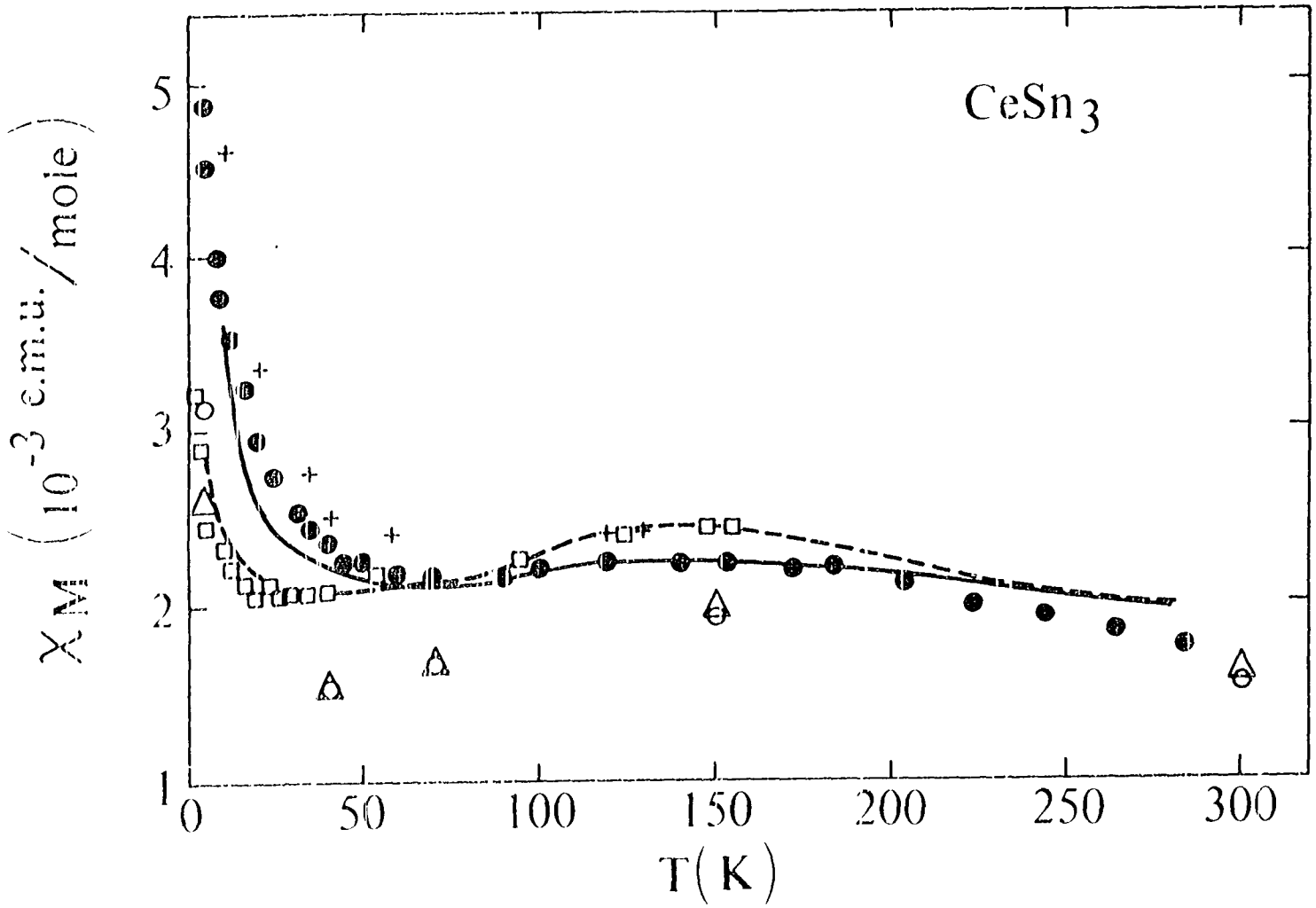

Figure 4.8. Comparison of the localized susceptibility obtained in the neutron measurements (triangles and open circles for the PN1 and PN2 crystals respectively) with susceptibility measurements by various workers (+, □ Ref. 59; full circles Ref. 56; solid line Ref. 55; dashed line Ref. 57)

The magnetic susceptibility of mixed valence systems has been studied by several workers (128-131) in a model which assumes that the 4f level is very close to the Fermi level and its position is fixed relative to the conduction band. Consider a collection of non-interacting localized 4f orbitals, one orbital per Ce site. If the average number of occupation of each orbital is $\langle n_f \rangle$, one would expect that such a system exhibits a Curie susceptibility given by

$$\chi \sim \langle n_f \rangle / T \tag{4.13}$$

where T is the temperature. To account for the almost constant susceptibility of $CeSn_3$ in the 40-300K temperature range, Liu et al. (123,132) have proposed that the 4f level shifted down by following rigidly the Fermi level. This assumption gives rise to an increase of the 4f population by 0.2 electron per Ce atom in a roughly linear fashion as the temperature is raised from 40 to 300K, as shown in Fig. 4.9 . Consequently, the T^{-1} factor in the Curie susceptibility of Eq. (4.14) is compensated by the increase of $\langle n_f \rangle$ with temperature; hence a roughly temperature independent susceptibility is obtained.

Without any quantitative handle on the amount of the 4f-level shift, Liu et al. (123,132) resorted to an oversimplified model in which the shift of the 4f level with population is the same as that of the Fermi level due to conduction electron depletion. This amounts to assuming a constant separation of the 4f-level from the Fermi level. Based on this simple assumption the magnetic susceptibility was calculated following the treatment of Varma and Yaffet (128). These calculations

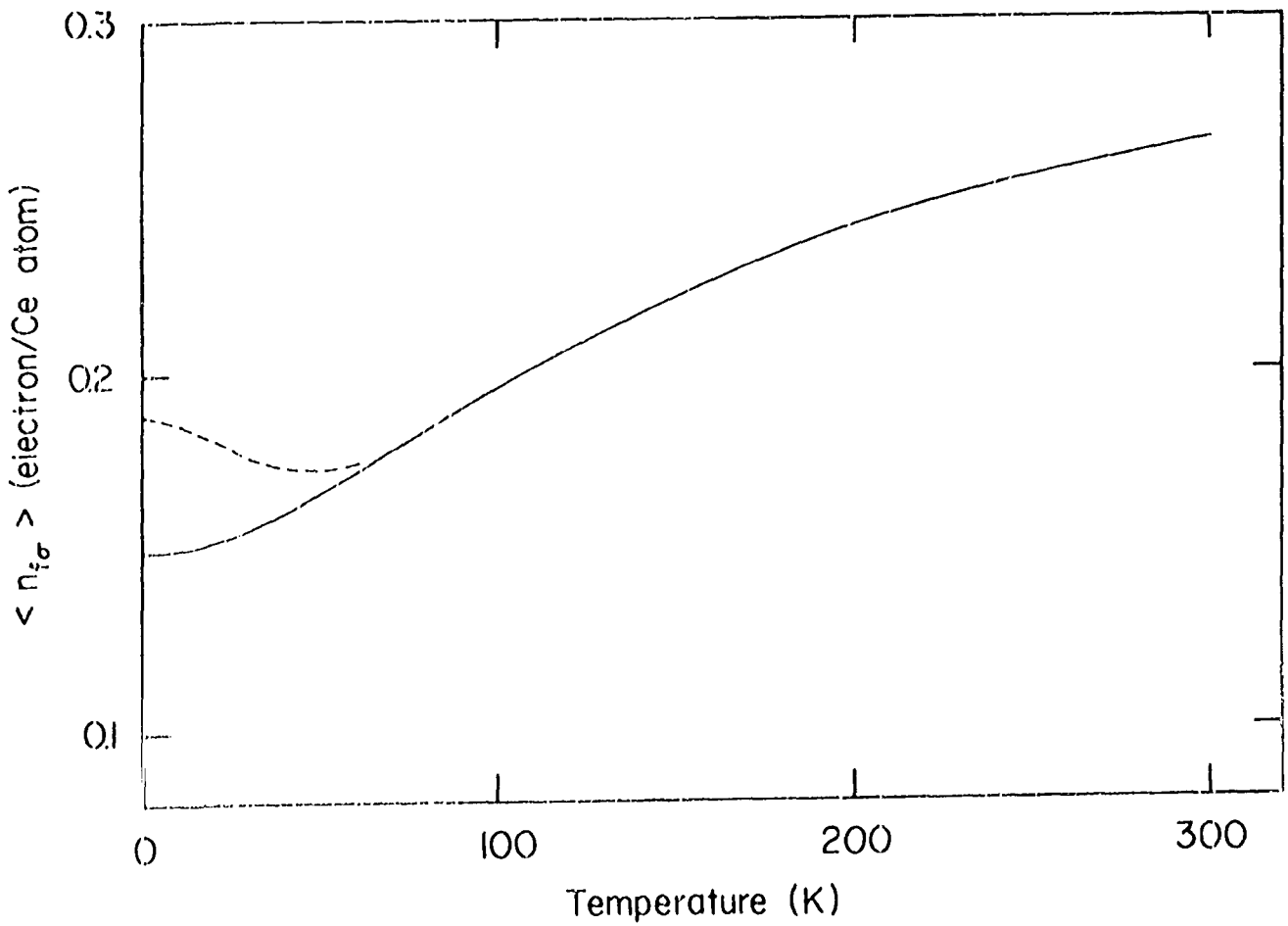

Figure 4.9. The predicted occupation of the Ce 4f level in $CeSn_3$, plotted as a function of the temperature. The dotted curve represents effect of Ce-Ce correlation (after Ref. 119)

were performed assuming strong spin-orbit coupling and ignoring the crystal field splitting. The magnetic susceptibility, obtained by assuming that the 4f electrons on the Ce sites are uncorrelated and by positioning the 4f level (of width P of 150K) at 200K above the Fermi energy, is plotted in Fig. 4.10. It can be seen that the calculated curve (solid line) exhibits roughly the main characteristics of the measured susceptibility. As we have already discussed, a more detailed comparison at low temperature is not possible because of the sample dependence of the bulk susceptibility at low temperature.

In calculating the bulk susceptibility represented by the solid line in Fig. 4.10 the 4f electrons on the Ce sites were assumed to be uncorrelated. However the hybridization with the band electrons provides a coupling of the neighboring Ce sites so that at low temperatures, $T<<\Gamma$, the 4f electrons form a narrow hybridized coherent band. This is reflected in the drastic change in the magnetic form factor below 40K. In fact using the mean-field theory of Ref. 128 it was found that in the coherent state there is a nearly equal mixture of the 4f and conduction band-wavefunctions at the Fermi level in quite good agreement with the neutron experiments. The calculated values for the magnetic susceptibility using mean field theory are only slightly higher than those obtained in the single site calculation.

At low temperatures the Varma-Yaffet theory was generalized to include in a self-consistent manner the thermally induced breakdown in nearest neighbor correlations. The calculated magnetic susceptibility

follows at high temperature the one site calculation and below approximately 100K follows the dotted curve shown in Fig. 4.10. In conclusion we have shown that the neutron magnetic form factor and the main features of the magnetic susceptibility of $CeSn_3$ can be understood on the basis of existing theories of mixed valence systems.

5. Field-direction dependence of the magnetic form factors at low temperatures

The rather unusual features of the magnetic form factor of $CeSn_3$ at low temperatures led us to perform measurements on the PN2 thick crystal at 40 and 4.2K with the magnetic field applied parallel to the [100] direction. The data obtained at 40K were found (see Fig. 4.2) to be in good agreement with those taken with the magnetic field applied parallel to the [110] direction. On the other hand the data at 4.2K exhibit differences outside experimental errors from those obtained with the magnetic field applied parallel to the [110] direction (see Fig. 4.3). As can be seen in Fig. 4.3 or Table 4.2 this dependence on the magnetic field direction is particularly pronounced for the (110) reflection.

It follows from Eq. (2.2) that for paramagnetic crystals of rare earth metals or compounds the spin part of the induced magnetization as a function of the scattering vector does not depend on the direction of the applied magnetic field. Therefore, the aforementioned field-direction dependence must arise from the orbital part of the induced magnetization and may be attributed to the conduction electron

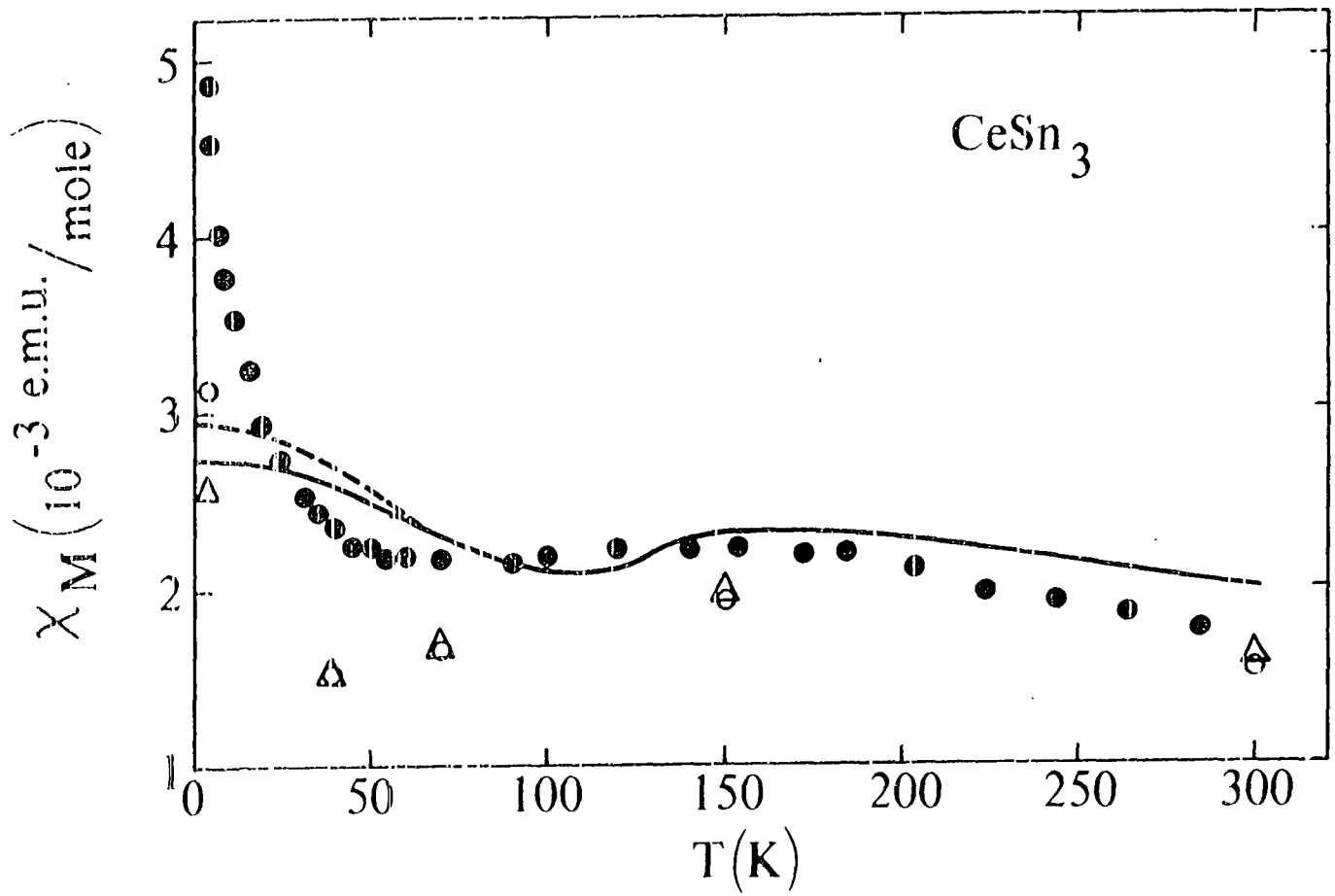

Figure 4.10. Comparison of bulk susceptibility (Ref. 55) and localized susceptibility obtained in the neutron measurements with model calculations of the bulk susceptibility of $CeSn_3$. The solid line was obtained by assuming uncorrelated 4f electrons on the Ce sites. The dotted line represents the effect of correlations on the magnetic susceptibility (see text)

spin-orbit interaction and/or crystal field effects on the 4f electrons of the Ce ion.

Given the preceding rationales and the experiental evidence of the presence of a large 5d electronic component of e_g character in the induced magnetization, we calculated the coherent magnetic scattering amplitudes of the e_g orbitals for a Ce 5d electron subjected to perturbations due to the spin-orbit interaction and an applied magnetic field ($\vec{H}$//[110] or $\vec{H}$//[001]) at 4.2K. A theoretical magnetic form factor is formed by combining this calculated e_g magnetic scattering amplitude with the 4f magnetic form factor of a Ce^{3+} ion. This approach to the problem is obviously an oversimplification of reality, nevertheless we hoped that the results of this calculation could provide some physical insight into the characters of the ground state electronic wavefunctions of the system. A nonlinear least-squares fitting procedure was used in the comparison between the theoretical magnetic form factor with the data obtained using the PN2 crystal with the fields parallel to the [110] and the [100] directions at 4.2K. In the nonlinear least-squares analysis a modified Levenberg-Marquardt algorithm (133) was used to find the minimum of the χ^2 function defined as

$$\chi^2 = \sum_i \frac{1}{\sigma 2_i} [y_i - x f_i^{e_g}(\varepsilon) - y f_i^{4f}]^2 \qquad (4.13)$$

It should be noted that the e_g magnetic form factor $f_i^{e_g}(\varepsilon)$ depends on ε, the ratio of the spin-orbit coupling coefficient and the crystal field splitting. f^{4f} is the 4f magnetic form factor of a Ce^{3+} ion and

x,y,ε are fitting parameters. As can be seen in Fig. 4.11 the best fit was achieved by assuming a 43% of 5d electronic component of e_g character and a value of ε = -0.143 (see Table 4.6 for numerical values). The field-direction dependence of the magnetic form factor is solely arised from the 5d electronic component; however, the difference between the calculated magnetic form factors in the two field directions is is not large enough, especially for the (110) reflections, to reproduce the observed difference of the magnetic form factors.

6. Band theoretical calculations

To obtain a more realistic understanding of the electronic structure of $CeSn_3$ and in particular the nature of the electronic wavefunctions in the vicinity of the Fermi level, Harmon and Symeondies in Ref. 132 have performed two non-self-consistent band theoretical calculations of $CeSn_3$ using the linearized APW method (with the Slater approximation (α = 1) for the exchange-correlation potential). In the first (see Fig. 4.12a) the 4f band, which cannot be reliably positioned in a non-self-consistent calculation, were simply ignored. A second calculation (see Fig. 4.12b) with the 4f resonance positioned just above the Fermi level was performed to determine the effect of hybridization between the 4f and conduction electrons. In both calculations it was found that the electronic wavefunctions at the Fermi level exhibit in addition to Ce-d a substantial amount of Sn-p character. Furthermore the calculated Ce-d charge density near the Fermi level was found to be almost isotropic. As a result the band

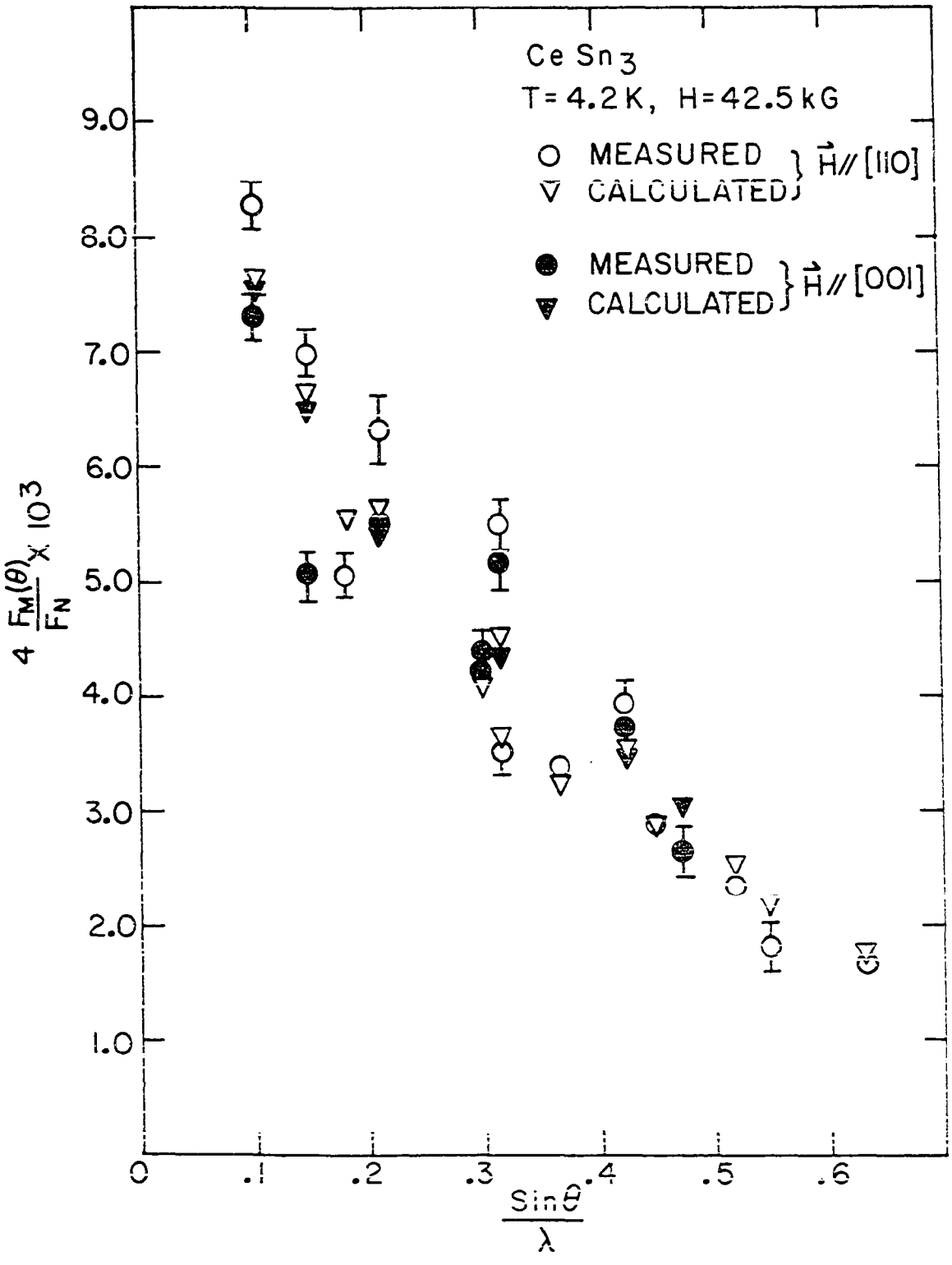

Figure 4.11. The results of fitting the magnetic form factor data obtained with the PN2 crystal with the field in both directions to the theoretical form factor described in Section 5

Table 4.6. Results of fitting the magnetic form factor data by assuming the 5d electronic component subjected to perturbations due to the spin orbit interaction and an applied magnetic field

	h k ℓ	$\sin\theta/\lambda$ ($\mathring{A}^{-1}$)	$y^{obs.}$ [a]	$y^{calc.}$ [a]
H//[110]	0 0 1	.106	8.288 ± .20	7.654
	1 $\bar{1}$ 0	.150	6.983 ± .20	6.636
	1 $\bar{1}$ 1	.183	5.055 ± .18	5.586
	0 0 2	.212	6.310 ± .30	5.657
	2 $\bar{2}$ 0	.300	4.369 ± .18	4.099
	2 $\bar{2}$ 1	.318	3.498 ± .18	3.645
	0 0 3	.318	5.501 ± .22	4.539
	2 $\bar{2}$ 2	.367	3.337 ± .18	3.223
	0 0 4	.424	3.925 ± .20	3.573
	3 $\bar{3}$ 0	.449	2.884 ± .39	2.854
	2 $\bar{2}$ 4	.519	2.339 ± .18	2.511
	3 $\bar{3}$ 3	.550	1.818 ± .20	2.165
	4 $\bar{4}$ 2	.635	1.694 ± .23	1.751
H//[100]	1 0 0	.106	7.308 ± .20	7.550
	1 1 0	.150	5.034 ± .19	6.478
	2 0 0	.212	5.500 ± .19	5.425
	2 2 0	.300	4.248 ± .23	4.490
	3 0 0	.318	5.165 ± .22	4.329
	4 0 0	.424	3.714 ± .20	3.442
	4 2 0	.474	2.649 ± .20	3.042

[a] $y = 4\ \bar{F}_M/\bar{F}_N \times 10^3$.

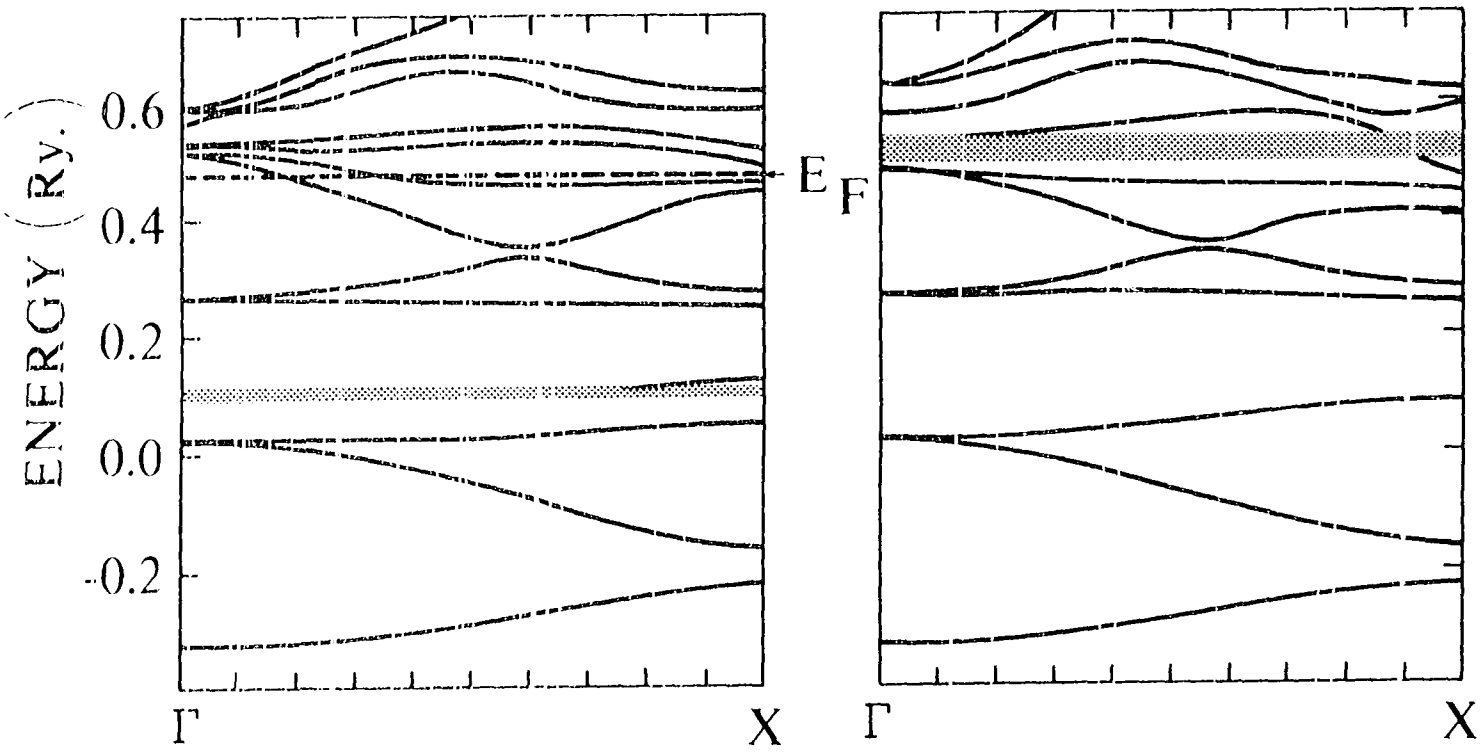

Figure 4.12. Non-self-consistent energy bands for $CeSn_3$. On the left the 4f bands are left out of the calculation. (They are found below the Fermi level, in the shaded region.) On the right the 4f level is put near the Fermi level. The width of the shaded region represents the amount of hybridization between 4f and band electrons (123, 132)

theoretical induced spin form factors cannot account for the neutron scattering observations at low temperatures. It is believed that by performing a self-consistent calculation or by including spin-orbit effects would not be affected by the present results significantly.

C. Concluding Remarks

In this chapter we have presented the analysis and discussion of the results in the study of the spatial distribution and temperature dependence of the field-induced magnetization of $CeSn_3$ using polarized neutron scattering techniques. In the 40-300K temperature range, the measured magnetic form factor is in good agreement with the 4f magnetic form factor of Ce^{3+}. Below 40K, on the other hand, the magnetic form factor measurements suggests that the induced magnetization contains a large component of 5d electronic character of e_g symmetry, which can account, at least partly, for the increase in the magnetic susceptibility of $CeSn_3$ at low temperatures. Thus, polarized neutron experiment provided direct evidence for the mixed valent character of this compound.

It is generally believed (5) that the rather spectacular properties of the mixed valence systems are dictated by the coexistence at the Fermi level of ionic-like localized 4f levels and a wide 5d conduction band. The low temperature results of the present experiment provided evidence for this viewpoint. Actually the results can be explained at least qualitatively by recent phenomenological models (128-131) of the mixed valence systems in which the highly correlated 4f bands are in

close proximity to the Fermi level and it hybridized with the conduction band. However, conventional band calculation results are not easily reconciled with the experimental data and there appears to be no satisfactory explanation of the observed field-direction dependence of the magnetic form factor at 4.2K. These difficulties suggest the need for a more detailed understanding of the ground state of the system. New techniques in band calculation providing proper treatment of the 4f electrons in rare earth metallic systems will be useful. Experimental studies of the Fermi surface, such as de Haas-van Alphen measurements, may be helpful in understanding the nature of the electronic wave-functions of the system in the vicinity of the Fermi level.

V. LATTICE DYNAMICS - THEORIES AND APPLICATIONS

The measured phonon dispersion curves contain significant information about the electronic and thermophysical properties of a solid. For instance, it is well-known that anomalies observed in the phonon spectra are related to the electron-phonon interaction and/or structural transformations. A complete microscopic understanding of the phonon dispersion curves is however a formidable task except in a few simple cases. This is due to the computational difficulties involved in the implementation of the microscopic theory (134) of lattice dynamics. Fortunately however, in most cases simplified models can provide insight and qualitative physical understanding of the origin of the phonon anomalies.

The problem of obtaining from the measured dispersion curves the lattice contribution to the thermophysical properties of a solid is a much easier task. The experimentally measured dispersion curves are fitted to a Born-von Kármán force constant model (135). Once the force constants of the model have been determined by fitting to the experimental measurements, the model can be used to obtain the phonon density of states on other more general average properties determined by the phonon spectrum of the solid. In this fashion the thermal factors and the lattice contribution to the specific heat of the solid can be determined.

In this chapter we will present first a brief outline of the Born-von Kármán formalism and then we shall proceed to explain the

force-constant models which have been constructed for the analysis of the dispersion curves of $CdSn_3$. Only a rudimentary introduction to the Born-von Kármán theory is presented here since this formalism has been the subject of many excellent monographs (136,137).

A. Born-von Kármán Formalism

1. Adiabatic approximation

Let us consider a crystal as a collection of nuclei and electrons whose position are described, respectively, by the collective symbols $\vec{R} = \{\vec{R}_1, \vec{R}_2, \ldots\}$ and $\vec{r} = \{\vec{r}_1, \vec{r}_2, \ldots\}$. The Hamiltonian for this system can be written in the form

$$\mathcal{H} = T^N(\vec{R}) + V^N(\vec{R}) + T^e(\vec{r}) + V^e(\vec{r}) + U(\vec{r},\vec{R}) \qquad (5.1)$$

where T is the kinetic energy, V is the potential energy, the superscript N refers to the nuclei (the nuclear system) and e to the electrons (the electronic systems), and $U(\vec{r},\vec{R})$ is the interaction between electrons and nuclei. Since $T^N(\vec{R})$ is small, as compared to the other terms in Eq. (5.1), owing to the large masses of the nuclei, it can be treated as a perturbation on the rest of the Hamiltonian. As a result, it can be shown that the Schrödinger equation for the nuclear system reduces to

$$[T^N(\vec{R}) + \phi_n(\vec{R})]\phi_{n\lambda}(\vec{R}) = E_{n\lambda}\phi_{n\lambda}(\vec{R}) \qquad (5.2)$$

where

$$\phi_n(\vec{R}) = E_n^e(\vec{R}) + V^N(\vec{R}) \qquad (B.3)$$

is an effective potential for the motion of the nuclei provided that the electronic system is in its n-th state. It should be noted that $\phi_n(\vec{R})$ depends only on the instantaneous nuclear coordinates. $E_n^e(\vec{R})$ in Eq. (5.3) satisfies the Schrödinger equation for the electronic system:

$$[T^e(\vec{r}) + V^e(\vec{r}) + U(\vec{r},\vec{R})]\psi_n^e(\vec{r},\vec{R}) = E_n(\vec{R})\psi_n^e(\vec{r},\vec{R}) \quad . \qquad (5.4)$$

The wavefunction of the overall system is approximated by

$$\Psi_{n\lambda}(\vec{r},\vec{R}) \simeq \phi_{n\lambda}(\vec{R})\psi_n^e(\vec{r},\vec{R}) \qquad (5.5)$$

This approximation, called the adiabatic approximation, was first introduced by Born and Oppenheimer (138) in the context of molecular vibrations and its extension to lattice dynamics has been studied by other authors (139-142). In this approximation it is assumed that during the nuclear motion the electronic system continually readjust itself so as to remain in the same configuration. This is justified by the fact that the electrons, due to their lighter masses, move much more rapidly than the nuclei. The validity of this approximation is obvious in the case of insulators or semiconductors, where owing to the energy gap between the occupied and unoccupied electronic states, the electronic (transition) frequencies are high. On the other hand, the adiabatic approximation would appear to breakdown in the case of metals since the energy separating neighboring states can be regarded as arbitrarily small. However, it has been shown (143,144) that the

adiabatic approximation can also be applied to metals because actually only a few electrons near the Fermi level can undergo transitions.

In the following sections, the effective potential will be constructed using a phenomenological approach to the theory of lattice dynamics. The electronic system is assumed to be at the ground state, hence the subscript n in Eq. (5.3) is omitted for simplicity.

2. Harmonic approximation

Given the adiabatic assumption and the existence of the crystal potential function Φ, we shall proceed to outline the Born-von Kármán formalism for the analysis of small amplitude motions of atoms in a crystal. We assume that the crystal is perfect and infinite; the atoms retain the rotational and translational symmetries governed by the crystal structure. Furthermore, in the equilibrium configuration, there is no net force acting on any atom and the crystal is free from stresses; at the absolute zero of temperature, the root mean square (rms) displacements due to zero-point motion are small compared to interatomic distances, hence their effects can be ignored. Based on the above assumptions, the Taylor series expansion of $\Phi(\vec{R})$ in the displacement components begins with the second-order term. If the amplitude of the atomic oscillations is small, Φ can be approximated by the second-order term alone. This approximation is known as the harmonic approximation since it leads to harmonic oscillations of the atoms in the crystal. The high-order (anharmonic) terms, presumably small, can then be studied by many-body perturbation theory.

Let us denote the instantaneous position of the k-th atom in the ℓ-th unit cell as

$$\vec{R}(\ell k) = \vec{x}(\ell k) + \vec{u}(\ell k) \tag{5.6}$$

where

$$\vec{x}(\ell k) = \vec{x}(\ell) + \vec{x}(k) \tag{5.7}$$

$$\vec{x}(\ell) = \ell_1\vec{a}_1 + \ell_2\vec{a}_2 + \ell_3\vec{a}_3 \quad . \tag{5.8}$$

In the above equations, $\vec{u}(\ell k)$ is the displacement from the equilibrium position $\vec{x}(\ell k)$; $\vec{x}(\ell)$ is the position of the ℓ-th cell, $\vec{x}(k)$ is the position k-th atom in the cell; $\vec{a}_1$, $\vec{a}_2$, $\vec{a}_3$ are the primitive translation vectors and ℓ_1, ℓ_2, ℓ_3 are integers. The crystal potential function in the harmonic approximation becomes

$$\Phi \cong \frac{1}{2} \sum_{\substack{\ell k \alpha \\ \ell' k' \beta}} \phi_{\alpha\beta}(\ell k, \ell' k') u_\alpha(\ell k) u_\beta(\ell' k') \tag{5.9}$$

where

$$\phi_{\alpha\beta}(\ell k, \ell' k') = \left. \frac{\partial^2 \Phi}{\partial u_\alpha(\ell k) \partial u_\beta(\ell' k')} \right|_0 \quad . \tag{5.10}$$

In the summation of Eq. (5.9) $\ell(\ell')$ runs over all the primitive cells, $k(k')$ runs over all the atoms in a unit cell; α, β are the Cartesian component indices. The subscript 0 in Eq. (5.10) denotes the evaluation of the derivatives with all the atoms in the equilibrium configuration.

Following standard techniques of classical mechanics, one obtains the equation of motion in the following form:

$$-m_k \frac{\partial^2 u_\alpha(\ell k)}{\partial t^2} = \sum_{\ell' k' \beta} \phi_{\alpha\beta}(\ell k, \ell' k') u_\beta(\ell' k') \quad ,$$

for $\alpha = x, y, z$;

$k = 1, 2, \ldots, n$ = number of atom per unit cell;

ℓ over the entire crystal. (5.11)

In the above equation, m_k denotes the mass of the k-th atoms in a unit cell. It follows that $\phi_{\alpha\beta}(\ell k, \ell' k')$ can be interpreted as the negative of the force exerted on atom (ℓk) in the α direction due to unit displacement of the atom $(\ell' k')$ in the β direction. Consequently, it is called the interatomic force constant. In the phenomenological approach to the theory of lattice dynamics, the interatomic force constants are regarded as parameters of the theory, whose values are to be determined from a comparison of the predictions of a phenomenological model with experimental data. This comparison is simplified greatly if one takes into account of the constraints imposed on the interatomic force constants under two types of general invariance conditions. The first type follow from the invariance and transformation properties of the crystal potential function, and of its derivatives with respect to atomic displacements, when the crystal is subjected to infinitesimal translation and rotation. The consideration of this type of conditions of this type of conditions and their resulting constraints and sum rules for the interatomic force constants have been discussed in detail in the literature (136,137). Thus we shall not discuss them here. The second type of restrictions on the interatomic force constants

follow from the symmetry properties of a particular crystal structure. We shall consider this type of conditions for Cu_3Au crystal structure materials in Section B of this chapter.

3. Solution of equation of motion - dynamical matrix

We choose a wave-like solution to the equation of motion (5.11) of the form

$$u_\alpha(\ell k,t) = \frac{1}{\sqrt{m_k}} U_\alpha(k|\vec{q})\exp\{i[\vec{q}\cdot\vec{x}(\ell) - \omega(\vec{q})t]\} \qquad (5.12)$$

where $\vec{q}$ is the wavevector and $\omega(\vec{q})$ is the angular frequency associated with the wave. It should be noted that the appearance of $\vec{x}(\ell)$, rather than $\vec{x}(\ell k) = \vec{x}(\ell) + \vec{x}(k)$, in the exponential factor of Eq. (5.12) implies the inclusion of a phase factor $\exp[i\vec{q}\cdot\vec{x}(k)]$ in the quantity $\vec{U}(k|\vec{q})$. In addition, the displacement of the atoms obtained from a linear combination of the independent solutions of this type must be real. Substituting $u_\alpha(\ell k,t)$ in Eq. (5.12) into Eq. (5.11), one obtains the following 3n simultaneous equations in the wave amplitudes $\{U_\alpha(k|\vec{q})\}$:

$$\omega^2(\vec{q})U_\alpha(k|\vec{q}) = \sum_{k'\beta} D_{\alpha\beta}(\vec{q}|kk')U_\beta(k'|\vec{q}) \quad , \quad \alpha = x,y,z;\ k = 1,\ldots,n \quad , \qquad (5.13)$$

where $D_{\alpha\beta}(\vec{q}|kk')$ is called the mass-adjusted dynamical matrix given by

$$D_{\alpha\beta}(\vec{q}|kk') = \frac{1}{\sqrt{m_k m_{k'}}} \sum_{\ell'} \phi_{\alpha\beta}(\ell k,\ell' k')\exp\{i\vec{q}\cdot[\vec{x}(\ell') - \vec{x}(\ell)]\}$$

$$= \frac{1}{\sqrt{m_k m_{k'}}} \sum_{\bar{\ell}=(\ell'-\ell)} \phi_{\alpha\beta}\begin{pmatrix} 0 & \bar{\ell} \\ k & k' \end{pmatrix}\exp[i\vec{q}\cdot\vec{x}(\bar{\ell})] \quad . \qquad (5.14)$$

The second part of Eq. (5.15) is a consequence of translational invariance. Equations (5.13) and (5.14) can be written in matrix notation as

$$\omega^2(\vec{q})\vec{U}(\vec{q}) = \underline{\mathcal{D}}(\vec{q})\vec{U}(\vec{q}) \tag{5.15}$$

where $\underline{\mathcal{D}}(\vec{q})$ is a 3n x 3n matrix:

$$\underline{\mathcal{D}}(\vec{q}) = \begin{pmatrix} \underline{D}(\vec{q}|11) & \underline{D}(\vec{q}|12) & \cdots & \underline{D}(\vec{q}|1n) \\ D(\vec{q}|21) & \cdot & \cdots & \cdot \\ \cdot & \cdot & & \cdot \\ \cdot & & \cdot & \cdot \\ \cdot & & & \cdot \\ \underline{D}(\vec{q}|n1) & \cdot & \cdots & \underline{D}(\vec{q}|nn) \end{pmatrix} \tag{5.16}$$

with $\underline{D}(\vec{q}|kk')$ a 3 x 3 matrix:

$$\underline{D}(\vec{q}|kk') = \begin{pmatrix} D_{xx}(\vec{q}|kk') & D_{xy}(\vec{q}|kk') & D_{xz}(\vec{q}|kk') \\ D_{yx}(\vec{q}|kk') & D_{yy}(\vec{q}|kk') & D_{yz}(\vec{q}|kk') \\ D_{zx}(\vec{q}|kk') & D_{zy}(\vec{q}|kk') & D_{zz}(\vec{q}|kk') \end{pmatrix} , \tag{5.17}$$

and $\vec{U}(\vec{q})$ is a 3n component vector.

$$\vec{U}(\vec{q}) = \begin{bmatrix} U_x(1|\vec{q}) \\ U_y(1|\vec{q}) \\ U_z(1|\vec{q}) \\ \cdot \\ \cdot \\ \cdot \\ U_x(n|\vec{q}) \\ U_y(n|\vec{q}) \\ U_z(n|\vec{q}) \end{bmatrix} . \tag{5.18}$$

The problem has reduced to an eigenvalue problem indicated by Eq. (5.15). To obtain the 3n eigenvalues and eigenvectors, one must solve the corresponding secular equation

$$|\underline{D}(\vec{q}) - \omega^2(\vec{q})\underline{1}| = 0 \quad . \tag{5.19}$$

The demand of physical meaningful solutions requires $\omega_j^2(\vec{q}) \geq 0$ for $j = 1, 2, \ldots, 3n$. We shall not discuss the general properties of the dynamical matrix, the eigenvalues and the eigenvector due to the lattice periodicity and crystal symmetry since they can be found in the literature (136,137). Specific examples common to Cu_3Au crystal structure materials will be pointed out in section B of this chapter.

4. Periodic boundary conditions - dispersion curves

In order to determine the allowed values of $\vec{q}$, or equivalently, the wavelengths that can be sustained by the lattice of an infinite crystal, Born and von Kármán (135) introduced the periodic boundary conditions in the following way:

One imagines the infinite crystal to be subdivided into large macrocells, each containing a very large number N of primitive cells, where N is comparable to the number of cells in the finite specimen being studied. For convenience, these macrocells are chosen as parallelepipeds with edges defined by the vector $L\vec{a}_1$, $L\vec{a}_2$, $L\vec{a}_3$ and they fill up all space without gaps or overlap. The periodic boundary conditions then demand that the atomic displacements be periodic with the periodicity of the macrocells, i.e.,

$$\vec{u}(\ell_1\ell_2\ell_3\ k) \;=\; \vec{u}(\ell_1 + n_1L, \ell_2 + n_2L, \ell_3 + n_3L\ k) \tag{5.20}$$

where n_1, n_2, n_3 are arbitrary integers. This condition together with Eq. (5.12) implies that $\vec{q}$ may be represented as

$$\vec{q} \;=\; h_1\vec{b}_1 + h_2\vec{b}_2 + h_3\vec{b}_3 \tag{5.21}$$

where

$$h_i \;=\; \frac{n_i'}{L} \quad , \qquad i = 1, 2, 3 \tag{5.22}$$

and n_i' is an integer. $\vec{b}_1$, $\vec{b}_2$, $\vec{b}_3$ in Eq. (5.21) are the basis vectors of the reciprocal lattice. They relate to the primitive translation vectors $\vec{a}_1$, $\vec{a}_2$, $\vec{a}_3$ through

$$\vec{a}\cdot\vec{b} \;=\; 2\pi\,\delta_{ij} \quad , \qquad i,j \;=\; 1, 2, 3 \tag{5.23}$$

where δ_{ij} is the Kronecker delta. The values of $\vec{q}$ determined by Eq. (5.21) form in the reciprocal space a fine mesh of points with a density $(L/2\pi)^3 v$, where v is the volume of the unit cell. Let $\vec{G}$ be a reciprocal lattice vector, it can be shown using Eqs. (5.12), (5.14), (5.15) and (5.23) that

$$\omega_j^2(\vec{q} + \vec{G}) \;=\; \omega_j^2(\vec{q}) \quad . \tag{5.24}$$

It follows that all the distinct values of $\vec{q}$ can be restricted inside the first Brillouin zone, a region centered on the origin of the reciprocal space and bounded by planes drawn as perpendicular bisectors of the vectors joining the origin to the nearest reciprocal lattice

points. The total number of distinct allowed values of $\vec{q}$ is equal to N. Graphically the 3nN frequencies can be shown by continuous curves as a function of $\vec{q}$, i.e., for each direction in $\vec{q}$-space, there are 3n branches of curves $\omega = \omega_j(\vec{q})$, (j = 1, 2, ..., 3n). These curves are called dispersion curves or dispersion relations.

To obtain the pattern of the atomic displacement for a particular mode $(j\vec{q})$, we rewire Eq. (5.15) as follows:

$$\omega_j^2(\vec{q})\vec{e}(j\vec{q}) = \underline{\mathcal{D}}(\vec{q})\vec{e}(j\vec{q}) \tag{5.25}$$

where

$$\vec{e}(j\vec{q}) = \begin{bmatrix} e_x(1|j\vec{q}) \\ e_y(1|j\vec{q}) \\ e_z(1|j\vec{q}) \\ \vdots \\ e_x(n|j\vec{q}) \\ e_y(n|j\vec{q}) \\ e_z(n|j\vec{q}) \end{bmatrix} \tag{5.26}$$

A typical element $e_\alpha(k|j\vec{q})$ in the 3n component vector $\vec{e}(j\vec{q})$ refers to the displacement in the α-direction of the k-th atom vibrating in the mode $(j\vec{q})$. The 3 x 1 component

$$\vec{e}(k|j\vec{q}) = \begin{pmatrix} e_x(k|j\vec{q}) \\ e_y(k|j\vec{q}) \\ e_z(k|j\vec{q}) \end{pmatrix} \tag{5.27}$$

of $\vec{e}(j\vec{q})$ is called the polarization vector of the k-th atom. It can

be shown that the eigenvalues $\vec{e}(j\vec{q})$ satisfy the orthonormality and closure conditions respectively

$$\sum_{k\alpha} e^{*}_{\alpha}(k|j\vec{q})e_{\alpha}(k|j\vec{q}) = \delta_{jj'} \tag{5.28}$$

$$\sum_{j} e^{*}_{\alpha}(k|j\vec{q})e_{\beta}(k'|j\vec{q}) = \delta_{kk'}\delta_{\alpha\beta} \quad . \tag{5.29}$$

It follows from the orthonormality condition that the 3n modes of vibration are independent of each other, hence are known as normal modes of vibration. The complex displacement vector for the k-th atom in mode $(j\vec{q})$ is given as

$$\vec{U}(k|j\vec{q}) = |A(j\vec{q})|\vec{e}(k|j\vec{q})\exp[i\vec{q}\cdot\vec{x}(k)] \tag{5.30}$$

where $|A(j\vec{q})|$ is the amplitude of the normal mode $(j\vec{q})$. The general solution for the displacemetn $\vec{u}(\ell k,t)$ is given by the superposition of the displacements from the lattice waves representing all 3nN modes of vibration, i.e.,

$$u_{\alpha}(k\ell,t) = \frac{1}{\sqrt{m_k}} \sum_{j\vec{q}} |A(j\vec{q})|e_{\alpha}(k|j\vec{q})\exp\{i[\vec{q}\cdot\vec{x}(k\ell) - \omega_j(\vec{q})t]\} \tag{5.31}$$

B. The Construction of the Dynamical Matrix for Cu_3Au-type Structure Materials

In setting up the dynamical matrix defined by Eqs. (5.16) and (5.14), we need to identify the neighboring atoms for each atom in the unit cell and then construct the corresponding force constant matrices for each pair of atoms. Since the summation on $\bar{\ell}$ in Eq. (5.14) extends to an infinite number of neighboring atoms, of course, in practice the

summation over $\bar{\ell}$ in Eq. (5.14) is restricted to a finite number of nearest neighbors. Following the Born-von Kármán interpretation of $\phi(\ell k,\ell' k')$ as interatomic forces, such an approximation appears to be quite reasonable since forces between more distant neighbors are bound to be weaker. However, as we have pointed out in the beginning of this chapter, interpretation of physical results in terms of Born-von Kármán force constants is often of restricted value. Therefore, we consider this approximation as a practical necessity rather than a physical consequence. Usually one prefers to construct the dynamical matrix using the least number of nearest neighbors yet achieves a satisfactory fit to the measured phonon spectrum so that reliable phonon density of states as well as other thermodynamical properties can be calculated.

$CeSn_3$ crystallizes to the simple cubic Cu_3Au structure belonging to the space group $Pm3m(O_h^1)$, no. 221, with the underlying point group $m3m(O_h)$. The four atoms in the cubic unit cell are shown in Fig. 5.1. With this definition (see Fig. 5.1) the Ce atoms are at positions b exhibiting cubic (m3m) site symmetry while the Sn atoms are at positions d exhibiting tetragonal (4/mmm) site symmetry (crystallographic information is tabulated in the International Tables (145)).

In the following we proceed to construct the dynamical matrix using the first nearest neighbor approximation. The distance between an atom and its first nearest neighbor (1st NN) is $\sqrt{2}/2$ a (a is the unit cell dimension). There are twelve 1st NN associated with each of the four atoms (k = 1, 2, 3, 4) in the unit cell containing the origin (ℓ = 000). We shall first consider the twelve 1st NN Sn atoms

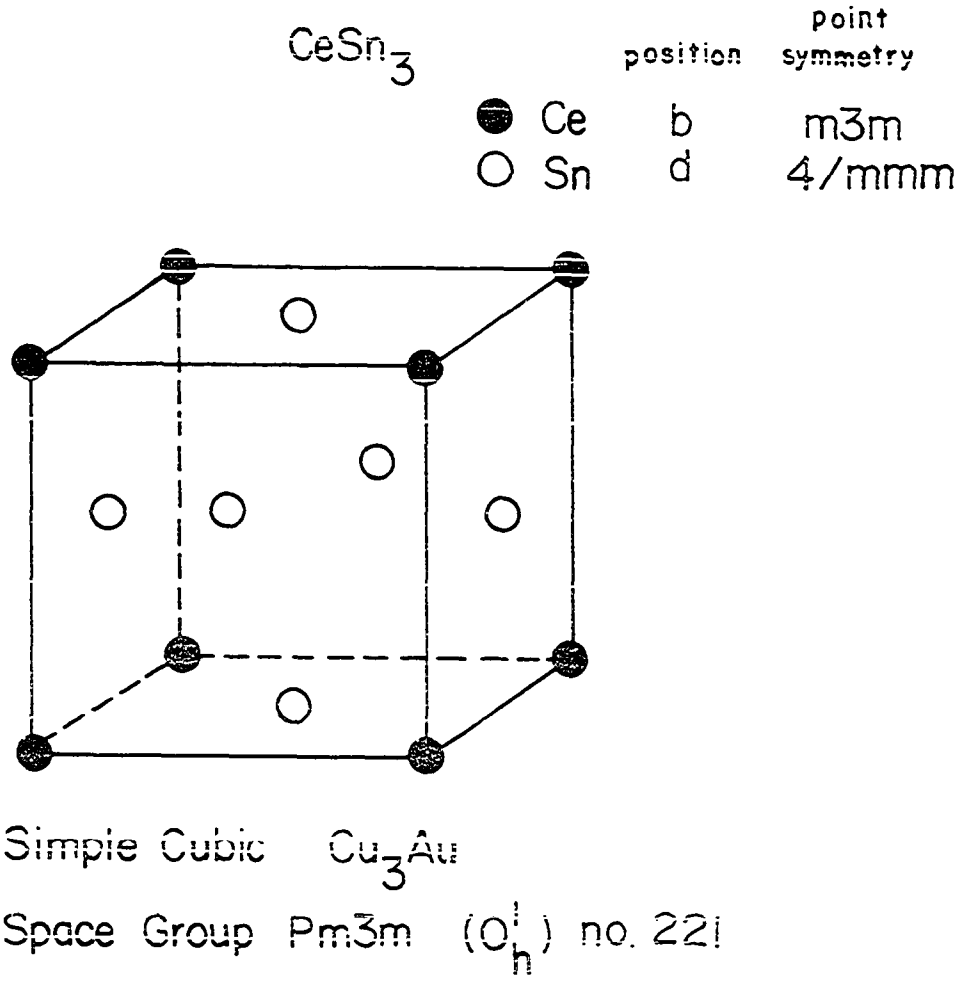

Figure 5.1. The four atoms in the unit cell of $CeSn_3$

(see Table 5.2) associated with the Ce atom in the unit cell (ℓ = 000, k = 4). The force constant matrix connecting atoms (ℓ = 000, k = 4) and (ℓ = 000, k = 1) can be written as

$$\phi\begin{pmatrix} \ell & \ell' \\ k & k' \end{pmatrix} = \phi\begin{pmatrix} 000 & 000 \\ 4 & 1 \end{pmatrix} = \begin{pmatrix} xx & yx & zx \\ xy & yy & zy \\ xz & yz & zz \end{pmatrix} \quad . \tag{5.32}$$

It can be shown from group theory (146) that the number of independent force constants for a given pair of atoms is given by

$$N = \frac{1}{g}\{\Sigma[\chi(S)]^2 + \Sigma\chi(S'^2)\} \quad . \tag{5.33}$$

In the above equation, g is the total number of symmetry operations which leave the 'bond' between an atom pair invariant or reversed; $\Sigma[\chi(S)]^2$ is the sum of the squares of the characters of the invariant operations and $\Sigma\chi(S'^2)$ is the sum of the characters of the squares of the reversal operations. The application of Eq. (5.33) to determine the number of independent force constants required for $\phi\begin{pmatrix} 000 & 000 \\ 4 & 1 \end{pmatrix}$ is illustrated in Table 5.1. As can be seen, only three independent force constants are required to define the matrix in Eq. (5.32). A force constant matrix of an atom pair (ℓk,ℓ'k'), after operated by a proper or improper rotation $\underline{R}$, must be equal to the force constant matrix of an equivalent pair (LK,L'K'). These two matrices are related by a similarity transformation:

$$\phi(\ell k,\ell' k') = \underline{R}\phi(LK,L'K')\tilde{\underline{R}} \tag{5.34}$$

where $\tilde{\underline{R}}$ is the transpose of the rotation matrix $\underline{R}$. An invariance

Table 5.1. Determination of the number of independent force constants for $\phi\binom{000\ 000}{4\quad 1}$

Invariant operations	S	$[\chi(S)]^2$
identity	$\underline{1}=\begin{pmatrix}100\\010\\001\end{pmatrix}$	$3^2=9$
reflection in the $(01\bar{1})$ plane	$\sigma(01\bar{1})=\begin{pmatrix}100\\001\\010\end{pmatrix}$	$1^2=1$
reflection in the (100) plane	$\sigma(100)=\begin{pmatrix}-100\\010\\001\end{pmatrix}$	$1^2=1$
two-fold rotation about the band axis	$C_2[011]=\begin{pmatrix}-100\\001\\010\end{pmatrix}$	$-1^2=1$

Reversion operators	S'	S'^2	$\chi(S'^2)$
inversion	$I=\begin{pmatrix}-1&0&0\\0&-1&0\\0&0&-1\end{pmatrix}$	$\begin{pmatrix}100\\010\\001\end{pmatrix}$	3
two-fold rotation about the x axis	$C_2[100]=\begin{pmatrix}1&0&0\\0&-1&0\\0&0&-1\end{pmatrix}$	$\begin{pmatrix}100\\010\\001\end{pmatrix}$	3
two-fold rotation about an axis perpendicular to the x axis and the bond axis	$C_2[01\bar{1}]=\begin{pmatrix}-1&0&0\\0&0&-1\\0&-1&0\end{pmatrix}$	$\begin{pmatrix}100\\010\\001\end{pmatrix}$	3
reflection in the (011) plane	$\sigma(011)=\begin{pmatrix}1&0&0\\0&-1&0\\0&0&-1\end{pmatrix}$	$\begin{pmatrix}100\\010\\001\end{pmatrix}$	3

$$N=\frac{1}{g}\{\Sigma[\chi(S)]^2+\Sigma\chi(S'^2)\}=\frac{1}{8}[(9+1+1+1)+(3+3+3+3)]=3$$

operation S, by definition, leaves a given pair of sites unchanged. Thus we arrive at the following important relation:

$$\phi(\ell k,\ell' k') = \underline{S}\phi(\ell k,\ell' k')\tilde{\underline{S}} \quad , \tag{5.35}$$

for invariance operation S. Next we apply invariance operations given in Table 5.1 to the force constant matrix of Eq. (5.32) according to Eq. (5.35) until the number of independence force constants is reduced to the calculated number determined by Eq. (5.33). For examples,

$$\phi\begin{pmatrix} 000 & 000 \\ 4 & 1 \end{pmatrix} = \sigma(01\bar{1})\,\phi\begin{pmatrix} 000 & 000 \\ 4 & 1 \end{pmatrix}\tilde{\sigma}(01\bar{1}) \tag{5.36}$$

implies yy = zz, yx = zx, xy = xz and yz = zy. Substituting these conditions into the force constants matrix in Eq. (5.32) then applying S = σ(100) to it according to Eq. (5.35), one obtains yx = -yx = 0 and xy = -xy = 0. At this point only three independent force constants, namely xx, yy and yz remain. Thus we can rewrite the matrix as

$$\phi\begin{pmatrix} 000 & 000 \\ 4 & 1 \end{pmatrix} = \begin{pmatrix} xx & 0 & 0 \\ 0 & yy & 0 \\ 0 & yz & yy \end{pmatrix} - -\begin{pmatrix} \beta & 0 & 0 \\ 0 & \alpha & \gamma \\ 0 & \gamma & \alpha \end{pmatrix} \tag{5.37}$$

where α, β and γ are three independent interatomic force constants for a pair of first nearest neighboring Ce-Sn atoms.

Once the above force constant matrix is obtained, other force constant matrices connecting atom ℓ = 000, k = 4 to the remaining eleven 1st NN can be determined from it by using appropriate symmetry operations according to Eq. (5.34). For examples (see Fig. 5.2),

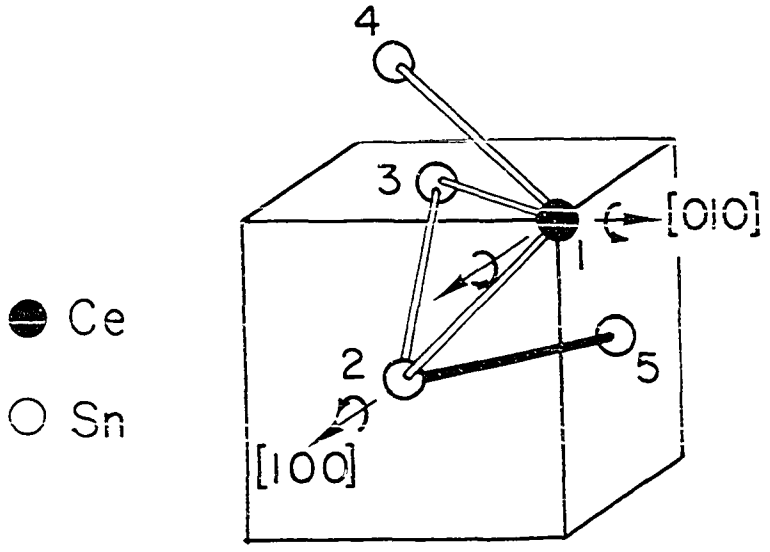

ATOMS $\begin{pmatrix} \ell \\ k \end{pmatrix}$

1	$\begin{pmatrix} 000 \\ 4 \end{pmatrix}$	$\phi\begin{pmatrix} 000 & 000 \\ 4 & 1 \end{pmatrix} = -\begin{pmatrix} \beta & 0 & 0 \\ 0 & \alpha & \gamma \\ 0 & \gamma & \alpha \end{pmatrix}$
2	$\begin{pmatrix} 000 \\ 1 \end{pmatrix}$	$\phi\begin{pmatrix} 000 & 001 \\ 4 & 1 \end{pmatrix} = C_{-4}[100]\phi\begin{pmatrix} 000 & 000 \\ 4 & 1 \end{pmatrix}\tilde{C}_{-4}[100]$
3	$\begin{pmatrix} 000 \\ 3 \end{pmatrix}$	$\phi\begin{pmatrix} 000 & 000 \\ 4 & 3 \end{pmatrix} = C_4[010]\phi\begin{pmatrix} 000 & 000 \\ 4 & 1 \end{pmatrix}\tilde{C}_4[010]$
4	$\begin{pmatrix} 000 \\ 1 \end{pmatrix}$	$\phi\begin{pmatrix} 000 & 000 \\ 1 & 2 \end{pmatrix} = -\begin{pmatrix} \alpha' & -\gamma' & 0 \\ -\gamma' & \alpha' & 0 \\ 0 & 0 & \beta' \end{pmatrix}$
5	$\begin{pmatrix} 000 \\ 2 \end{pmatrix}$	$\phi\begin{pmatrix} 000 & 000 \\ 1 & 3 \end{pmatrix} = C_4[100]\phi\begin{pmatrix} 000 & 000 \\ 1 & 2 \end{pmatrix}\tilde{C}_4[100]$

Figure 5.2. The independent interatomic force constants for the first nearest neighbor approximation are defined by two force constant matrices connecting respectively the 1st NN Ce-Sn and 1st NN Sn-Sn atoms. Other force constant matrices connecting the 1st NN atom pairs are related by symmetry operators

$$\phi\begin{pmatrix} 000 & 001 \\ 4 & 1 \end{pmatrix} = C_{-4}[100]\phi\begin{pmatrix} 000 & 000 \\ 4 & 1 \end{pmatrix}\tilde{C}_{-4}[100] = -\begin{pmatrix} \beta & 0 & 0 \\ 0 & \alpha & -\gamma \\ 0 & -\gamma & \alpha \end{pmatrix} \tag{5.38}$$

where $C_{-4}[100]$ is a clockwise rotation by 90° about the [100] direction. Or

$$\phi\begin{pmatrix} 000 & 000 \\ 4 & 3 \end{pmatrix} = C_4[010]\phi\begin{pmatrix} 000 & 000 \\ 4 & 1 \end{pmatrix}\tilde{C}_4[010] = -\begin{pmatrix} \alpha & \gamma & 0 \\ \gamma & \alpha & 0 \\ 0 & 0 & \beta \end{pmatrix} \tag{5.39}$$

where $C_4[010]$ is an anticlockwise rotation by 90° about the [010] direction. The force constant matrices connecting the Ce atom in the unit cell of $\ell = 000$ and its twelve first nearest neighboring Sn atoms are summarized in Table 5.2.

As a result of translational invariance, the 'self force constant', $\phi_{\alpha\beta}(\ell k,\ell k)$, is given by the negative of the sum of the force constants describing the forces acting on atom (ℓ,k) due to every other atom in the lattice. That is,

$$\phi_{\alpha\beta}(\ell k,\ell k) = -\sum_{\ell',k'}{}' \phi_{\alpha\beta}(\ell k,\ell' k') \tag{5.40}$$

where the prime with the summation sign implies the exclusion of $\ell' = \ell$, $k' = k$. Therefore, using the results in the first part of Table 5.2 and Eq. (5.40), we obtain

$$\phi\begin{pmatrix} 000 & 000 \\ 4 & 4 \end{pmatrix} = -\sum_{\ell' k'}{}' \phi\begin{pmatrix} 000 & \ell' \\ 4 & k' \end{pmatrix} = \begin{pmatrix} 4\beta+8\alpha & 0 & 0 \\ 0 & 4\beta+8\alpha & 0 \\ 0 & 0 & 4\beta+8\alpha \end{pmatrix}. \tag{5.41}$$

Table 5.2. Force constant matrices of the twelve 1st NN Ce-Sn atom pairs

$$\phi\begin{pmatrix}000 & 000\\ 4 & 1\end{pmatrix}=\phi\begin{pmatrix}000 & 011\\ 4 & 1\end{pmatrix}=-\begin{pmatrix}\beta & 0 & 0\\ 0 & \alpha & \gamma\\ 0 & \gamma & \alpha\end{pmatrix}$$

$$\phi\begin{pmatrix}000 & 001\\ 4 & 1\end{pmatrix}=\phi\begin{pmatrix}000 & 010\\ 4 & 1\end{pmatrix}=-\begin{pmatrix}\beta & 0 & 0\\ 0 & \alpha & -\gamma\\ 0 & -\gamma & \alpha\end{pmatrix}$$

$$\phi\begin{pmatrix}000 & 000\\ 4 & 2\end{pmatrix}=\phi\begin{pmatrix}000 & 101\\ 4 & 2\end{pmatrix}=-\begin{pmatrix}\alpha & 0 & \gamma\\ 0 & \beta & 0\\ \gamma & 0 & \alpha\end{pmatrix}$$

$$\phi\begin{pmatrix}000 & 001\\ 4 & 2\end{pmatrix}=\phi\begin{pmatrix}000 & 100\\ 4 & 2\end{pmatrix}=-\begin{pmatrix}\alpha & 0 & -\gamma\\ 0 & \beta & 0\\ -\gamma & 0 & \alpha\end{pmatrix}$$

$$\phi\begin{pmatrix}000 & 000\\ 4 & 3\end{pmatrix}=\phi\begin{pmatrix}000 & 110\\ 4 & 3\end{pmatrix}=-\begin{pmatrix}\alpha & \gamma & 0\\ \gamma & \alpha & 0\\ 0 & 0 & \beta\end{pmatrix}$$

$$\phi\begin{pmatrix}000 & 010\\ 4 & 3\end{pmatrix}=\phi\begin{pmatrix}000 & 100\\ 4 & 3\end{pmatrix}=-\begin{pmatrix}\alpha & -\gamma & 0\\ -\gamma & \alpha & 0\\ 0 & 0 & \beta\end{pmatrix}$$

$$\phi\begin{pmatrix}000 & 000\\ 4 & 4\end{pmatrix}=-\sum_{\ell'k'}{}'\begin{pmatrix}000 & \ell'\\ 4 & k'\end{pmatrix}$$

$$=\begin{pmatrix}4\beta+8\alpha & 0 & 0\\ 0 & 4\beta+8\alpha & 0\\ 0 & 0 & 4\beta+8\alpha\end{pmatrix}$$

Next, we consider the force constant matrices connecting the three Sn atoms (k = 1, 2, 3) in the unit cell ℓ = 000 and their 1st NN. Each of these Sn atoms has twelve 1st NN of which four are Ce atoms and eight are Sn atoms. While those force constant matrices connecting the Sn atoms and their first nearest neighboring Ce atoms can be determined by using Eq. (5.34) and the symmetry operations given in Table 5.2, the force constant matrices connecting the Sn atoms and their first nearest neighboring Sn atoms need to be constructed. Following the same procedure as in the construction of $\phi\binom{000\ 000}{4\quad 1}$, it is straightforward to form the first force constant matrix for a pair of 1st NN Sn-Sn atoms. We define

$$\phi\begin{pmatrix} 000 & 000 \\ 1 & 2 \end{pmatrix} = -\begin{pmatrix} \alpha' & -\gamma' & 0 \\ -\gamma' & \alpha' & 0 \\ 0 & 0 & \beta' \end{pmatrix} \tag{5.42}$$

where α', β' and γ' are another three independent interatomic force constants describing the forces between a pair of first nearest neighboring Sn-Sn atoms. All the other force constant matrices are obtained in the same manner mentioned earlier, e.g. (see Fig. 5.2),

$$\phi\begin{pmatrix} 000 & 000 \\ 1 & 3 \end{pmatrix} = C_4[100]\phi\begin{pmatrix} 000 & 000 \\ 1 & 2 \end{pmatrix}\tilde{C}_4[100] = -\begin{pmatrix} \alpha' & 0 & -\gamma' \\ 0 & \beta' & 0 \\ -\gamma' & 0 & \alpha' \end{pmatrix} . \tag{5.43}$$

The three sets of twelve force constant matrices for the three Sn atoms and their self force constants are listed in Table 5.3.

Table 5.3. Force constant matrices for the three sets of 1NN of the Sn atoms

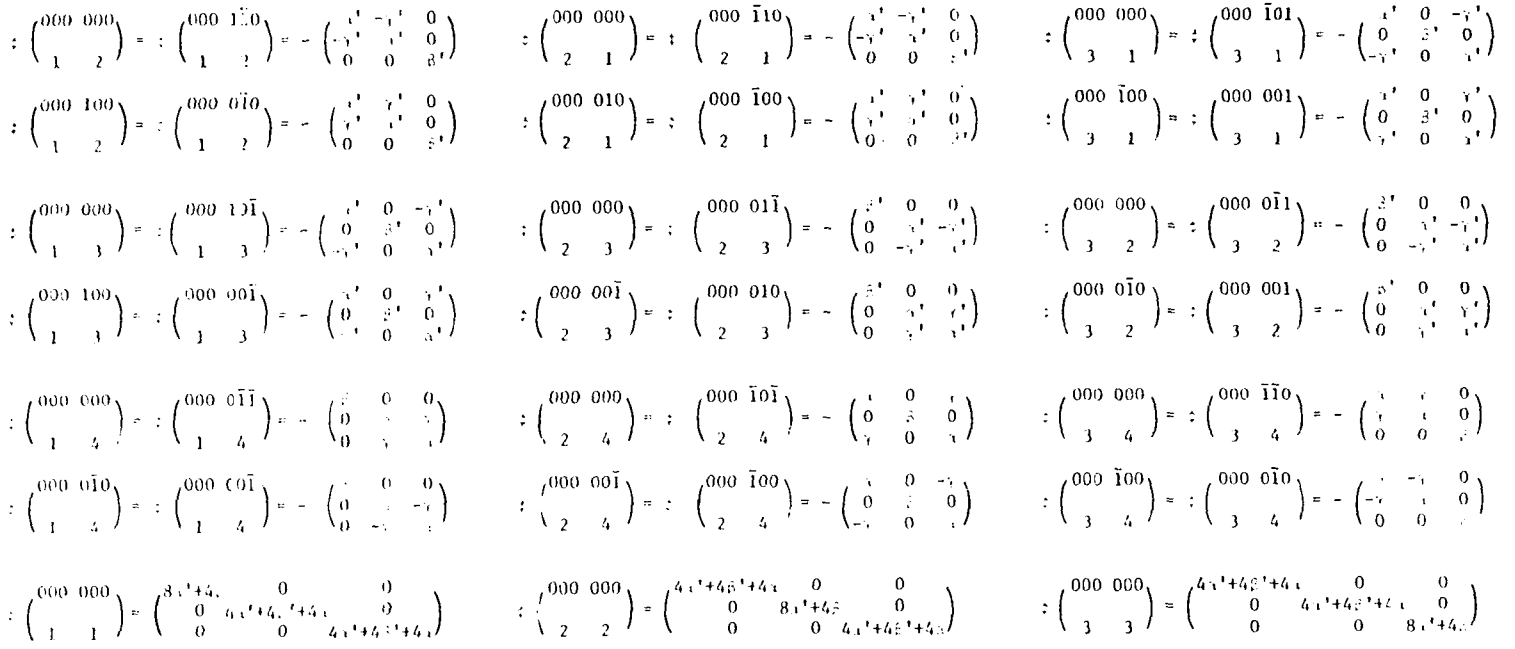

In the next step the 3 x 3 matrices $D_{\alpha\beta}(\vec{q}|kk')$ defined by Eq. (5.14) are constructed. Let us express the position vector of the ℓ-th cell $\vec{x}(\ell)$ in units of a and the wavevector $\vec{q}$ in units of 1/a. Using the force constant matrices in Table 5.2 and Eq. (5.14), we

$$\begin{aligned}
\underline{D}(\vec{q}|41) &= \frac{1}{\sqrt{m_1 m_2}}\Big[\phi\binom{000\ 000}{4\ \ 1}\exp\{i\vec{q}\cdot\vec{0}\} + \phi\binom{000\ 011}{4\ \ 1}\exp\{i2\pi(q_x,q_y,q_z) \\
&\quad \times (0,1,1)\} + \phi\binom{000\ 001}{4\ \ 1}\exp\{i2\pi(q_x,q_y,q_z)(0,0,1)\} + \phi\binom{000\ 010}{4\ \ 1} \\
&\quad \times \exp\{i2\pi(q_x,q_y,q_z)(0,1,0)\}\Big] \\
&= -\frac{1}{\sqrt{m_1 m_2}}\Big[\begin{pmatrix}\beta & 0 & 0\\ 0 & \alpha & \gamma\\ 0 & \gamma & \alpha\end{pmatrix}(1+\exp\{i2\pi[q_y+q_z]\}) + \begin{pmatrix}\beta & 0 & 0\\ 0 & \alpha & -\gamma\\ 0 & -\gamma & \alpha\end{pmatrix} \\
&\quad \times (\exp[i2\pi q_z] + \exp[i2\pi q_y])\Big] \\
&= -\frac{1}{m_{12}}\begin{pmatrix}\beta[E_2+1][E_3+1] & 0 & 0\\ 0 & \alpha[E_2+1][E_3+1] & \gamma[E_2-1][E_3-1]\\ 0 & \gamma[E_2-1][E_3-1] & \alpha[E_2+1][E_3-1]\end{pmatrix} .
\end{aligned} \tag{5.44}$$

For brevity, we have adapted the following symbols:

$$m_1 = m_{Sn} = \text{the mass of a Sn atom} \tag{5.45a}$$

$$m_2 = m_{Ce} = \text{the mass of a Ce atom} \tag{5.45b}$$

$$m_{12} = [m_1 m_2]^{1/2} \tag{5.45c}$$

$E_{\pm\alpha} = \exp[\pm i2\pi q_\alpha]$, $\alpha = 1, 2, 3$ are the Carestian component indices, e.g., $E_{-1} = \exp[-i2\pi q_x]$, etc. (5.45d)

Other $\underline{D}(\vec{q}|kk')$ matrices are obtained in the same manner. Finally, the dynamical matrix with the 1st NN approximation $\underline{\mathcal{D}}^{(1)}(\vec{q})$ is composed according to Eq. (5.16). The result is presented in Table 5.4. Since the dynamical matrix is a Hermitian matrix, only the lower triangle of the 12 x 12 dynamical matrix $\underline{\mathcal{D}}^{(1)}(\vec{q})$ is given in Table 5.4. As can be seen, a set of six interatomic force constants is required to determine the eigenvalues, $\omega_j^2(\vec{q})$, j = 1, 2, ..., 12.

C. Results of Group Theoretical Analysis

The Brillouin zone of the system is shown in Fig. 5.3. We shall discuss various properties of the phonon dispersion curves, resulting from the group theoretical analysis, along three symmetry directions, namely, the [100]Δ, [110]Σ and [111]Λ directions.

1. Along [100]Δ direction (see Fig. 5.4)

The decomposition of the reducible representation, Γ_Δ, of the point group $G_o(\vec{q} = [0\xi 0]) = C_{4v}$ into irreducible representation (IR) is given by

$$\Gamma_\Delta = 3\Delta_1 + \Delta_2 + 4\Delta_5 \text{ (2 dim.)} \quad . \tag{5.46}$$

This implies that in the decomposition of Γ, three of the normal modes transform as the (one-dimensional) IR Δ_1; consequently three phonon branches in this direction are labeled Δ_1. The dimensionality of an IR corresponds to the number of orthonormal eigenvectors belonging to an eigenvalue, that is, the degree of degeneracy of the corresponding mode. Therefore, the term $4\Delta_5$ (2 dim.) in Eq. (5.46) implies that

Table 5.4. The dynamical matrix for the 1NN Born-von Kármán force constant model of $CeSn_3$

$$
\underline{A}^{(1)}(\vec{q}|kk') = \left(\begin{array}{cccc}
\frac{8\alpha'+4\beta}{m_1} & & & \\
0 & \frac{4\alpha'+4\beta'+4\alpha}{m_1} & & \\
0 & 0 & \frac{4\alpha'+4\beta'+4\alpha}{m_1} & \\
\frac{-\alpha'(E_{-1}+1)(E_2+1)}{m_1} & \frac{\gamma'(E_{-1}-1)(E_2-1)}{m_1} & 0 & \frac{4\alpha'+4\beta'+4\alpha}{m_1} \\
\frac{\gamma'(E_{-1}-1)(E_2-1)}{m_1} & \frac{-\alpha'(E_{-1}+1)(E_2+1)}{m_1} & 0 & 0 \\
0 & 0 & \frac{-\beta'(E_{-1}+1)(E_2+1)}{m_1} & 0 \\
\frac{-\alpha'(E_{-1}+1)(E_3+1)}{m_1} & 0 & \frac{\gamma'(E_{-1}-1)(E_3-1)}{m_1} & \frac{-\beta'(E_{-1}+1)(E_3+1)}{m_1} \\
0 & \frac{-\beta'(E_{-1}+1)(E_3+1)}{m_1} & 0 & 0 \\
\frac{\gamma'(E_{-1}-1)(E_3-1)}{m_1} & 0 & \frac{-\alpha'(E_{-1}+1)(E_3+1)}{m_1} & 0 \\
\frac{-\beta(E_2+1)(E_3+1)}{m_{12}} & 0 & 0 & \frac{-\alpha(E_1+1)(E_3+1)}{m_{12}} \\
0 & \frac{-\alpha(E_2+1)(E_3+1)}{m_{12}} & \frac{-\gamma(E_2-1)(E_3-1)}{m_{12}} & 0 \\
0 & \frac{-\gamma(E_2-1)(E_3-1)}{m_{12}} & \frac{-\alpha(E_2+1)(E_3+1)}{m_{12}} & \frac{-\gamma(E_1-1)(E_3-1)}{m_{12}}
\end{array}\right)
$$

$m_1 = m_{Sn}$ = mass of a Sn atom

$m_2 = m_{Ce}$ = mass of a Ce atom

$m_{12} = [m_1 m_2]^{1/2}$

$E_{\pm\alpha} = \exp[\pm i 2\pi q_\alpha]$, $\alpha = 1, 2, 3$ are Cartesian component indices.

$$
\begin{array}{cccccccccc}
\frac{8\alpha'+4\beta}{m_1} & & & & & & & & & \\
0 & \frac{4\alpha'+4\beta'+4\alpha}{m_1} & & & & & & & & \\
0 & 0 & \frac{4\alpha'+4\beta'+4\alpha}{m_1} & & & & & & & \\
\frac{-\alpha'(E_{-2}+1)(E_3+1)}{m_1} & \frac{\gamma'(E_{-2}-1)(E_3-1)}{m_1} & 0 & \frac{4\alpha'+4\beta'+4\alpha}{m_1} & & & & & & \\
\frac{\gamma'(E_{-2}-1)(E_3-1)}{m_1} & \frac{-\alpha'(E_{-2}+1)(E_3+1)}{m_1} & 0 & 0 & \frac{8\alpha'+4\beta}{m_1} & & & & & \\
0 & \frac{-\gamma(E_1-1)(E_3-1)}{m_{12}} & \frac{-\alpha(E_1+1)(E_2+1)}{m_{12}} & \frac{-\gamma(E_1-1)(E_2-1)}{m_{12}} & 0 & \frac{8\alpha+4\beta}{m_2} & & & & \\
\frac{-\beta(E_1+1)(E_2+1)}{m_{12}} & 0 & \frac{-\gamma(E_1-1)(E_2-1)}{m_{12}} & \frac{-\alpha(E_1+1)(E_2+1)}{m_{12}} & 0 & 0 & \frac{8\alpha+4\beta}{m_2} & & & \\
0 & \frac{-\alpha(E_1+1)(E_3+1)}{m_{12}} & 0 & 0 & \frac{-\beta(E_1+1)(E_2+1)}{m_{12}} & 0 & 0 & \frac{8\alpha+4\beta}{m_2} &
\end{array}
$$

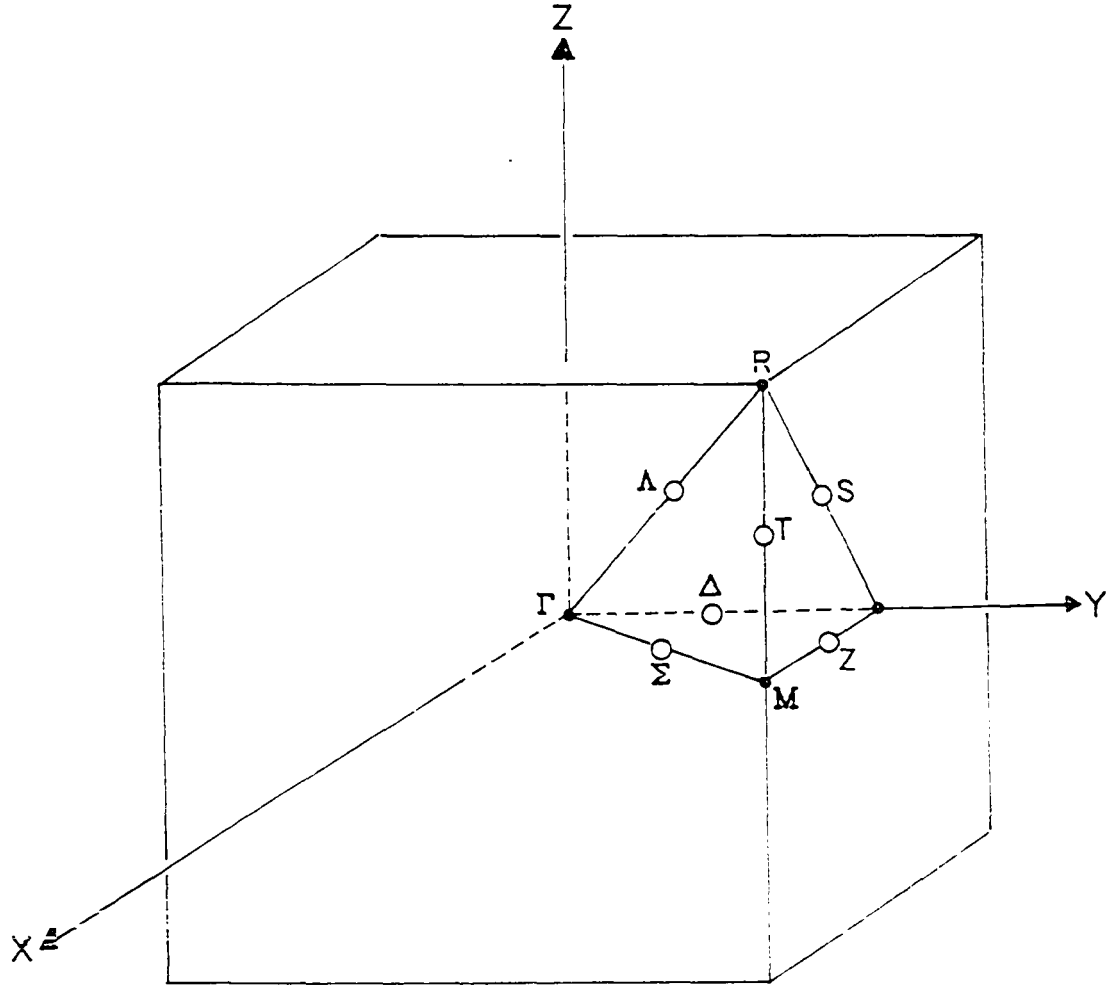

Figure 5.3. The Brillouin zone of the simple cubic Cu_3Au crystal structure

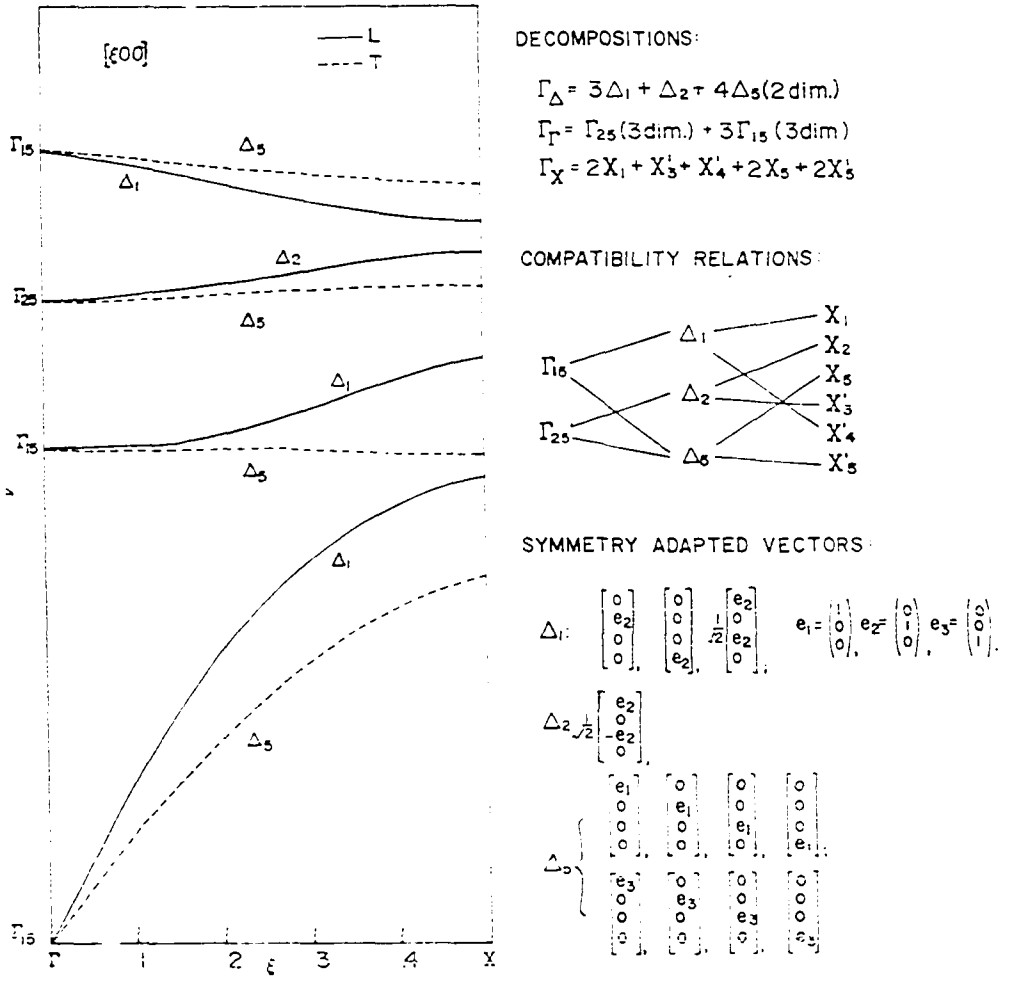

Figure 5.4. Results of the group theoretical analysis of the dispersion curves of $CeSn_3$ along the [100] direction

there are four doubly degenerate phonon branches labeled Δ_5. Finally, there is a single branch (labeled Δ_2) which transforms as the (one-dimensional) IR Δ_2. Note that the total number of branches is twelve, equal to the number of degrees of freedom of the four atoms in a unit cell.

The decomposition of Γ at the zone center Γ and the zone boundary X are written as

$$\Gamma_\Gamma = \Gamma_{25}(3 \text{ dim.}) + 3\Gamma_{15}(3 \text{ dim.}) \tag{5.47}$$

$$\Gamma_X = 2X_1 + X_3' + X_4' + 2X_5(2 \text{ dim.}) + 2X_5'(2 \text{ dim.}) \tag{5.48}$$

Now let us examine the symmetry-adapted vectors for the modes (see Fig. 5.4) which transform as each IR of the point group along Δ. Recall that the direction of propagation of all the modes is along the y-axis. As can be seen in Fig. 5.4, the displacement of each atom in the Δ_1 and Δ_2 modes are parallel to the direction of propagation whereas those in the Δ_5 modes are perpendicular to the direction of propagation; in other words, the former are purely longitudinal modes and the latter are purely transverse modes. In addition, it is known that a longitudinal acoustic mode in the long wavelength limit ($\vec{q} \to 0$) corresponds to all the atoms displaced uniformly along the direction of propagation. This mode can only be obtained from a linear combination of the symmetry-adapted vectors of the Δ_1 modes; thus the longitudinal acoustic branch must belong to one of the Δ_1 modes.

Figure 5.4 includes a schematic diagram of the phonon dispersion curves along the [100] direction predicted by group theory. Notice

that modes which transform as the same IR cannot cross each other. It should be stressed that the assignment of phonon branches and their degeneracies for this crystal structure cannot be determined uniquely by crystal symmetry. As can be seen in Fig. 5.4, in addition to the origin (Γ_{15}) there are three Γ points (two Γ_{25} and one Γ_{15}) from which two branches originate. One of them is a purely longitudinal mode and the other is a doubly degenerate purely transverse mode.

The purely longitudinal optical branch Δ_2 which originates from Γ_{25} at the zone center is noteworthy. Since it is the only mode which transforms as the IR Δ_2, its polarization vector is uniquely defined by the symmetry-adapted vector of this mode. It can be shown (by using Eq. (6.2) in the next chapter) that the inelastic coherent neutron structure factors of this mode for wavevectors in the {110} planes are identically zero. Consequently, the Δ_2 mode can only be measured in a mirror plane of the crystal other than the {110} planes, such as the [100] plane.

2. Along [110] direction (see Fig. 5.5)

Along the [110] direction none of the modes is degenerate. As can be seen from Fig. 5.5 there are four longitudinal-like (i.e., not purely longitudinal) modes labeled Σ_1. Among the eight transverse branches, Σ_2 and Σ_3 are purely transverse modes with polarization vectors parallel to the z-axis; Σ_4 are four transverse-like modes with polarization vectors perpendicular to the z-axis. An examination of the compatibility relations along $\Gamma\Sigma M$ reveals that at the zone

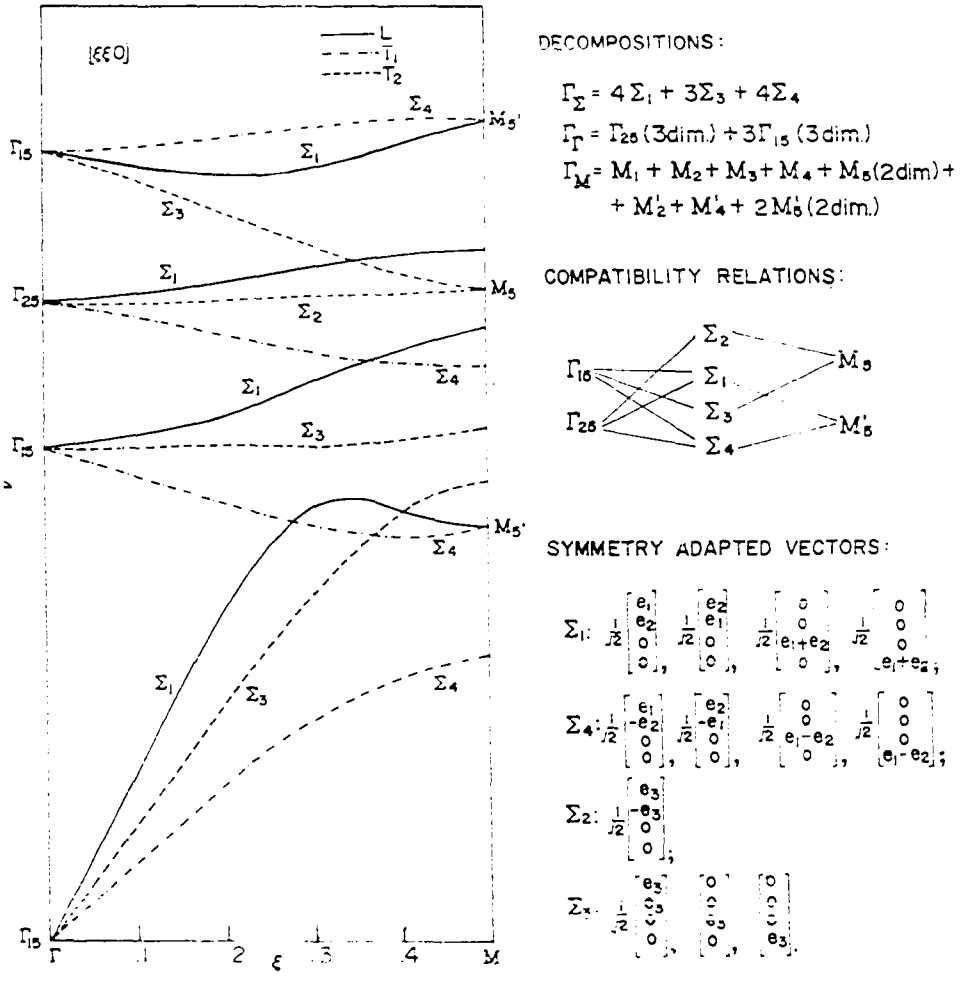

Figure 5.5. Results of the group theoretical analysis of the dispersion curves of $CeSn_3$ along the [110] direction

boundary there are three degeneracies corresponding to two M_5' and one M_5 points. At M_5' the degeneracy is between a Σ_1 and a Σ_4; at M_5 the degeneracy is between a Σ_2 and a Σ_3.

From a consideration of the inelastic neutron structure factors for all the modes, we arrive at the following results:

1) The Σ_3 and Σ_4 modes can be measured separately without interference from each other in two different crystal mirror planes; that is, with the $[1\bar{1}0]$ axis vertical in the first case and the [100] axis vertical in the latter.
2) The purely transverse optical mode Σ_2 <u>cannot</u> be measured in either of the two planes mentioned above. It can be shown that the branch can be detected in the $[1\bar{1}1]$ plane.

<u>3. Along [111]Λ direction</u> (see Fig. 5.6)

Along the [111]Λ direction each of the four Λ_3 branches is doubly degenerate. With the exception of Λ_2 mode, none of the modes is purely longitudinal or purely transverse. Actually due to the complexity of the symmetry-adapted vectors of these modes, the longitudinal or transverse character of a mode can only be defined at wavevectors very close to the zone center. At the zone boundary R there are three degeneracies corresponding to two R_{25}' and one R_{15}' points. At R_{25}' the degeneracy is between a Λ_1 and a Λ_3 mode; at R_{15}' the degeneracy is between a Λ_2 and a Λ_3 mode.

While the Λ_2 and Λ_3 modes can be measured in the $(1\bar{1}0)$ plane, the inelastic structure factor of the purely transverse optical branch Λ_2

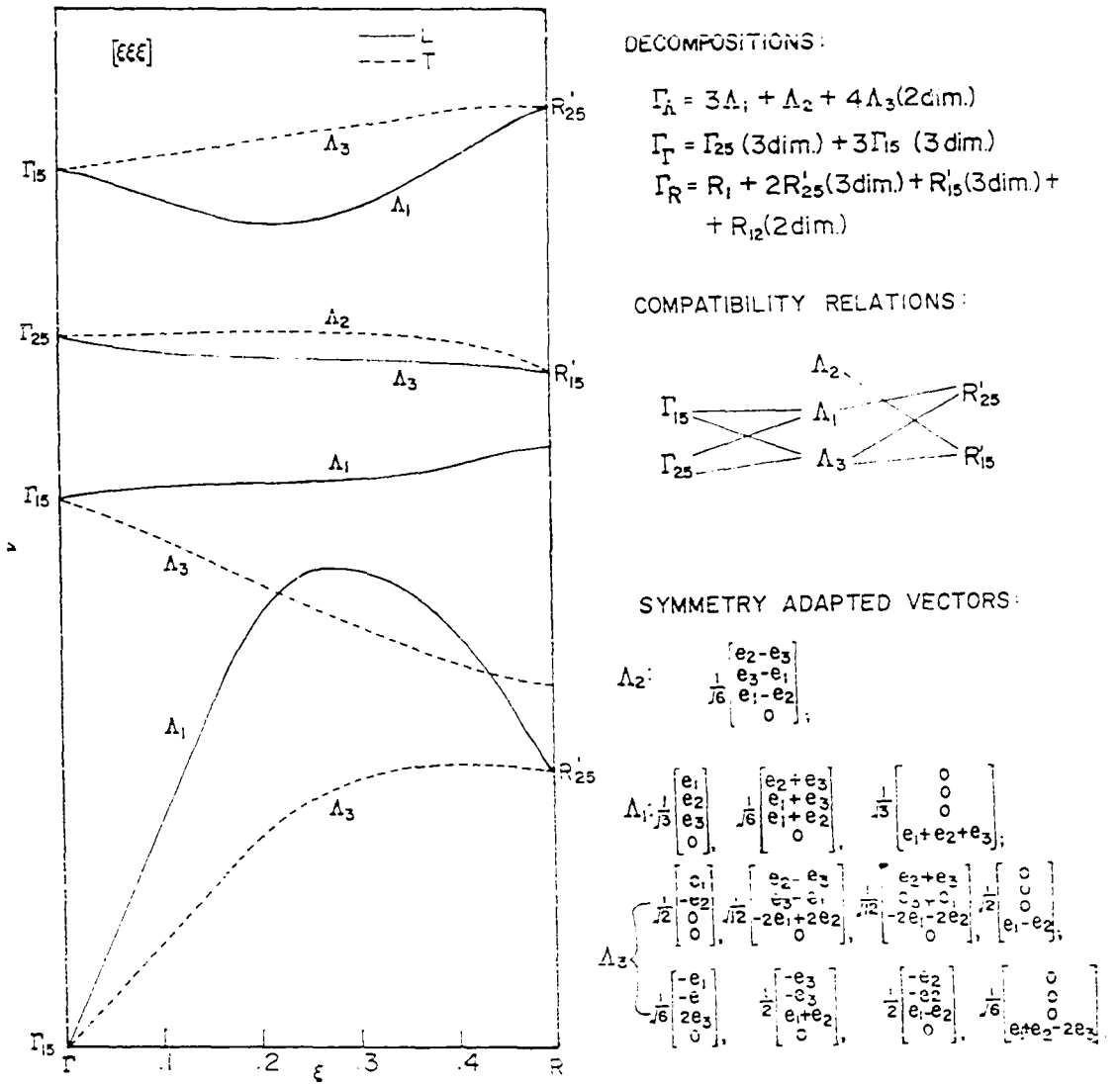

Figure 5.6. Results of the group theoretical analysis of the dispersion curves of $CeSn_3$ along the [111] direction

is identically zero in this plane. It can be shown that Λ_2 can be measured in the crystal mirror plane with the $[11\bar{2}]$ axis vertical.

VI. EXPERIMENTAL CONSIDERATIONS AND RESULTS

A. Technique of Inelastic Neutron Scattering

1. One-phonon inelastic coherent scattering

In contrast to X-rays and electromagnetic radiation such as the infrared radiation, slow neutrons have wavelengths and energies comparable with the interatomic spacings and phonon energies of solids respectively. This is the chief reason for slow neutron scattering being an ideal tool for the study of dynamical properties of crystalline solids. In the present investigation we are interested in the inelastic scattering processes which involve the exchange of one phonon between the radiation and the crystal. Other contributions to the measurement including incoherent and multi-phonon scattering processes are considered as background. The differential cross section of one-phonon inelastic coherent scattering (111) is given by

$$\frac{d^2\sigma_i^{coh}}{d\Omega dE} = \frac{2\pi}{V} \sum_{j,\vec{q},\vec{\tau}} \frac{k'}{k_o} \frac{h^2(n + \frac{1}{2} \pm \frac{1}{2})}{2\nu} |F_j(\vec{Q})|^2 \delta[h\nu \mp h\nu_j(\vec{q})]\delta[\vec{Q} - (\vec{q}+\vec{\tau})] \tag{6.1}$$

where

V = volume of the unit cell

$\vec{q}$ = phonon wavevector

j = phonon mode index

$\vec{\tau}$ = reciprocal lattice vector

$\vec{k}'$ = scattered neutron wavevector

$\vec{k}_o$ = incident neutron wavevector

$h\nu = \dfrac{\hbar^2(k_o^2 - k'^2)}{2m_n}$ = energy change of the neutron (m_n is the mass of neutron)

$h\nu_j(\vec{q})$ = energy of the created or annihilated phonon

$\vec{Q} = \vec{k}_o - \vec{k}'$ = momentum transfer vector of the neuron = scattering vector

n = average phonon occupation number = $\langle n_{j\vec{q}} \rangle = \dfrac{1}{\exp[h\omega_j(\vec{q})/k_B T] - 1}$

$F_j(\vec{Q})$ = inelastic coherent neutron structure factor

$$= \sum_k \frac{b_k}{m_k} \vec{Q} \cdot \vec{e}(k|j\vec{q}) \exp[i\vec{Q} \cdot \vec{x}(k)] \exp[-W_k(\vec{Q})] \tag{6.2}$$

with the k summation over the atoms in the unit cell,

m_k = mass of the k-th atom

b_k = coherent nuclear scattering amplitude for the k-th atom

$\vec{x}(k)$ = position vector for the k-th atom of the basis with respect to the origin of the unit cell

$\vec{e}(k|j\vec{q})$ = polarization vector of the k-th atom for mode $(j\vec{q})$ (see Eq. (5.27))

$W_k(\vec{Q})$ = the Debye-Waller factor

$$= \overline{\frac{1}{2} [\vec{Q} \cdot u(\ell k, t)]^2} \tag{6.3}$$

($\vec{u}(\ell k, t)$ is defined by Eq. (5.31), $\overline{\ }$ denotes the time-average).

The upper and lower signs in Eq. (6.1) correspond to phonon creation and annihilation respectively. There are two conservation

relations indicated by the two delta functions in Eq. (6.1). First, energy conservation requires that the energy lost or gained by the neutron must be equal to the energy change of the crystal--the energy of the phonon being created or annihilated. That is,

$$h\nu = \frac{\hbar^2}{2m_n}(k_o^2 - k'^2) = \pm h\nu_j(\vec{q}) \quad . \tag{6.4}$$

Second, the momentum change of the neutron must be equal to the quasi-momentum change of the lattice. That is,

$$\vec{Q} = \vec{k}_o - \vec{k}' = \vec{\tau} + \vec{q} \quad . \tag{6.5}$$

Equations (6.4) and (6.5) together with the dispersion relations $\nu_j(\vec{q})$ versus $\vec{q}$ constitute a system of five equations with four unknowns for which only a finite number of solutions can be found. This situation is illustrated graphically in Fig. 6.1. Given the wavelength and direction of the incident neutrons, the 'scattering surfaces' in the reciprocal space are determined by Eqs. (6.5) and the following equation

$$k' = \sqrt{k_o^2 + \frac{4\pi m \nu_j(\vec{q})}{\hbar}} \quad . \tag{6.6}$$

Figure 6.1 shows some scattering surfaces for one-phonon processes with neutron energy gain in the [001] zone of aluminum, calculated for 4 Å neutrons along the [010] direction. As can be seen, the scattering surfaces intersect the line defining the scattering direction at points A, B, C, D, and E which correspond to five solutions to the

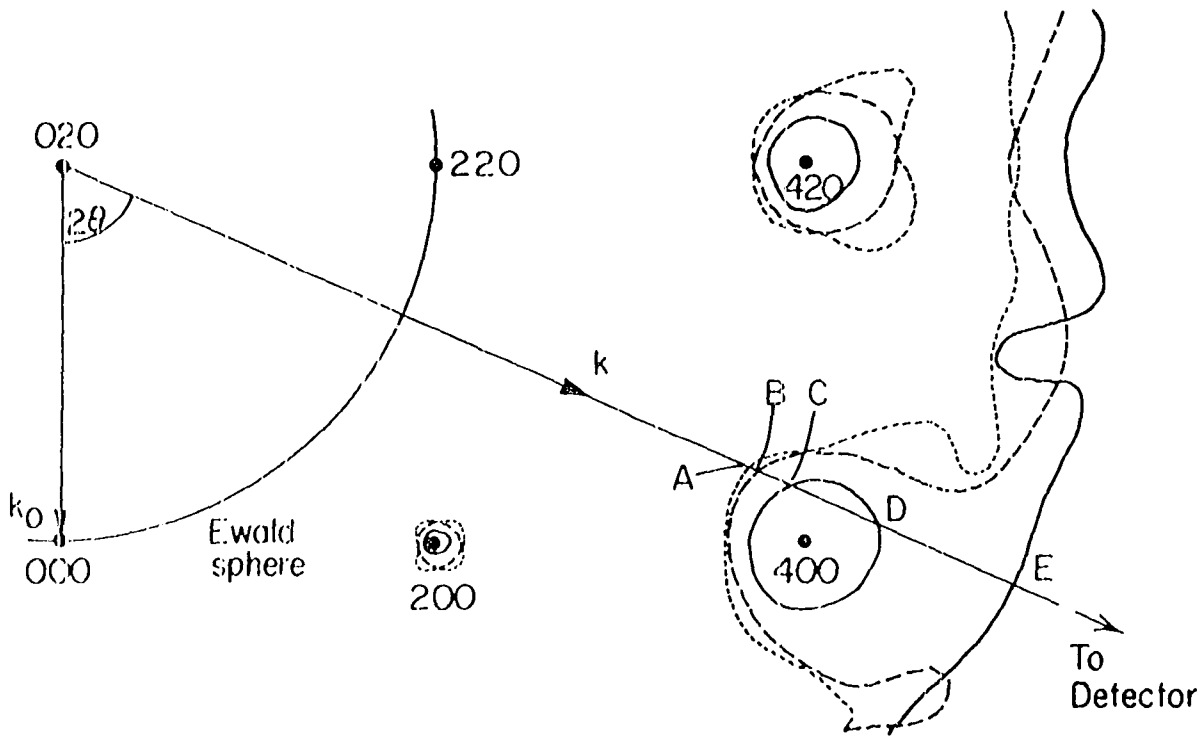

Figure 6.1. Some scattering surfaces for one-phonon processes with neutron energy gain in the [001] zone of aluminum, calculated for 4 A neutrons along the [010] direction (after Ref. 125)

aforementioned system of equations. The measurements of phonon frequencies $\nu_j(\vec{q})$ associated with various intersecting points on the scattering surfaces by varying $\vec{k}_o$ and $\vec{k}'$ would yield the phonon spectrum. The principle instrument for this type of measurements is the triple axis spectrometer.

2. The triple axis spectrometer

A schematic diagram of a triple axis spectrometer (147) is shown in Fig. (6.2). A large single crystal (e.g., beryllium, pyrolitic graphite) X_m is used as a monochromator to Bragg reflect neutrons of a particular wavelength from the reactor spectrum. The wavelength of this monochromatic beam can be varied by relating the glancing angle θ_M and the scattering angle $2\theta_M$ at the monochromator in a 1:2 ratio. The momentum $\vec{k}_o$ of the incident neutrons of energy E_o is then determined by the direction of the beam and the relation

$$E_o = \frac{\hbar^2 k_o^2}{2m_n} = \frac{\hbar^2}{2m_n}\left[\frac{\pi \sin\theta_M}{d_M}\right]^2 \qquad (6.7)$$

Where m_n is the mass of the neutron and d_M is the spacing of the reflecting planes of the monochromating crystal.

The beam is then incident on the sample crystal S set at the angle ψ and is scattered at a scattering angle φ upon an analyzing crystal X_A. The energy analysis of the scattered neutrons is performed by means of the analyzer which is set for Bragg reflecting neutrons of a given energy E' into the detector. Consequently the analyzer has to rotate with the detector in a 1:2 angular relationship (i.e.,

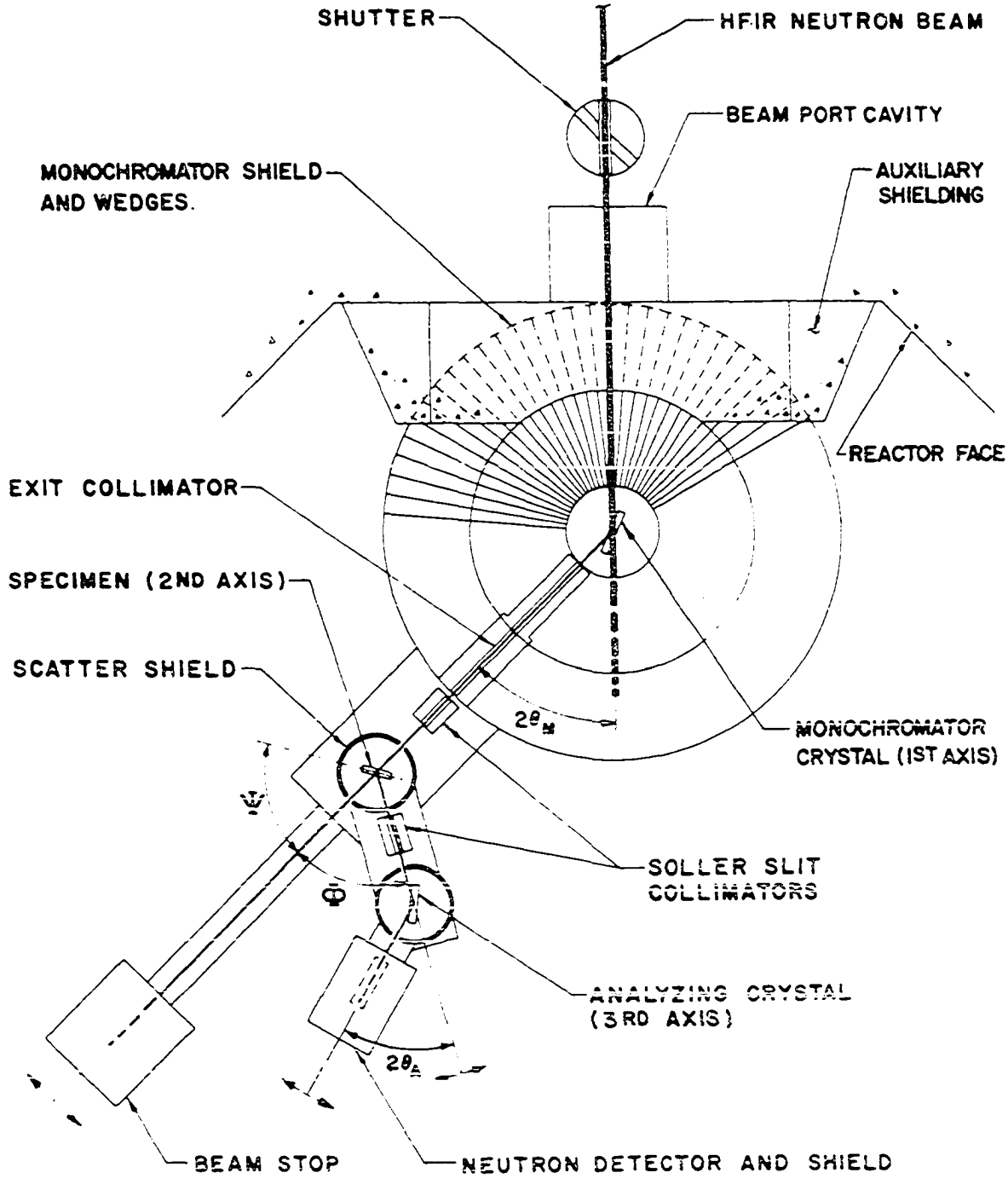

Figure 6.2. Schematic diagram of a typical triple axis spectrometer viewed from above (after Ref. 147)

$\Delta\theta_A = \Delta\theta_{2A} = 1{:}2$). The final momentum of the neutrons $\vec{k}'$ is determined from the angle ϕ and the relation

$$E' = \frac{\hbar^2 k'^2}{2m_n} = \frac{\hbar^2}{2m_n}\left[\frac{\pi \sin\theta_A}{d_A}\right]^2 \qquad (6.8)$$

where θ_A is the glancing angle at the analyzer and d_A is the spacing of the reflecting planes of the analyzing crystal. Therefore both the energy change $E_o - E'$ and momentum transfer vector $\vec{k}_o - \vec{k}'$ of the neutrons can be obtained.

A monitor M is placed between the monochromator and the sample to control the signal counting times so that the number of neutrons incident on the sample during each step in a scan is the same. Collimators consisted of parallel strips of cadmium-plated steel (Soller slits) are inserted along the neutron paths to limit the horizontal divergence of the beams. The calculation of the angle variations, the control of instrumentation and the acquisition of experimental data are performed by an on-line computer.

The technical details of the triple axis spectrometers has been reviewed by Iyengar (149). More recent advancements in spectrometer designs and automation, experimental considerations of reflectivity of the monochromating and analyzing crystals, and methods of dealing with problems such as order contaminations can be found in the article by Dolling (150). A discussion of the relative merits of various instruments used for inelastic neutron scattering experiments has been presented by Brockhouse (151). It was found that the triple

axis spectrometer had many definite advantages in the study of phonon dispersion relations.

3. The constant-Q method

Probably the most widely used method in the determination of phonon dispersion relations using a triple axis spectrometer is the 'constant-Q method'. In this method the scattering vector, $\vec{Q} = \vec{k}_o - \vec{k}'$ is held constant while the energy transfer, $h\nu \frac{\hbar^2}{2m} (k_o^2 - k'^2)$ is varied. The relationships between the neutron wavevectors and the orientation of the sample crystal for the two cases of fixed-k_o and fixed-k' are illustrated in Fig. (6.3). Assuming that the xy plane in the reciprocal lattice space contains the incident and scattered neutron wavevectors $\vec{k}_o$ and $\vec{k}'$, then the crystal orientation (ψ) may be defined by the angle between a selected crystal axis, say y, and the incident neutron beam $\vec{k}_o$. In this case, the x, y components of $\vec{Q}$ can be expressed in terms of the spectrometer angles:

$$Q_x = -|\vec{k}_o| \sin \psi - |\vec{k}'| \sin(\phi \quad \psi) \quad , \tag{6.9}$$

$$Q_z = |\vec{k}_o| \cos \psi - |\vec{k}'| \cos(\phi - \psi) \quad . \tag{6.10}$$

Differentiating these expressions and putting $\delta Q_x = \delta Q_y = 0$ yields the fixed relations between the increments in k_o, k', ϕ and ψ for a constant-Q energy scan. As can be seen in Fig. (6.4a), this results in a vertical scan through the dispersion curve; the peak of the 'neutron groups' (see Fig. 6.4b) recorded in this way define the frequency $\nu_j(\vec{q})$, of the phonon branch with a chosen wavevector $\vec{q}$.

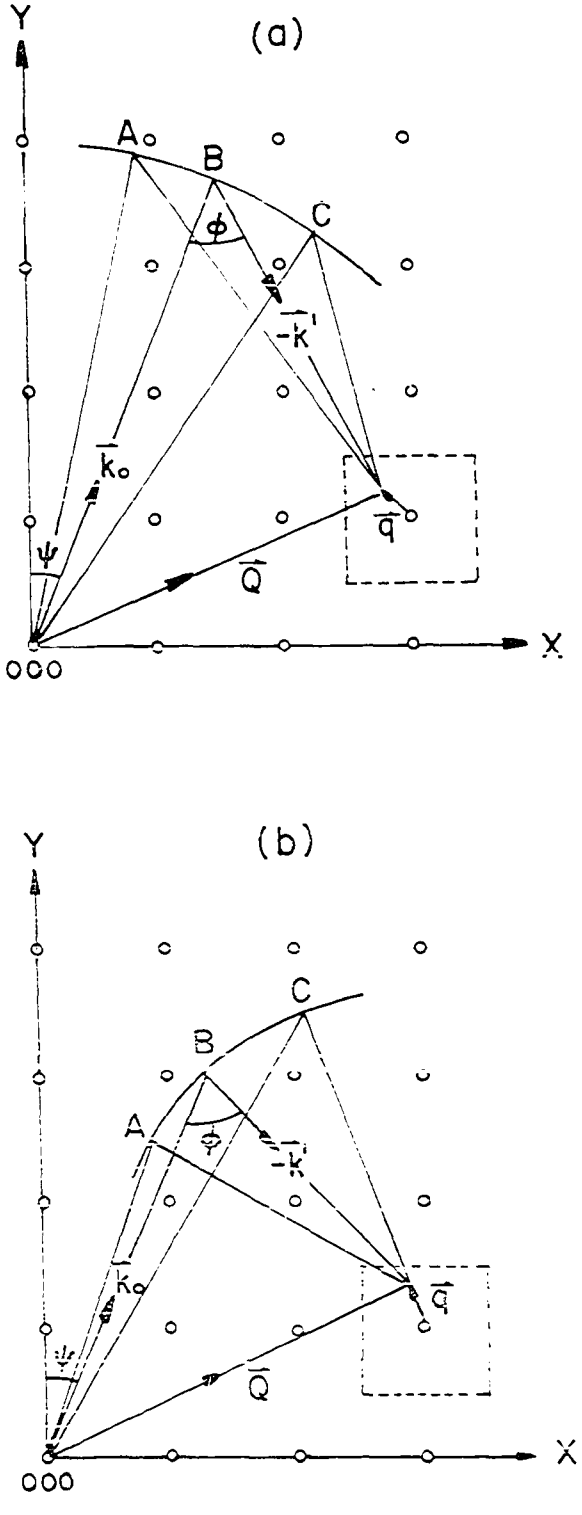

Figure 6.3. Diagrams in reciprocal space showing three possible combinations (A, B and C) of k' and k_o vectors for energy scans at constant Q: (a) fixed incident wavelength, (b) fixed scattered wavelength

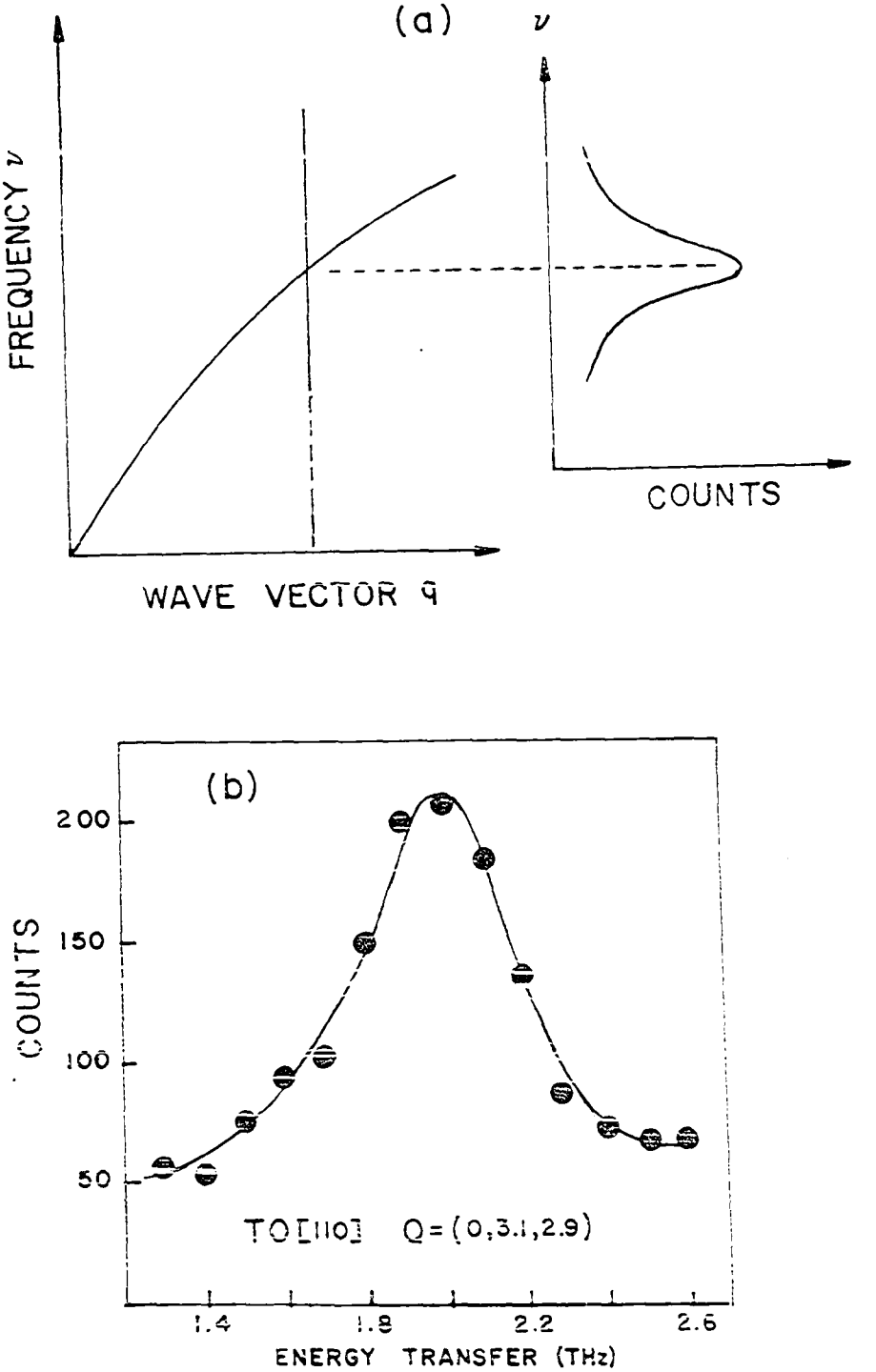

Figure 6.4. (a) A vertical scan through a dispersion curve as produced by the 'constant-Q' method; (b) a neutron group obtained from the scan above yields the phonon frequency of a certain branch at a given wave vector

For most lattice dynamical studies, the phonon dispersion relations are measured along certain $\vec{q}$-directions of high symmetry. Consideration of focusing properties to ensure optimum resolution conditions for the experiment has been presented by Cooper and Nathans (152).

We have briefly discussed the experimental methods in the measurements of phonon dispersion relations. In the following section, we shall present the experimental results in the lattice dynamical study of $CeSn_3$.

B. Experimental Results

The inelastic neutron experiment was performed on a large sample of $CeSn_3$ using the HB-2 triple axis spectrometer at the HFIR of Oak Ridge National Laboratory. Some phonon measurements were also conducted using the Ames Laboratory HB-4 triple axis spectrometer installed at the Oak Ridge Research Reactor (ORR). The sample was a cylinder of 1.3 cm in diameter and about 4 cm in length. Examination of the sample using a double axis neutron diffractometer established the existence of a large single crystal of $CeSn_3$ which occupied the entire cross section of the sample and was approximately 3.2 cm in length. At the end which is not a part of the single crystal a face parallel to the $(1\bar{1}0)$ planes of the single crystal was opened by using a slow speed diamond cutter.

Most of the measurements of phonon dispersion curves were performed with either the [100] axis or the $[1\bar{1}0]$ axis of the crystal in the vertical direction. However, for measurements of phonon frequencies of the Λ_2 mode, the crystal was oriented with its $[11\bar{2}]$

axis vertical. Attempt was also made to detect the Σ_2 phonon branch by alligning the crystal with its [1$\bar{1}$1] axis vertical. All the phonons were measured by the 'constant-Q method' with neutron energy loss and the spectrometer operated in a fixed E' mode. To achieve optimal experimental conditions and to avoid, as much as possible, contaminations due to various spurious processes, standard measurement techniques, such as the application of effective filters, the utilization of different monochromating and analyzing crystals, the selection of various scattered neutron energy etc., have been employed (see Table 6.1). Throughout the experiment the sample was kept either under vacuum or in a helium atmosphere to avoid oxidation of the sample. A majority of the measurements were performed at room temperature. Selected phonon branches were also measured at low temperatures (T between 5 to 15 K) by using either a conventional cryostat or a cryogenic refrigerator installed on the sample table of the spectrometer.

The phonon dispersion curves of $CeSn_3$ at room temperature were measured in three symmetry directions, namely, the [100] Δ, [110] Σ and [111] Λ directions. The measured phonon frequencies and their associated errors, the reciprocal lattice vectors $\vec{\tau}$ at which phonons of certain modes and wavevector $\vec{q}$ were measured and the experimental conditions (monochromator and analyzer settings, scattering neutron energies) are tabulated in Table 6.1. The phonon frequencies were assigned to the modes listed on the left of the table. The assignment of measured phonon frequencies to the phonon modes were determined based on the agreement between the observed frequencies and the neutron

intensities with the calculated ones using a 3NN Born-von Kármán force constant model. Given the maximal information provided by the data, the present assignment represents the best agreement between the theory and experimental observation. Nevertheless, the possibility of a different assignment of phonon modes cannot be eliminated. More data on the lattice dynamics of $LaSn_3$ and detailed comparison between these two materials will provide more information about the assignment of phonon modes.

Table 6.1. Measured phonon frequencies of $CeSn_3$ (T = 295K)

BRANCH	$\vec{q}$	$\vec{\tau}$	ν(THz)	$\pm\Delta\nu$(THz)	M-A-E'(THz)[a]
$LA[100]\Delta_1$	0 0 .1	002	.66	.04	G2-G2-3.6
	0 0 .2	002	1.31	.05	G2-G2-3.6
	0 0-.2	$00\bar{4}$	1.20	.06	B2-G2-8.4
	0 0-.2	$00\bar{4}$	1.15	.05	G2-G2-6.0
	0 0 .25	002	1.62	.05	G2-G2-3.6
	0 0-.3	$00\bar{4}$	1.72	.06	B2-B2-8.4
	0 0-.3	$00\bar{4}$	1.77	.10	G2-G2-6.0
	0 0 .35	002	2.16	.07	G2-G2-3.6
	0 0-.35	$00\bar{4}$	2.02	.08	G2-G2-6.0
$LO_1[110]\Delta_1$	0 0 0	003	1.95	.10	G2-G2-3.6
	0 0 0	$00\bar{3}$	1.92	.08	G2-G2-3.6
	0 0 .1	003	1.95	.05	G2-G2-3.6
	0 0 .1	003	1.96	.07	G4-G4-6.0
	0 0 .1	034	2.07	.06	B1-G4-8.0
	0 0 .1	015	2.10	.12	B1-G4-8.0
	0 0 .1	015	1.95	.06	G4-G4-8.0[b]
	0 0 .1	005	2.02	.08	G4-G4-8.0[b]
	0 0-.1	$00\bar{3}$	1.83	.08	G2-G2-6.0
	0 0 .2	003	1.98	.06	G2-G2-3.6
	0 0 .2	003	1.97	.06	G4-G4-6.0
	0 0 .2	005	2.21	.15	B1-B4-8.0

[a] M-A denotes the monochromator and analyzer settings: G2, pyrolitic graphite (002); G4, pyrolitic graphite (004); B1, beryllium (101); B2, beryllium (002). E' is the scattered neutron energy.

[b] Measurements performed using the Ames Laboratory triple axis spectrometer at the ORR.

Table 6.1. Continued

BRANCH	$\vec{q}$	$\vec{\tau}$	ν(THz)	$\pm\Delta\nu$(THz)	M-A-E'(THz)[a]
	0 0 .2	015	1.90	.15	G4-G4-8.0[b]
	0 0 .2	005	2.09	.10	G4-G4-8.0[b]
	0 0-.2	00$\bar{3}$	1.96	.05	G2-G2-3.6
	0 0-.2	00$\bar{3}$	1.90	.07	G2-G2-3.6
	0 0 .25	003	2.02	.12	G4-G4-6.0
	0 0-.25	00$\bar{3}$	1.98	.06	G2-G2-6.0
	0 0 .3	004	1.98	.06	G4-G4-6.0
	0 0-.3	00$\bar{3}$	2.06	.08	G2-G2-6.0
LO_1 100 Δ_1	0 0-.35	00$\bar{3}$	2.18	.10	G2-G2-6.0
	0 0 .4	002	2.37	.08	G2-G2-3.6
	0 0-.4	004	2.45	.05	G4-G2-3.6
	0 0 .4	004	2.31	.10	G4-G4-6.0
	0 0-.4	006	2.40	.07	B2-B2-8.4
	0 0-.4	003	2.42	.12	G2-G2-6.0
	0 0 .45	002	2.64	.10	G2-G2-3.6
	0 0-.45	004	2.63	.07	G4-G2-3.6
	0 0-.45	005	2.60	.07	G4-G4-6.0
	0 0-.5	003	2.73	.12	G2-G2-3.6
	0 0-.5	00$\bar{5}$	2.80	.09	B2-B2-8.4
	0 0-.5	00$\bar{3}$	2.66	.12	G2-G2-6.0
$LO_3[100]\Delta_1$	0 0 0	003	4.30	.15	G2-G2-3.6
	0 0 0	003	4.27	.15	G4-G4-6.0
	0 0 .1	003	4.21	.10	G2-G2-3.6
	0 0 .2	003	4.11	.10	G2-G2-3.6
	0 0 .2	005	4.14	.10	B1-G4-8.0
	0 0 .3	003	3.85	.12	G2-G2-3.6
	0 0 .3	003	3.81	.08	G4-G2-3.6
	0 0 .35	003	3.64	.10	G4-G2-3.6
	0 0-.4	005	3.54	.10	G4-G4-6.0
	0 0 .45	003	3.47	.15	G4-G4-6.0

Table 6.1. Continued

BRANCH	$\vec{q}$	$\vec{\tau}$	ν(THz)	$\Delta\nu$(THz)	M-A-E'(THz)[a]
$LO_2[100]\Delta_2$	0 0 0	003	3.19	.07	G2-G2-3.6
	0 0 0	330	2.96	.10	G2-G2-6.0
	0 0 .2	015	3.13	.10	B1-G4-8.0
	0 0 .35	015	3.15	.10	B1-64-8.0
$TA[100]\Delta_5$	0 0-.15	220	.69	.03	G2-G2-3.6
	0 0-.15	040	.62	.04	G4-G4-8.0[b]
	0 0-.2	220	.90	.04	G2-G2-3.6
	0 0 .2	$\overline{220}$	.85	.04	B2-B2-8.4
	0 0-.3	220	1.26	.03	G2-G2-3.6
	0 0-.3	220	1.31	.05	G2-G2-6.0
	0 0-.4	220	1.57	.03	G2-G2-3.6
	0 0-.4	220	1.56	.08	B1-G4-10.0
	0 0-.4	220	1.57	.04	B1-G4-6.0
	0 0-.4	220	1.60	.05	G2-G2-6.0
	0 0-.4	220	1.59	.03	G2-G2-3.6
	0 0 .5	220	1.70	.06	G2-G2-3.6
	0 0-.5	220	1.74	.06	G2-G2-6.0
	0 0-.5	110	1.76	.07	G2-G2-3.6
$TO_1(100]\Delta_5$	0 0-.05	221	1.89	.08	G2-G2-3.6
	0 0-.2	221	1.93	.08	G2-G2-3.6
	0 0-.2	330	1.90	.08	G4-G2-6.0
	0 0-.3	221	1.96	.05	G2-G2-3.6
	0 0-.4	221	2.05	.12	G2-G2-3.6
$TO_2[100]\Delta_5$	0 0-.1	221	3.07	.08	G2-G2-3.6
	0 0-.2	221	3.08	.10	G2-G2-3.6
	0 0-.3	221	3.16	.10	G2-G2-3.6
	0 0 .3	330	3.11	.10	G4-G4-6.0
	0 0-.4	221	3.17	.06	G2-G2-3.6
	0 0-.5	221	3.08	.15	G2-G2-3.6

Table 6.1. Continued

BRANCH	$\vec{q}$	$\vec{\tau}$	ν(THz)	$\pm\Delta\nu$(THz)	M-A-E'(THz)[a]
$TO_3[100]\Delta_5$	0 0-.1	330	4.20	.15	B1-G4-10.0
	0 0 .15	330	4.15	.10	G4-G4-6.0
	0 0 .2	330	3.95	.06	G4-G4-6.0
	0 0-.2	050	4.26	.12	B1-G4-8.0
	0 0 .4	050	3.80	.20	B1-B4-10.0
	0 0-.4	220	4.00	.20	G2-G2-3.6

Table 6.1. Continued

BRANCH	$\vec{q}$	$\vec{\tau}$	ν(THz)	$\pm\Delta\nu$(THz)	M-A-E'(THz)[a]
LA[110]Σ_1	.1 .1	220	.92	.05	G2-G2-6.0
	-.1-.1	220	1.02	.05	G2-G2-6.0
	.1 .1 0	220	1.0	.04	G2-G2-3.6
	.15.15 0	220	1.49	.04	G2-G2-3.6
	.15.15 0	220	1.42	.05	G2-G2-6.0
	.15.15 0	220	1.51	.08	G2-G2-3.6
	.2 .2 0	220	1.93	.08	G2-G2-3.6
	-.3-.3 0	330	1.97	.07	G2-G2-3.6
	-.4-.4 0	330	1.91	.06	G2-G2-3.6
	.4 .4 0	220	2.02	.08	G2-G2-3.6
	.4 .4 0	220	1.98	.15	G4-G4-6.0
	-.4-.4 0	330	1.94	.06	B1-G4-6.0
	-.45-.45 0	330	1.86	.12	B1-G4-3.6
	-.45-.45 0	330	1.97	.08	G2-G2-3.6
	-.5-.5 0	330	2.06	.10	G2-G2-3.6
	-.5-.5 0	330	2.00	.20	G4-G4-3.6
	-.5-.5 0	330	2.06	.08	G2-G2-3.6
LO_1[110]Σ_2	.1 .1 0	221	1.97	.10	G2-G2-3.6
	.1 .1 0	221	1.92	.10	G2-G2-3.6
	.2 .2 0	110	2.10	.10	G2-G2-3.6
	.25.25 0	220	2.19	.08	G2-G2-6.0
	.3 .3 0	220	2.58	.15	G2-G2-3.6
	.35.35 0	220	2.80	.15	G2-G2-3.6
	.4 .4 0	220	2.80	.15	G2-G2-3.6

Table 6.1. Continued

BRANCH	$\vec{q}$	$\vec{\tau}$	ν(THz)	$\pm\Delta\nu$(THz)	M-A-E'(THz)[a]
$LO_2[110]\Sigma_1$	.1 .1 0	221	3.10	.10	G2-G2-3.6
	-.1-.1 0	$\bar{3}\bar{3}0$	3.04	.10	B2-G2-6.0
	-.2-.2 0	$\bar{3}\bar{3}0$	3.08	.11	B2-B2-8.4
	.2 .2 0	332	3.14	.17	G2-G2-6.0
	.3 .3 0	330	3.20	.15	G2-G2-3.6
	-.35-.35 0	330	3.15	.15	G2-G2-3.6
	-.4-.4 0	330	3.20	.15	G2-G2-3.6
$LO_3[110]\Sigma_1$	.3 .3 0	221	3.70	.15	G2-G2-3.6
	-.35-.35 0	330	3.82	.10	G2-G2-3.6
	-.35-.35 0	330	3.76	.08	G4-G2-3.6
	.4 .4 0	110	3.98	.08	G2-G2-3.6
	.4 .4 0	330	3.99	.08	G4-G4-6.0
	-.5-.5 0	330	4.15	.08	G2-G2-3.6
	-.5-.5 0	330	4.05	.10	G2-G2-3.6
	.5 .5 0	330	4.15	.20	G4-G4-6.0
$TA[110]\Sigma_3$	-.1-.1 0	$00\bar{2}$	.67	.04	G2-G2-3.6
	-.15-.15 0	$00\bar{2}$	.98	.04	G2-G2-3.6
	-.2-.2 0	$00\bar{4}$	1.20	.05	G2-G2-6.0
	.2 .2 0	002	1.28	.05	G2-G2-3.6
	.2 .2 0	002	1.31	.04	B1-G4-10.0
	.2 .2 0	002	1.28	.05	B1-G4-6.0
	-.25-.25 0	$00\bar{2}$	1.58	.05	G2-G2-3.6
	-.3-.3 0	$00\bar{4}$	1.72	.07	G2-G2-6.0
	.3 .3 0	002	1.80	.04	G2-G2-3.6
	-.35-.35 0	$00\bar{4}$	1.94	.05	G2-G4-6.0
	.35 .35 0	002	2.11	.05	B1-G4-3.6
	-.4-.4 0	$00\bar{4}$	2.16	.05	G2-G2-6.0

Table 6.1. Continued

BRANCH	$\vec{q}$	$\vec{\tau}$	ν(THz)	$\pm\Delta\nu$(THz)	M-A-E'(THz)[a]
	.45 .45 0	$00\bar{2}$	2.17	.05	G2-G2-3.6
	-.45-.45 0	$00\bar{3}$	2.24	.04	G2-G2-3.6
	.45 .45 0	003	2.35	.08	G4-G2-3.6
	-.5 -.5 0	$00\bar{3}$	2.26	.05	G2-G2-3.6
	.5 .5 0	002	2.25	.12	G2-G2-3.6
$TO_1[110]\Sigma_3$	.1 .1 0	003	1.92	.07	G2-G2-3.6
	.2 .2 0	003	2.11	.06	G4-G2-3.6
	.3 .3 0	003	2.20	.10	G2-G2-3.6
	-.3 -.3 0	$00\bar{3}$	2.17	.08	G2-G2-3.6
	.45 .45 0	003	2.41	.10	G4-G4-6.0
	.45 .45 0	003	2.50	.08	B1-G4-6.0
	.5 .5 0	003	2 40	.15	G2-G2-3.6
$TO_3[110]\Sigma_3$	.1 .1 0	$00\bar{5}$	4.08	.16	G2-G2-6.0
	-.2 -.2 0	003	4.02	.15	G2-G2-3.6
	-.2 -.2 0	003	4.10	.15	G4-G4-6.0
	-.3 -.3 0	003	3.78	.10	G2-G2-3.6
	.3 .3 0	003	3.76	.10	G4-G2-3.6
	-.35-.35 0	003	3.58	.06	G4-G2-3.6
	-.4 -.4 0	003	3.33	.05	G2-G2-3.6
	-.4 -.4 0	003	3.37	.05	G4-G2-3.6
	-.45-.45 0	003	3.20	.05	G4-G2-6.0
$TA[110]\Sigma_4$	0 .1 -.1	022	.50	.03	B1-G4-8.0
	0 .25-.25	022	1.04	.05	B1-G4-8.0
	0 .4 -.4	022	1.22	.08	B1-G4-8.0
	0 .5 -.5	022	1.29	.10	B1-G4-8.0

Table 6.1. Continued

BRANCH	$\vec{q}$	$\vec{\tau}$	ν(THz)	$\pm\Delta\nu$(THz)	M-A-E'(THz)[a]
$TO_1[110]\Sigma_4$	0 .1 -.1	033	2.09	.05	B1-G4-8.0
	0 .3 -.3	033	2.01	.12	B1-G4-8.0
	0-.4 .4	033	1.82	.10	B1-G4-8.0
	0 .5 -.5	022	1.80	.10	B1-G4-8.0
	0 .5 .5	032	1.78	.10	B1-G4-8.0
$TO_2[110]\Sigma_4$	0 .1 -.1	033	3.17	.08	B1-G4-8.0
	0-.3 .3	033	3.05	.10	B1-G4-8.0
	0-.4 .4	033	2.80	.10	B1-G4-8.0
	0 .5 -.5	033	2.78	.08	B1-G4-8.0
	0-.5 .5	033	2.70	.10	B1-G4-8.0
$TO_3(111]\Sigma_4$	0-.1 .1	033	4.20	.15	B1-G4-8.0
	0-.2 .2	033	4.20	.15	G4-G4-8.0[b]

Table 6.1. Continued

BRANCH	$\vec{q}$	$\vec{\tau}$	ν(THz)	$\pm\Delta\nu$(THz)	M-A-E'(THz)[a]
$LA[111]\Lambda_1$	-.05-.05-.05	222	.685	.05	B1-G4-3.6
	-.1 -.1 -.1	222	1.38	.10	G2-G2-3.6
	-.1 -.1 -.1	222	1.37	.06	G4-G2-3.6
	-.1 -.1 -.1	222	1.43	.07	B1-G4-3.6
	.13 .13 .13	221	1.66	.06	G4-G2-3.6
	-.15-.15-.15	222	1.96	.06	G4-G2-3.6
	.15 .15-.15	$22\bar{2}$	1.88	.07	G2-G2-3.6
	.15 .15-.15	$22\bar{2}$	1.88	.10	G2-G2-6.0
	-.2 -.2 -.2	$\bar{1}\bar{1}\bar{3}$	2.34	.08	B2-B2-8.4
	.2 .2 .2	$22\bar{2}$	2.38	.12	G2-G2-6.0
	-.3 -.3 -.3	223	2.48	.04	G2-G2-3.6
	-.3 -.3 -.3	223	2.61	.04	G4-G4-6.0
	-.3 -.3 -.3	223	2.48	.10	B1-G4-10.0
	-.35-.35-.35	223	2.12	.10	G4-G2-3.6
	-.35-.35-.35	223	2.01	.08	G4-G2-6.0
	-.35-.35-.35	223	2.08	.06	G4-G4-6.0
$LO_1[111]\Lambda_1$	.05 .05 .05	222	2.09	.09	G2-G2-3.6
	.05 .05 .05	221	2.01	.07	G2-G2-3.6
	.05 .05 .05	221	2.00	.04	G4-G2-3.6
	.1 .1 -.1	$22\bar{2}$	2.23	.06	G2-G2-3.6
	.25 .25-.25	$22\bar{2}$	2.84	.10	G2-G2-6.0
	.3 .3 -.3	$22\bar{3}$	2.87	.12	G2-G2-6.0
	-.4 -.4 -.4	222	2.93	.10	G2-G2-3.6
	-.4 -.4 -.4	223	2.82	.10	G2-G2-3.6
	.4 .4 .4	222	3.05	.15	G4-G4-6.0
	.4 .4 -.4	223	3.06	.05	B1-G4-6.0
	.4 .4 .4	222	3.14	.10	B1-G4-6.0
	.5 .5 .5	222	3.18	.10	B1-G4-6.0

Table 6.1. Continued

BRANCH	$\vec{q}$	$\vec{\tau}$	ν(THz)	±Δν(THz)	M-A-E'(THz)[a]
$LO_3[111]\Lambda_1$	.1 .1 .1	223	4.17	.10	G4-G2-6.0
	-.1 .1 -.1	334	4.18	.09	B1-G4-10.0
	-.15-.15-.15	223	3.91	.15	G4-G2-3.6
	.15 .15-.15	334	3.94	.20	B1-G4-10.0
	.35 .35 .35	222	3.85	.20	G4-G2-3.6
	.35 .35-.35	$11\bar{3}$	3.82	.13	G2-G2-3.6
	.4 .4 .4	222	4.22	.15	G4-G4-6.0
	.4 .4 -.4	$22\bar{4}$	4.12	.13	G2-G2-3.6
	-.5 -.5 -.5	$\bar{2}\bar{2}\bar{2}$	4.40	.12	B2-B2-8.4
	.5 .5 -.5	$22\bar{2}$	4.30	.15	G2-G2-6.0
$TO_2[111]\Lambda_2$	.1 .1 .1	$3\bar{3}0$	3.10	.12	B1-G4-6.0
	-.1 -.1 -.1	$3\bar{3}0$	3.16	.10	B1-G4-6.0
	.2 .2 .2	$3\bar{3}0$	2.93	.10	B1-G4-6.0
	.3 .3 .3	$3\bar{3}0$	2.97	.12	B1-G4-6.0
	-.3 -.3 -.3	$3\bar{3}0$	3.11	.12	B1-G4-6.0
	-.4 -.4 -.4	$3\bar{3}0$	2.75	.15	B1-G4-6.0
$TA[111]\Lambda_3$	.1 .1 -.1	111	.65	.03	G2-G2-3.6
	.1 .1 -.1	111	.65	.03	G4-G2-3.6
	.1 .1 -.1	111	.63	.02	B1-G4-3.6
	-.1 -.1 -.1	$2\bar{2}0$	.69	.04	B1-G4-6.0
	.15 .15-.15	111	.98	.05	G2-G2-3.6
	.15 .15-.15	111	.99	.03	G4-G2-3.6
	.2 .2 -.2	221	1.10	.07	G2-G2-3.6
	.2 .2 -.2	221	1.15	.12	G4-G2-3.6
	.2 .2 -.2	222	1.11	.08	G4-G4-6.0
	.25 .25-.25	222	1.26	.08	G4-G4-6.0
	-.3 -.3 -.3	223	1.22	.10	G4-G4-6.0
	-.3 -.3 -.3	223	1.15	.05	G4-G2-6.0

Table 6.1. Continued

BRANCH	$\vec{q}$	$\vec{\tau}$	ν(THz)	$\pm\Delta\nu$(THz)	M-A-E'(THz)[a]
TA [111] Λ_3	-.3 -.3 -.3	223	1.22	.10	G4-G4-6.0
	-.3 -.3 -.3	223	1.15	.05	G4-G2-6.0
	-.35-.35-.35	223	1.1	.05	G4-G2-6.0
	-.35-.35-.35	223	1.11	.07	G4-G4-6.0
	-.35-.35-.35	223	1.10	.12	B1-G4-10.0
	-.35-.35 .35	223	1.22	.05	B1-G4-6.0
	-.4 -.4 .4	222	1.00	.04	G2-G2-3.6
	-.4 -.4 -.4	223	.94	.04	G2-G2-3.6
	-.4 -.4 -.4	223	.94	.04	G4-G2-3.6
	-.4 -.4 .4	222	.99	.05	G4-G2-3.6
	-.4 -.4 -.4	223	.93	.05	G4-G2-6.0
	-.4 -.4 -.4	223	.95	.05	G4-G4-6.0
	-.4 -.4 -.4	223	.91	.08	B1-G4-10.0
	-.4 -.4 .4	222	1.02	.10	B1-G4-10.0
	-.4 -.4 -.4	222	.95	.06	B1-G4-3.6
	-.4 -.4 .4	222	.99	.04	B1-G4-3.6
	-.45-.45-.45	223	.72	.08	G4-G2-3.6
	-.45-.45-.45	223	.69	.06	G4-G2-6.0
	-.45-.45 .45	222	.74	.05	G4-G2-6.0
	-.45-.45-.45	223	.71	.04	B1-G4-3.6
	-.5 -.5 .5	222	.44	.05	G4-G2-3.6
	-.5 -.5 .5	222	.45	.04	B1-G4-3.6
TO_1 [111] Λ_3	-.1 -.1 .1	221	2.12	.10	G2-G2-3.6
	.1 .1 -.1	221	2.05	.05	G2-G2-3.6
	.1 .1 -.1	334	2.00	.10	B1-G4-10.0
	.1 .1 -.1	223	2.12	.10	B1-G4-6.0
	.1 .1 -.1	223	2.07	.06	B1-G4-6.0
	.1 .1 .1	330	2.04	.06	B1-G4-6.0

Table 6.1. Continued

BRANCH	$\vec{q}$	$\vec{\tau}$	ν(THz)	$\pm\Delta\nu$(THz)	M-A-E'(THz)[a]
$TO_1[111]\Lambda_3$	.15 .13 .15	$3\bar{3}3$	2.10	.15	B1-G4-10.0
	-.15-.15-.15	$3\bar{3}0$	2.17	.05	B1-G4-10.0
	.2 .2 .2	$3\bar{3}0$	2.06	.10	B1-G4-10.0
	.3 .3 -.3	221	1.60	.20	G2-G2-3.6
	.3 .3 .3	$3\bar{3}0$	1.75	.10	B1-G4-10.0
	.35 .35 .35	$3\bar{3}0$	1.70	.18	B1-G4-10.0
	.4 .4 -.4	111	1.53	.10	G2-G2-3.6
	.4 .4 -.4	221	1.58	.10	G2-G2-3.6
	.45 .45 .45	$3\bar{3}0$	1.54	.15	B1-G4-10.0
	-.5 -.5 -.5	221	1.40	.08	G2-G2-3.6
	.5 .5 .5	$3\bar{3}0$	1.50	.20	B1-G4-10.0
$LO_2[111]\Lambda_3$	.1 .1 .1	221	3.09	.07	G2-G2-3.6
	.1 .1 -.1	$22\bar{3}$	2.93	.14	G2-G2-6.0
	.2 .2 .2	221	3.11	.08	G2-G2-3.6
	.25 .25 .25	222	3.22	.08	G4-G2-3.6
	.25 .25-.25	223	3.22	.08	B1-G4-6.0
	-.3 -.3 -.3	222	3.10	.10	G2-G2-3.6
	-.3 -.3 -.3	223	3.00	.08	G2-G2-3.6
	-.3 -.3 -.3	222	3.03	.10	G4-G2-3.6
	-.4 -.4 -.4	222	2.93	.10	G2-G2-3.6
	-.4 -.4 -.4	223	2.82	.10	G2-G2-3.6
	.4 .4 .4	222	3.05	.15	G4-G4-6.0
	.45 .45-.45	$22\bar{2}$	2.70	.17	G2-G2-6.0
	-.1 -.1 .1	$\bar{2}2\bar{3}$	4.18	.15	B2-B2-8.4
	.25 .25-.25	$22\bar{3}$	4.26	.15	G4-G4-6.0
	-.2 -.2 .2	$\bar{2}2\bar{3}$	4.18	.09	B2-B2-8.4
	-.3 -.3 .3	$\bar{2}2\bar{3}$	4.24	.18	B2-B2-8.4
	.4 .4 -.4	223	4.35	.12	G4-G4-6.0
	-.4 -.4 -.4	$22\bar{3}$	4.22	.13	G2-G2-6.0
	-.5 -.5 -.5	$11\bar{3}$	4.12	.08	G2-G2-3.6

VII. ANALYSIS AND DISCUSSION OF THE EXPERIMENTAL RESULTS ON THE LATTICE DYNAMICS OF $CeSn_3$

A. Qualitative Discussion - Phonon Anomalies

The experimentally measured dispersion curves of $CeSn_3$ along the [100], [110] and [111] symmetry directions are plotted in Fig. 7.1. The most spectacular aspects of the dispersion curves are in the [111] direction where anomalously low frequency modes were observed close to the zone boundary. To verify that these features are indeed anomalous, we performed a systematic experimental study of the dispersion curves of $LaSn_3$. In the absence of any specific effects due to the mixed valent character of $CeSn_3$, one would expect identical dispersion curves for these two compounds (153), since La and Ce have approximately equal masses and the two compounds have similar electronic structures (La, of course, unlike Ce, has no 4f electrons). A comparison of the dispersion curves of these two compounds is given in Fig. 7.2. In this figure, the solid lines and dashed lines represent respectively the measured longitudinal and transverse branches for $LaSn_3$, the solid circles and empty circles denote respectively the measured longitudinal and transverse phonon frequencies of $CeSn_3$. As can be seen, we did not observe any sizable difference in the phonon frequencies between the $LaSn_3$ and $CeSn_3$ data along the [100] and [110] directions. Also, along the [111] direction, the phonon frequencies of the upper branches of these materials agree quite well. On the other hand, the low frequency acoustic Λ_1 and Λ_3 modes of $CeSn_3$ near the zone boundary were not

Figure 7.1. Phonon dispersion curves of $CeSn_3$ at room temperature along the [100], [110], and [111] directions. The solid and the dashed lines are, respectively, the calculated longitudinal and transverse branches based on a 3NN Born-von Kármán model. The solid and empty circles are, respectively, the experimentally measured phonon frequencies of the longitudinal and transverse modes. Notice the very low frequency of the acoustic Λ_1 and Λ_3 modes at the zone boundary in the [111] direction. These anomalies in the dispersion curves are due to the mixed-valent character of this compound (see text)

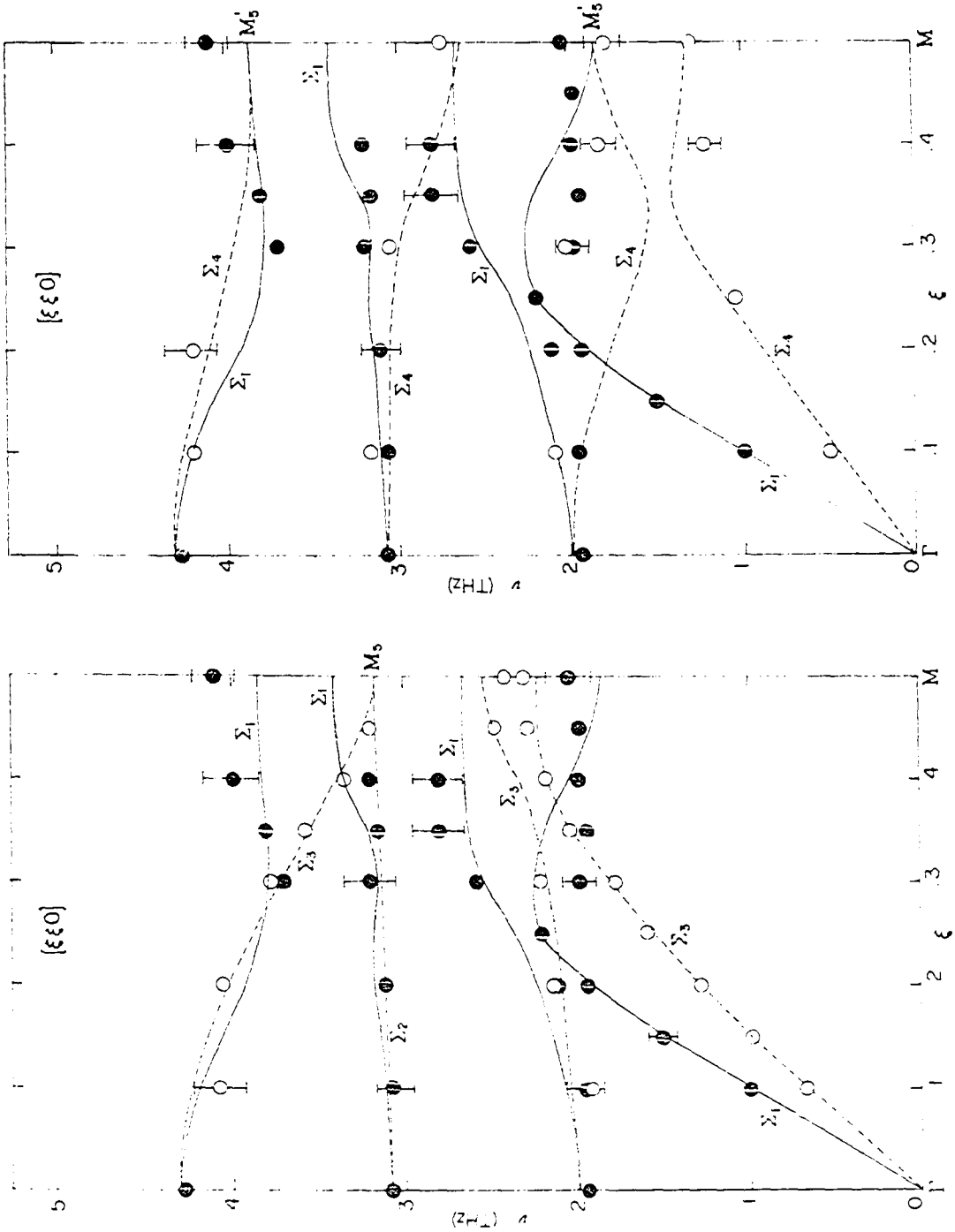
[ξξ0]
Γ
M
M5'
M5
Σ1
Σ2
Σ3
Σ4
ν (THz)
ξ

[ξξξ]
[00ξ]
ν (THz)
Γ
R
X
Λ1
Λ3
Λ2
Δ1
Δ5
Δ2

Figure 7.2. Comparison of phonon dispersion curves of $CeSn_3$ and $LaSn_3$. The solid lines and dashed lines represent, respectively, the measured longitudinal and transverse branches for $LaSn_3$; the solid circles and empty circles denoted, respectively, the measured longitudinal and transverse phonon frequencies of $CeSn_3$. Notice that the low frequency acoustic Λ_1 and Λ_3 modes of $CeSn_3$ near the zone boundary were not observed in $LaSn_3$. The phonon anomalies observed in $CeSn_3$ can be understood qualitatively as a result of the $4f \leftrightarrow 5d$ electronic transitions induced by the nuclear motion in these phonon modes (see text). On the other hand, the rather large differences between the phonon frequencies of these two compounds in the first optical branches near the zone center are believed to be related to the fact that $LaSn_3$ is a superconductor with relatively high T_c (see text)

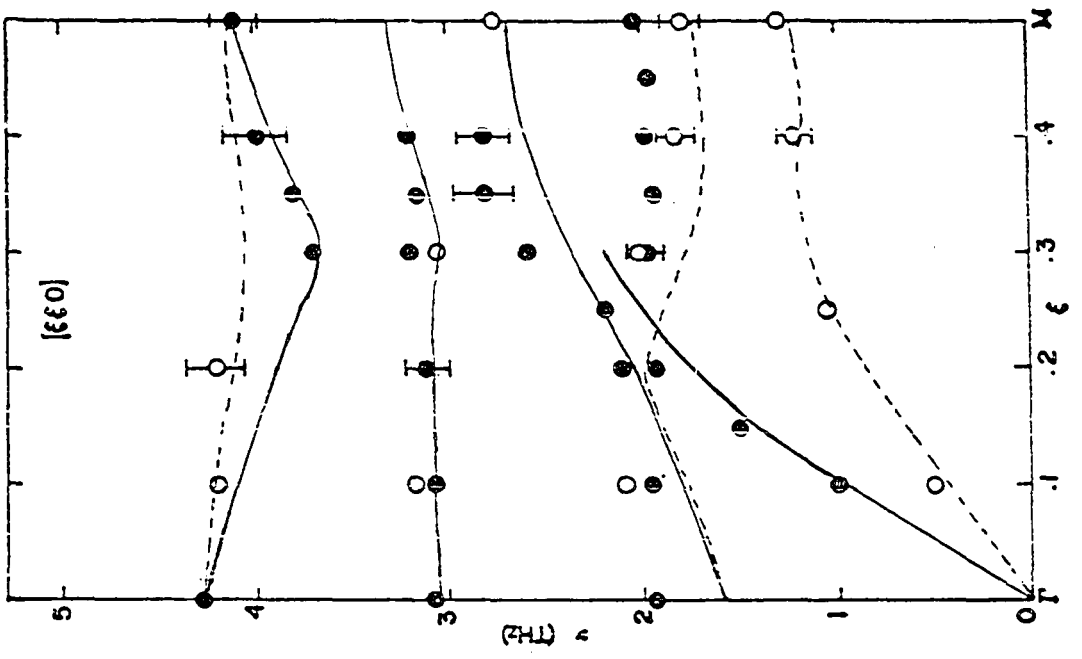
[033]
[220]
ν (THz)
ζ
0
1
2
3
4
5
.1
.2
.3
.4

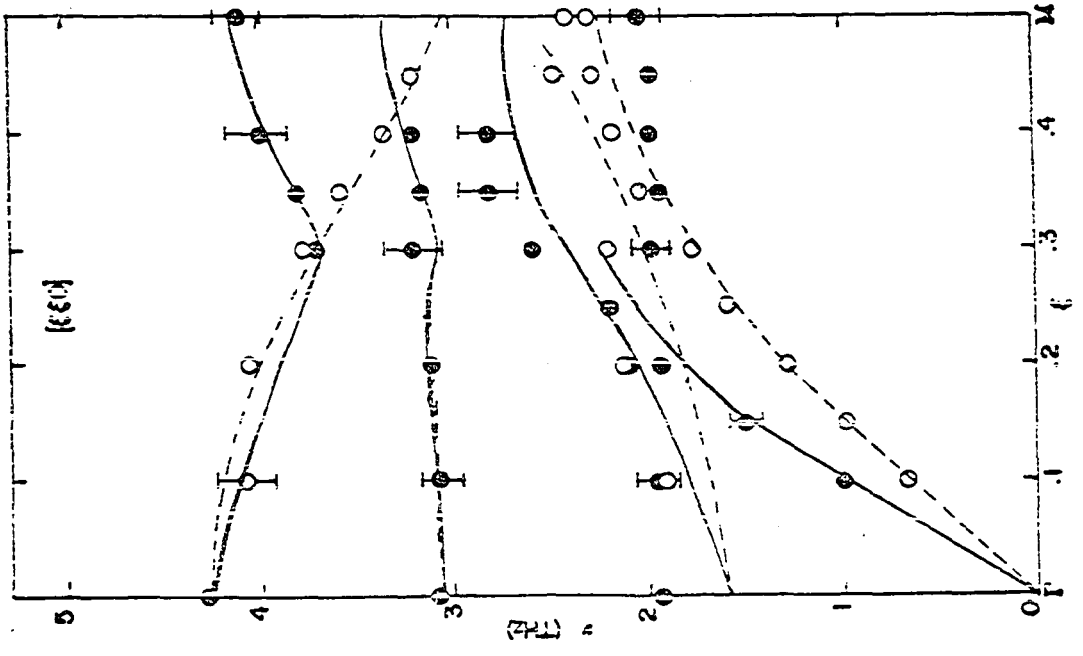
[133]
[311]
ν (THz)
ζ
0
1
2
3
4
5
.1
.2
.3
.4

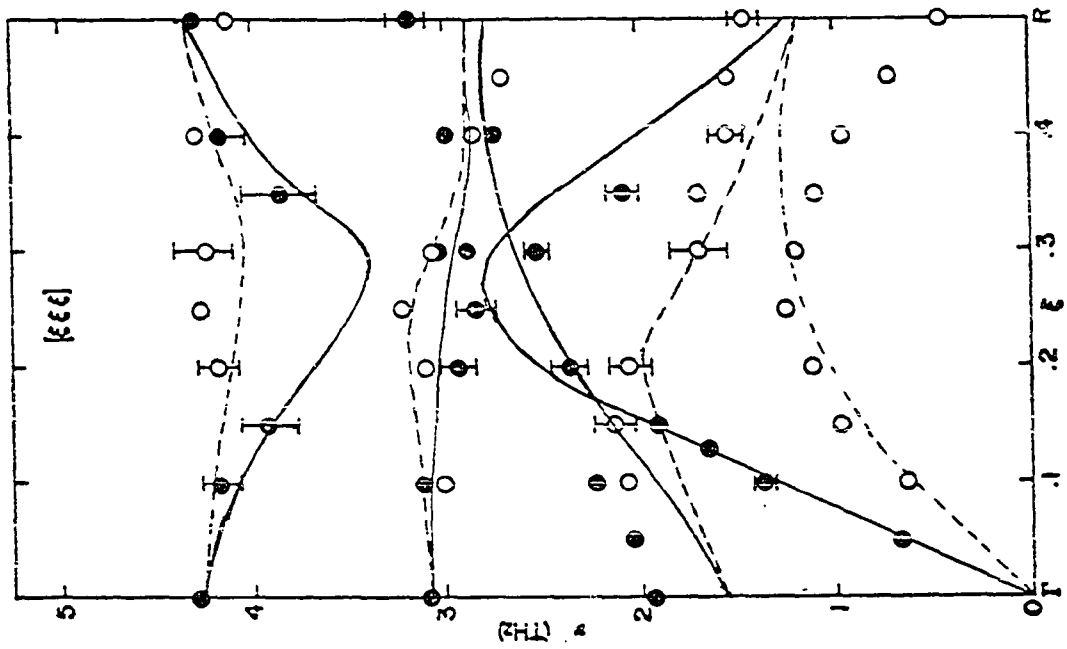
[ξξξ]
ν (THz)
ξ
R

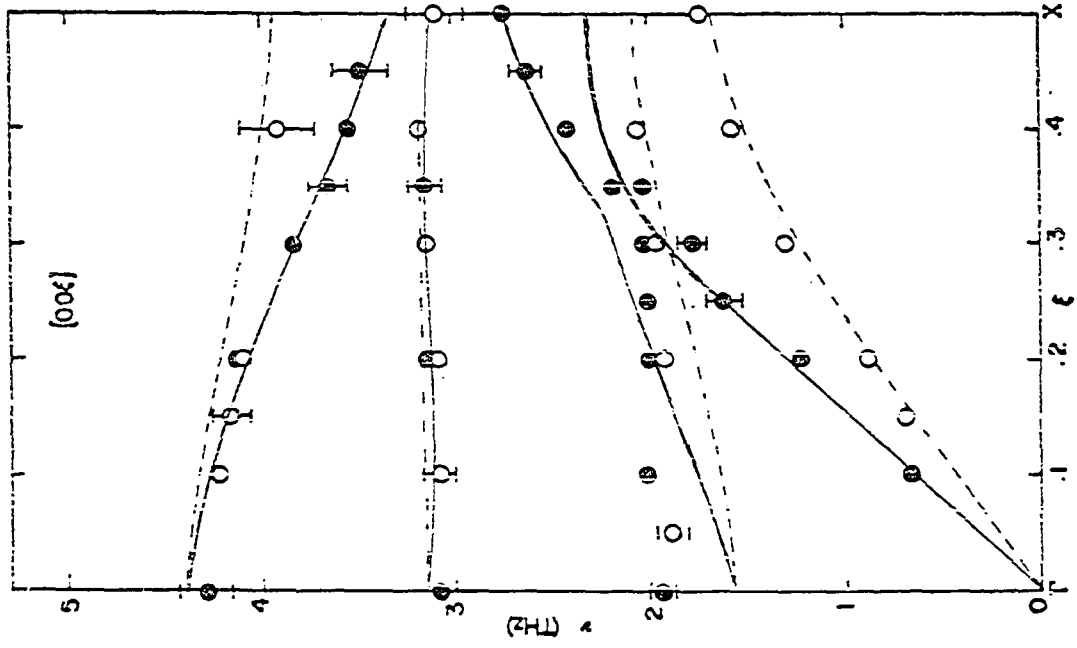
[00ξ]
ν (THz)
ξ
X

observed in $LaSn_3$. Thus, the anomalies observed in the dispersion curves of $CeSn_3$ are characteristic of this compound.

The origin of these anomalies can be understood, at least qualitatively, by considering the 4f ↔ 5d electronic transitions induced by the nuclear motion associated with these anomalous modes. Since only phonon modes which involve a volume change are expected to be strongly affected by valence fluctuation, we examine the relative motion of the atoms in the longitudinal modes at the zone boundary in various directions. As shown in Fig. 7.3, along the [100] direction, the Ce atoms denoted by the solid circles and the Sn atoms, the open circles, are stationary. Along the [110] direction, both the Ce and Sn atoms are moving in phase. Thus in both [100] and [110] symmetry directions no significant effects due to the mixed valent character of $CeSn_3$ are expected at the zone boundary. On the other hand, along the [111] direction, the neighboring Ce and Sn atoms are moving out of phase; consequently, the atomic distance between neighboring atoms are modulated by this vibration mode. Therefore, we expect that this type of motion along the [111] direction will favor the 4f ↔ 5d electronic transitions and consequently strong effects on the phonon frequencies. Such a consideration (154-156) of the phonon-induced 5d ↔ 4f transitions has also been applied to explain the phonon anomalies in another mixed valence system $Sm_{.75}Y_{.25}S$ observed by Mook and Nicklow (47). Thus, the inelastic neutron experimental results show that the electron-phonon coupling in these systems is quite significant and any fundamental

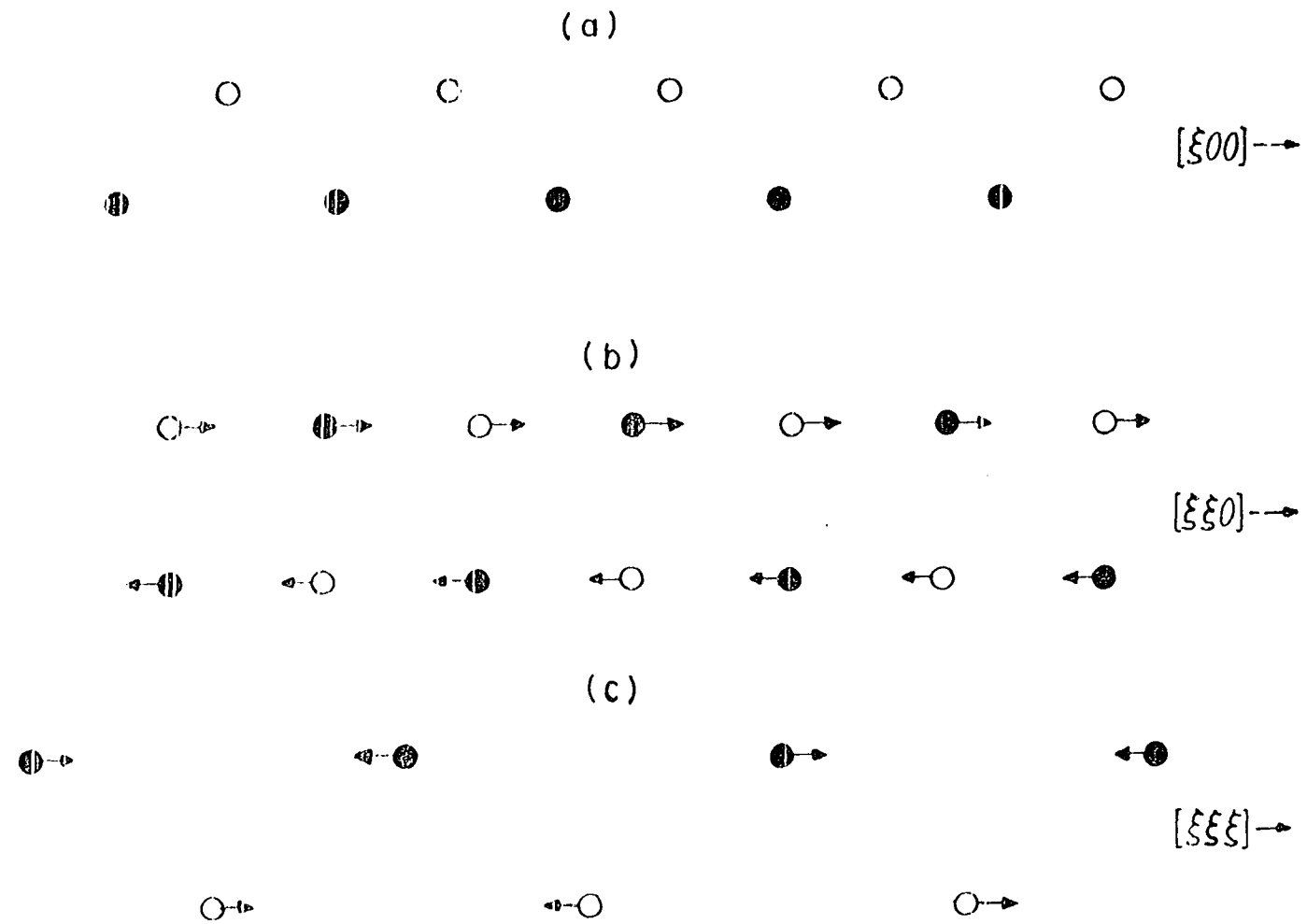

Figure 7.3. The relative motion of the atoms in the longitudinal modes at the zone boundary in the [100], [110] ard [111] directions

theory of these materials should consider the strong interaction between the electrons and the lattice.

Finally, we should point out another significant difference between the dispersion curves of $LaSn_3$ and $CeSn_3$: the frequency of the first zone center optical mode of $LaSn_3$ is considerably lower than that of the corresponding mode of $CeSn_3$ (see Fig. 7.2). It is rather unlikely that this anomaly is due to mixed valence effects since this mode corresponds to the neighboring atoms moving in phase with each other. On the other hand, it is quite possible that this anomaly is characteristic of the lattice dynamics of $LaSn_3$, since this compound is a superconductor with relatively high T_c (T_c = 6.42K) (157). Additional experimental and theoretical studies of $LaSn_3$ may provide more insight into the origin of this anomaly. Specifically, experiments are being planned to assess any temperature dependence of this mode; this type of experiment was successful in identifying the origin of the anomalies observed in the dispersion curves of the superconducting elements Zr, Ti and Hf (158-162).

B. Dispersion Curves Fitting

A complete quantitative analysis of the results presented here is not presently possible because of the lack of a general theory of the lattice dynamics of the mixed valence systems. However, the measured dispersion curves contain valuable information about the thermophysical properties of the system and this information can be obtained quite independently of any specific theoretical models. First, one fits the measured dispersion curves to a Born-von Kármán force constant model and

then one uses the model to obtain the phonon density of states and other more general average properties determined by the phonon spectrum of the solid.

The measured phonon frequencies were fitted to a Born-von Kármán model using a nonlinear least square fitting procedure (133). The procedure minimized the chi-squared (χ^2) function defined by

$$\chi^2 = \frac{1}{N_o - N_v + 1} \sum_{1}^{N_o} \left(\frac{\nu_{obs}^2 - \nu_{calc}^2}{2\nu_{obs}\Delta\nu_{obs}} \right)^2 \qquad (7.1)$$

where N_o is the number of observed frequencies, N_v is the number of adjustable parameters, ν_{calc} are the frequencies calculated by the model and ν_{obs} are the observed frequencies with associated errors $\Delta\nu_{obs}$. It is well-known that multiple minima in the χ^2 function in a nonlinear least-squares fitting are possible. Therefore, a computer program was developed to produce random points in the N_v by N_v parameter space using the irrational vector sampling method. After comparing the χ^2 for over 10,000 points generated in the parameter space, ten parameter sets corresponding to the smallest ten χ^2 values were used as initial sets in the nonlinear squares analysis.

Based on the assignment of phonon branches given in Table 6.1, a total of 149 independent data points (see Table 7.1) were available for the fitting. Initially, the data were fitted to a 2NN Born-von Kármán model which contained ten adjustable parameters. A fair agreement between the experiment and theory was attained with a resulting χ^2 of 3.15. A substantial improvement in the fitting was achieved by

Table 7.1. Assignment of phonon frequencies to various branches of $CeSn_3$

BRANCH	q	$\nu \pm \Delta\nu$(THz)	BRANCH	q	$\nu \pm \Delta\nu$(THz)
$LA[100]\Delta_1$	.1	.66 ±.05	$TO_1[100]\Delta_5$	.05	1.89 ±.08
	.2	1.22 ±.05		.2	1.92 ±.06
	.25	1.62 ±.10		.3	1.96 ±.05
	.3	1.77 ±.07		.4	2.05 ±.12
	.35	2.02 ±.08	$TO_2[100]\Delta_5$	.1	3.07 ±.08
$LO_1[100]\Delta_1$	.0	1.94 ±.06		.2	3.08 ±.10
	.1	2.01 ±.05		.3	3.13 ±.08
	.2	2.00 ±.05		.4	3.17 ±.06
	.25	2.00 ±.07		.5	3.08 ±.15
	.3	2.02 ±.08	$TO_3[100]\Delta_5$	.1	4.20 ±.15
	.35	2.17 ±.08		.15	4.15 ±.10
	.4	2.41 ±.07		.2	4.10 ±.15
	.45	2.62 ±.07		.4	3.90 ±.20
	.5	2.73 ±.11	$LA[110]\Sigma_1$	.1	1.0 ±.05
$LO_3[100]\Delta_1$	.0	4.28 ±.15		.15	1.50 ±.08
	.1	4.21 ±.10		.2	1.93 ±.08
	.2	4.12 ±.10		.3	1.97 ±.09
	.3	3.83 ±.10		.35	1.93 ±.10
	.35	3.64 ±.10		.4	1.97 ±.08
	.4	3.54 ±.10		.45	1.97 ±.10
	.45	3.47 ±.15		.5	2.03 ±.12
$LO_2[100]\Delta_2$	.0	3.08 ±.10	$LO_1[110]\Sigma_1$	.1	1.95 ±.10
	.2	3.13 ±.08		.2	2.10 ±.10
	.35	3.14 ±.08		.25	2.19 ±.08
$TA[100]\Delta_5$	.15	.69 ±.03		.3	2.58 ±.15
	.2	.88 ±.04		.35	2.8 ±.15
	.3	1.29 ±.04		.4	2.8 ±.15
	.4	1.57 ±.03	$LO_2[110]\Sigma_1$	.1	3.07 ±.10
	.5	1.72 ±.06		.2	3.11 ±.12

Table 7.1. Continued

BRANCH	q	$\nu\pm\Delta\nu$(THz)	BRANCH	q	$\nu\pm\Delta\nu$(THz)
	.3	3.20 ±.15	$TA[110]\Sigma_4$	.1	.50 ±.03
	.35	3.15 ±.15		.25	1.04 ±.05
	.4	3.20 ±.15		.4	1.22 ±.08
				.5	1.29 ±.10
$LO_3[110]\Sigma_1$	.3	3.70 ±.15			
	.35	3.80 ±.12	$TO_1[110]\Sigma_4$	.1	2.09 ±.05
	.4	3.99 ±.08		.3	2.01 ±.15
	.5	4.10 ±.10		.4	1.82 ±.10
				.5	1.79 ±.10
$TA[110]\Sigma_3$	.1	.67 ±.04			
	.15	.98 ±.04	$TO_2[110]\Sigma_4$	.1	3.17 ±.08
	.2	1.27 ±.05		.3	3.05 ±.10
	.25	1.58 ±.05		.4	2.80 ±.10
	.3	1.76 ±.05		.5	2.74 ±.10
	.35	2.03 ±.07			
	.4	2.16 ±.10	$TO_3[110]\Sigma_4$	.1	4.20 ±.15
	.45	2.27 ±.10		.2	4.20 ±.15
	.5	2.29 ±.12			
			$LA[111]\Lambda_1$	.05	.685±.05
$TO_1[110]\Sigma_3$	.1	1.92 ±.07		.1	1.37 ±.06
	.2	2.11 ±.06		.13	1.66 ±.06
	.3	2.2 ±.10		.15	1.91 ±.08
	.45	2.47 ±.12		.2	2.36 ±.10
	.5	2.40 ±.15		.3	2.52 ±.05
				.35	2.08 ±.08
$TO_3[110]\Sigma_3$	.1	4.08 ±.16			
	.2	4.06 ±.10	$LO_1[111]\Lambda_1$	.05	2.03 ±.05
	.3	3.77 ±.08		.1	2.23 ±.06
	.35	3.58 ±.06		.25	2.84 ±.10
	.4	3.35 ±.05		.3	2.87 ±.12
	.45	3.20 ±.05		.4	2.99 ±.08
				.5	3.18 ±.10

Table 7.1. Continued

BRANCH	q	$\nu \pm \Delta\nu$(THz)	BRANCH	q	$\nu \pm \Delta\nu$(THz)
$LO_3[111]\Lambda_1$	.1	4.17 ±.10	$TO_1[111]\Lambda_3$	.1	2.07 ±.05
	.15	3.92 ±.15		.15	2.14 ±.10
	.35	3.85 ±.20		.2	2.06 ±.10
	.4	4.17 ±.12		.3	1.70 ±.15
	.5	4.30 ±.20		.35	1.70 ±.18
$TO_2[111]\Lambda_2$	.1	3.12 ±.06		.4	1.55 ±.10
	.2	2.93 ±.10		.45	1.54 ±.15
	.3	3.03 ±.12		.5	1.45 ±.08
	.4	2.75 ±.15	$LO_2[111]\Lambda_3$	.1	3.01 ±.10
$TA[111]\Lambda_3$	.1	.65 ±.03		.2	3.11 ±.08
	.15	.98 ±.04		.25	3.22 ±.10
	.2	1.12 ±.08		.3	3.04 ±.10
	.25	1.26 ±.08		.4	2.85 ±.15
	.3	1.20 ±.08		.45	2.70 ±.10
	.35	1.10 ±.05	$TO_3[111]\Lambda_3$	.2	4.18 ±.15
	.4	.96 ±.04		.25	4.26 ±.15
	.45	.72 ±.04		.3	4.24 ±.18
	.5	.446±.04		.4	4.29 ±.15
				.5	4.12 ±.15

extending this model to include the third nearest neighbor terms. Such a 3NN Born-von Kármán model contained eighteen adjustable parameters. The final value of χ^2 was reduced to 1.28. In all the calculations of phonon frequencies, the block-diagonalized dynamical matrices obtained by group theoretical analysis were used so that any ambiguity as to which computed frequency belongs to which mode was eliminated.

The experimental data along with the calculated phonon dispersion curves obtained from the fit to the 3NN Born-von Kármán model ($\chi^2 = 1.28$) are shown in Fig. 7.1. The solid lines and the dashed lines are, respectively, the calculated longitudinal and transverse branches labeled using group theoretical notation (see Section C of Chapter V). As can be seen, the data are fitted quite well by such a simple Born-von Kármán model. The interatomic force constants obtained from the fits to the 2NN model ($\chi^2 = 3.15$) and the 3NN model ($\chi^2 = 1.28$) are tabulated in Table 7.2.

Using the dispersion relations obtained from the 2NN model and the method of long wavelength due to Born and Huang (163), the elastic constants associated with the acoustic modes were calculated (see Table 7.2). As can be seen in Table 7.2, these calculated values are found to be in good agreement with the elastic constants of $CeSn_3$ obtained by ultrasonic measurements (164).

C. Phonon Density of States

To calculate various thermodynamical properties, one needs first to evaluate the phonon frequency distribution function, or phonon density of states, $g(\omega)$ defined by

Table 7.2. Interatomic force constants obtained from the Born-von Kármán fits and the elastic constants

Force Constants[a] (dyne/cm)	2NNFIT(χ^2 = 3.51)	3NNFIT(χ^2 = 1.28)
α	11735.90	12340.96
β	-3602.33	-4118.31
γ	11735.93	12846.93
α'	6003.36	4406.79
β'	1387.48	1691.80
γ'	-6388.57	-4994.79
δ	20.768	703.10
ε	-1290.96	- 192.68
σ	- 605.142	-3229.72
ν	1168.588	1637.73
a		619.60
b		84.23
c		-734.48
d		153.62
e		443.26
f		- 92.03
g		- 26.05
h		-440.16

[a] The interatomic force constants are defined by the following force constant matrices.

$$1\left\{\begin{array}{l}\text{Ce-Sn}\quad \phi\begin{pmatrix}000 & 000\\ 4 & 1\end{pmatrix} = -\begin{pmatrix}\beta & 0 & 0\\ 0 & \alpha & \gamma\\ 0 & \gamma & \alpha\end{pmatrix}\\ \text{Sn-Sn}\quad \phi\begin{pmatrix}000 & 000\\ 1 & 2\end{pmatrix} = -\begin{pmatrix}\alpha' & -\gamma' & 0\\ -\gamma' & \alpha' & 0\\ 0 & 0 & \beta'\end{pmatrix}\end{array}\right.$$

$$2\left\{\begin{array}{l}\text{Sn-Sn}\quad \phi\begin{pmatrix}000 & 010\\ 1 & 1\end{pmatrix} = -\begin{pmatrix}\delta & 0 & 0\\ 0 & \varepsilon & 0\\ 0 & 0 & \delta\end{pmatrix}\\ \text{Ce-Ce}\quad \phi\begin{pmatrix}000 & 010\\ 4 & 4\end{pmatrix} = -\begin{pmatrix}\sigma & 0 & 0\\ 0 & \nu & 0\\ 0 & 0 & \sigma\end{pmatrix}\end{array}\right.$$

$$3\left\{\begin{array}{l}\text{Ce-Sn}\quad \phi\begin{pmatrix}000 & 100\\ 1 & 4\end{pmatrix} = -\begin{pmatrix}a & b & b\\ b & c & d\\ b & d & c\end{pmatrix}\\ \text{Sn-Sn}\quad \phi\begin{pmatrix}000 & 110\\ 1 & 3\end{pmatrix} = -\begin{pmatrix}e & h & f\\ h & g & h\\ f & h & e\end{pmatrix}\end{array}\right.$$

Table 7.2 Continued

ELASTIC CONSTANTS OF $CeSn_3$ (ROOM TEMPERATURE)

Branch	Cj	Present Work (10^{11}dyne/cm^2)	Edelstein et al. (10^{11}dyne/cm^2)
L[100] Δ_1	C_{11}	6.942	8.06
T[100] Δ_5	C_{44}	3.173	4.26
L[110] Σ_1	$1/2(C_{11}+C_{12}+2C_{44})$	8.897	10.41
T_2[110] Σ_3	C_{44}	3.173	4.26
T_1[110] Σ_4	$1/2(C_{11}-C_{12})$	1.219	1.91
L[111] Λ_1	$1/3(C_{11}+2C_{12}+4C_{44})$	9.549	11.19
T[111] Λ_3	$1/3(C_{11}-C_{12}+C_{44})$	1.870	2.70

$$g(\omega) = \frac{1}{3nN} \sum_{j} \sum_{\vec{q}} \delta\{\omega - \omega_j(\vec{q})\}$$

$$= \frac{v}{3n(2\pi)^3} \sum_{j} \int \frac{dS}{|\text{grad } \omega_j(\vec{q})|} \qquad (7.2)$$

where v is the volume of the crystal and dS is an elementary area on a constant-frequency surface S corresponding to frequency ω (for the j-th branch). Note that the above definition ensures the normalization condition of $g(\omega)$, i.e.,

$$\int_0^\infty g(\omega)d\omega = 1 \quad . \qquad (7.3)$$

Therefore, once the phonon density of states is determined, the summation over all the allowed modes for a quantity A, $\sum_{j\vec{q}} A(j\vec{q})$, can be replaced by the integral of $\int_0^\infty A(\omega)g(\omega)d\omega$ after a change of variable from $(j\vec{q})$ to ω in A.

In the present analysis, the phonon density of states was calculated by a numerical method due to Lehmann et al. (165-167). In this method the Brillouin zone is divided into thousands (typically 2000 in 1/24 of the BZ) of small tetrahedrons in which the integrand of Eq. (7.2) is evaluated by linear interpolation. The phonon density of states is then obtained by summing the contributions from all the tetrahedrons for all the branches. The phonon density of states for $CeSn_3$ calculated from the force constants obtained from the 3NN Born-von Kármán fit is shown in Fig. 7.4.

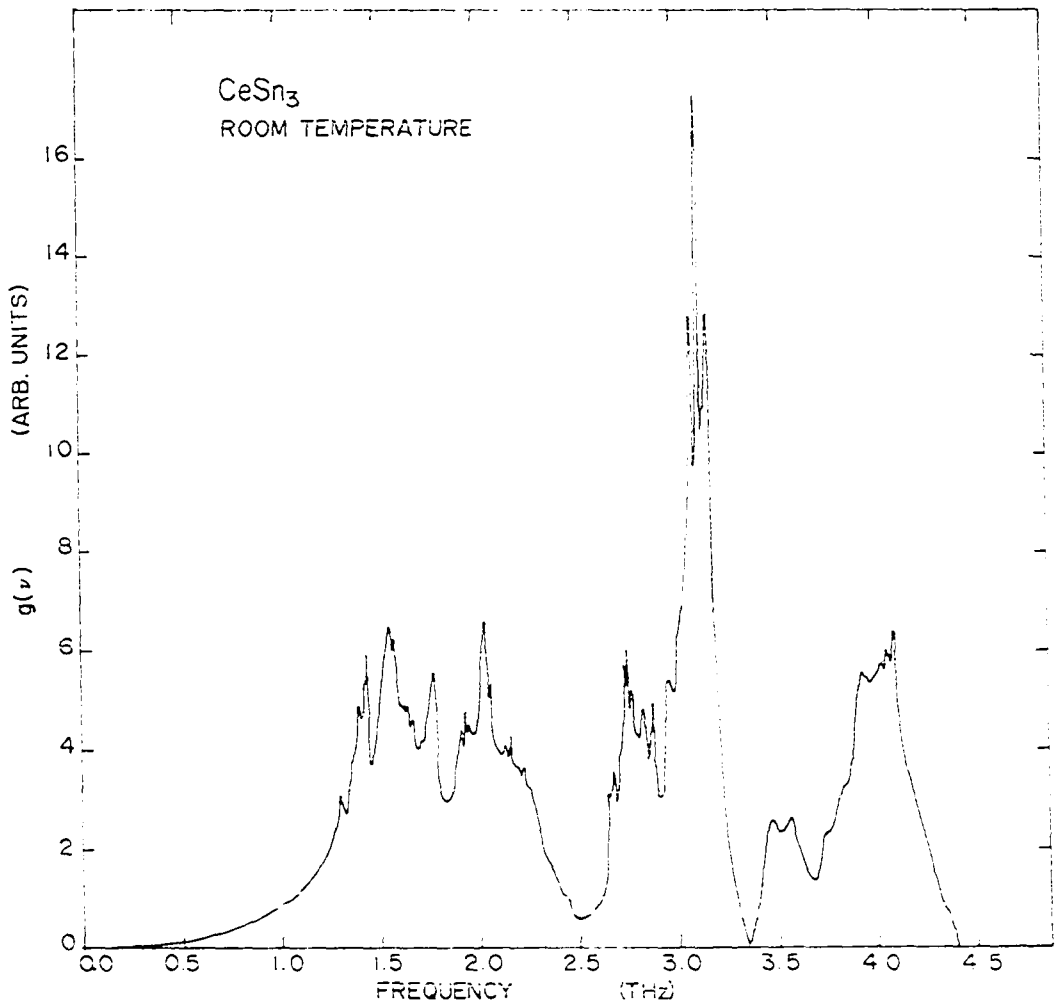

Figure 7.4. Phonon density of states of $CeSn_3$

D. Lattice Specific Heat - Debye Temperature

The lattice specific heat at constant volume is given by

$$C_V^{\ell} = \frac{\hbar^2}{k_B T^2} \int_0^{\infty} \frac{d\omega g(\omega)\omega^2 \exp(\hbar\omega/k_B T)}{[\exp(\hbar\omega/k_B T) - 1]^2} \quad . \tag{7.4}$$

Using the phonon density of states obtained above, C_V^{ℓ} for $CeSn_3$ as a function of temperature was calculated numerically using Eq. (7.4). The result is shown in Fig. 7.5. As can be seen, at room temperatures the value of C_V^{ℓ} approaches, of course, the classical Dulong-Petit value of 3nR (n = 4) where R is the universal gas constant. Also, at room temperatures, the lattice specific heat varies as T^3 over a small region as predicted by the Debye model.

The above lattice specific heat information expressed in terms of the temperature variation of the effective Debye temperature, Θ_D, is shown in Fig. 7.6. We obtained a Debye temperature of 175K for $CeSn_3$ at room temperature. Although no measured value of the Debye temperature of $CeSn_3$ (e.g., by ultrasonic method) is presently available, this calculated value of Θ_D appears to be quite reasonable since the Debye temperatures for γ-Ce and β-Sn are about 135 and 190K respectively. Using the lattice specific heat obtained in the present experiment and the measured total specific heat, the electronic contribution can be evaluated.

The specific heat at constant pressure, C_p, obtained from thermodynamical measurement can be expressed as (168)

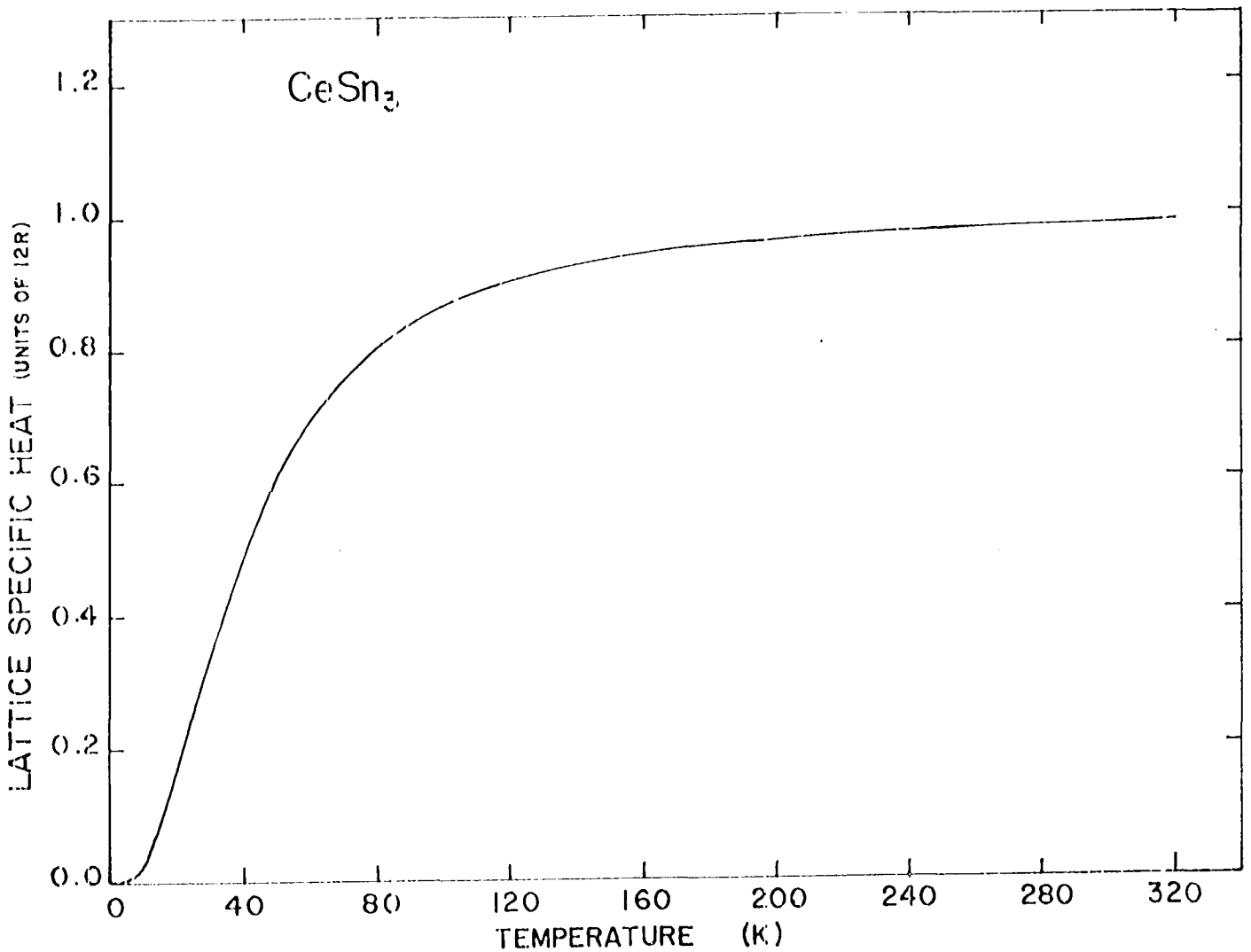

Figure 7.5. The lattice specific heat of $CeSn_3$

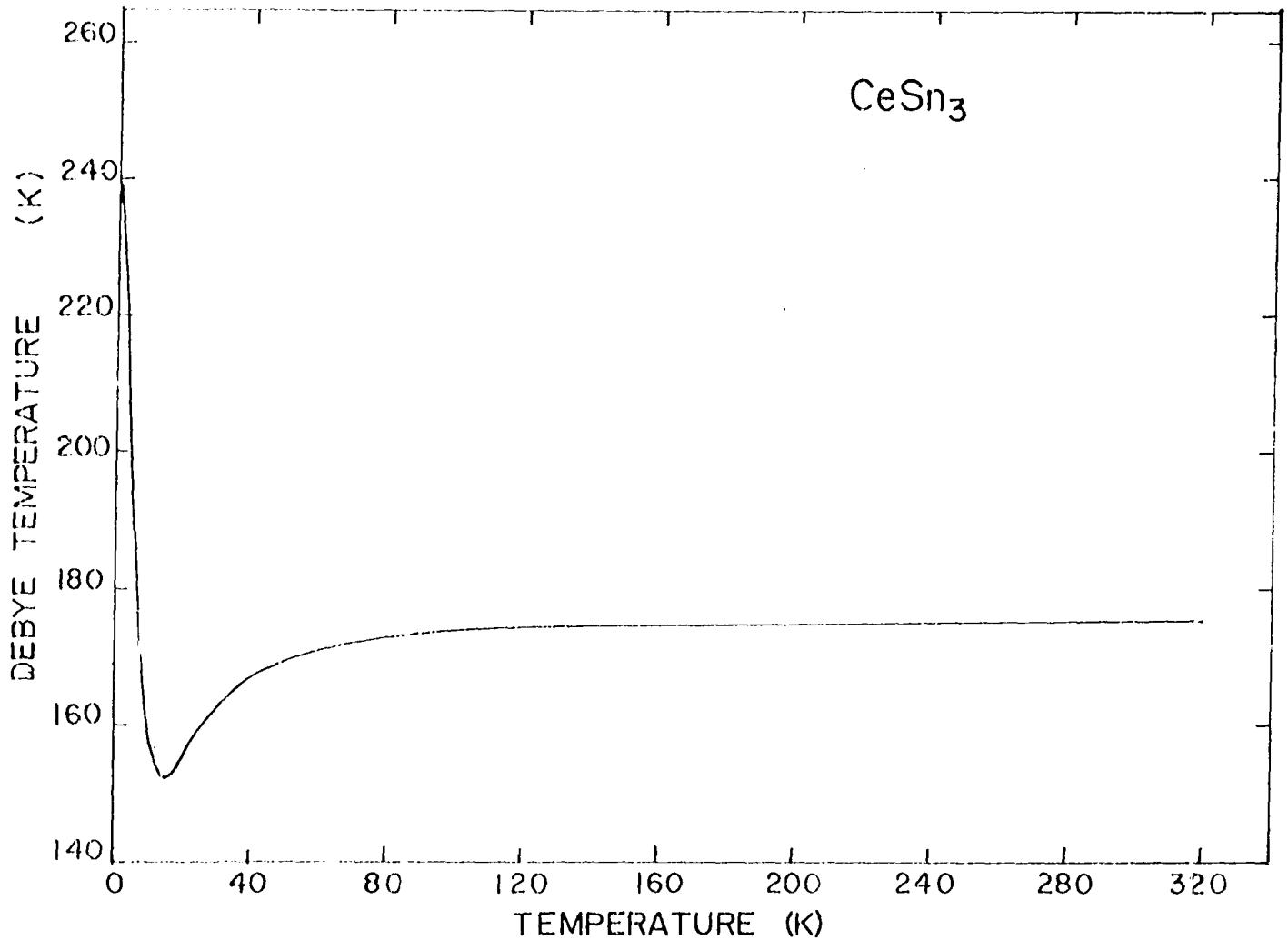

Figure 7.6. The effective Debye temperature as a function of temperature obtained from the lattice dynamical calculation

$$C_p = C_V^{\ell} + C^{e\ell} + C^f + C_d \quad . \tag{7.5}$$

In the above equation $C^{e\ell}$ is the electronic specific heat arising from the conduction electron contribution, C^f is the contribution to the specific heat arising from the thermal excitation of the 4f electrons, and C_d is the dilation term given by

$$C_d = \frac{TV(3\alpha)^2}{K_T} \quad . \tag{7.6}$$

Here T is the absolute temperature, V is the atomic volume, α is the linear thermal expansion coefficient, and K_T is the isothermal compressibility.

For $CeSn_3$ we calculated C_d using the recently reported values of $\alpha = 22 \times 10^{-6}(K)^{-1}$ by Umlauf et al. (169) and $K_T = (2.3 \pm .3) \times 10^{-3}$ $(kbar)^{-1}$ by Beille et al. (61); C^f was estimated to be less than 0.01 cal/K-mole at temperatures below 300K based on the specific heat data for Ce given by Arajs and Colvin (170). Using these estimated quantities and the calculated lattice specific heat (Fig. 7.5), we have extracted the electronic specific heat for $CeSn_3$ from the low temperature specific heat data measured by Cooper et al. (58). The results are shown in Fig. 7.6. We obtained a coefficient of electronic specific heat γ equal to 84 $mJ/mole\text{-}K^2$ which is in good agreement with the value $\gamma = 53 \pm 10$ $mJ/mole\text{-}K^2$ reported in Ref. 58. The large value of γ ($\gamma \cong 10$ $mJ/mole\text{-}K^2$) for $LaSn_3$) implies a large density of states at the Fermi level, presumably due to the 4f level which in the mixed valence systems is believed to be closed to the Fermi level.

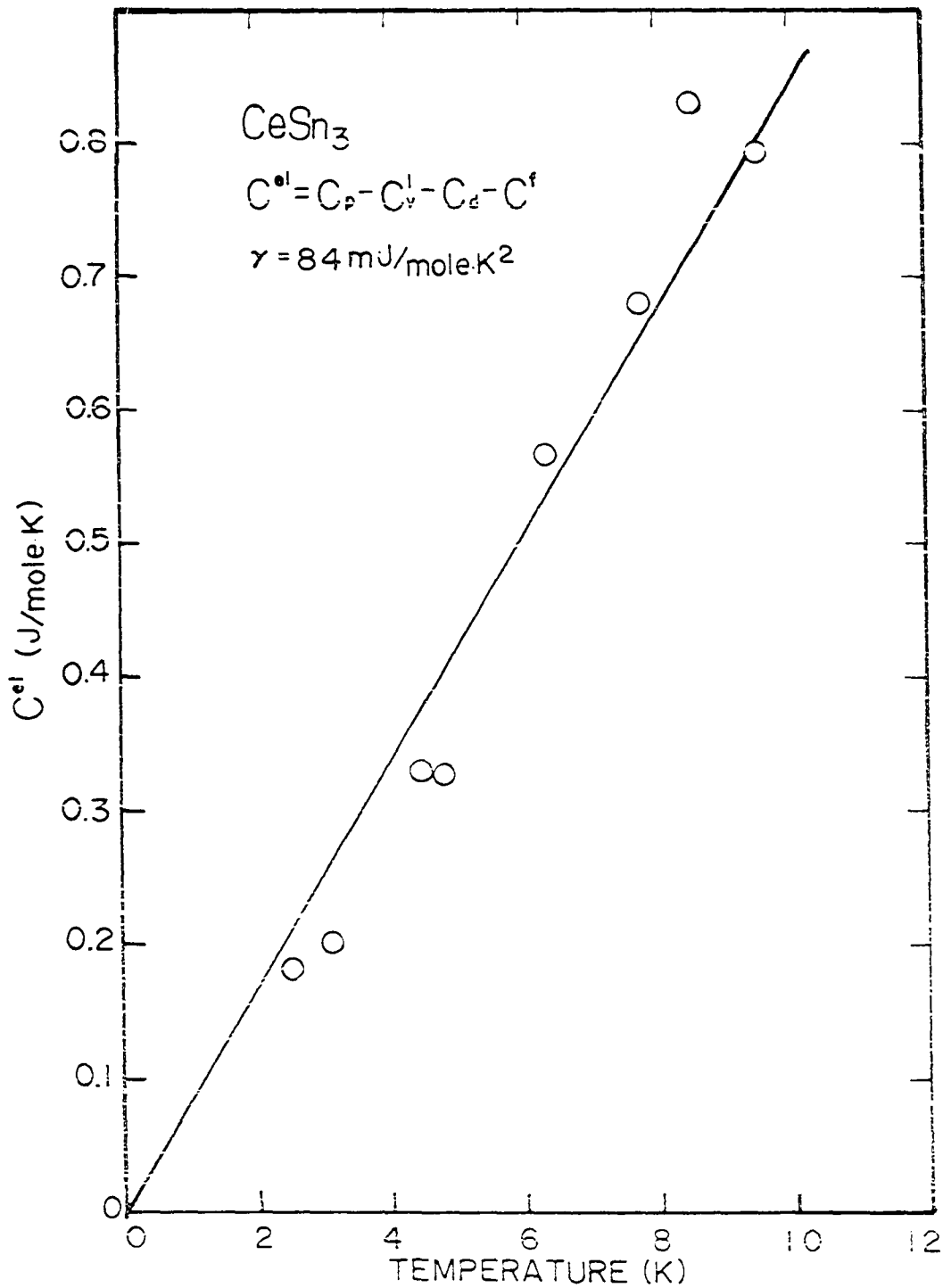

Figure 7.7. The electronic contribution to the specific heat of $CeSn_3$ extracted from the total specific heat measurements (58) using the results of lattice dynamical calculation

E. Atomic Thermal Factors

The atomic thermal factors of a solid are of considerable importance since they determine the temperature dependence of the intensities of the Bragg reflections in x-ray and neutron experiments. In addition, since these factors are essentially the average square displacements of the atoms they provide information about the stability of the solid at finite temperatures.

The B-factors (125) for the Ce atom can be calculated as follows:

$$B_2 = \frac{4a^2}{m_2} \sum_{j\vec{q}} \frac{E_j(\vec{q})}{\omega_j^2(\vec{q})} |\vec{e}(4|\vec{q}j)|^2$$

$$= \frac{4a^2}{m_2} \sum_{j\vec{q}} \frac{\hbar\omega_j(\vec{q}) \left\{ \frac{1}{2} + \frac{1}{\exp[\hbar\omega_j(\vec{q})/k_B T] - 1} \right\}}{\omega_j^2(\vec{q})} |\vec{e}(4|\vec{q}j)|^2$$

$$= \frac{4a^2}{m_2} \int_0^\infty d\omega \; g_2'(\omega) \frac{\hbar}{\omega} \left\{ \frac{1}{2} + \frac{1}{\exp[\hbar\omega/k_B T] - 1} \right\} \tag{7.7}$$

where

$$g_2'(\omega) = \frac{V}{3n(2\pi)^3} \sum_j \int \frac{dS}{|\text{grad}\ \omega_j(\vec{q})|} |\vec{e}(4|\vec{q}j)|^2 \tag{7.8}$$

In Eq. (7.7) $\vec{e}(r|\vec{q}j)$ is the (complex) polarization vector of the Ce atom (see Eq. (5.27) in Chapter V), m_2 is the mass of the Ce atom and a is the lattice constant. $g_1'(\omega)$ in Eq. (7.8) is a 'weighted' density of states defined in the same sense as in Eq. (7.2).

Similarly, the two B-factors for the Sn atom, B_1 and $B_1^{//}$ (see Section B of Chapter IV) are

$$B_1^{\perp} = \frac{4a^2}{m_1} \int_0^{\infty} d\omega \; g'_{1x}(\omega) \frac{\hbar}{\omega} \left\{ \frac{1}{2} + \frac{1}{\exp[\hbar\omega/k_B T] - 1} \right\} \quad , \tag{7.9}$$

$$B_1^{//} = \frac{4a^2}{m_1} \int_0^{\infty} d\omega \; g'_{1y}(\omega) \frac{\hbar}{\omega} \left\{ \frac{1}{2} + \frac{1}{\exp[\hbar\omega/k_B T] - 1} \right\} \quad , \tag{7.10}$$

where

$$g'_{1x}(\omega) = \frac{v}{3n(2\pi)^3} \sum_j \int \frac{dS}{|\text{grad } \omega_j(\vec{q})|} |e_x(1|\vec{q}j)|^2 \quad , \tag{7.11}$$

$$g'_{1y}(\omega) = \frac{v}{3n(2\pi)^3} \sum_j \int \frac{dS}{|\text{grad } \omega_j(\vec{q})|} |e_y(1|\vec{q}j)|^2 \quad . \tag{7.12}$$

In Eqs. (7.9) to (7.12) m_1 is the mass of the Sn atom; $e_x(1|\vec{q}j)$ and $e_y(1|\vec{q}j)$ are the x and y components of the polarization vector of the k = 1 Sn atom.

The weighted density of states $g'_2(\omega)$, $g'_{1x}(\omega)$ and $g'_{1y}(\omega)$ were calculated by the 'tetrahedron method' described above. Using the 3NN Born-von Kármán model (see Table 7.2), the B-factors for the Ce and Sn atoms were calculated numerically according to Eqs. (7.7) to (7.12). In collaboration with J. Faber of the Argonne National Laboratory, we measured the B-factors of $CeSn_3$ using standard elastic neutron and x-ray scattering techniques. The values of the B-factors obtained in these experiments are compared to those evaluated from the lattice dynamics of $CeSn_3$ in Table 7.3

Table 7.3. Comparison of B-factors obtained by lattice dynamics, neutron diffraction and x-ray diffraction (126) experiments

Atoms	B-factors		Lattice Dyn. (3NN)	Neutron	X-ray
	$B_1^{\perp}$	($\mathring{A}^2$)	1.31	1.95	1.78
Sn	$B_1^{//}$	($\mathring{A}^2$)	.74	1.34	1.17
	$\bar{B} = \frac{1}{3}(B_1^{\perp} + 2B_1^{//})$	($\mathring{A}^2$)	.93	1.54	1.37
Ce	B_2	($\mathring{A}^2$)	.97	1.54	1.20

It should, however, be pointed out that subtle differences exist between the significance of the quantities obtained by neutron and x-ray elastic measurements and those obtained from the lattice dynamical calculations. As can be seen from the above table, the B-factors obtained from the three independent experiments differ from each other by up to about 50 percent. However, the direction of anisotropy in the thermal vibrations of the Sn atoms determined by all the three methods are consistent, namely, the B-factor perpendicular to the face of the cube is approximately 50% larger than that of in the plane of face. Furthermore, the value of the averaged Sn B-factor, $\bar{B}$, in each case is very close to the value of the Ce B-factor.

VIII. SUMMARY

In the present work the electronic and lattice dynamical properties of $CeSn_3$ were investigated using the powerful techniques of neutron spectroscopy. The electronic properties of this compound were studied using polarized neutrons and its dynamical properties were investigated by inelastic neutron scattering techniques.

In our polarized neutron study we find that the field induced magnetization in $CeSn_3$ is of 4f electronic character at high temperatures (>40K). On the other hand, below 40K the experimental results can be explained by assuming a 4f-5d mixed electronic character for the induced magnetization of this compound. Thus, the polarized neutron experiments provided direct evidence for the mixed-valent character of this compound. The 5d component of the magnetization density was found to be of e_g symmetry and it can account, at least partly, for the increase in the magnetic susceptibility of $CeSn_3$ at low temperatures. In addition, the e_g symmetry of the electronic wavefunctions (with their lobes along the edges of the cubic unit cell) is consistent with the absence of any significant isomer shift at the Sn sites.

A detailed quantitative analysis of the polarized neutron results is hindered by the lack of any adequate theoretical model for the ground state of the mixed valence systems. However, the results can be explained qualitatively within the framework of recent phenomenological models (128-131) of the mixed valence systems. In a simple model advanced by S. Liu and collaborators (123,132), the magnetic

susceptibility, obtained by assuming that the 4f electrons on the Ce sites are uncorrelated and by positioning the 4f level (of width Γ of 150K) at 200K above the Fermi energy, exhibits roughly the main characteristics of the measured susceptibility. The hybridization of the 4f electrons with the band electrons provides a coupling of the neighboring Ce sites so that at low temperatures, $T \ll \Gamma$, the 4f electrons form a narrow hybridized coherent band. What is extraordinary in this model, in view of its simplicity, is that in coherent ground state of $CeSn_3$, there is a nearly equal mixture of the 4f and conduction band wavefunctions at the Fermi level in quite good agreement with the polarized neutron experiment.

In our inelastic neutron scattering study of the dispersion curves of $CeSn_3$, we observed anomalously soft modes in the [111] symmetry direction near the zone boundary. The presence of these anomalies was verified by comparison with the dispersion curves of $LaSn_3$. (In the absence of mixed valent character, one would expect the dispersion curves of $LaSn_3$ to be identical with those of $CeSn_3$.) As we discussed in Chapter VII, the anomalies can be understood qualitatively as a result of the $4f \leftrightarrow 5d$ electronic transitions induced by the nuclear motion in these phonon modes. Recently phonon anomalies have also been observed in another mixed valence system $Sm_{.75}Y_{.25}S$ (47). Thus, the inelastic neutron experimental results show that the electron-phonon coupling in these systems is quite significant.

Using standard techniques of analysis, we evaluated from our measurements of the dispersion curves the phonon density of states, the

lattice specific heat and the atomic thermal factors. Two important results should be pointed out. First, from the comparison of the lattice specific heat obtained in our measurements with total specific heat measurements, it is clear that the electronic contribution is very large ($\gamma \simeq 84$ mJ/mole-K^2). This implies a large density of states at the Fermi level, as expected if the 4f level is close to the Fermi level. Second, the thermal motion of the Sn atoms is highly anisotropic and as a consequence the thermal factor of Sn atoms for motion normal to the faces of the cubic unit cell is considerably larger than that for motion in the faces of the cube. Thus, it seems that in this compound, the Sn atoms exhibit a tendency to move towards the empty space in the center of the cube.

To summarize, a fundamental theory of these systems should consider both electrons and phonons coupled by relatively strong interactions. Some progress (155-156) in this direction has been made recently. Clearly, additional experimental and theoretical investigations are necessary to understand the detailed behavior of the mixed valence systems.

IX. APPENDIX

In this appendix we shall consider the effects of instrumental imperfection, crystal effects, etc. on the magnetic form factor measurements in a polarized neutron experiment and the corrections need to be made to the observed intensity ratios $4F_M/F_N$. If the experiment is properly designed, errors will amount to not more than a few percent and can be caculated by using the corresponding formulas given below.

A. Incomplete Beam Polarization and Imperfect Spin Flipping

The polarization of the incident beam is defined as

$$P_o = \frac{N^+ - N^-}{N^+ + N^-} = 1 - 2\delta_o \qquad (A.1)$$

where N is the number of neutrons incident on the sample, the superscripts + and - for N (and for other quantities defined later in this section) respectively denote the neutron spin states parallel (up) and antiparallel (down) to the magnetic field, and $2\delta_o = N^-/(N^+ + N^-)$ is the probability that a down spin neutron will be reflected by the polarizer. In practice for a good polarizer one would expect that $N^+ >> N^-$ or $\delta_o << 1$. Let σ represent the average probability that a neutron in a particular spin state will be reflected by the sample when it is set for a certain reflection. With the flipper off, the number of reflected neutrons can be written as

$$N = N^+\sigma^+ + N^-\sigma^- \quad . \qquad (A.2)$$

When the flipper is on, let δ_f be the probability that a neutron with a given trajectory and wavelength will pass through the flipper with its spin unchanged. Then, the number of neutrons passing through the flipper with spin up is

$$(N^+)' = N^-(1 - \delta_f) + \delta_f N^+ \quad . \tag{A.3a}$$

Similarly, the number with spin down is

$$(N^-)' = N^+(1 - \delta_f) + \delta_f N^- \quad . \tag{A.3b}$$

Of course, when the efficiency of the flipper is properly optimized, $\delta_f \cong 0$. It follows immediately that the flipper polarization is given by

$$P_f = \frac{(N^+)' - (N^-)'}{(N^+)' + (N^-)'} = 1 - 2\delta_f \quad . \tag{A.4}$$

Furthermore, if the initial polarization is P_o, the polarization after passing through the flipper will be $-P_o P_f$.

By analogy with Eq. (A.2) we can write the number of reflected neutrons with the flipper on as $N' = (N^+)'\sigma^+ + (N^-)'\sigma^-$. Using this expression and Eqs. (A.2), (A.3a) and (A.3b), we can express the measured intensity ratio (see Eq. (2.5)) as follows:

$$R = \frac{\frac{\sigma^+}{\sigma^-}\left[1 + \frac{N^-\sigma^-}{N^+\sigma^+}\right]}{1 + \frac{1}{N^+\sigma^-}\left[N^-\sigma^+ + \delta_f(N^+ - N^-)(\sigma^+ - \sigma^-)\right]} \quad . \tag{A.5}$$

It can be shown that R can also be written in the following form:

$$R = \frac{1 + \rho_o \rho_x}{1 - \rho_o \rho_f \rho_x} \tag{A.6}$$

where

$$\rho_x = \frac{\sigma^+ - \sigma^-}{\sigma^+ + \sigma^-} = 1 - 2\delta_x \quad . \tag{A.7}$$

Notice that σ^+/σ^- in Eq. (A.5) is the <u>corrected</u> intensity ratio, R_c, which we wish to obtain. By using Eqs. (A.1), (A.4) and (A.5), it can be shown that

$$R_c = \frac{\sigma^+}{\sigma^-} = \frac{R}{C} \tag{A.8}$$

where

$$C = \frac{1 + \rho_o - R(1-\rho_o\rho_f)}{1 + \rho_o\rho_f - \frac{1-\rho_o}{R}} \quad . \tag{A.9}$$

Substituting Eqs. (A.1) and (A.4) into Eq. (A.9) and neglecting second order terms in δ_o and δ_f, one obtains

$$\begin{aligned} C &= 1 - (R - \tfrac{1}{R})\delta_o - (R - 1)\delta_f \\ &\simeq 1 - r(2\delta_o + \delta_f) \end{aligned} \tag{A.10}$$

where

$$r = R - 1 \qquad \text{and} \qquad r \ll 1 \quad . \tag{A.11}$$

Substituting Eq. (A.10) into Eq. (A.8) and writing $r_c = R_c - 1$, we obtain

$$R_c \cong R[1 + r(2\delta_o + \delta_f)]$$

or

$$\begin{aligned} r_c &= r[1 + (1 + r)(2\delta_o + \delta_f)] \\ &\cong r[1 + 2\delta_o + \delta_f] \quad . \end{aligned} \tag{A.12}$$

Next, we need to express the quantity $2\delta_o + \delta_f$ in terms of R_o, the flipping ratio of the incident beam, which is obtained experimentally by analyzing the polarization of the beam using a Co-Fe analyzer. The efficiency of an analyzer can be written as

$$P_a = \frac{N_a^+ - N_a^-}{N_a^+ + N_a^-} = 1 - \delta_a \quad , \tag{A.13}$$

and by analogy to Eq. (A.6), we obtain

$$\frac{1}{R_o} = \frac{1 - P_o P_f P_a}{1 + P_o P_a} \quad , \tag{A.14}$$

or

$$\frac{1}{R_o} \cong \delta_o + \delta_f + \delta_a \tag{A.15}$$

where second order terms in δ_a, δ_f and δ_a have been neglected.

It is well-known experimentally that a flipping ratio near 100 can be attained if both the polarizer and analyzer are Co-Fe crystals and

the flipper is properly optimized. Therefore, according to Eq. (A.15),

$$0.01 = 2\delta_{Co-Fe} + \delta_f \quad . \tag{A.16}$$

With the Si-Fe crystal as polarizer, we obtain by using the above relation and Eq. (A.15)

$$\frac{2}{R_o} = 2\delta_{Si-Fe} + 2\delta_f + 2\delta_{Co-Fe}$$

or

$$2\delta_{Si-Fe} + \delta_f = \frac{2}{R_o} - 0.01 \quad . \tag{A.17}$$

By comparing Eq. (A.17) with Eq. (2.6b) in Chapter II, it follows that $r = 4F_M/F_N$, which we <u>measure</u>. As a result, we obtain the final formula for the <u>corrected</u> value of $4F_M/F_N$:

$$\left(\frac{4F_M}{F_N}\right)_c = \frac{4F_M}{F_N}\left(1 + \frac{2}{R_o} - 0.01\right) \tag{A.18a}$$

The correction for incomplete beam polarization and imperfect spin flipping to the measure value of $4F_M/F_N$ is defined as

$$(\Delta R)_{flip} = \left(\frac{4F_M}{F_N}\right)_c - \left(\frac{4F_M}{F_N}\right)_{measured} \quad . \tag{A.18b}$$

Some numerical values of $(\Delta R)_{flip}$ for the $CeSn_3$ data are listed in column 6 of Table A.1.

B. Secondary Extinction

It was shown by Bacon and Lowde (82) that in a general case, the integrated reflectivity $\mathfrak{R}$ can be written in the following form:

$$\frac{1}{n}\,\mathfrak{R} = \psi\left(\frac{\mu t}{\sin\theta}, \frac{1}{n}\,\frac{Q}{\mu_o}\right) \tag{A.19}$$

where all the quantities were defined in Chapter II, and ψ can be evaluated numerically (82). By definition, the measured intensity ratio R is given by

$$R = \frac{I_+}{I_-} = \frac{\mathfrak{R}(\varepsilon^+)}{\mathfrak{R}(\varepsilon^-)} \tag{A.20}$$

where ε is the argument of $\mathfrak{R}$ dependent on the structure factor in the following way:

$$\varepsilon^{\pm} = \varepsilon_o \pm \varepsilon' \sim F_N^2\left(1 \pm 2\,\frac{F_M}{F_N}\right) \quad . \tag{A.21}$$

Expanding the right hand side of Eq. (A.20) and retaining terms to the first order in ε' yields

$$R = \frac{1 + \frac{1}{\mathfrak{R}}\frac{\partial \mathfrak{R}}{\partial \varepsilon}\Big|_{\varepsilon_o}\varepsilon'}{1 - \frac{1}{\mathfrak{R}}\frac{\partial \mathfrak{R}}{\partial \varepsilon}\Big|_{\varepsilon_o}\varepsilon'} \quad . \tag{A.22}$$

Solving for ε' gives

$$\varepsilon' = \frac{\frac{R-1}{R+1}}{\left(\frac{1}{\mathfrak{R}}\frac{\partial \mathfrak{R}}{\partial \varepsilon}\right)_{\varepsilon_o}} \quad . \tag{A.23}$$

As a good approximation, we use the integrated reflectivity $\mathcal{R}$ calculated for an ideally imperfect nonabsorbing crystal and express ε' in terms of $4F_M/F_N$. Thus we obtain the corrected value of $4F_M/F_N$:

$$\left(\frac{4F_M}{F_N}\right)_c = 2\left(\frac{R-1}{R+1}\right) \Big/ \left[\frac{\alpha}{\eta}\left(\frac{\mathcal{R}'(\frac{\alpha}{\eta})}{\mathcal{R}/\eta}\right)\right] \qquad \text{(A.24a)}$$

where $\mathcal{R}'(\frac{\alpha}{\eta})$ is the derivative of $\mathcal{R}$ with respect to the variable $\frac{\alpha}{\eta} = \frac{Qt}{\eta \sin\theta}$. For this particular case, the quantity $\mathcal{R}/\eta$ as a function of α/η is obtained numerically and is shown in Fig. A.1. The correction for secondary extinction to the measured value of $4F_M/F_N$ is defined as

$$(\Delta R)_{ext} = \left(\frac{4F_M}{F_N}\right)_c - \left(\frac{4F_M}{F_N}\right)_{measured} . \qquad \text{(A.24b)}$$

Some numerical values of $(\Delta R)_{ext}$ for $CeSn_3$ data are listed in column 7 of Table A.1.

C. Field Induced Diamagnetism

By considering the interaction of the neutron magnetic moment with the induced current density due to the Larmar precession of the electronic envelope of an atom (ion) about the direction of the external magnetic field, it can be shown that the scattering amplitude $p_d(\theta)$ in Eq. (3.4) in the first Born approximation is given by

$$p_d(\theta) = -\mu_n \chi_d \left(\frac{eH}{\hbar c}\right) f_d(\theta) . \qquad \text{(A.25a)}$$

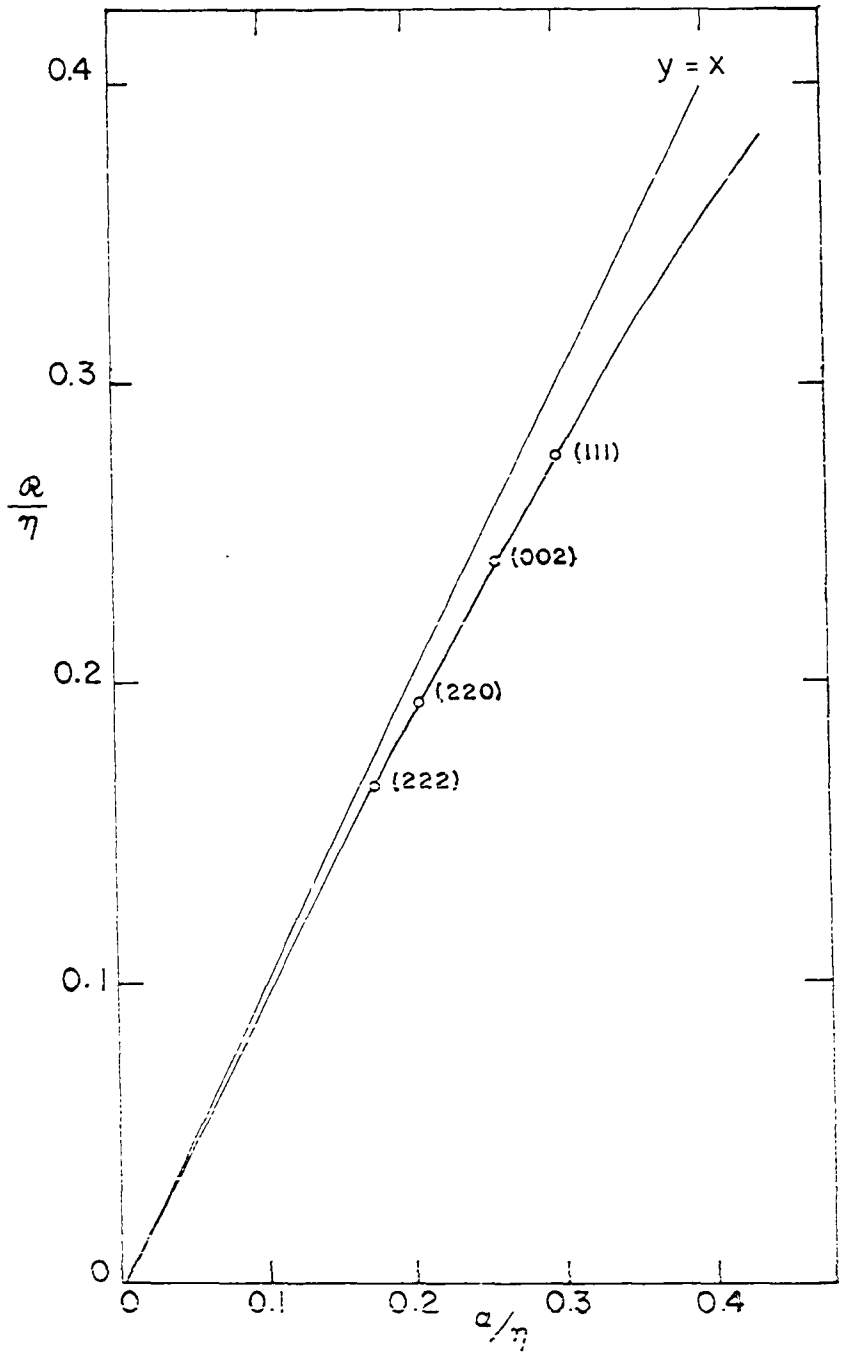

Figure A.1. The calculated integrated reflectivity for an ideally imperfect crystal as compared to the extinction-free y = x straight line in the figure. The values of a/η shown in this figure correspond to the Bragg reflections of using the PNI crystal and neutrons of wavelength 1.05 A

In the above equation, χ_d is the atomic (ionic) diamagnetic susceptibility defined as

$$\chi_d = -\frac{z\,e^2}{6mc^2}\langle r^2\rangle \quad , \tag{A.25b}$$

$f_d(\theta)$ is the normalized diamagnetic form factor of the atom (ion) defined as

$$f_d(\theta) = -\frac{3}{\langle r^2\rangle}\,\frac{1}{q}\,\frac{df_c(q)}{dq} \tag{A.25c}$$

where $f_c(q)$ is the atomic (ionic) <u>charge</u> form factor calculated using the relativistic self-consistent field Dirac-Slater wavefunctions (171) of the atom (ion). Other quantities in Eq. (A.25) were defined following Eq. (3.4) of Chapter III.

For $CeSn_3$, this gives rise to a correction term $(\Delta R)_{dia}$ to the measured values of $(4F_M/F_N)$:

$$(\Delta R)_{dia} = \begin{cases} 4\,\dfrac{(p_d)_{Ce} + 3(p_d)_{Sn}}{b_{Ce} + 3b_{Sn}} & \text{for the unmixed Miller indices reflections} \\ 4\,\dfrac{(p_d)_{Ce} - (p_d)_{Sn}}{b_{Ce} - b_{Sn}} & \text{for the mixed Miller indices reflections} \end{cases} \tag{A.26}$$

where the subscripts Ce and Sn denote, respectively the Ce^{3+} and Sn^{4+} ions. Some numerical values of $(\Delta R)_{dia}$ are listed in column 8 of Table A.1.

D. Neutron Spin-Neutron Orbit Interaction

In the neutron spin-neutron orbit interaction the moving neutron magnetic moment senses the nuclear charge, and this produces an asymmetrical scattering potential across the scattering atom along with the symmetrical nuclear scattering potential (see Eq. (3.1) of Chapter III). Consequently, the spin-orbit scattering amplitude is imaginary. If we denote by b' the imaginary part of the nuclear scattering amplitude, the total coherent scattering amplitude becomes

$$f(\theta) = b + ib' + i[\gamma_o \cot\theta \, \vec{\sigma} \cdot \vec{n}] \quad , \tag{A.27}$$

where γ_o (as defined in Eq. (3.7)) determines the strength of the spin-orbit interaction. The intensity ratio of the scattered beams with neutron spins parallel ($\vec{\sigma} \cdot \vec{n} = +1$) and antiparallel ($\vec{\sigma} \cdot \vec{n} = -1$) to the magnetic field is

$$R_{s.o.} = \frac{f^+(\theta)[f^+(\theta)]^*}{f^-(\theta)[f^-(\theta)]^*}$$

$$= \frac{b^2 + b'^2 + \gamma_o^2 \cot^2\theta + 2b'\gamma_o \cot\theta}{b^2 + b'^2 + \gamma_o^2 \cot^2\theta - 2b'\gamma_o \cot\theta} \quad . \tag{A.28}$$

In most cases of interest $b^2 + b'^2 + \gamma_o^2 \cot^2\theta \gg 2b'\gamma_o \cot\theta$, and so we obtain as the correction for the spin-orbit interaction

$$(\Delta R)_{s.o.} \cong 1 + \frac{4b'\gamma_o \cot\theta}{b^2 + b'^2 + \gamma_o^2 \cot^2\theta} \quad . \tag{A.29}$$

One should note that the contribution of the spin-robit interaction to the measured polarization ratio is mainly due to its interference

with the imaginary part of the nuclear coherent scattering amplitude. Moreover, this will become significant in case of small coherent scattering (small b) or in cases where the imaginary part of the nuclear scattering amplitude is large (large b').

For $CeSn_3$, the quantities γ_o, b' and b in Eq. (A.29) will be replaced by their corresponding values for the two types of reflections with different structure factors; for example, $\gamma_o = \gamma_{Ce} + 3\gamma_{Sn}$ for the unmixed Miller indices reflections and $\gamma_o = \gamma_{Ce} - \gamma_{Sn}$ for the mixed Miller indices reflections (γ_{Ce} and γ_{Sn} are values of γ_o for the Ce^{3+} and Sn^{4+} ions, respectively). Some numerical values of $(\Delta R)_{s.c.}$ for $CeSn_3$ data are listed in column 9 of Table A.1.

Table A.1. Typical values for various terms of corrections

Experimental conditions: Sample: PN1, T = 150K, $\vec{H}$//[110], H = 42.5 kG, plutonium filter after the sample.

1	2	3	4	5	6
hkℓ	$\sin\theta/\lambda$ ($A^{\circ -1}$)	λ (A°)	R_o	$(4F_M/F_N)_{exp}(10^{-3})$	$(\Delta R)_{flip}(10^{-3})$
001	0.106	1.055	43.38	-116.9 ± 1.4	-4.224
110	0.150	1.050	42.68	-112.4 ± 1.7	-4.144
111	0.183	1.035	42.36	5.413 ± .11	0.201
220	0.300	1.055	43.38	4.409 ± .11	0.1592
221	0.318	1.065	43.38	- 85.31 ± 1.9	-3.080
222	0.367	1.055	43.38	4.103 ± .17	0.148
330	0.449	1.050	42.68	- 73.35 ± 2.6	-2.703
331	0.462	1.045	42.13	3.455 ± .10	0.129
442	0.635	1.065	43.38	2.087 ± .17	0.0754

λ = neutron wavelength.

R = measured polarization ratio of the incident neutron beam, Si-Fe monochromator Co-Fe analyzer.

$(4F_M/F_N)_{exp}$ = observed value of $4F_M/F_N$ after counting rate and background corrections.

$(\Delta R)_{flip}$ = correction for incomplete beam polarization and imperfect spin flipping.

$(\Delta R)_{ext}$ = correction for secondary extinction.

$(\Delta R)_{dia}$ = correction for field induced diamagnetism

$(\Delta R)_{s.o.}$ = correction for neutron spin-neutron diamagnetism.

$(4F_M/F_N)_{corr} = (4F_M/F_N)_{exp} + (\Delta R)_{flip} + (\Delta R)_{ext} - (\Delta R)_{dia} + (\Delta R)_{s.o.}$.

$(4F_M/F_N)^{norm}_{corr}$ = $(4F_M/F_N)_{corr}$ normalized to the primary reflection (see Eq. (4.3)).

Table A.1. Continued

1	7	8	9	10	11
hkℓ	$(\Delta R)_{ext}$ (10^{-3})	$(\Delta R)_{dia}$ (10^{-3})	$(\Delta R)_{s.o.}$ (10^{-3})	$(4F_M/F_N)_{corr}$ (10^{-3})	$(4F_M/F_N)^{norm}_{corr}$ (10^{-3})
001	0.00	0.559	-0.0166	-121.6 ± 1.4	6.73 ± .10
110	0.00	0.438	-0.0204	-116.9 ± 1.7	6.474 ± .10
111	0.468	-0.208	0.0105	6.280 ± .12	6.280 ± .12
220	0.253	-0.134	0.0138	4.941 ± .11	4.941 ± .11
221	0.0	0.0406	-0.0192	- 88.41 ± 1.9	4.895 ± .11
222	0.206	-0.101	0.0142	4.544 ± .17	4.544 ± .18
330	0.0	-0.00217	-0.0126	- 76.042 ± 2.6	4.210 ± .14
331	0.152	-0.0539	0.0137	3.776 ± .11	3.776 ± .11
442	0.105	-0.0348	0.0110	2.291 ± .18	2.291 ± .18

X. REFERENCES

1. Valence Instabilities and Related Narrow-Band Phenomena, edited by R. D. Parks (Plenum, New York, 1977).

2. U.S.-Japanese Seminar on Mixed Valence Compounds, Sendai, Japan, October 5-7, 1977 (unpublished).

3. J. M. Robinson, Physics Reports 51, 1 (1979) and references therein.

4. A. Jayaraman, in Handbook on the Physics and Chemistry of Rare Earths, Vol. II, edited by K. A. Gschneidner, Jr. and L. Eyring (North Holland Publishing Co., Amsterdam, 1978), Chapter 20 and references therein.

5. C. M. Varma, Rev. Mod. Phys. 48, 219 (1976).

6. J. H. Jefferson and K.W.H. Stevens, J. Phys. C: Solid State Phys. 11, 3919 (1978) and references therein.

7. N. F. Mott, Phil. Mag. 30, 403 (1974).

8. B. Cogblin, F. Gonzales-Jimenez, A. K. Bhattacharjee, J. R. Iglesias-sicardi, B. Cornut, and R. Jullien, J. Magnetism and Mag. Mater. 3, 67 (1976).

9. R. Suryanarayanan, Phys. Stat. Sol. (b) 85, 9 (1978).

10. M. E. Foglio and L. M. Falicov, Phys. Rev. B 20, 4554 (1979); B 21, 4154 (80); and M. E. Foglio, C. A. Balseiro, and L. M. Falicov, Phys. Rev. B 20, 4560 (1979).

11. L. Pauling, J. Am. Chem. Soc. 69, 542 (1947).

12. W. H. Zachariasen, in The Metal Plutonium, edited by A. S. Coffinberry and W. N. Miner (U. Chicago, Chicago, 1961).

13. K. A. Gschneidner, Jr., Rare Earth Alloys (D. Van Nostrand Co., New York, 1961).

14. D. C. Koskenmake and K. A. Gschneidner, Jr., in Handbook on the Physics and Chemistry of Rare Earths, Vol. I, edited by K. A. Gschneidner, Jr. and L. Eyring (North Holland Publishing Co., Amsterdam, 1978), chap. 4.

15. R. V. Colvin, S. Arajs and J. M. Peck, Phys. Rev. 122, 14 (1961).

16. C. R. Burr and S. Ehara, Phys. Rev. 149, 551 (1966).

17. C. Stassis, C.-K. Loong, G. R. Kline, O. D. McMasters and K. A. Gschneidner, Jr. J. Appl. Phys. 49, 2113 (1978).

18. E. King, J. A. Lee, I. R. Harris and T. F. Smith, Phys. Rev. B 1, 1380 (1970).

19. K. A. Gschneidner, Jr., R. O. Elliott and R. R. McDonald, J. Phys. Chem. Solids 23, 555 (1962).

20. E. Franceschi and G. Oscese, Phys. Rev. Lett. 22, 1299 (1969).

21. A. Jayaraman, Phys. Rev. 137, A179 (1965).

22. J. Wittig, Phys. Rev. Lett. 21, 1250 (1968).

23. J. M. Lock, Proc. Phys. Soc. London B 70, 566 (1957).

24. M. R. MacPherson, G. E. Everett, D. Wahlleben and M. B. Maple, Phys. Rev. Lett. 26, 20 (1971).

25. K. A. Gschneidner, Jr. and R. Smoluchowski, J. Less-Common Metals 5, 374 (1963).

26. D. C. Koskimaki and K. A. Gschneidner, Jr., Phys. Rev. B 11, 4463 (1975).

27. N. E. Phillips, J. C. Ho and T. F. Smith, Phys. Lett. 27A, 49 (1968).

28. N. E. Phillips, Crit. Rev. Solid State Sci. 2 467 (1972).

29. F. H. Ellinger and W. H. Zachariasen, Phys. Rev. Lett. 32, 773 (1974).

30. K. A. Gschneidner, Jr., in Valence instabilities and related narrow band phenomena, edited by R. D. Parks (Plenum, New York, 1977), p. 89.

31. A. J. T. Grimberg, C. J. Sehinkel and A. P. L. M. Zander, Solid State Comm. 11, 1579 (1972).

32. D. R. Gustafson, J. D. McNutt and L. O. Roellig, Phys. Rev. 183, 435 (1969).

33. Y. Baer and G. Busch, J. Electron. Spectrosc. Related Phenom. 5, 611 (1974).

34. M. Owen, Ann. Phys. Leipzig 37, 657 (1912).

35. A. W. Lawson and T. Tang, Phys. Rev. 76, 301 (1949).

36. A. F. Schuch and J. H. Sturdivant, J. Chem. Phys. 18, 145 (1950).

37. K. A. Gschneidner, Jr., R. O. Elliott and R. R. McDonald, J. Phys. Chem. Solids 23, 1191 (1962).

38. S. M. Shapiro, J. D. Axe, R. J. Birgeneau, J. M. Lawrence and R. D. Parks, Phys. Rev. B 16, 2225 (1977).

39. A. Jayaraman, P. D. Dernier and L. D. Longinotti, High Temperatures-High Pressures 7, 1 (1975) and references therein.

40. A. Jayaraman, A. K. Singh, A. Chatterjee and S. Usha Devi, Phys. Rev. B 9, 2513 (1974).

41. E. Bucher, V. Narayanamurti and A. Jayaraman, J. Appl. Phys. 42, 1741 (1971).

42. M. P. Maple and D. Wohlleben, Phys. Rev. Lett. 27, 511 (1971).

43. A. Chatterjee, A. K. Singh and A. Jayaraman, Phys. Rev. B 6, 2285 (1976).

44. A. Jayaraman, V. Narayanamurti, E. Bucher and R. G. Maines, Phys. Rev. Lett. 25, 368, 1430 (1970).

45. A. Jayaraman, in Proceedings of the 11th Rare-Earth Research Conference, Vol. 2, p. 830 (1974).

46. S. D. Bader, N. E. Phillips and D. B. McWhan, Phys. Rev. B 7, 4686 (1973).

47. H. A. Mook and R. M. Nicklow, Phys. Rev. B 20, 1656 (1979).

48. K. A. Gschneidner, Jr., R. O. Elliott and R. R. McDonald, J. Phys. Chem. Solids 23, 1201 (1962).

49. C. S. Barret, Structure of Metals (McGraw-Hill, New York, 1952), p. 221.

50. I. R. Harris and G. V. Raynor, J. Less-Common Metals 6, 70 (1967).

51. I. R. Harris and G. V. Raynor, J. Less-Common Metals 7, 11 (1964).

52. I. R. Harris and M. Norman, J. Less-Common Metals 15, 285 (1968).

53. I. R. Harris and G. V. Raynor, J. Less-Common Metals 7, 1 (1964).

54. I. R. Harris and G. V. Raynor, J. Less-Common Metals 9, 7, 263, 270 (1965).

55. T. Tsuchida and W. E. Wallace, J. Chem. Phys. 43, 3811 (1965).

56. C Stassis, C.-K. Loong, O. D. McMasters and R. M. Moon, J. Appl. Phys. 50, 2091 (1979).

57. S. K. Malik, R. Vijayaraguavan, S. K. Garg and R. J. Rimpeester, Phys. Stat. Sol. (b) 68, 399 (1975).

58. J. R. Cooper, C. Rissuto and G. Olcese, J. De Physique 37, C1-1136 (1971).

59. A. M. Toxen, IBM Watson Research Center, Yorktown Heights, New York (unpublished).

60. S. Misawa, Solid State Commun. 15, 507 (1974).

61. J. Beille, D. Bloch, J. Voiron and G. Parisot, Physica 86-88B, 231 (1977).

62. B. Staliński, Z. Kletowski and Z. Henkie, Phys. Stat. Sol. (a) 19, K165 (1973).

63. A. Maury, P. Scoboria, J. E. Crow and T. Mihalisin, J. Appl. Phys. 50, 7572 (1979).

64. P. Lethuillier, and C. Lacroix-Lyon-Caen, J. de Physique 39, 1105 (1978).

65. A. Benoit, J. Flouquet and M. Ribault, J. de Physique Lett. 39, L-63 (1978).

66. G. K. Shenoy, B. D. Dunlap, G. M. Kalvius, A. M. Toxen and R. J. Gambino, J. Appl. Phys. 41, 1317 (1970).

67. L. B. Welsh and J. B. Darby, Jr., AIP Conf. Proc. 10, Pt. 2, 1325 (1972).

68. F. Borsa, R. G. Barnes and R. A. Reese, Phys. Stat. Sol. 19, 359 (1967).

69. S. K. Malik, R. Vijayaraghavan, S. K. Garg and R. J. Ripmeester, Pure Appl. Chem. 40, 223 (1975).

70. K. H. J. Buschow, V. Goebel and E. Dormann, Phys. Stat. Sol. (b) 93, 607 (1979).

71. R. Nathans, C. G. Shull, G. Shirane and A. Andresen, J. Phys. Chem. Solids 10, 138 (1959).

72. Y. Ito, S. Takahashi, Y. Kawamura, K. Motoya and M. Nishi, Nukleonika, 24, 699 (1979).

73. F. Mezei, Physica 86-88B, 1049 (1977).

74. L. W. Alvarez and F. Bloch, Phys. Rev. 57, 111 (1940).

75. R. M. Moon, W. C. Koehler and J. W. Cable, in Proceedings of the Conference on Neutron Scattering, Gatlinburg, 1976 (CONF-760601-P2) p. 577.

76. O. Steinsvoll, G. Shirane, R. Nathans and M. Blume, Phys. Rev. 161, 499 (1967).

77. P. W. Bridgman, Proc. Amer. Acad. Art Sci. 60, 305 (1925).

78. G. E. Bacon, Neutron Diffraction, 3rd ed., (Clarendon Press, Oxford, 1975) p. 67.

79. C. G. Darwin, Phil. Mag. 43, 800 (1922).

80. W. H. Zachariasen, Theory of X-ray Diffraction in Crystals (John Wiley, New York, 1945).

81. W. H. Zachariasen, Acta Cryst. 23, 558 (1967).

82. G. E. Bacon and R. D. Lowde, Acta Cryst. 1, 143 (1948).

83. M. Bonnet, A. Delapalme, P. Becker and H. Fuess, Acta Cryst. A 32, 945 (1976) and references therein.

84. R. Wagner, Phys. Z. 21, 632 (1920).

85. M. Renninger, Z. Phys. 106, 141 (1937).

86. J. B. Hastings, A. L. Andreassen and W. R. McIntire, Report #1788, Cornell University, Ithaca, New York (1972) (COO-3164-4).

87. H. Cole, F. W. Chambers and H. M. Dunn, Acta Cryst. 15, 138 (1962).

88. S. Collins, Massachusetts Institute of Technology, Cambridge, Massachusetts (private communication).

89. R. M. Moon and C. G. Shull, Acta Cryst. 17, 805 (1964).

90. E. Fermi, Ricera Scientifica 1, 1936).

91. C. Stassis, Phys. Rev. Lett. 24, 1415 (1970).

92. M. E. Rose, U. S. Atomic Energy Commission Report AECD-2183 (1948) (unpublished).

93. C. G. Shull and R. P. Ferrier, Phys. Rev. Lett. 10, 295 (1963).

94. L. L. Foldy, Rev. Mod. Phys. 30, 471 (1958).

95. J. Schwinger, Phys. Rev. 73, 407 (1948).

96. C. G. Shull, Phys. Rev. Lett. 10, 297 (1963).

97. F. Bloch, Phys. Rev. 50, 259 (1936).

98. J. Schwinger, Phys. Rev. 51, 544 (1937).

99. O. Halpern and M. H. Johnson, Phys. Rev. 55, 898 (1939).

100. G. T. Trammell, Phys. Rev. 92, 1387 (1953).

101. S. Odiot and D. Saint-James, J. Phys. Chem. Solids, 17, 117 (1960).

102. E. U. Condon and G. H. Shortley, The Theory of Atomic Spectra (Cambridge University Press, London, 1935).

103. D. F. Johnston, Proc. Phys. Soc. Land. 88, 37 (1966).

104. D. F. Johnston and D. E. Rimmer, J. Phys. C 2, 1151 (1969).

105. S. W. Lovesey and D. E. Rimmer, Rep. Prog. Phys. 32, 333 (1969).

106. E. Balcar and S. W. Lovesey, Phys. Lett. A 31, 67 (1970).

107. E. Balcar, in Proc. Int. Magnetism Conf. Moscow, Vol. 2 (Moscow: Nanka), 250 (1973).

108. S. W. Lovesey, J. Phys. C 2, 470 (1969).

109. E. Balcar, S. W. Lovesey and F. A. Wedgewood, J. Phys. C 3, 1292 (1970).

110. A. Mahendra and D. C. Khan, J. Phys. C 4, 3307 (1971).

111. W. Marshall and S. W. Lovesey, Theory of Thermal Neutron Scattering (Oxford University Press, London, 1970).

112. C. Stassis and H. W. Deckman, Phys. Rev. B 12, 1885 (1975).

113. C. Stassis and H. W. Deckman, in Magnetism and Magnetic Materials-1975, 29, 274 (1976).

114. C. Stassis and H. W. Deckman, J. Phys. C 9, 2241 (1976).

115. C. Stassis and H. W. Deckman, Phys. Rev. B 13, 4943 (1976).

116. C. Stassis, H. W. Deckman, B. N. Harmon, J. P. Desclaux and A. J. Freeman, Phys. Rev. B 15, 369 (1977).

117. S. K. Sinha, in Handbook on the Physics and Chemistry of Rare Earths, Vol. I, edited by K. A. Gschneidner, Jr. and L. Eyring (North Holland Publishing Co., Amsterdam, 1978), Chapter 7.

118. C. Stassis, Nukleonika, 24, 765 (1979).

119. S. H. Liu, Physics Department, Iowa State University, Ames, Iowa, to be published.

120. A. J. Freeman, in Magnetic Properties of Rare Earth Metals, edited by R. J. Elliott (Plenum, New York, 1972), Chapter 6.

121. K. H. Oh, B. N. Harmon, S. H. Liu and S. K. Sinha, Phys. Rev. B 14, 1283 (1976).

122. C. Stassis, C.-K. Loong, O. D. McMasters and R. M. Moon, J. Applied Phys. 50, 2901 (1979).

123. C. Stassis, C.-K. Loong, B. N. Harmon, S. H. Liu and R. M. Moon, J. Applied Phys. 50, 7567 (1979).

124. The values of coherent neutron scattering amplitudes were obtained from a compilation by C. G. Shull, M.I.T., Cambridge, Massachusetts (1972).

125. B. T. M. Willis and A. W. Pryor, Thermal Vibrations in Crystallography (Cambridge University Press, Cambridge, England, 1975), Chpater 4.

126. J. Faber, C.-K. Loong and C. Stassis, "Neutron and X-ray Scattering Study of Mixed Valent $CeSn_3$," Phys. Rev. B to be published.

127. R. J. Weiss and A. J. Freeman, J. Phys. Chem. Solids, 10, 147 (1959).

128. C. M. Varma and Y. Yaffet, Phys. Rev. B 13, 2950 (1976).

129. A. Bringer and H. Lustfeld, Z. Physik B 28, 213 (1977).

130. H. Lustfeld and A. Bringer, Solid State Commun. 28, 119 (1978).

131. S. K. Sinha and A. J. Fedro, J. de Physique 40, C4-214 (1979).

132. S. H. Liu, B. N. Harmon, C. Stassis and S. Symeonides, J. Magnetism and Magnetic Materials 15, 942 (1980).

133. K. M. Brown and J. E. Dennis, Numerische Mathematik 18, 289 (1972).

134. E. P. Wigner and F. Seitz, Solid State Physics 1, 97 (1955).

135. M. Born and Th. von Kármán, Z. Physik 13, 297 (1912).

136. M. Born and K. Huang, Dynamical Theory of Crystal Lattices (Clarendon, Oxford, 1954).

137. G. Venkataraman, L. A. Feldkamp and V. C. Sahni, Dynamics of Perfect Crystals (M.I.T., Cambridge, 1975).

138. M. Born and J. R. Oppenheimer, Ann. Physik 84, 457 (1927).

139. See reference 136 above, Chapter IV and Appendix VII.

140. J. C. Slater, Quantum Theory of Molecules and Solids (McGraw-Hill New York, 1963), Vol. I.

141. F. Seitz, Modern Theory of Solids (McGraw-Hill, New York, 1940), p. 470.

142. J. Ziman, Principles of the Theory of Solids, 2nd edition (Cambridge University Press, London, 1972), p. 200.

143. G. V. Chester, Advan. Phys. 10, 357 (1961).

144. E. G. Brovman and Yu. Kagan, Zh. Eksp. Theor. Fiz. 52, 557 (1967) [Sov. Phys. - JETP 25, 365 (1967)].

145. K. Londsdale, International Tabes of X-ray Crystallography (Kynoch, Birmingham, 1965), Vol. I. p. 330.

146. M. Lax, Symmetry Principles in Solid State and Molecular Physics (John Wiley & Sons, New York, 1974), p. 161.

147. H. G. Smith and N. Wakabayashi, in Dynamics of Solids and Liquids by Neutron Scattering, edited by S. W. Lovesey and T. Springer (Springer-Verlag, New York, 1977) p. 77.

148. See reference 125 above, p. 221.

149. P. K. Iyengar, in Thermal Neutron Scattering, edited by P. A. Egelstaff (Academic Press, New York), 98.

150. G. Dolling, in Dynamical Properties of Solids edited by G. K. Horton and A. A. Maradudin (North-Holland, Amsterdam, 1974), p. 541.

151. B. N. Brockhouse, S. Hautecler and H. Stiller, in The Interaction of Radiation with Solids, edited by R. Strumane, J. Nihoul, R. Gevers and S. Amelineky (North-Holland, Amsterdam, 1964).

152. M. J. Cooper and R. Nathans, Acta Cryst. 23, 357 (1967).

153. B. N. Harmon, Physics Department, Iowa State University, Ames, Iowa (private communication).

154. S. K. Ghatak and K. H. Bennemann, J. Phys. F 8, 571 (1978).

155. N. Grewe and P. Entel, Z. Physik B 33, 331 (1979).

156. P. Entel, N. Grewe, M. Sietz and K. Kowalski, Phys. Rev. Lett. 43, 2002 (1979).

157. R. J. Gambino, N. R. Stemple and A. M. Toxen, J. Phys. Chem. Solids 29, 295 (1968).

158. C. Stassis, J. Zarestky and B. N. Harmon, Solid State Commun. 26, 161 (1978).

159. C. Stassis, J. Zarestky, D. Arch, O. D. McMasters and B. N. Harmon, Phys. Rev. B 18, 2632 (1978).

160. C. Stassis. D. Arch, B. N. Harmon and N. Wakabayashi, Phys. Rev. B 19, 181 (1979).

161. C. Stassis, D. Arch, J. Zarestky, O. D. McMasters and B. N. Harmon, Solid State Commun. 35, 259 (1980).

162. D. Arch, Ph.D. Thesis (Iowa State University, 1980) (unpublished).

163. See reference 136 above, p. 229.

164. A. S. Edelstein, S. K. Sengupta, R. L. Carlin and O. D. McMasters, Phys. Rev. B, to be published.

165. G. Lehmann, P. Rennert, M. Taut and H. Wonn, Phys. Stat. Sol. 37, K27 (1970).

166. G. Lehmann and M. Taut, Phys. Stat. Sol. (b) 54, 469 (1972).

167. O. Jepsen and O. K. Andersen, Solid State Commun. 9, 1763 (1971).

168. T. Gould, M.S. Thesis (Iowa State University, 1978) (unpublished).

169. E. Umlauf, P. Sütsch, E. Hess, in Proceedings of the International Conference on Crystalline Electric Field and Structural Effects in f-Electron Systems, Philadelphia, November 1979 (Plenum Press, New York) to be published.

170. S. Arajs and R. V. Colvin, J. Less-Comm. Metals 4, 159 (1962).

171. D. T. Cromer and J. T. Waber, LA-3056, UC-34, Physics, TID-4500 (27th Ed.) Los Alamos Scientific Laboratory (1964).

XI. ACKNOWLEDGEMENTS

The author wishes to express his gratitude to Prof. C. Stassis for his expert guidance and support throughout the course of this work. Special thanks are also extended to other members of the neutron scattering group of the Ames Laboratory, in particular Drs. J. Zarestky, J.-L. Staudenmann, D. Arch and Ms. C. Theisen for their assistance and encouragement. The author is indebted to Prof. B. N. Harmon for many helpful discussions concerning the analysis of the experimental results and for his support and encouragement during the author's graduate career. Appreciation is extended to Prof. S. H. Liu for providing invaluable theoretical guidance, Prof. K. A. Gschneidner and Mr. O. D. McMasters for supplying the samples used in the experiments, and Prof. S. Legvold for performing the susceptibility measurements. Sincere thanks are given to Ms. Lesley Swope for her excellent preparation of the manuscript.

The author is grateful for having at his disposal the excellent experimental facilities of the Ames Laboratory, Oak Ridge National Laboratory and Argonne National Laboratory and the scientific expertise of their members. Special appreciation is extended to Drs. M. Wilkinson, W. Koehler, R. M. Moon, R. M. Nicklow and N. Wakabayashi of ORNL for the consideration given to the author during this work. The experimental assistance of Mr. J. L. Sellers and Mr. C. Zulliger of ORNL is gratefully acknowledge. The author has profited from the enlightening discussions with Drs. J. Faber, G. H. Lander, M. H. Mueller and S. K. Sinha of ANL.

Finally, the author wishes to thank his close friend Prof. D. C. Wendell for his invaluable assistance and encouragement throughout the author's professional development.